

School of Mechanical, Materials and Manufacturing Engineering



**University of  
Nottingham**  
UK | CHINA | MALAYSIA

**Surface Texturing on Dry-Lubricated Transmissions and  
Power Systems to Deliver Better Performance and  
Simplified Systems in Aerospace Engineering**

*By*

*Liang Ding*

*September 2020*

**Thesis submitted to the University of Nottingham for the degree of  
Doctor of Philosophy**



# Contents

Abstract.....	1
Acknowledgement .....	3
Publications.....	4
Nomenclature .....	5
Chapter 1.....	8
Introduction .....	8
1.1 Background.....	8
1.2 Problem overview .....	10
1.3 Aims and objectives .....	11
1.4 Structure of the thesis.....	12
1.5 Highlights and contributions of the thesis .....	14
Chapter 2.....	16
Literature review.....	16
2.1 Tribology and dry-lubricated bearings .....	16
2.1.1 History and development of tribology and bearing systems .....	16
2.1.2 Dry-lubricated bearings and the applications in aerospace .....	18
2.2 Surface texturing in contact applications .....	38
2.2.1 Development in surface texturing technologies .....	38
2.2.2 Surface texturing for tribological performance in dry contact.....	43
2.2.3 Surface texturing for bonding performance.....	49
2.3 Summary and research gaps .....	54
Chapter 3.....	58
Methodology.....	58
3.1 Sliding wear test for tribological effects of counterface textures .....	58
3.1.1 Sliding wear test with pin-on-plate test scheme .....	58
3.1.2 Sample preparation .....	61
3.1.3 Test monitoring and signal analysis.....	69
3.1.4 Surface analysis and transfer film characterisation.....	75
3.1.5 Finite Element analysis for contact mechanics.....	79
3.2 Bonding strength test for bearing liner on sleeve surface.....	83
3.2.1 Basic test methods for bonding strength .....	83
3.2.2 Sample preparation .....	86

3.2.3	Post-test analysis methods .....	88
Chapter 4.....		90
The effects of surface texturing on the tribological performance and transfer film formation of dry-lubricated bearings.....90		
4.1	Introduction.....	90
4.2	Preliminary trials .....	91
4.2.1	Trials for test condition benchmarking.....	91
4.2.2	Trials for texturing parameters selection .....	95
4.3	Friction and wear tests for the effects of textured counterface .....	97
4.4	Surface analysis results .....	103
4.4.1	Transfer film characterisation: Benchmark on smooth counterface .....	104
4.4.2	Transfer film analysis: Towards understanding of textured counterface .....	109
4.5	Finite element analysis for the contact mechanics.....	115
4.5.1	Model evaluation and relevant adaptations.....	116
4.5.2	Analysis of the contact condition with different textured counterface.....	124
4.6	Conclusions.....	129
Chapter 5.....		132
The effect of surface texturing on the anisotropy of the tribological performance .....132		
5.1	Introduction.....	132
5.2	Analysis of the kinematics of the pitch-control-bearings in helicopter main rotor.....	133
5.2.1	Proposed modelling principle for the kinematics - output-oriented strategy .....	133
5.2.2	The kinematic model of helicopter pitch-control-bearings.....	136
5.3	Wear test for the anisotropy in the tribological performance .....	145
5.3.1	Friction and wear measurements.....	146
5.3.2	Post-test surface analysis.....	147
5.3.3	FE analysis of the stress re-distribution effect from counterface textures.....	153
5.4	Conclusions.....	156
Chapter 6.....		159
The effects of surface texturing on the bonding strength of the bearing liner.....159		
6.1	Introduction.....	159
6.2	Experimental scheme and sample surface characterisation .....	159
6.3	Lap shear tests – for quantification analysis.....	165
6.3.1	Investigating the influence by surface texturing- comparison between surfaces with different texturing methods.....	166

6.3.2	Contact angle measurements .....	168
6.3.3	Post-test SEM analysis .....	171
6.4	Bearing liner peel tests – for qualitative final check.....	176
6.5	Wettability analysis for the roughened/textured surfaces.....	179
6.5.1	Interpretation using conventional models and the inefficiency .....	179
6.5.2	Derivation of the wettability model based on surface free energy analysis...	181
6.5.3	Evaluation and application of the wettability model .....	188
6.6	Conclusions.....	200
7	Conclusions, discussions and future work.....	202
7.1	Aims and objectives met .....	203
7.2	Contributions and conclusions obtained .....	204
7.3	Discussion based on the findings .....	206
7.4	Future work.....	209

## Abstract

Dry-lubricated contact systems are widely used in varied engineering applications, among which the spherical plain bearing (with dry-lubricating liner) in aerospace applications is one with increasing demands in performance. To achieve the improvements, the surface texturing is a propitious technique since it has seen a rapid development in the last few decades as it achieved promising effects in friction, wear and adhesion with different forms. However, to tailor the surface textures to the needs in tribological performance, it is essential to fill the gap of knowledge in the aspects such as the interaction between the liner surface and the textured counterface and the influence of the kinematics of the transmission system. Meanwhile, the relationship between the bonding strength of the liner and texturing morphology and adhesion force needs to be investigated.

The research in this thesis firstly aims at explaining the effects of surface texturing on the tribological performance of the dry contact pair (Polytetrafluoroethylene, or PTFE composite against steel surfaces), conducting systematic test series investigating the friction and wear performance with different texturing parameters (e.g. depth, coverages). To obtain understanding of the tribological phenomenon occurring with the dry contact, a novel transfer film characterisation technique based on multi-accelerating-voltage Scanning electron microscope (SEM) and Secondary ion mass spectrometry (SIMS) is developed. With this method, previous obscurity in the transfer film characterisation, particularly with worn counterface is eradicated. Combined with contact mechanics analysis using Finite Element (FE) methods, the mechanism of micro-abrasion and transfer film formation/re-distribution are identified.

Moreover, in this work a new aspect of the effects of the surface texturing on tribological performance is explored, considering the kinematics of the transmission system. With the proposed novel output-oriented modelling method of the kinematics of the transmission, a series of anisotropy tests of the tribological performance is instructed, leading to the finding that surface texturing may alter the anisotropy of the dry contact. Fundamentally, the introduced surface textures convert the contact between an anisotropic surface (composite) and a homogenous counterface into a contact between two heterogeneous surfaces.

Finally, this work investigates the effects surface texturing/roughing in bonding strength and improvement. The basic mechanism and phenomenon related with bonding strength are discussed. After identifying the inefficiency in describing the wettability of textured surfaces

with conventional contact angle models, the surface free energy analysis is modified with a droplet morphology analysis. The theoretical support for anisotropic wettability of surfaces with directional surface textures is formulated.

To conclude, focusing on the physical phenomenon and working mechanism of surface textures in dry-lubricated contact system, this thesis illustrates the influence of surface texturing on tribological performance and bonding strength of bearing liner in aerospace applications. With the innovative transfer-film characterisation technique, systematic contact mechanics analysis, the output-oriented kinematic modelling and the modified surface free energy analysis for wettability, knowledge is added to the corresponding aspects that have opacity in previous research.

## **Acknowledgement**

Firstly, I would like to express my highest gratitude to my main supervisor Professor Dragos Axinte, for his support and guidance on my way to pursue the PhD degree at the University of Nottingham. His helps are valuable in both my academic research and life perspectives, and his work ethic and wisdom have inspired me all the way to achieve the outcome now. I really value the experience working under his supervision.

Then, I would like to thank to the support from SKF UK Ltd. for establishing the subject and providing the materials needed for my research. Particularly I would like to mention the help and suggestions given Mr Michael Colton, Dr Johnpaul Woodhead, and Dr Grant Dennis. Moreover, my gratitude also goes to the administration from Institute of Aerospace Technology in the University of Nottingham, who together with the Marie Sklodowska-Curie INNOVATIVE programme supported by European Commission offered the generous financial support for me.

In addition, I would like to thank my second supervisor Paul Butler-Smith, who also gave me valuable suggestions and guidance during the research. Similar appreciation also goes to the help I received from the Advanced manufacturing group, including Ali Abdelhafeez who helped me with the Finite Element model, David Cha who helped me with the laser surface texturing and Dorian Lachowicz who assisted me with the strain gauge frame design.

What is more, I would like to thank my family back in China, as they provided their mental support all the time with their endless love.

Finally, special thanks go to the NHS workers, the medical workers back in my hometown China and all over the world. Their heroic actions in this hard time protect us from devastation from the Covid-19.

Liang Ding

20th, Sep, 2020

Nottingham, UK

## **Publications**

The research work in this thesis has contributed in part or full to the following publications and conference meetings:

Liang Ding, Dragos Axinte, Michael Colton. On the influence of surface texturing on the bonding strength and wettability with three dimensional surface energy analysis. (Revising)

Liang Ding, Dragos Axinte, Paul Butler-Smith, Michael Colton, Zhirong Liao. On the significance of composite orientation and counter-surface heterogeneity in an output-oriented sliding system with transcendental spherical sliding curves. *Wear*. (Submitted)

L. Ding, D. Axinte, P. Butler-Smith, A. Abdelhafeez Hassan, Study on the characterisation of the PTFE transfer film and the dimensional designing of surface texturing in a dry-lubricated bearing system, *Wear*. 448–449 (2020). <https://doi.org/10.1016/j.wear.2020.203238>.

# Nomenclature

## Chapter 2

$H_n$	Hersey number
$\nu$	Dynamic viscosity
$P$	Average pressure/ nominal pressure on the bearing surfaces
$\lambda$	Relative film thickness ratio
$h_{min}$	Minimum fluid film thickness
$R_q$	Root mean square average of the roughness profile of a surface
$V$	Sliding speed between two surfaces
$R_a$	Arithmetic average of the roughness profile
$G$	Practical adhesion (in the form of energy)
$G_0$	Fundamental adhesion (in the form of energy)
$\psi$	Energy from other absorbing processes

## Chapter 3

$dep$	Depth of concavity texture
$p_c$	Area coverage (percentage) of texture
$d$	Diameter of circular concavity texture
$P_l$	Laser output power
$t_l$	Laser dwell time
$L$	Distance between adjacent surface texture
$d_0$	Diameter of original circular concavity texture before polishing
$F_N$	Normal force applied for polishing
$\omega$	Rotating speed applied for polishing
$t_p$	Polishing time
$V_0$	Output voltage of strain gauge bridge
$R_i$	Resistance of strain gauge number i
$V_{EX}$	Excitation voltage for strain gauge bridge
$F_{x,y,z}$	Measured force in x, y and z axis by dynamometer
$\Pi$	Virtual work in Finite Element (FE) model
$U$	Work done by the external force in Finite Element (FE) model
$W$	Work done by the equilibrating stresses in Finite Element (FE) model

$\tau$	Material stress
$\varepsilon$	Material strain
$\mathbf{t}$	Unit surface force
$\mathbf{f}$	Body force of a point
$v$	Body volume
$h$	Overclosure between two contact surfaces
$\tau_{eq}$	Equivalent stress under sliding friction
$\dot{\gamma}_i$	Tangential slip velocities of the implemented velocity fields ( $i = 1,2$ )
$\dot{\gamma}_{eq}$	Combined velocities of both tangential slip velocities

#### Chapter 4

$p$	Probability-value of null hypothesis
$PV$	Product of contact pressure $P$ and sliding velocity $V$
$LPV$	Limiting $PV$ value
$S. Mises$	Von Mises Stress in FE model
$C. Press$	Contact pressure in FE model
$\sigma_{LPV}$	Critical stress under $LPV$ condition
$\sigma_{y-compo}$	Equivalent Yield stress of the composite

#### Chapter 5

$\alpha$	Tilting angle of swashplate on the initial position
$\alpha_v$	Viewing angle for liquid droplet for contact angle measurement
$\beta$	Projection of angle $\delta$ on the horizontal plane
$\gamma$	Tilting angle of swashplate
$\delta$	Rotation angle of the pitch-control bearing from its initial position
$\varepsilon$	Angle between the projection of pitch-control rod on $Z'OP$ plane and the $Z$ axis
$\eta$	Angle $Z_0OP$ in the coordinate system for the pitch control bearing
$\theta_0$	Pitch angle of a rotor blade
$\varphi$	Angle between the pitch-control rod and the $X$ axis (bearing local coordinate)
$l_i$	Length of the quadrilateral composed of main rotor components

## Chapter 6

$\sigma_u$	Ultimate bonding strength
$\sigma_y$	Yield bonding strength
$\theta$	Modelled contact angle
$\theta_c$	Measured contact angle
$\theta_Y$	Young's contact angle
$r$	Coefficients of correlation for Pearson analysis
$\rho$	Coefficients of correlation for Spearman analysis
$A_c$	Cohesive failure area on lap shear specimen
$A_r$	Adhesive failure area on lap shear specimen
$A_o$	Overlapped area
$w$	Trench/groove width
$l$	Blank (non-textured) length between trench/grooves
$W$	Surface energy
$\gamma_{lg}$	Surface tension between the liquid and the gas
$\gamma_{sl}$	Surface tension between the solid and the liquid
$\gamma_{sg}$	Surface tension between the solid and the gas
$A_{lg}$	Contact area between the liquid and the gas
$A_{sl}$	Contact area between the solid and the liquid
$A_{sg}$	Contact area between the solid and the gas
$F$	Normalized surface energy
$G$	Increase of liquid-gas interfacial area
$S$	Increase of liquid-solid interfacial area
$y_s$	Half base width of the droplet on the smooth surface
$h_p$	Relative penetration ratio of liquid droplet in the texture concavity
$r_d$	Depth-width ratio of the texture
$\alpha_v$	Viewing angle on the liquid droplet for contact angle measurement
$r_a$	Real area ratio between the rough surface and smooth surface
$V_i$	Volume of the liquid droplet above smooth ( $i=1$ ) or textured surface ( $i=2$ )
$V_{pen}$	Volume of the liquid droplet penetrating into the concavity texture
$w_a$	Half base width of the liquid droplet on the smooth surface
$w_{di}$	Half base width of the liquid droplet on smooth ( $i=1$ ) or textured surface ( $i=2$ )
$h_d$	Height of liquid droplet

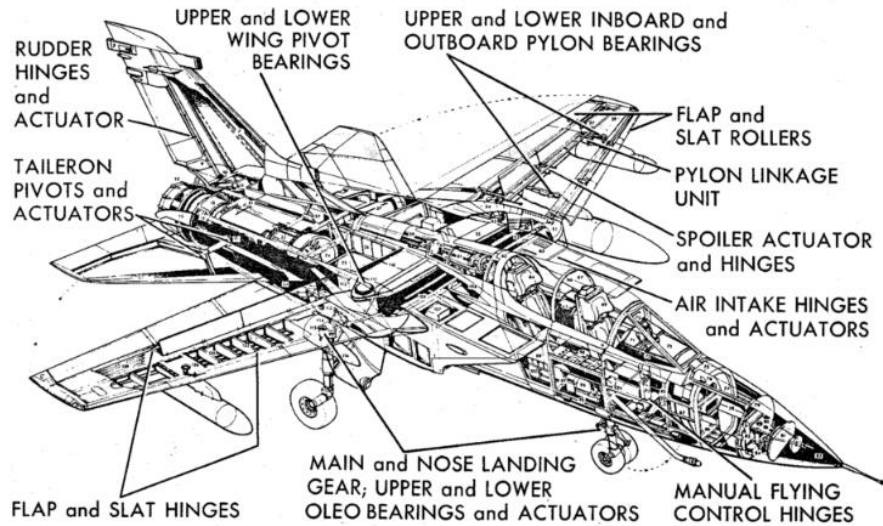
# Chapter 1

## Introduction

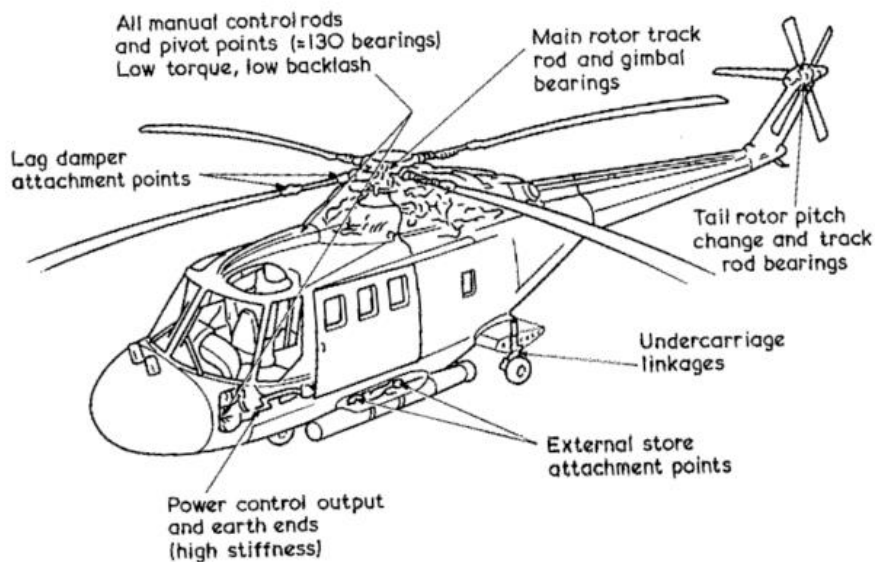
### 1.1 Background

The last few decades witnessed the growing of aerospace industry, and flights have now become an essential part to peoples' lives. According to the *European Aviation Environmental Report 2019*, the annual flight number to and from the airports in just European Union and European Free Trade Association reached 9.56 million in 2017 [1]. In every flight, it is of utmost importance to ensure the functionality of the all the different systems, as the slightest fault or failure may lead to catastrophic incident and loss of lives on board. Apart from the requirement in performance and reliability, the ever-increasing concern in environmental issues also urges for less energy consumption and carbon emission. Starting from 1 January 2020, the latest global environmental standards adopted by International Civil Aviation Organization have become effective through enforcement by European legislation [2]. In the new CO<sub>2</sub> standard, an additional requirement is given to the design process to prioritise the fuel efficiency in the overall aeroplane design. Aiming at these requirements, the designers and manufacturers in the aero-industry are constantly searching for engineering solutions that lead to higher performance efficiency and reduced energy cost.

Previously, improvements have been made in the transmission and drivetrain of the aircrafts for the pursuits stated above. Among them, the dry-lubricated bearing emerges and evolves to be an essential piece of mechanical component. Compared with its predecessors - the rolling element bearing and the oil-sintered bearing, the dry-lubricated bearing requires no re-application of lubricant or specific operation condition (i.e. rotational speed for fluid-film build-up), namely becoming 'maintenance free' and 'self-lubricating'. Benefiting from these features, the lubricating system have been simplified tremendously, leading to weight reduction and contributing to the speed performance, manoeuvrability, and fuel efficiency of aircrafts. The drawings in **Figure 1** [3] can give a brief view on the wide applications of dry-lubricated bearings in both fixed-wing aircrafts and helicopters.



(a)



(b)

**Figure 1.** Typical applications of dry-bearing liners for flight control in (a) a fixed wing aircraft (Tornado fighter jet) and (b) a helicopter [3]

As dry-lubricated bearings have witnessed many advancements, the pursuit for performance improvement never stops. While there is always room for reducing the dry-lubricated friction when compared with the fluid-lubricated conditions, the improved wear life and reliability are equally, if not even more urged. Apart from its connectivity with the aircraft safety, the bearing replacing interval (i.e. the number of hours for continuous aircraft operation before the end of bearing lives) also needs to be extended as long as possible considering that the overall cost of grounding an aircraft for such a servicing is huge (estimated at €35,000 per time [4]).

When reflected on the properties and performance of the bearings, the following three basic performance pursuits in the development of self-lubricating bearings are urged:

- Lower friction of the dry-lubrication for reduction in emission and energy consumption
- Longer wear life of the bearing liner for prolonged replacing interval
- Higher bonding strength of the bearing liner for superior reliability

Along with other concerns like cost and waste reduction in the manufacturing process, these pursuits compose the motivations for the work in this thesis.

## **1.2 Problem overview**

During the development history of dry-lubricated bearings, great effort has been put into the development of the self-lubricating liner [5–9] and the counterface material [3,10,11]. Nowadays, self-lubricating liner made of polymer composites (e.g. PTFE composites) and various types of counterface (e.g. hardened stainless steel, ceramic coatings) have become an efficient bearing system with established tribological performance. However, the improvement on counterface topography is often conservative, only confined within the optimization of surface roughness and hardness. Recently, with the development of advanced manufacturing technologies, the prospect has emerged on using novel surface texturing technologies, such as laser-surface-texturing (LST) to tailor the counterface topography for performance pursuits. Therefore, this thesis conducts a first effort to fill the gap on exploring this field.

Firstly, the biggest motivation for counterface texturing is from the functioning mechanism of self-lubricating polymers – the transfer film formation on the counterface. To investigate whether the proposed enhancement can be achieved by counterface textures, the previous issues with observing and characterising the transfer film need to be addressed. Meanwhile, other effects accompanying the counterface texturing (e.g. contact pressure lift), and how the parameters of the surface textures (e.g. geometric dimensions) influence those effects need to be identified.

Moreover, depending on the transmission applications the bearings may be undergoing different motions. In these occasions, the influence of kinematics should also be considered, as they may pose great difference in performance particularly considering the possible anisotropy incurred by the composite heterogeneity. Hereto, the introduction of counterface textures converts the original contact problem between an anisotropic surface (composite) and an

isotropic surface (smooth counterface) into two surfaces with heterogeneity (one in material the other in topography), so it would be interesting to investigate what difference counterface textures would incurred in this aspect.

Finally, apart from the sliding contact between the liner and the inner-ring counterface, the bonding between the liner back and the sleeve surface is also of great importance- it fundamentally influences the reliability of the system as an insufficient bonding strength may lead to detachment of the liner during operation and consequently catastrophic failure. Therefore, as proposed in **Figure 2**, the possibility of using different texturing technologies to improve the bonding strength between the liner and the sleeve surface can also be explored.

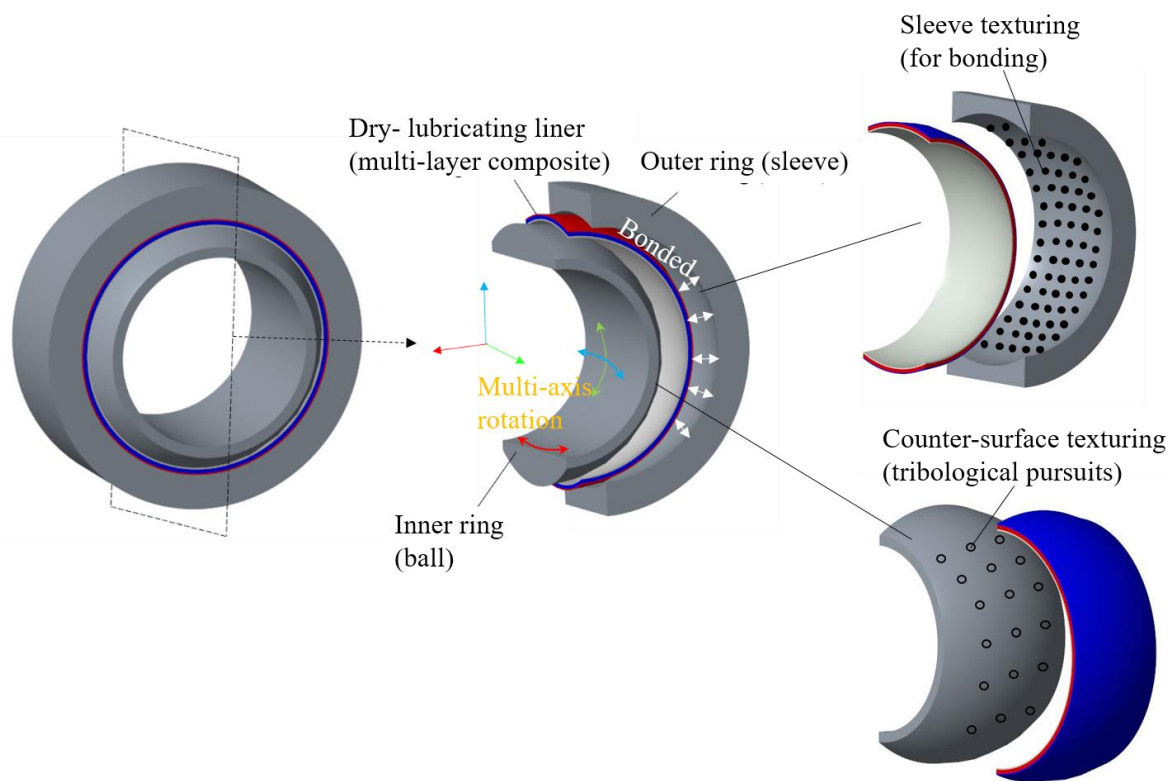


**Figure 2.** Configuration of a spherical bearing with self-lubricating composite liner and the proposed texturing schemes for different performance pursuits

### 1.3 Aims and objectives

This thesis aims at exploring the possibility of using surface texturing to improve the tribological performance of a dry-lubricated bearings, and the bonding strength of the self-lubricating liner. To achieve this goal, the following objectives are proposed for the fulfilment of the project:

- ❑ To investigate the tribological phenomenon and effects created by counterface texturing on dry-lubricated contact. The mechanism how the surface textures affect the tribological performance should be found through a series of systematic tribological tests with a typical self-lubricating contact pair (PTFE composite vs steel counterface), while the focus should not only be on the optimization of the texture parameters. To fulfil this, necessary analysis methods (surface analysis and contact mechanics, etc.) also need to be developed.
- ❑ To develop a comprehensive methodology for characterising PTFE transfer film, as it is the key analysis for identifying the effects from counterface modifications in dry-lubricated bearings. The existing problems in characterising the transfer film in previous research should be targeted, and the novel method should solve the problems with universality among similar dry-lubricated scenarios (by self-lubricating polymer) by considering the general physical phenomenon in this sliding contact.
- ❑ To investigate the effect of sliding direction/ composite orientation on the tribological performance of self-lubricating bearings. Due to possibility of the self-lubricating composite to establish anisotropic tribological behaviour (originating from the heterogeneity in material distribution), understanding the tribological performance with different sliding direction can help optimize liner alignment. To achieve this, the study will be conducted on the phenomenon that can contribute to the anisotropy in the tribological performance, as well as on the bearing kinematics to help identify the test methodology related with the realistic operation conditions.
- ❑ To study the influence of surface texturing/roughening on the bonding strength of the liner- sleeve bond. The effects created by different surface topographic modifications need to be identified, along with the development of novel surface texturing/roughening process tailored for fulfilling established effects. Analysis should be taken to identify if any resultant physical properties and phenomenon would contribute to the improvement in bonding, while theoretical explanations should be built to guide the development in the future.

## **1.4 Structure of the thesis**

In chapter 2, an extensive literature reviewed will be given, covering the related fields including: history and development of dry-lubricated bearings, with focus on their aerospace applications;

history and development of surface texturing technologies, with focus on their applications in contact problems, including sliding contact and bonding process. In this report, the critical reviewing of the principles and theories of self-lubricating bearings, as well as the analysing methods for its performance (e.g. surface analysis and contact mechanics etc.) will be emphasized, thus giving guidance for the research aims set for this thesis.

In Chapter 3 the methodology adopted for reaching the aims in this thesis, including the test approaches, equipment and setups and data processing will be presented. Divided in two parts: the investigation of the surface texturing's effects on the dry-lubricated sliding wear performance and on the bonding strength of the bearing liner, the main test strategy adopted, the samples and processing (surface texturing and other treatment), as well as the post-analysis (e.g. surface analysis and theoretical modelling) are discussed in details.

The chapter 4 will present the test results and analysis for investigating the influence of counterface textures on the tribological performance of a self-lubricating PTFE composite. A preliminary test for an initial selection of the texture dimensions will be conducted firstly, followed by a refined systematic test session targeting at revealing the influences posed by varying texture parameters (e.g. coverages and depths). For surface analysis, the development and outcomes of a novel transfer-film characterising method will be highlighted. In addition, a Finite element (FE) model for the contact mechanics will be developed to give theoretical explanations for certain observed effects.

In chapter 5, the significance of the bearing motions on the dry-lubricated contact will be investigated. To improve the current approach for studying this issue, a model was first proposed to relate the sliding of bearing with the realistic kinematics of the helicopter main rotor, providing guidance for the tests to investigate the effects related to the varying sliding directions. The test and analysis will be conducted on both smooth and textured counterface to find out the effects of various surface heterogeneities (different material in composite and counterface topography) in this issue.

Then in chapter 6, new texturing methods (using laser and electro-chemical etching) for bonding strength improvement were proposed. Along with the conventional technologies, the new techniques were tested for their bonding performance of sleeve surfaces. To identify the physical phenomenon contributing to the change incurred by surface texturing, related tests and surface analysis were performed. Then, in order to provide theoretical supports and a useful

tool for predicting the bonding performance of textured surfaces, an improved model of wetting angle on textured surfaces were built based on surface free energy analysis.

Finally, to conclude, chapter 7 will produce the discussions and conclusions of this thesis. Achieved academic and industrial advancements will be pointed out, and the recommendations for guiding and instructing the surface texturing, for both tribological and bonding performance pursuits will be given based on the findings formed in the previous sections. Possible future works and plans are also reported in the final section.

## **1.5 Highlights and contributions of the thesis**

Through the work presented in this thesis, many findings regarding the surface texturing in dry-lubricated bearings were discovered, concerning both the tribological and bonding performance aspects. The highlights of the thesis and the contributions to either academic or industrial advancement are as following:

- ❑ The tribological effects of textured counterface in dry-lubricated bearings was studied systematically for the first time. In the comprehensive test and analysis session, a thorough analysis and discussion on the influences of various texture parameters is included. For the surface analysis, a novel method for characterising dry-lubricating transfer-film under real engineering contact was developed and evaluated. This new technique solves the issues encountered in realistic contact condition but were rarely addressed previously.
- ❑ An improved bearing designing principle was formulated to help instructing parametric design of counterface textures based on the Limiting-Pressure-Velocity (*LPV*) and Finite element (FE) model. With the help of FE analysis, the contact pressure and stress under dry-lubricated contact were analysed, leading to an improved criterion. In the improved criterion, it is pointed out that the variation of material properties in the composite, and the effect of stress concentration incurred by surface textures need to be considered to find the ‘real contact pressure/stress’ and ‘real *PV*’ of the polymer composite, instead of simply using nominal pressure.
- ❑ The significance of sliding motions in dry-lubricated contact with composite bearing liner was identified. Based on the proposed modelling principles, the first kinematic model to relate the motions of the bearing with the mechanism of its application (i.e.

pitch-control in helicopter main rotor) was built, providing guidance for the tribological test to consider motion effects.

- ❑ Novel sleeve surface texturing methods were developed based on laser processing and electro-chemical etching, and found to be improving the bonding strength of sleeve surfaces through benefiting wettability and mechanism like asperities inter-locking and wettability improvement.
- ❑ A novel wettability model based on surface energy analysis was built to predict the how different surface textures can influence on wetting angle compared with smooth surfaces. With the proposed new wetting model (partial penetration into texture) and constraints (droplet volumetric consistency), this model has the advantage in predicting the change in wetting angles (particularly with oriented surface textures, e.g. trenches) compared with classical models. With this model, the parametric design of surface textures can be instructed for pursuits in enhanced wettability and adhesion.

## Chapter 2

### Literature review

#### 2.1 Tribology and dry-lubricated bearings

##### 2.1.1 History and development of tribology and bearing systems

It is believed that the history of bearings can be dated back to around 3200 B.C., accompanying the use of wheels in Mesopotamian culture [12]. Evidences of the application of this type of bearings, composing of a plain sleeve and a rotating shaft has also been seen in the wheels in Ancient Greece and China [13]. The use of cylindrical elements to convert sliding to rolling may originates from the wood rollers Egyptians used for transporting building blocks, but the first recorded application of ball bearings is on a first-century Nemi ships [14].

Over centuries, concepts belong to modern bearings have been constantly employed, such as the application of lubricants (oil and grease) and rollers to facilitate smooth operation of mechanisms, such as the shaft-wheel of bicycles. On 1500s, Leonardo Da Vinci filed the first design of ball bearing in his journals, although it was never successfully implemented. It was no until 1883 when F. Fischer founded his bearing company (later branded as 'FAG') based on the standard grinding process later patented by him [15] that the first modern bearing industry was founded. Then, on 1907, S. Wingquist [16] patented his design of self-aligning ball bearings and founded the company of SKF. With the capability of accommodate misalignments, the self-aligning ball bearings soon became widely used in varied engineering applications.

Nowadays bearings exist in many different forms, like shown in **Figure 3** [17], in all mechanical systems involving rotating motion. In the simplest form - plain journal bearings, the lubrication system is generally consisted of a cylindrical sleeve, a bush and the lubricant within the interface. For the spherical plain bearings, the sleeve and bush are spherical, giving more rotational degrees of freedom. In the rolling elements bearings, cylindrical rollers or balls sit between the sleeve and the bush, converting the relative sliding between the two surfaces into rolling between the rollers and the two surfaces. As for the thrust bearing, the races are arranged in the axial direction to take the axial load.

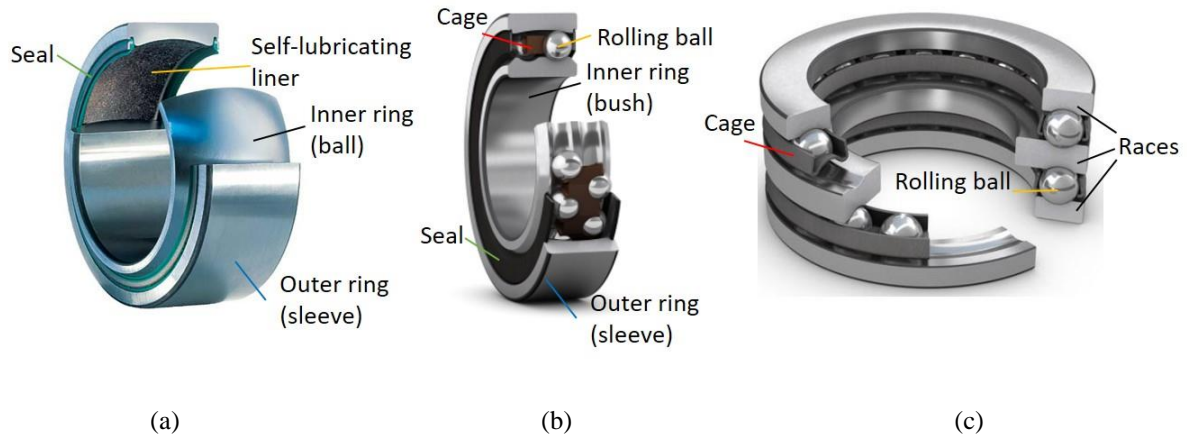


**Figure 3.** The composition of (a) a spherical plain bearing, (b) a self-aligning ball bearing and (c) thrust ball bearing [17]

Along with the development of bearings and other contact components like gears, studies on the interfacial friction, lubrication and wear are also progressing.

The first systematic study on friction should be from Leonardo Da Vinci, dating back to 1500. He never published his theories, but his journals showed that he used mechanisms like weight and pulley, and obtained findings such as the rolling friction is very small, and that friction is independent of contact area [18].

From 1695, G. Amontons [19,20] published a series of work proving the two basic laws of friction. The first law is that the force of friction is directly proportional to the applied load, namely the frictional coefficient (or Coefficient of friction,  $CoF$ ) is a constant for a contact pair. Then, the second law is that the force of friction is independent of the apparent area of contact. In his theory, friction was described as predominately a result of the work to drive a surface over the roughness of the counter surface. C. Coulomb then supplemented his theory, adding to the second law that the kinetic friction is independent of the sliding velocity. The second law of friction is then often referred as the "Amontons-Coulomb Law" to acknowledge the understanding achieved by the both scientists.

Then, in 1950, F. Philip Bowden and David Tabor [21] formulated another physical explanation for the laws of friction. They determined that the real area of contact- those between surface asperities is a very small percentage of the apparent contact area. Therefore, as the normal force increases, more asperities would come into contact, and the real contact area grows. Consequently, the true contact area determines the frictional force. In their theory, adhesion is the intuitive cause of friction as it is proportional to the real contact area.

In modern engineering, the development of lubrication theories [22–25] helps pushing the friction and wear to increasingly low level in engineering contact components. Despite the developments achieved on the contact components and progresses made in the knowledge and understanding, it was not until 1960s that a separate discipline was proposed to summarise the knowledge in this field. ‘Tribology’, derived from the Ancient Greek word *tribos*, “to rub”, is defined as “the science and technology of interacting surfaces in relative motion” [26]. In Greek mythology, the Titan Prometheus stole fire from Zeus and helped human, while in reality, the first invention in tribology by human race was probably the creation of fire by rubbing wood and grass together [27]. In a sense, the word ‘tribology’ pays tribute to the many genius like Prometheus, as they paved the way to our understanding in tribology, delivering their intelligence to the human.

### 2.1.2 Dry-lubricated bearings and the applications in aerospace

Among the early development in bearings, a striking one was the first aerospace bearing, designed by Leonardo Da Vinci in around 1500, along with his famous invention of the first helicopter. As in the re-constructed version shown in **Figure 4** [28], the bearing features in the ball elements that facilitate rolling contact, resembling the modern ball bearings. While the first taking-off of helicopters took place at 1900s [29] - around 400 years later, the ball bearing also remained at the design stage until similar time when issues like cage structures and precision manufacturing were solved.

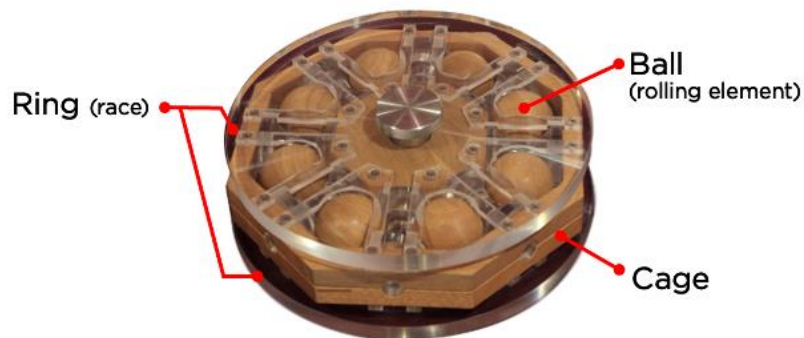


*Figure 4. Bearing design of Da Vinci reproduced by JTEKT engineers [28]*

At the 1930s, when the aerospace industry saw its first boom, rolling-element bearings and the oil-impregnated journal bearings are the most commonly used in aeroplanes and helicopters. With liquid lubricant applied, the bearings were designed to achieve full-film lubrication. However, the former one is not capable of operating at a very high load and needs frequent re-greasing, while the latter is limited in single-direction rotation and has poor performance at low

rotating speed. Consequently, the lubrication condition became very condition-dependent. In the mid-nineteenth century, the development of helicopters surged and it was at stage that a more capable type of bearing for helicopter is urged to be developed. To fulfil the task, the bearings need to meet the following requirements:

- 1) The lubrication system should be simple, and has least components possible so that the weight can be reduced for saving fuel and improving performance.
- 2) The maintenance interval should be long, because the overall cost for ceasing the flight and servicing is high- estimated €35,000 per time [4].
- 3) The bearings should have a high tolerance of oscillations and high load-carry-capacity at relatively low-speed, which derives intrinsically from the transmission and loading condition of the rotor-head.

Under these demands, the idea of using a maintenance-free self-lubricating spherical plain bearing emerged in the 1950s [4]. This type of bearings has a liner that can serve as a solid lubricant in the interface. Meanwhile, this concise system can also facilitate a lightweight system. Almost at the same time, chemist Roy J. Plunkett accidentally discovered Polytetrafluoroethylene (PTFE) and trademarked it as Teflon [18]. Since it is one of the solid material with the lowest  $CoF$  (0.05 to 0.2 against polished steel in most condition [19]), and has relatively good thermal resistance than other self-lubricating polymers like polyethylene, it automatically became the best candidate for the basis of the bearing liners.

#### **2.1.2.1 Dry lubricating liner**

In the beginning, the early application of the PTFE bearings was not so successful in scenario like helicopter rotors. The Teflon rod-end bearings in some of the U.S. military helicopters experienced excessive wear, and would last for only 150 hours while the scheduled TBO (time before overhaul) is over 3000 hours [30]. To solve this, other ways to incorporating PTFE in the bearings were developed.

To improve the wear life of the PTFE, the employment of hard fillers were tested by many researchers. Lancaster [31] introduced hard inorganic fillers to reduce the wear of PTFE at first. It was postulated that the fillers can partially take the applied load so that the PTFE matrix is protected. Later tests on different micro-fillers revealed that the fillers can also function by regulating the morphology of wear debris [32,33]. Moreover, explanation by Briscoe[34] proposed an explanation that micro-filler improved the adhesion through enhancing the chemical bond between the PTFE transfer film and the counterface. This claim, however, was

questioned [33,35] because adhesion would only affect the first layer formed between the PTFE and the metallic counterface, while most wear occurs at layers atop the deposited layers. Therefore, the enhancing in the chemical bond (which is already strong) should pose minimal effect on the wear performance.

The introduction of hard fillers, however, may lead to third-body abrasions, jeopardising the counterface topography and the compromising the frictional performance. Aiming at relieving this issue, many researches have been conducted on the potential of softer fillers, like polyoxy-benzoate [36] and fluorinated ethylene propylene (FEP)[37], or nano-fillers such as alumina nano-particles [36,38] and carbon nano-particles[36].

However, the load-carry-capacity required in the aerospace applications is usually higher than these filled PTFE. According to the summary by Evans and Senior in **Figure 5** [39], only by interweaving PTFE with reinforcing fibres or impregnating solid lubricants in porous bronze can the required load-carry-capacity be achieved under the relatively low sliding speed (e.g. around 40MPa with around 0.1m/s sliding speed in helicopter rotors).

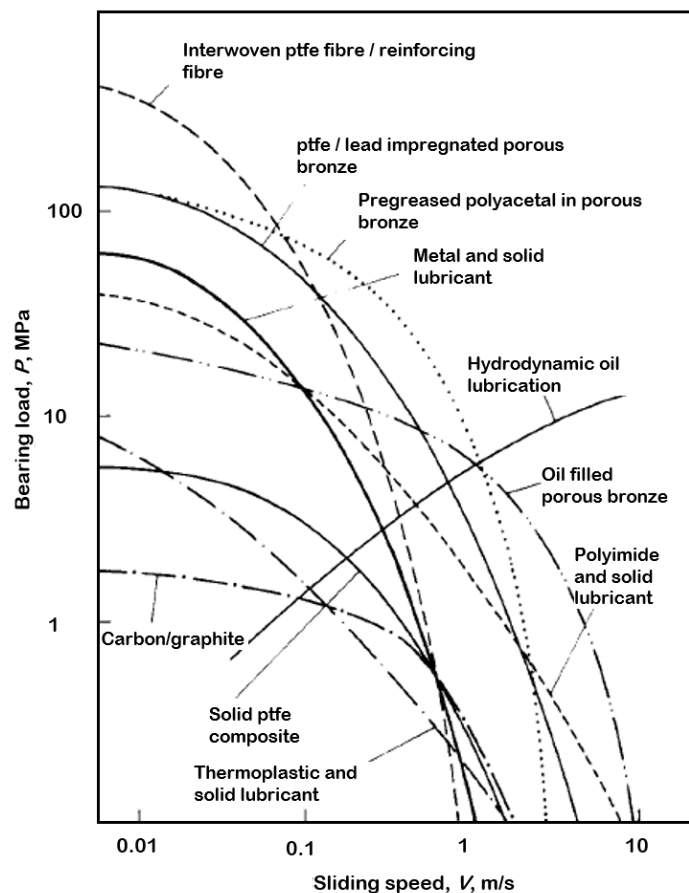
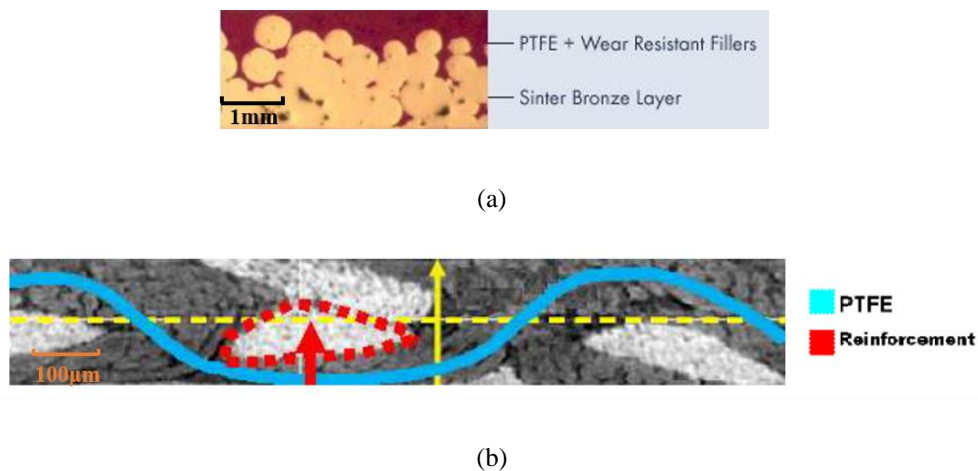


Figure 5. Limiting loads and speeds of varied self-lubricating materials [39]

In the late 1940s, Glacier Metal Ltd. developed “Glacier DU”. PTFE and lead were impregnated in porous sintered bronze strip. The copper matrix not only guarantees the high overall stiffness of the structure, like shown in **Figure 6** (a) [40], but also provides high thermal conductivity, enabling the composite’s application in a wide range of sliding speed and temperature. Many modified versions of solid-lubricant-filled bronze bearings were developed later on based on this produced, such as “Glacier DP” - a lead-free version of “Glacier DU” to meet the environmental regulation [41].



**Figure 6.** Microscopic image of section of (a) DU porous bronze bearing [40] and (b) an interwoven liner of PTFE and reinforcement [4]

In comparison, the interwoven composite of PTFE and reinforcing fibres (e.g. glass fibres, polyester) can achieve even higher load-carry-capacity and superior frictional behaviour (close to PTFE) with particular weave arrangement. For example, in the mid-1960s, Ampep Ltd. (now affiliated to SKF Ltd.) developed “Fiberslip”, in which PTFE and glass-fibre multi-filament yarns were included in warps to provide lubrication and reinforcement properties, like shown in **Figure 6** (b) [4]. The “warp” of a fabric consists of the yarns which are held tight in the loom, while the “weft” threads are passed over and under them [4]. The arrangement of the warp and weft was designed in a manner that a continuous face of PTFE can appear on the upper surface. Embedded in the phenolic resin and adhered to the sleeve backing, this woven fabric of PTFE and glass fibres achieved dramatically prolonged wear life, excellent load-carrying capability and maintenance-free feature. Soon after its release, the “Fiberslip” became the predominating dry-sliding bearing liner material used in aircraft applications.

Based on this interwoven structure, modifications were made to cater to the different conditions. For example, reinforcing fibres softer than glass fibres like polyesters (e.g. Dacron) [42] was

used to substitute glass fibres for reduction of abrasion in less-demanding conditions, and Aramid fibres (e.g. Nomex) were used where high temperature resistance is required [43,44]. In addition, weave structure has also been improved [45,46]. In AMPEP Ltd (now SKF Ltd), developed from “Fiberslip”, the “X1” creates an even better wear performance by an optimized weave pattern for arranging PTFE and glass fibres. What is more, when combined with modifications on the counterface, the new developed contact pair (e.g. “XL”, “XLNT”) is seeing a more promising wear life [47].

Despite the predominance in aircraft applications and the constant progress made, there are still aspects that need improvement on bearings with PTFE-based woven composites. The main ones are:

- The self-lubricating liner could never have the mechanical lock with the steel backing as in porous bronze bearings. Instead, the liner needs to be bonded on the steel backing with adhesive, so special attention is required to ensure the bonding strength.
- In porous bronze, the thermal effect is dramatically reduced by the effective heat conduction, but the influence can still be significant in interwoven liners, even though PTFE is already more resistant to heat than many other self-lubricating polymers (e.g. UHMWPE, used only in less-demanding scenarios like artificial joints). Therefore, the wear under high  $PV$  factor (product of the nominal Pressure and Velocity) needs careful monitoring since it indicates thermal input of the sliding contact (as frictional heating is theoretically denoted by  $\mu PV$ , where  $\mu$  is the frictional coefficient).

For further improvement on the performance of the dry-lubricated bearings, attentions would be needed on these aspects.

### **2.1.2.2 Tribological behaviour and characteristics**

#### **- Basic frictional and wear behaviour**

For PTFE, the dry lubricant in self-lubricating liners, the main tribological features are the low  $CoF$  and poor wear resistance exhibited when sliding against metallic engineering surfaces [48]. Primarily, the root cause of these features is the special molecular structure of PTFE. As shown in **Figure 7** [49], a PTFE chain has a rigid carbon ‘rod’ with fluorine atoms running helically on the surface, leading to a smooth profile and low shear resistance between the molecular chains. Moreover, when rubbed against a hard surface, the PTFE chains slip and break easily, creating active groups which chemically bond with the counterface [48]. The strong adhesion would then assist the formation of a coherent transfer film on the counterface as the sliding and

wear progresses. According to the test by Briscoe et al. [50] with pure PTFE pins, the development transfer film can actually start with the first generation of wear debris, i.e. the first strike of sliding. As the transfer film is formed, subsequent interaction would be between the transfer film and the polymer layer atop, reducing the effective roughness of the counterface.

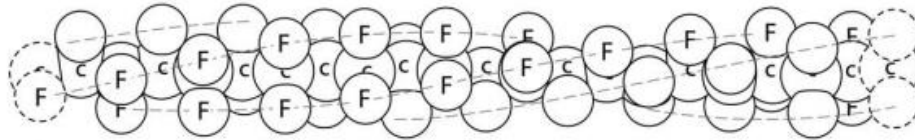


*Figure 7. PTFE molecular chain [49]*

As has been discussed previously, interwoven with reinforcing fibres the wear resistance of the PTFE can be improved. For the dry-lubricating liners, Lancaster conducted a series of experiments from 1970s to 1980s to provide the initial benchmark of the tribological performance [3,6,51,52]. From his comprehensive test series on different PTFE bearing liners, it was concluded that the relationship between wear depth of PTFE composite liner and time can generally be idealized as **Figure 8** [53]. Three different stages to the liner wear process can be identified:

1. The running-in stage: the liner wears rapidly, so the PTFE transfer film gradually develops. The initially high wear rate would gradually decrease as the transfer film builds up, until it rises to a 'knee'. Correspondingly, the  $CoF$  experiences up-and-downs.
2. The steady wear stage ('plateau' region), where the transfer film develops fully, and the liner wears at a relatively low and uniform rate. The  $CoF$  in this stage also stabilised at close to pure PTFE.
3. The final wear stage (or 'wearing-out' stage): a substantial wear volume is reached, then the liner experiences the last rapid wear phase and quickly turns to failure. This stage is also accompanied with rapid friction increase and oscillations.

In real aircraft application, where the reliable operation and flight safety is of paramount importance, it is crucial to know when the wear of the liner would enter phase 3 and finally fail. The requirement of the liner's wear life is therefore specified in international standard like American Aerospace Standard SAE AS81820 [54].

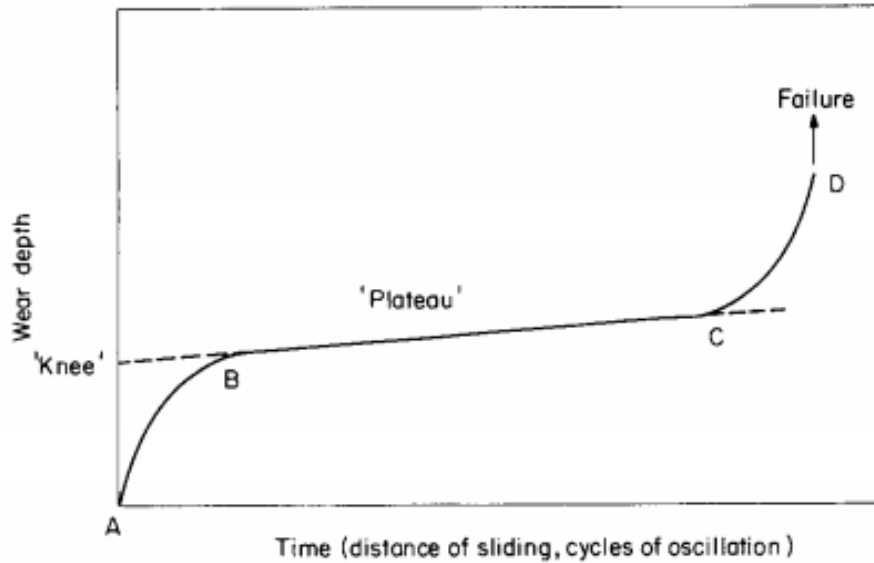


Figure 8. Typical wear depth progression over life of a PTFE-based self-lubricating bearing [53]

Due to the link between the wear behaviour and the transfer film formation, it was hypothesised that the transition between the first and the second stage is due to the development transfer film, and the transition between the second and third is due to the breakdown of the film under cyclic stress and plastic deformation [55,56]. However, through experiments analysing the wear progression by liner layers, as shown in **Figure 9** (a) [44], it can be concluded that the final reduction of film protection is more a result of low presence of PTFE and high occupation of reinforcing elements in the final layers (e.g. Layer IV and V), instead of stress condition. Namely, it is not because the film breaks down so the wear enters the final stage, but because the wear progresses to the final layers so the film reduces, contributing to accelerated wear.

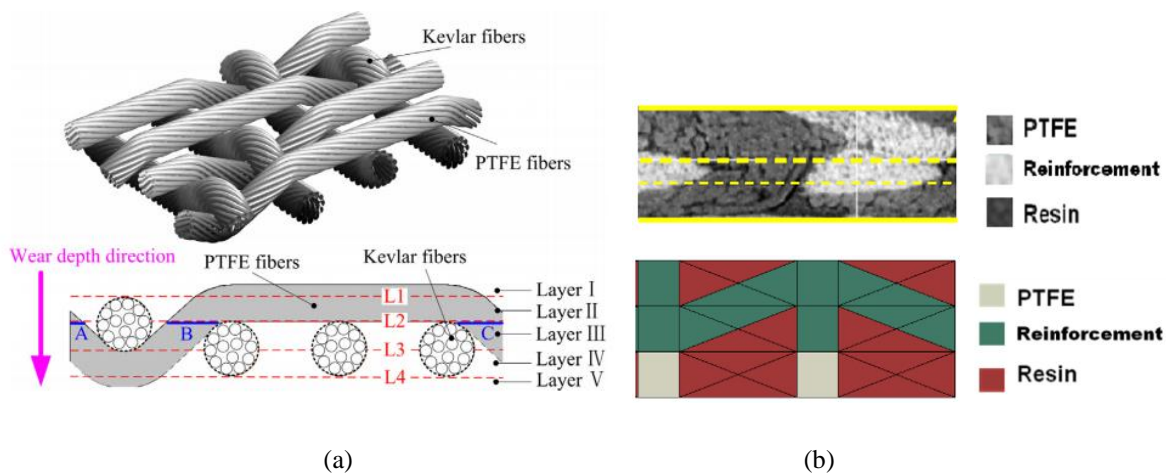


Figure 9.(a) Schematic showing the textile structure of the broken twill weave [44]; (b) Modelling part of a cross-section through the weft of a fabric composite with "unit cell" [4]

The work of Gu *et al.*[44] also revealed the possibility of a nonlinear wear progression, explained by the different stiffness drawn by different proportion of reinforcement in textile layers like in **Figure 9(a)**. This can occur with fabrics with complex overlapping layers. Similar phenomenon was also found through the simulation by Russell using “unit cell” model for another fabric structure, like shown in **Figure 9(b)** [4].

For a more detailed understanding of the wear mechanism of the fabric composite, Su, Zhang *et.al* [57] identified the following types of wear mechanisms of fibres: (a) matrix wear and fibre thinning, (b) fibre broken, (c) interfacial de-bonding and (d) fibre peeling-off.

Apart from the basic friction and wear pattern, and the influences from the properties of the liner itself, other factors like loading, kinematics and counterface are also found affecting the tribological performance of the dry-lubricated bearing system, as will be introduced more in the following sections.

#### **- Relationship on operating conditions**

Operating conditions, including normal load (or pressure), sliding speed, temperature and other environmental factors can all play an important role in the tribological performance of PTFE composites.

Firstly, it has been reported in agreement that the *CoF* of PTFE decreases with increasing normal load [48,53,58]. In dry-lubricated spherical and journal bearings, Play and Pruvost [59] have also observed the same *CoF*-load relationship with PTFE-based woven composites. Summarising the results in studies that involves test conditions with varied loads, it can be concluded that this *CoF*-load relationship is common in all PTFE-based composites as long as the transfer film is fully developed, while a threshold pressure (above which the induced *CoF* reduction is minimal) exists.

Then, for pure PTFE, the *CoF*-speed relationship is not monotonic. Generally, the *CoF* would first rise with increasing speed to a peak point, and then decreases, while the curves under different temperatures in can be associated considering the inherent viscoelasticity of PTFE (i.e. shear resistance dependent on deforming rate), like shown in **Figure 10** [48]. When fillers or reinforcing fibres are introduced, the relationship also varies. While in some cases the relationship becomes monotonic [60,61], others saw little variance with changing speed [62]. It can be deduced that the change in speed may lead to difference in the effects of

fillers/reinforcing fibres, such as in abrasion, so the  $CoF$ -speed relationship would need to be analysed on a case-by-case basis.

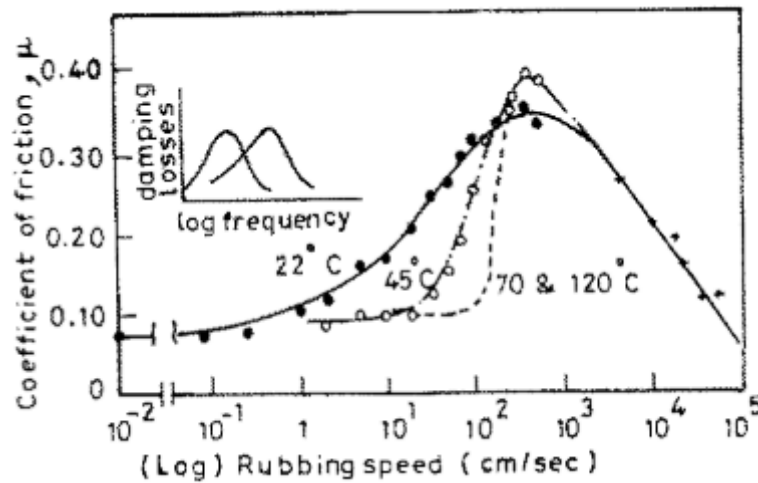


Figure 10.  $CoF$  of PTFE as a function of sliding speed. The inset shows damping losses as a function of frequency.

For the wear performance, both increase in pressure and sliding speed would lead to an increase of wear rate (by time), as found in both pure PTFE and PTFE composites [48,53,58–62], while it was occasionally observed one or the other can be the more influential parameter [63]. However, a more comprehensive consideration of the loading conditions would be the  $PV$  factor – the product of pressure ( $P$ ) and sliding velocity ( $V$ ), since it also reflects the thermal input of the contact system (as frictional heating equals to the product of  $CoF$  and  $PV$ ), thus relating to another influencing parameter- temperature. When the temperature reaches to a certain regime (so-called ‘thermal control regime’), tribological performance of polymers can be significantly influenced by the temperature due to property change incurred [64,65]. Moreover, when the interfacial temperature reaches the melting or softening temperature of thermoplastic, drastic changes would occur in the friction and wear behaviour [52,66,67]. To reflect this phenomenon, Lancaster [52] plotted the  $PV$  map for a self-lubricating liner, as shown in **Figure 11**. In **Figure 11**, each curve (obtained experimentally by finding the critical  $V$  under the same  $P$ , or vice versa) denotes a  $PV$  boundary (with a certain bearing geometry), above which the resultant frictional heating would incur accelerated wear.

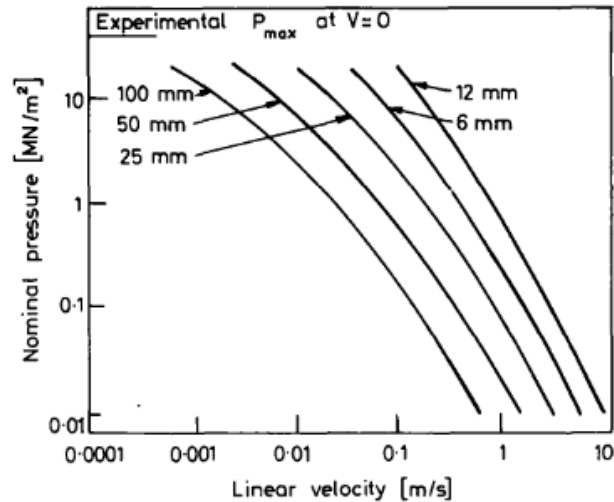


Figure 11. Limiting PV curves for acetal bearings of different sizes. Length/breadth ratio = 1 [52]

The assessment of tribological performance based on PV factor has been adopted as a design principle in developing dry-lubricating polymers, and *LPV* has also become a parameter bearing manufacturers would provide to instruct the operation. However, it is noticed that in most previous works involving analysing *LPV* on polymer composites [68–70], the pressure employed in the reported *LPV* is always simply the nominal pressure. Nonetheless, in the composites, the load was taken more by the reinforcing fibres/ fillers, so it is worth discussing whether using the nominal pressure – an averaged representation of the load is appropriate, considering that the *PV* factor is concerned with the polymer.

Besides, other environmental conditions like humidity [71] and contamination [53,72] can also influence the performance of the bearings, and thus need attention particularly with specific working condition.

#### - Consideration on kinematics

Apart from sliding speed, which has been discussed above, the main influence from kinematics comes from the variation of sliding direction on the sliding path, in applications like helicopter main rotors. According to A. Zmitrowicz's work [73], for dry sliding contact between two surfaces, the non-homogeneity in material distribution, micro-structures (e.g. highly-oriented crystallographic structure of a crystal [73]) or surface topography can all lead to anisotropic (dependent on orientation/direction) or heterogeneous (dependent on relative position) frictional and wear. For PTFE-based interwoven liner, not only the distribution of constitutive material is not uniform, the PTFE itself also has anisotropic frictional performance [74], so the

tribological performance is possible to be anisotropic. Consequently, the overall tribological performance of the bearings should be dependent on the sliding path.

Because in fiber-reinforced-polymer (FRP) composites, the anisotropy can exist in basic mechanical properties (e.g. elastic modulus and strengths [75]), there is the willingness to directly correlate the anisotropy in these properties with that in friction and wear. Ning et al [76], for instance, built a strength-based model to predict the anisotropic wear behaviour unidirectional continuous fiber-reinforced-polymer (FRP) composites. In the experiments from Godet & Play [77] and Z. Rasheva [78], however, the direction-dependence of friction and wear of FRP composites has not been found correlated with elastic modulus or tensile/compressive strength. In fact, the basic mechanical properties (e.g. elastic modulus) represent the overall base material, while surface properties (e.g. hardness) determines the tribological performance, so direct linking those two may not always give a good explanation of the anisotropy.

As for the sliding path, experimentally, there have been some efforts on including the variation in sliding direction in the tribological test. Briscoe and Stolarski conducted pioneer works, including the changing of sliding direction by introducing the self-spinning motion into the originally linear motion [79,80] or circular rotation [81] in the tests of polymeric pins, like shown in **Figure 12**. Through these works, they observed essential changes in wear and friction for some polymeric pins taking into account various curvatures of circular sliding trajectories. Based on the methodology used in these tests, many modifications have been developed to include varied additional rotations to the single direction translation/rotation in different applications [82–85]. In these explorations, the focus was mainly on the application of artificial joints (using polyethylene), while aerospace applications were rarely covered. However, all these approaches share some common drawbacks. Taking **Figure 12** as an example, under the applied rotations on both the pin and the disc, the simulated sliding path were essentially the combination of two circular paths, which does not necessarily reflect the real moving mechanism. Moreover, with the constant rotational speeds, it essentially assumed the variation of sliding direction is in a uniform fashion, indiscriminating the occurring frequency. Overall, despite the consideration, the dependence of the sliding path on the kinematic mechanism has not been revealed comprehensively.

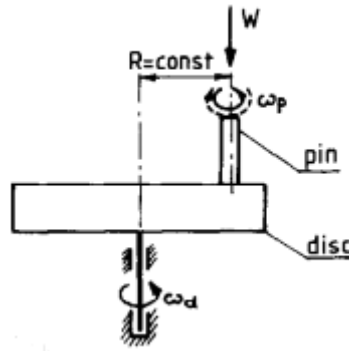


Figure 12. Configuration of pin-on-disc machine with imposed pin rotation [81]

Then, a progress first took place in the application of artificial joints: in related standards (ISO 14242:1 and ISO 14243:1), models were provided describing the real motions of prosthesis joint for human gaits, instructing the wear tests on multi-degree-of-freedom wear simulators. However, in aerospace applications, comprehensive consideration on the real kinematics can rarely be found. Even though efforts have been made by Ming et.al [44], including the development of test simulators with the capability of multi-degree-rotation, as shown in **Figure 13**, the PTFE woven liners were still undergoing the motions in empirical models (uniform tilting and swivelling [44] or only swivelling [86]). Essentially, the simulated motion is no different with the real motion under the operation of the helicopter rotorhead. Therefore, an improvement on the kinematics models is needed to reveal the real motions undergoing in aerospace applications (e.g. helicopter main rotors). As the variation of sliding direction is neglected in previous models, a new model considering this aspect can assist understanding if the test methodology can reflect the real sliding condition, and if consideration need to be given to anisotropic performance of the composite liner.

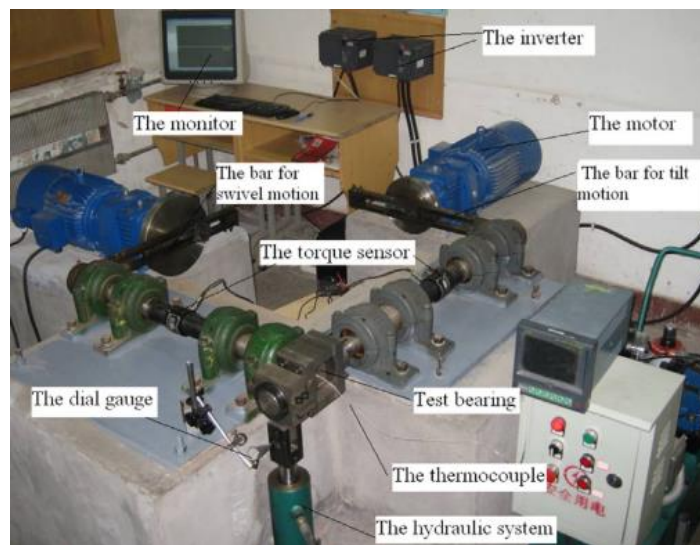
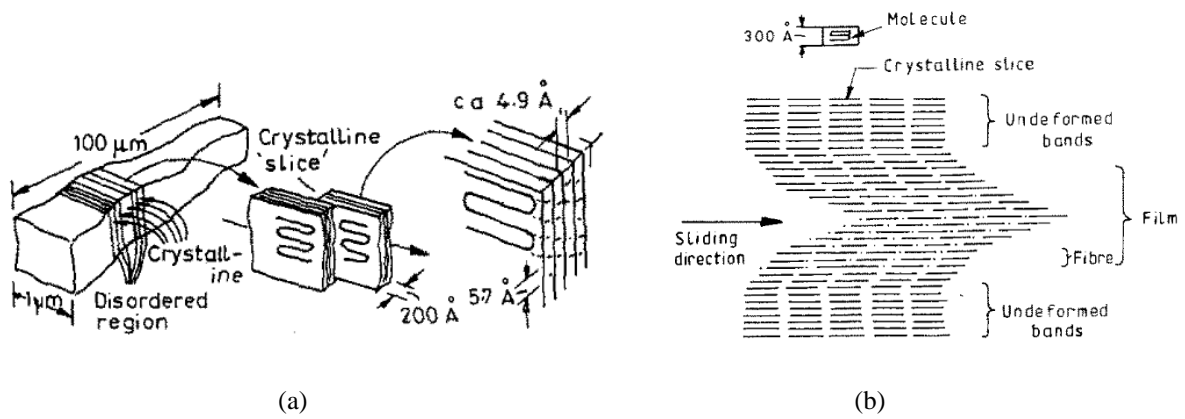


Figure 13. Photography of the tester for self-lubricating radial spherical plain bearings [44]

### 2.1.2.3 Transfer film formation and characterisation

As has been pointed out, the formation of transfer film is the main phenomenon contributing to the self-lubricating property of PTFE and PTFE-based composites. In PTFE composites, fillers can influence the frictional and wear performance by inducing different transfer film morphology [32,33]. As for the PTFE-based woven fabrics, the full-development of transfer film determines whether a steady state with relatively low wear rate can be reached[53]. On the other hand, for the counterface, it was found that modification on the hardness [51], the value of the average roughness (Ra) [3] and the pattern of the roughness (from different finishing process) [87,88] can all have a great impact on the formation of transfer film, which consequently affects the tribological performance of the bearings. Therefore, when studying the tribological effects of a modification on the contact system, the analysis on the influence on transfer film has always been a key to illustrate the mechanism. To help guide the experimental work of developing a comprehensive characterising methodology in this thesis, characterisation methods of PTFE transfer film and some similar transfer mechanism are reviewed, and in this section.

Makinson and Tabor [89] first observed the transfer film (formed by pure PTFE balls on glass counterface) with electron microscope, and measured the film thickness as 10 to 40 nm (except for thicker lumps under higher speed) using a Baker-shearing interference microscope. However, the condition of the counterface was described ‘not optically ideal’, and the error of the measurement was estimated in the order of 5 to 10 nm. Relating with the established crystalline structures of PTFE [90,91], it was postulated that the transfer film formation is a result of intra-crystalline slip between the crystalline bands, like shown in **Figure 14** (a), and a van der Waals type of adhesion from the counterface (considering PTFE is chemically inert). Then, on similar glass counterface, Pooley and Tabor [92] identified the presence of transfer film by observing the reflected light from the glass surfaces. The estimated film thickness was 2.5nm to 100nm depending on the operating conditions, calculated from shadow lengths on the electron microscope (detailed calculation not elaborated). Afterwards, by observing the worn PTFE surfaces the transfer film morphology under electron microscope, K. Tanaka et al. [58] found a strong relationship between the transfer film formation and the different crystalline band widths, and proposed that the film formation is a result of relative slipping, dislocation and deformation damage of the band structures, like shown in **Figure 14**(b).



*Figure 14. (a) Band structure of PTFE crystalline based on [90,91] and slipping mechanism deduced in [89] and (b) Mechanism of formation of PTFE film due to change in structures as proposed in [58]*

Later on, a series of studies were conducted in NASA to understand the transfer film formation on metallic surfaces. At first, when using field ion microscopy, W. Brainurd and D. Bivckley [93] found that the bond between transfer film and counterface can withstand the helium image field without desorbing, implying that the bond is actually strong chemical bond. Then, S. Pepper and D. Buckley [94] postulated that the transfer film can be only monolayers thick, considering that the film was not affecting the visibility of tungsten peak in the Auger spectrum, when the spectroscopy was sensitive only to the first few layers on the surface. Finally, through Ellipsometry measurement, J. Lauer and B. Bunting [95] identified ultra-thin film (under 10nm) on the stainless steel counterface.

Apart from the early pioneering works, another study that adds knowledge on the nature and mechanism of the transfer films is from Gong et al. [20-22]. Since it was found that the wear rate of pure PTFE was not affected by the chemical properties of the counterface, they concluded that once a transfer film was formed, it would never be peeled from the counterface by the PTFE layer atop. Moreover, through electron spectroscopy for chemical analysis (ESCA) on the frictional tracks, it was further proven that the bond between the PTFE film and metallic counterface is a chemical bond (e.g. Zn-F bond). Then, with the development in PTFE composites and their ever-growing applications, the conditions for observation become increasingly complex, so modern characterising technologies, such as Scanning Electron Microscopy (SEM) have been used to identify and characterise them in different situations. To help guide the experimental work of developing a comprehensive characterising methodology in this thesis, the representative characterising examples and reported characteristics are reviewed, listed by methods in Table 1.

Table 1. Summary of representative characterising methods for polymeric transfer film

<b>Characterising method</b>	<b>Examples and reported properties</b>	<b>Capabilities / advantages</b>	<b>Limitations / drawbacks</b>	
<b>Optical method</b>	Optical microscopy (OM)	Film free-space length (1e5 to 0.1 $\mu\text{m}$ ) and film coverage evolution recorded [96,97] Film coverage start at 85%, reduced to around 0 on stainless steel counterface [98]	- Revealing appearance features of thick film in 2D (surface morphology, coverages etc.) - Most time-efficient	- Difficult to identify ultra-thin film - Unable to reveal film thickness - Disturbance from other optical effects (contrast etc.)
	Optical interferometer	Film thickness 2.5 - 100 nm on glass steel counterface [92] Film thickness around 74 nm on stainless steel counterface [98]	- Revealing appearance features of thick film in the 3rd dimension (thickness) - Revealing counterface wear - Time-efficient	- Difficulty to identify ultra-thin film - Difficulty to distinguish film and roughness effects
	Ellipsometry	Film thickness under 10nm on glass counterface [95];	- Revealing appearance features of thick film in the 3rd dimension (thickness)	- Model-dependent
<b>Contact measurement</b>	Surface profilometer	Film thickness is a few micrometre thick on aluminium counterface [99]	- Revealing appearance features of thick film in the 3rd dimension (thickness) - Revealing counterface wear - Time-efficient	- Difficulty to identify ultra-thin film - Difficulty to distinguish film and roughness effects - Film prone to be scratched

	Atomic force microscopy (AFM)	At lowest around 0.5nm, at highest 10nm thick on silicon wafer [100]; A few hundred nanometre thick (poly-oxy-methylene) on steel [101]	- High measurement precision	- Difficult to distinguish film and roughness effects - Strict requirement on the substrate roughness
<b>Analysis of emitted signals</b>	Auger emission spectroscopy	Monolayers thick film [94]	- Capable of deducing film thickness	- Incapable to measure thick film thickness due to sensitivity range
	Scanning electron microscope (SEM)	Thick and grainy transfer film [101] but the identification is questionable; Hard to observe the ultrathin film [102]; Lamellar PTFE transfer film [43] but the identification is questionable; Film coverage recorded [98]	- High resolution & magnification image - Composition distinguishing (BSE) - Composition analysis with EDX - Relatively time-efficient	- Information dependent on accelerating voltages - Insufficient EDX under low acceleration voltage
	X-ray photoelectron spectroscopy (XPS)	PTFE transfer film identified by chemical shifts of F1s peak etc [103]; Film thickness under 100 nm [104];	- Composition analysis - Relatively low penetration depth (nm level)	- Thickness model pre-assumed - Non-straight forward output
	Secondary-ion mass spectrometry (SIMS)	PTFE transfer identified with peaks like CF+, CF3+ etc [105] Transfer film coverage revealed differently with SEM [106]	- Composition analysis - Low penetration depth (nm level)	- Time-consuming

It can be seen from Table 1 that depending on the counterface and studied condition, the detected film characteristics vary greatly. The thickness, for example, have been reported as monolayers at lowest [94], and micrometre-thick at highest [99]. More importantly, among all the investigations conducted, a few points were found frequently encountered in the characterising process, hindering the reflection of the real picture of the transfer film:

**- Sensitivity to surface topographic interference**

The outcome of many characterising methods are prone to topographic interference - when substantial topographic variation exists within the contact area on the counterface.

For example, the computation of transfer film coverage in [97] was done by distinguishing the dark areas after converting the microscopic image into binary, like shown in **Figure 15** (a). However, counterface abrasion tracks (not the initial roughness discussed in the work) can pose similar optical effect, so without evaluating this influence, the estimated coverage would have errors. Then, in [96], as shown in **Figure 15** (b), even though abrasion tracks were identified in SEM images, the estimation of film coverage still depends only on the contrast. In this aspect, composition analysis, such as EDX, XPS and SIMS would be more reliable, but they may have their own issues like have stated (in Table 1).

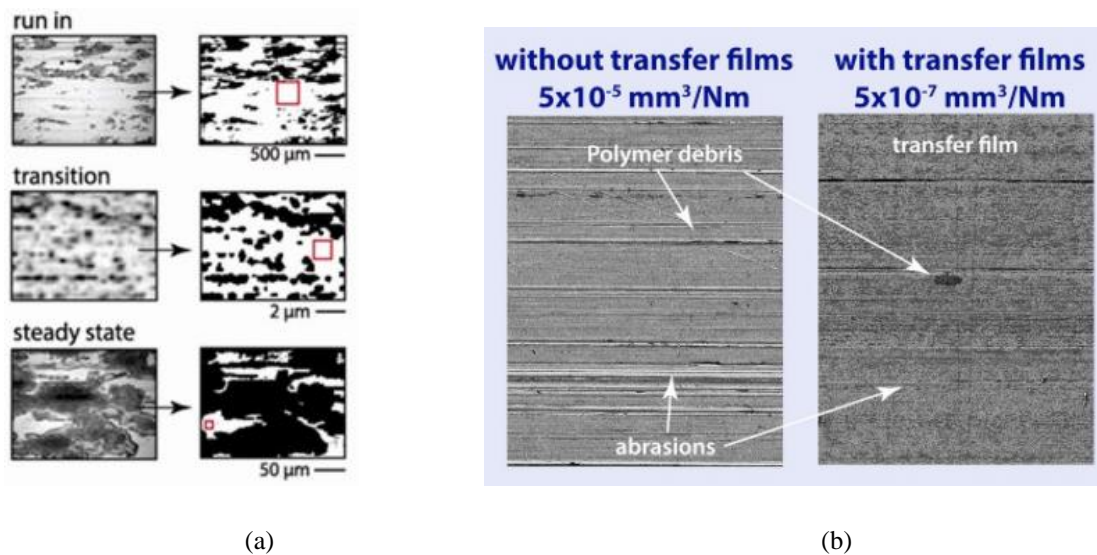


*Figure 15. (a) Conversion to binary image from optical microscopic image to collect transfer film coverage [97] (b) A counterface with the presence of both transfer film and abrasions[96]*

Moreover, with the presence of significant topographic variation, the measurement of film thickness would be influenced as well. Be it from an optical interferometer [98] or AFM [101], the measured profile would be a combination of the surface topographic variation and the film thickness. What is more, if the film is actually ultra-thin (nanometre level), then even the initial

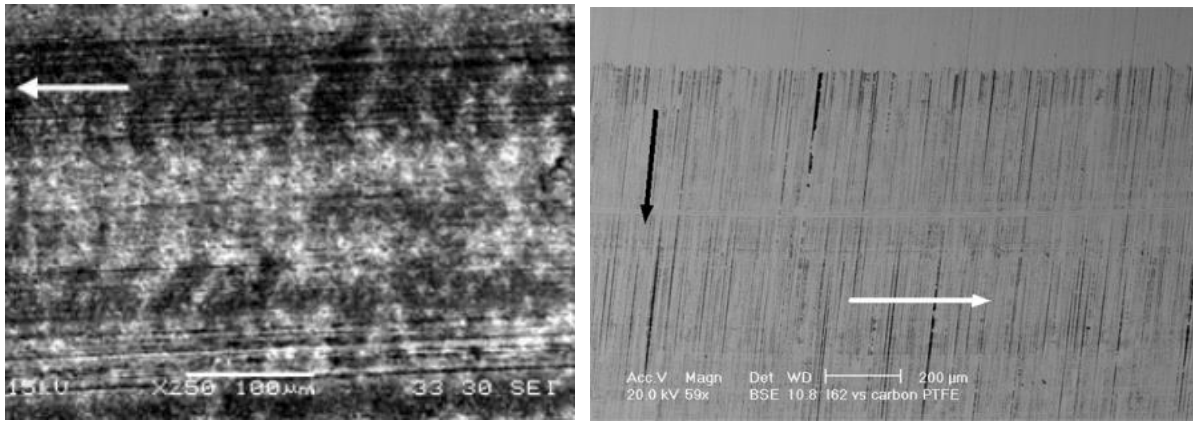
roughness of the counterface may become huge interference, since the information of nanometre-thick film would simply be flooded in the surface asperities in micrometre-level. Therefore, normally the reported film thickness can only be reliable on ultra-smooth counterface, such as silicon wafer [100], with the absence of hard reinforcement/fillers.

#### **- Incomprehensive identification**

In many cases, the identification of the transfer film was arbitrary. Apart from ignoring the sensitivity to topographic interference as stated above, this can also be caused by lack of consideration on the principles of the adopted techniques.

Taking the use of SEM as an example, it was quite often that Secondary Electron (SE) mode was used to scan the surface, like shown in **Figure 16(a)** [101]. The obtained SE image is more suitable for revealing topographic features, but only with Back-Scattered Electron (BSE) mode can different composition be distinguished by contrast (related to atomic number). Therefore, the claim on the identification of transfer film in this image was arbitrary, let alone the suspicion of wear tracks in this image.

Moreover, the information obtained with SEM is dependent on the accelerating voltage applied- higher the voltage, larger the penetration/information depth. Considering this, even though in [107], the BSE image indicated clearly dark areas, denoting lighter composition (possibly PTFE), as shown in **Figure 16(b)**, the 20keV accelerating voltage applied would lead to penetration depth in micro-meter level according to theoretical estimations [108]. Therefore if the transfer film is just monolayers or nano-metres thick as some postulated [95], the information of it can be overwhelmingly surpassed by the substrate below, so the dark areas reveal only partial information of the film.



(a)

(b)

**Figure 16.** (a) Claimed appearance of transfer film under SEM (SE mode) [101] and (b) BSE image of counterface after sliding against PTFE-C (white arrow –sliding direction, black arrow- grinding direction) [107]

Overall, despite the massive studies conducted with transfer film characterisation, many arbitrary results have been produced because insufficient attention has been given on the technical limits and related mechanism of the employed techniques. Therefore, a reliable and comprehensive characterising methodology is needed.

#### 2.1.2.4 Counterface and sleeve surface modifications

The friction and wear are outcomes of the system, including both contact surfaces and external conditions. In the bearings with dry-lubricating liners, the liner has to be incorporated with counterface to achieve the desired tribological performance. Meanwhile, a strong bond between the liner back and the sleeve surface (outer ring) guarantees the full play of tribological performances as well as the reliability of the system.

##### - Counterface modifications

Lancaster [3] firstly investigated the influence of counterface (steel) roughness on the tribological performance of PTFE liner. Through comparisons between the tested surfaces with arithmetical mean roughness ( $R_a$ ) of  $0.65\mu\text{m}$ ,  $0.20\mu\text{m}$ ,  $0.05\mu\text{m}$  and  $0.015\mu\text{m}$ , it was found with reduced surface roughness, the wear life would always be prolonged, until  $0.015\mu\text{m}$ , with which the improvement becomes negligible. To reduce the  $R_a$  to  $0.015\mu\text{m}$ , however, incurs dramatic rise in cost, therefore the  $R_a$  value around  $0.05\mu\text{m}$  is still more commonly adopted in aerospace industry.

In comparison, in the investigation of the roughness effect on polyethylene [109] – the dry-lubricant commonly used in artificial joints, a turning point ( $0.1\mu\text{m}$   $R_a$ ) was found for the

tribological performance. This phenomenon was attributed to the optimal film formation at this point.

In addition, Play's study on [110] includes a thorough set of parameters characterising the counterface topography. In the whole set, five parameters were essential to evaluate the surface: profile mean roughness ( $Ra$ ) or surface mean roughness ( $Rq$ ), Skewness ( $Sk$ ), Kurtosis ( $Kt$ ), radii of curvature of peak asperity ( $RCP$ ) and number of peaks per mm ( $NPM$ ). Besides, the surface finish method must also be considered as the finish direction may affect lump arrangements of wear, and consequently wear life.

Apart from the influence from roughness, Lancaster also studied the influence of counterface hardness [51]. It was found that a softer counterface is never favoured because abrasion on the counterface is more likely to happen. This can in turn lead to even more abrasion on both surfaces by introducing third-body wear particles. Moreover, the increase in the counterface roughness also jeopardise the wear life.

Based on these findings, many bearing manufacturers have made improved surfaces. Roller Bearing Company of America, for example, used titanium alloy as the bearing surface and treated it with physical vapour deposition (PVD) to further increase the hardness[111]. Later on, tungsten carbide enhanced bearings were also patented [112]. Another useful coating is thin dense chrome, which was also used for the purposes of corrosion protection[113]. SKF incorporated the X1 liner with a ceramic-coated surface. Benefiting from higher hardness and lower roughness of the coated counterface, this combination called "XLNT" is able to guarantee even lower friction and longer life.

#### **- Sleeve surface modifications**

A strong bond between the liner and the sleeve surface guarantees the fulfilment of tribological performances as well as the reliability of the system. Apart from the aspects of bearing liner and improvement on adhesives, improvement were also done on the sleeve surfaces to achieve the bonding strength needed.

The pre-treatment methods for improving the composite-metal bond were rarely reported specifically on bearing sleeve surfaces, but more generally as in aerospace applications. It is commonly believed that a smooth metallic surface would yield very poor bond, whereas surface roughness can lead to a certain degree of improvement in the bond, depending on the roughness [114]. Therefore, a common practice for both bearing sleeve and other aerospace

metallic surface is grit blasting for artificial roughness creation, occasionally succeeded with passive solvent for oxidation film formation [115]. However, grit-blasting process can cause problems like void contact volume[116], residual stress[117,118], and environmental issues [119]. For alternative pre-treatment, G. Critchlow and D. Brewis [120] found abrading the metal substrate using 180/220 -mesh alumina can produce macro-roughness ( $R_q$  1.3–3.6 $\mu\text{m}$ ), increasing the bonding durability to a certain extent [120]. Moreover, sodium hydroxide and chromic-acid anodization (CAA) (TURCO) was found capable of producing a large amount of surface structures with 3.4  $\mu\text{m}$  peak to valley height along with the oxide film [114]. Nevertheless, considering its efficiency and the micro-roughness (leading to superiority in bonding strength) created, grit blasting is still the most used treatment for improving bonding strength of sleeve surfaces.

From the review on the dry-lubricating technology in aerospace applications, it can be seen that massive efforts have been put into the development of the dry-lubricating liner, while the modifications on the counterface were mostly focused on the optimization of surface roughness and improvement of hardness. However, considering the key mechanism of the dry-lubricating liners- the transfer film formation, there is potential in employing more radical counterface modifications – surface texturing, while the transfer film may need to be characterised with a more comprehensive method firstly. Moreover, the relationship between the bonding strength and topographic variations also incites more radical modifications on surface topography. Considering these prospects, the development and status in the surface texturing technology and the research on related aspects are reviewed in the following sections.

## **2.2 Surface texturing in contact applications**

### **2.2.1 Development in surface texturing technologies**

A real surface always has a certain topographic variations. Varying from nano-meter scale to macro scale, the surface topography influences the lubrication in different regimes. Different with surface roughness, surface textures are the surface topographic structures in a regulated and patterned manner. Like roughness, surface textures can exist in natural beings, such as the asperities on the lotus leaves and the ripples on the gecko skins, or artificially, such as the dimples on the golf ball.

The first widely adopted surface texturing in tribological applications is the cross-hatch texture created by honing [121] in cylinder liner of engines. By retaining more oil, this texture solved the issue of seizure (on piston ring- cylinder liner interface) encountered by automotive industry in 1940s. Then on 1966, Hamilton et al. [122] produced micro-asperities on mechanical seals by an etching technique. The dimensions were further optimized theoretically and experimentally. After that, except for the mechanical texturing technology (polishing with alumina particles [123,124]) developed for memory drive disc in electronic industry, the successful implementation of surface texturing in tribological applications were rarely seen, and most studies remained theoretical [125]. It was not until 1990s the surface texturing saw a boom in tribological applications - the development in laser technology enabled efficient manufacturing of high-resolution surface structures and consequently proficiency in optimizing surface texture parameters. R. Ranjan [126] first found that memory drive disc textured by pulsed laser has a superior frictional performance than mechanical textured, owing to the smooth surface contour. Then, using laser surface texturing (LST), Etsion and his colleagues started with an experimental and analytical optimization on the textures applied on mechanical seals [127,128], developing a series of principles on the surface texturing on different mechanical components[129–132].

Now, along with the development in advanced manufacturing technologies, such as ultrasonic machining [133] and additive manufacturing [134], more availability have been created for surface texturing. To have a view about the current status about the surface texturing technology and achieved outcomes in the aspect of tribology, a collection of the representative texturing techniques are listed in Table 2. This summary is not aiming at covering all the studies on surface texturing, but listing the representative texturing methods and tribological effects identified. In it, depending on the working principle of the texturing technologies, texturing the texturing methods are categories into three types: mechanical techniques, chemical techniques and high energy beam machining. Most mechanical means use an oscillating tool, be it a cutter or an insert, or a blast in waterjet [135] for periodical material removal. Chemical ways are those using chemical etching reactions for removal of the base material. High energy beams, such as laser beam and electron beam, can ablate a very confined area on the surface to create textures.

Table 2. Collection of representative texturing techniques

Texturing category	Textured method	Example	Tribological effects	Advantages and drawbacks
<b>Mechanical</b>	Honing/micro-honing	Texturing of cylinder liner in automotive engine piston-liner pairings [136]	<ul style="list-style-type: none"> <li>- Providing lubricant reservoirs</li> <li>- Boosting film thickness in mixed and boundary lubrication regime.</li> </ul>	<ul style="list-style-type: none"> <li>-Cost-efficient;</li> <li>-Work-pieces may be hard to mount and fix[137]</li> </ul>
	Micro-powder injection moulding	Mico-patterning in high-grade engineering plastics and different polymeric composites replacing the metals[138].	<ul style="list-style-type: none"> <li>- Reducing the contact area between the plastic materials and steel, thus reducing friction and wear rate.</li> </ul>	<ul style="list-style-type: none"> <li>-Each pattern needs a specific set of moulds and dies;</li> <li>-reproduction hindered by expensive low-life tools.</li> </ul>
	Ultrasonic machining	Ultrasonic vibration assisted milling [133]	<ul style="list-style-type: none"> <li>- Entrapment of wear debris can lead to improved wear resistance</li> </ul>	<ul style="list-style-type: none"> <li>-High precision</li> <li>- High surface quality</li> <li>- Low tool wear.</li> </ul>
	Vibro-mechanical texturing (VMT)	Texturing on cylindrical surfaces for journal bearings [139]	<ul style="list-style-type: none"> <li>- Forming micro-bearings;</li> <li>- Providing lubricant reservoirs and boosting film thickness in mixed and boundary lubrication regime.</li> </ul>	<ul style="list-style-type: none"> <li>-High-efficiency;</li> <li>- convenient for cylindrical surfaces;</li> <li>- Texture shape and dimensions constrained by the inserts.</li> </ul>

<b>Chemical</b>	Reactive ion etching	Creating micro-pits on SiC seal [140]	- Containing water for tribo-film formation as well as hydrodynamic effect	- Efficient control of material removal; - Easy to apply on irregular and complex geometry - Mask needed for protecting base material
	Anisotropic etching	Lithography and anisotropic etching of silicon wafers used as wear-resistant coatings[141]	Forming thicker and better covering tribo-film	- Efficient control of material removal; easy to apply on irregular and complex geometry - No mask needed
<b>High energy beam</b>	Laser surface texturing	Micro-dimpling of steel rotor seals [128]	- Micro-dimples can serve as micro-air-bearings; - Generating a weak hydrodynamic effect	-Precise machining; easy fixture and control of patterning; - Heat affected Zone; - Post-processing needed for re-deposition; - High initial cost.

Electrical beam machining	Texturing working rollers for producing auto-industry sheets [142]	<ul style="list-style-type: none"> <li>- Altering the film thickness under mixed lubrication;</li> <li>- Reducing <i>CoF</i> under high pressure.</li> </ul>	<ul style="list-style-type: none"> <li>- Great scope for variation of the micro-topographic parameters;</li> <li>- No mechanical stress</li> <li>- Risk of irregularities; complex manoeuvring</li> </ul>
Focused ion-beam	Island-type texture on hard-slider disks [143]	<ul style="list-style-type: none"> <li>- Forming air-bearing;</li> <li>- Avoiding stick-slip.</li> </ul>	<ul style="list-style-type: none"> <li>- High resolution;</li> <li>- No restrictions on substrate material;</li> <li>- Low surface roughness</li> <li>- Low efficiency;</li> <li>- surface defects such as ripple structures</li> </ul>
3D-printing	Texturing soft plastic material using Multijet Printing (MJP) [134]	Reducing contact area and consequently adhesion	<ul style="list-style-type: none"> <li>- Ideal for complex texture geometry;</li> <li>- time-consuming;</li> <li>- post-processing(re-machining and heat-treatment)</li> </ul>

Apart from the methods collected in the Table 2, there are also many other methods used by some researchers in their research. These methods, however, are often either too time/labour-consuming, such as miniature engraving [144] and indentation [145], or too insufficient to reproduce, such as patterned embossing [146] and therefore may only be used in the research work and may see very limited applications currently.

Benefiting from recent developments in computer-assisted numerical analysis, more theoretical studies have been performed on the effects of texturing in fluid-lubricated contact [147,148]. As for dry contact, because of the material-dependent nature, more experimental studies have been conducted, as will be introduced in the following section.

### **2.2.2 Surface texturing for tribological performance in dry contact**

Unlike in fluid-lubricated condition, where the influence of liquid film is dominating, the effects in dry-contact are more material-dependent. Therefore, the tribological phenomenon often need to be reported case by case. To give an overall view, a summary of the representative works of this topic is listed in Table 3, along with the main findings discovered.

Table 3. Collection of studied of surface texturing in dry sliding

Application	Studied objects	Textured material	Texturing techniques	Texture patterns	Main effects
<b>Mechanical components</b>	Friction torque and temperature rise in dry gas seals [128]	Steel rotor seal/ carbon ring	LST	Micro-dimples	- Forming micro-gas-bearing with the absence of liquid lubricant.
	Friction behaviour of magnetic hard disk[149]	Magnetic hard disk/ Al <sub>2</sub> O <sub>3</sub> .TiC slider	LST	Crater-type dimples	- Reducing friction build-up by round smooth texture contour
<b>Electrical components</b>	Wear debris in fretting wear of electrical contact[131]	Bronze and steel contact rings/ steel ring or ball	LST and super-polishing	Dimples	- Helping removing of oxide wear debris from the contact zone.
<b>Cutting tools</b>	Cutting performance of cemented carbide tools [150]	Rake face of cemented carbide tools/ 6061 aluminium alloy tubes	LST	Linear, circular, and rectangular textures	- Benefiting frictional performance in low-speed cutting by reducing real contact area - Swallowing softened material in high-speed, increasing friction.
	Cutting performance of textured WC/Co carbide tools [151]	Rake-face of the WC/Co carbide tools/ 6061	LST; burnishing solid lubricant MoS <sub>2</sub>	Elliptical/linear grooves	- Serving as reservoirs for pre-deposited solid lubricants, benefiting the cutting process

		aluminium alloy tubes			
	Wear resistance of carbide tools[152]	Flank-face of carbide tools /against green alumina ceramics	LST	Linear grooves	- Flank face textures facilitate derivative cutting, removing third-body abrasion
<b>Coupon test samples</b>	Friction and wear of polypropylene surfaces [153]	Polypropylene surfaces /against roughened steel pins	Microinjection moulding	Micro-bumps	- Increasing the density of edge contacts- affecting <i>COF</i> . - Postponing run-in period in wear through easier exits for debris, hindering transfer layer formation
	Friction and wear of Al <sub>2</sub> O <sub>3</sub> /TiC ceramic surfaces[154]	Al <sub>2</sub> O <sub>3</sub> /TiC ceramic discs/ AISI 1045 steel balls	LST	Micro-grooves	- Increasing friction due to increased surface roughness and micro-cutting - Entrapment of wear debris can lead to improved wear resistance
	Wear behaviour of TC11 alloy [155]	TC11 alloy discs/ GCr15 steel pins	LST	Micro-dimples	- Assisting tribo-layer formation by increasing oxygen contact

	Friction and wear of textured Si <sub>3</sub> N <sub>4</sub> /TiC ceramic surfaces [151]	Si <sub>3</sub> N <sub>4</sub> /TiC ceramic discs / AISI stainless steel balls	LST	Regular-arranged micro-grooved textures	- Improving stress distribution
<b>New machining technology</b>	Friction and wear performance of UVAT textured surface [152]	Al7075-T6 aluminium alloy surface (against chrome steel pins)	Ultrasonic vibration assisted face-turning (UVAT)	Micro-dimple arrays	- Improving friction and wear performance by influencing 3D roughness parameters such as Surface Area Ratio ( <i>Sdr</i> ) and Density of Summits ( <i>Sds</i> )

---

Without the protective film of fluid, the surface textures would inevitably serve as protrusion for the solid-solid contact, so texturing is not intuitively favoured under dry contact from the perspective of friction. However, there are still many effects of surface texturing reported in dry conditions. Concluding from Table 3, up to the writing of this thesis, the most frequently reported effects of surface textures in dry contact are:

1. Altering the contact pressure distribution.
2. Trapping hard wear debris.
3. Acting as reservoirs for dry-lubricant and benefiting tribo-film

First of all, a commonly-acknowledged effect of surface texturing in dry sliding contact is that it would alter the contact area and cause stress concentration, thus affecting the contact pressure distribution [151]. However, despite the frequent reporting on this effect, the identification and analysis on this phenomenon could have progressed more. For example, in  $\text{Al}_2\text{O}_3/\text{TiC}$  contact [154], high friction was experienced due to micro-cutting on the groove edge. Meanwhile, in the study of the frictional performance of UHMWPE on textured counterface [88], the induced alteration of hysteresis friction was identified. In fact, in all these cases, the root cause of the effects should be the stress alteration created by the textures. Therefore, instead of being reported with hypothetic explanation as in each case, like shown in **Figure 17** (b), explaining them with the theory of contact mechanics and failure criterion can help relate the contact condition with the texture parameters, forming a more comprehensive principle to help the texture design. Recently, there have been a trend of applying Finite Element (FE) analysis tool to provide theoretical guidance from the contact mechanics perspective. The applications have been frequently seen in dry-cutting cases [156–158], and it is a promising prospect to exploit the use of FE in more occasions.

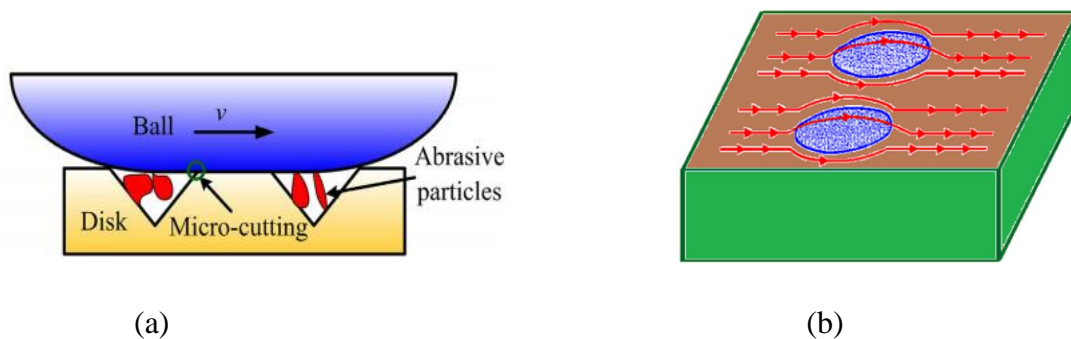


**Figure 17.** (a) Proposed micro abrasion mechanism on textured surface [154], (b) Schematic of flow pattern of a soft material over sphere texture[88]

Apart from pressure alteration, another function with concave surface textures is the trapping of material. On one hand, abrasive wear debris can be contained by the concavities, so third body abrasions can therefore be reduced, preventing phenomenon like friction transition- an abrupt friction surge in dry contact [159]. On the other, this trapping function can also assist forming thicker transfer film in certain self-lubricating contact-pairs [154,155]. What should be noticed is that, these effects of surface textures were also very dependent on the operating conditions. For instance, for polymer-metal contact, such as the sliding between poly-oxy-methylene (POM) or (poly-ether-ether-ketone) PEEK sliding against steel surface [160], reduced wear rate was observed only under very low loading (0.25MPa). The employment of this very low pressure may be due to the concern that textures in dry-contact inherently increase the contact stress [160] and lead to micro-cutting [44]. Moreover, for the wear life of VisiJet M3 Crystal plastic materials, textures may reduce the contact area to a point which creates benefits both friction while not compromising too much [134]. This optimized point is unique to this plastic. Due of this dependence, the surface texturing in dry contact is more complex, and usually need to be analysed on a condition-to-condition basis.

Similarly, in dry-lubricated conditions with self-lubricating polymers, apart from the common issue of stress alteration by surface texturing, textures also have the potential of boosting the formation of transfer film for some self-lubricating contact, as the dry lubricant film in this occasion can also be stored by the textures [154,155]. As a result, the induced overall influence on the frictional and wear performance of the dry-lubricated bearings would be the result of the combination of the different effects incurred (e.g. micro-abrasion and lubricant reservation). In addition, the weighing of these effects and alteration of related tribological phenomena would be dependent on texturing dimensions, as analogous phenomena have been observed in previous research on the surface roughness. Taking the study from Kennedy et al. [109] as an example, it was found that the variation of the wear life of polyethylene is a result of the combined effects of friction and third body film thickness, leading to a turning point where the substantial third body film can be reserved between asperities to reduce the resistance. Considering this, similar to the study of Kennedy et al. [109], a systematic test series on the texture parameters would be the required for both comprehensive view of the effects from surface textures and parametric optimization of the textures on dry-lubricating condition.

To conclude, benefiting effects have also been found with surface texturing on dry contact in previous literatures. Regarding the self-lubricating polymeric composite bearings used in aerospace industry, effects such as wear-debris and material transfer can incite motivations in

adopting surface texturing. However, due to the high relevance between these effects and the contact condition, studies about different texturing parameters such as dimensions and densities need to be conducted to advance understanding on the overall influence with this specific contact-pair (the PTFE composite and the steel counterface).

### 2.2.3 Surface texturing for bonding performance

At first, it should be noted when referring to the ‘bonding strength’ of the bond between the composite liner and sleeve surfaces, like many similar occasions in engineering field, it actually corresponds to the ‘practical adhesion’, which is defined as ‘magnitude of mechanical force or the quantity of energy which has to be applied to break an adhesive bond’ [161]. Meanwhile, ‘fundamental adhesion’ is ‘forces and mechanisms on, or approaching, the molecular scale, which are involved in holding together the different components of an adhesive bond’.

Basically, ‘practical adhesion’, or the ‘bonding strength’ concerns the macroscopic reflection of the strength of the adhesive bond, while ‘fundamental adhesion’ deals with the microscopic interfacial attraction. These two are interconnected as [161]:

$$G = G_0 + \psi \quad (2.1)$$

where  $G$  is the ‘practical adhesion’ (in the form of energy);  $G_0$  is the ‘fundamental adhesion’, which depends on the surface energy and should be the lower one of adhesion energy and cohesive energy; and  $\psi$  is energy from other absorbing processes like plastic and viscoelastic deformation.

As for when surface texturing is used to influence bonding strength, the pursuit is a stronger reacting force - a higher resistance to shear (contrary to when it is applied in sliding bearing interface). Many studies have also been conducted in this aspect.

#### - Influence on bonding strength

The motivation of using surface textures to improve bonding strength comes from that surface roughness can greatly affect bonding strength. Jennings first summarized the influence of the surface roughness[162], and categorized the bonding strength into 3 different types- tensile adhesion strength, shearing strength and the peeling strength. Uehara [163] further supplement the theory. He tested the influence of surface roughness on three different types of bonding strength using pull tests, single-lap shearing tests and peeling tests. The difference between the measured and the theoretically predicted strength of the adhesive was explained by the additional surface area effect and the notch effect (incision of roughness) from different

roughness. The basic trend of the strengths versus varying surface roughness was postulated, as shown in **Figure 18**.

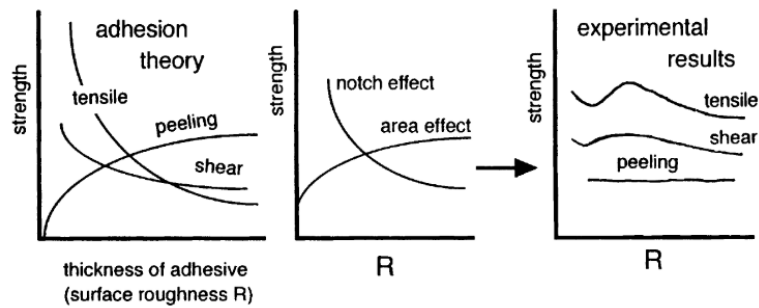


*Figure 18. Schematic illustration of bonding strength of the adhesion (as a combination of three factors) [163]*

Based on Uehara’s theory, the surface should not be too smooth so as the notch effect would disappear and the area effect would be the smallest. Instead, micro-roughness, or micro-structures, has been always favoured for bonding strength performance. It is believed that micro-roughness, or even nano-roughness is created, the contact area between the adhesive and the surface can be multiplied, leading to huge area effect. Moreover, the reserved adhesive within the channels and pores in the micro-asperities may interfere and interlock mechanically. In the mechanical theory that describes ‘fundamental adhesion’[164], it is also believed that if porous microstructures are created, a strong continuous film of partly embedded adhesive can be formed in situ, contributing to a good joint.

The employment of surface texturing in bonding process are generally motivated by the concept of micro-irregularities. To relate with the work in this thesis, representative examples of surface texturing for bonding strength improvement are summarised, as shown in Table 4.

Table 4. Collection of representative studies in surface texturing for bonding strength improvement

<b>Texturing methods</b>	<b>Bonded material</b>	<b>Texture patterns</b>	<b>Main effects / findings</b>
<b>Photolithography</b>	Aluminium panels [165]	Micro-pores (70 to 90 $\mu\text{m}$ diameter, depth 8 to 13 $\mu\text{m}$ )	Small pores in the range created better effect in bonding strength enhancement
<b>LST</b>	Zinc coated sheet steel [166]	Ripples (10 to 20 $\mu\text{m}$ wide)	Small scale structure more benefiting than denser largescale patterning
<b>LST</b>	Ceramic to metal [167]	Conical microstructures	Maximum bonding strength with full surface of conical microstructures
<b>LST</b>	Copper [168]	Island-like structures	Area increase contributed to bonding strength
<b>LST, Sand blasting</b>	Ti6Al4V Alloy [169]	Dimples (60 $\mu\text{m}$ diameter, 150 $\mu\text{m}$ deep); Grid (60 $\mu\text{m}$ wide, 450 $\mu\text{m}$ deep);  Chaotic(250 $\mu\text{m}$ deep);	Area increase contributed to bonding strength; Sand blasting is inferior than LST possibly due to brittle oxides or under- cuts
<b>Micro-rolling</b>	Aluminium sheets [170]	Micro-channels, Grid patterns (200 $\mu\text{m}$ wide, 10 $\mu\text{m}$ deep)	Contact area increase leads to bonding strength improvement

It can be seen that most of the improvements that brought by surface roughening/texturing were attributed to the enhancement in contact areas. Correspondingly, finer structures [166] and larger coverage of the micro-roughness were advocated. Consequently, the creation of a surface with well-spread micro-irregularities has become the key in improving bonding strength.

#### **- Influence on wettability**

Wettability is closely related with the bonding strength. If the solid surface can be wetted by a liquid droplet by a larger span, the solid- liquid interfacial area would be larger, leading to higher interfacial adhesion. According to the equation 2.3, this increase in fundamental adhesion would contribute to higher bonding strength.

Wettability is often quantified by contact angles, since ‘more wetted’ condition correspond to lower contact angle of a liquid droplet on the surface. To explain the influence of surface topography on wetting angles, three classical models have been formulate since 1800s, with different application regimes as illustrated in **Figure 19**. First of all, the famous Young’s model [171] describes the relations between the contact angles and the surface tensions between different medium (solid, liquid and gas) on an ideally smooth surface. Then, the Wenzel’s model [172] assumes a completely wetting of the micro-asperities on a rough surface, and modify the Young’s model by introducing a relative roughness ratio  $r_a$ . Finally, the Cassie-Baxter’ model (later referred as ‘CB’s model’) [173], which was firstly used to analyse contact angles on composite surfaces, treats the surfaces with certain textures as a combination of a smooth part that can be completely wetted (proportion  $p_s$ ), and textured concavities (proportion  $1-p_s$ ) in which gas pockets would separate the liquid and solid surfaces. It has been interpreted that, the Wenzel’s model is used for explaining wettability on rough surface, and CB’s model is used for explaining wettability on textured surface, using the contact angle on smooth surface as the basis.

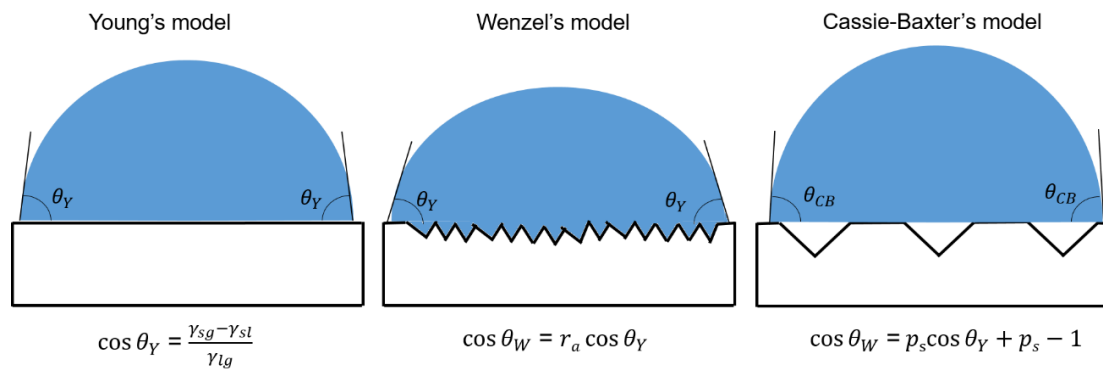


**Figure 19.** Visual conception of (a)Young’s (b)Wenzel’s and (c) Cassie-Baxter’s model

Effective as the classical models on some surfaces with topographic structures, the models were usually used for explaining the observed change on wettability, rather than predicting the wettability with certain forms of textures. For instance, for the surfaces in **Figure 20** [174], the textured surface leads to a smaller contact angle- greater hydrophilicity, which was explained by the Wenzel’s model. However, if the term of ‘surface texture’ is applied, and the CB’s

model was employed, the predicted change in wettability would go opposite direction. In fact, similar issues (including with ‘rough’ surface) can be seen in many cases [174,175]. The cause for this problem is the difficulty in distinguishing ‘texture’ and ‘roughness’. Simply using the common criterion that ‘texture’ is well patterned and ‘roughness’ is more irregular would ignore that it was the dimensions and geometries of the topographic structures that influence the contact area, and further on the wetting behaviour of the droplet. Therefore, deciding which tendency the wettability would vary to would need case-to-case analysis associating with the geometrical features of the topographic structures, instead of an arbitrary selection between ‘texture’ and ‘roughness’. To solve this issue, the work from K Kubiak et al [176] analyse systematically the change of surface area that can be incurred by different types of machining, and testing the updated model on different kinds of surfaces. The consistency of the outcomes was good, but the updated model still shared a same issue with the classical models: the models can only deal with two-dimensional (2D) scenario, while encountered with textures like grooves, the variation of contact angles in different viewing angles could not be revealed.

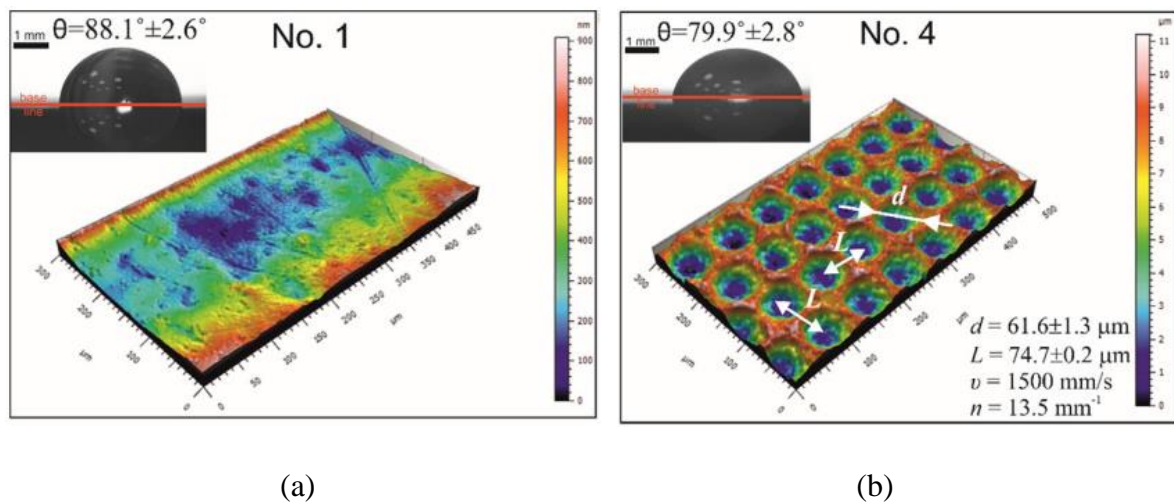


*Figure 20. Wetting angle and surface topography of (a) untreated grinded surface and (b) laser dimpled surface [174]*

To solve the inefficiency in modelling anisotropic contact angles, the model based on the fundamental thermodynamic analysis is a more useful approach. W. Li [177] first revisited the surface free energy analysis, which was the basis for the derivation of the Young’s model, to formulate the contact angle prediction. By searching the minimized energy state- the local minimum of the zigzag free energy path, the contact angle (leading to meta-stable state) can be found. Moreover, in this work, the anisotropic wetting angles on surfaces with directional textures (grooves) was related with the different surface free energy derived from varied viewing angle/ cutting angle. However, the correct identification of wetting angles in different

viewing direction was not comprehensive - the computation of the free energy path in the work was based on the preconception whether the textures would see full wetting or gas-pockets: it misinterpreted CB's model and simply claimed that if the surface is a composite, then the texture will always be gas-pockets.

In recent years, Y. Liang et al. [178] and J. Long [179] made some improvements in Li's model, such as including the prediction of the anisotropic wetting angles. However, the approach of simply setting the first and last equilibrium point of one free energy curve (i.e. single viewing angle) to be the contact angles on the main orthogonal directions [178] seems having no valid physical support. Moreover, the issue of presuming wetting behaviour in the texture concavities remains unsolved.

For the issue of predicting the wetting behaviour in the textures, partial penetration models of droplets were proposed [173,174], indicating general wetting conditions within textures. However, the implementation of this concept would need a determining mechanism of the penetration ratio. By this means, there may be potential in integrating it with the surface free-energy analysis, since the searching of equilibrium state in the thermodynamic analysis is an automatic mechanism for state determination. Moreover, studies on the droplet morphology [180–182] discussed possible droplet morphology, such as elliptical cap, providing more modelling support for analyse the anisotropic wetting angles.

### **2.3 Summary and research gaps**

From the extensive literature review presented above, it can be seen that surface texturing technology has a potential in aerospace dry-lubricated bearings, in both tribological performance modification (by trapping wear debris and reserving transfer film etc.) and bonding strength improvement (by increasing contact area etc.). However, despite the prospect, a comprehensive understanding on the effects of different texture parameters (e.g. dimensions, densities) in self-lubricating bearings has not been achieved, delaying the prompt fulfilment of its application. Among the studies on surface texturing in real dry-lubricated condition, the main issue is not only the limited spectrum of the studied cases, in which the self-lubricating system in aerospace application (featuring woven fabric composite) has not been covered, but that the studies tend to only report the observations and findings by cases. How an alteration in operating conditions (such as sliding direction nor composite orientation) would change the situation was rarely discussed. In addition, the links between the performance and texture properties, including dimensions and coverages were often reported only focusing on the

observatory influences, without identifying the internal connection with the occurring physical phenomena. Therefore, a systematic test series and comprehensive analysis sessions are needed to establish some principles for surface texturing under certain dry-lubricated conditions, with emphasis on revealing the tribological phenomena that incur the difference with varied texture parameters.

For the effects of surface texturing on bonding strength, even though some effects have been associated with the properties of the surface topographic features, such as dimensions, the relationship was often described in a qualitative way. For quantification, wettability- an important surface property associated closely with the bonding strength was frequently used. In terms of the influence of surface textures on the wettability, both improving and reducing effects have been reported. However, the theoretical explanations for the varied influence were often produced by using preconceived notions: either the texture enhance the hydrophilicity because the wetting should follow a full-wetting model (Wenzel's), or it leads to hydrophobicity because it would create gas-pockets (Cassie-Baxter's). Meanwhile, as for the models built for predicting contact angles under different texture dimensions, through a critical review it was found they may still have issues like failing to simulate the three-dimensional morphology of the droplet when predicting anisotropy. Therefore, a wettability model with predicting ability on the influence from varied surface texturing shape and dimensions is needed.

Academic challenge 1: The tribological effects induced by surface textures in dry-lubricated contact have not been comprehensively, or associated systematically with texture properties. The interconnection with texturing features such as dimensions and the area coverage have not been established.

Industrial benefit 1: The possibility of employing counterface texturing to improve tribological performance in helicopter self-lubricating bearings can be explored. With the developed principles, the designing of the counterface texturing can be tailored, saving the time and cost, which would have been put into trial and errors.

Academic challenge 2: As a key phenomenon influencing the tribological performance of self-lubricating bearings, the formation of PTFE transfer film has not been characterised reliably.

Even though the characterising has been included in many previous researches, problems were identified as: the identification of the film was often empirical, lacking validation, sometime only partial view of the transfer film was generated and that characterising technique was only feasible in some ideal condition. The reason behind it is that most of the techniques are not robust enough, i.e. could only work in ideal conditions, while disturbing factors like a high roughness on the counterface would influence the accuracy and validity of the methods. Therefore, a characterising method with sufficient reliability and robustness needs to be developed, and a comprehensive understanding of the transfer film needs to be achieved to give guidance to counterface texturing.

Industrial benefit 2: The target- a robust and reliable surface analysis method for transfer film should provide an efficient analysing tool for engineering applications involving sliding contact of polymers or other types of material transfer. The methodology and principles formulated can help instruct surface analysis sharing similar difficulties.

Academic challenge 3: It has not been revealed how the tribological effects from counterface textures would vary under different kinematics. In fact, even the kinematics of many mechanisms in aerospace applications have not been studied comprehensively. However, the heterogeneity in the composite liner could lead to prominent difference under varying sliding direction. The main issue was that oversimplified or empirical model was often used for complex transmission (e.g. helicopter main rotor), so a realistic representation of the kinematics was missing. Therefore, the study on the kinematic model needs to be performed, and the influence of the kinematics, integrated with the possible anisotropic tribological performance of the bearings need to be investigated.

Industrial benefit 3: Firstly, the developed kinematic model can provide aerospace industry with a design and simulation tool for complex transmission (e.g. helicopter main rotor). Then, the study on the influence of kinematics help bearing industry instruct the alignment orientation of the composite liner, as well as generating bearing design bespoke to flight conditions.

Academic challenge 4: For the surface texturing in bonding strength improvement, many previous researches have provided general guidance: the key would be in controlling the patterns and dimensions of the textures. However, the instructions are still qualitative, and detailed test sessions and comprehensive analysis are needed to quantitatively identify how the

features of the surface textures are influencing the bonding strength. For an important surface property has quantitative characterisation – the wettability (denoted by contact angles), improvements can be made to fulfil its potential of becoming a principle guide. The improved model, should have the physically validity, and the capability of instructing the dimensional analysis of the surface texturing for the bonding strength purpose.

Industrial benefit 4: Firstly, varied conventional machining and innovative texturing technologies would be explored for their potential in bonding strength improvement. Therefore, prototyping and possibly efficient solution can be generated. Moreover, the model development aims at building a designing tool of surface textures to achieve dimensional design for bonding strength improvement.

## Chapter 3

### Methodology

In this chapter, the experimental methods, including the test approaches, equipment and setups and data processing are presented to give a comprehensive understanding of the procedures conducted for achieving the research goals set in Chapter 1. Divided in two parts: the investigation of the surface texturing's effects on the dry-lubricated sliding wear performance and on the bonding strength of the bearing liner, the main test strategy adopted, the samples and processing (surface texturing and other treatment), as well as the post-analysis (e.g. surface analysis and contact mechanics analysis) are discussed in details.

#### 3.1 Sliding wear test for tribological effects of counterface textures

To investigate what effects the counterface textures may produce on the tribological performance of the composite bearing liner, sliding friction and wear tests need to be conducted on the contact pair. In the experiments, the generated test conditions should be representative of those in the real applications (i.e. in the helicopter rotors), while the performance parameters (friction and wear rate etc.) need to be reliably monitored. Moreover, the critical phenomenon occurring on the surfaces and interface, including topographic change, material transfer etc. should be analysed systematically, so that the optimization of the surface textures can be carried out strategically.

##### 3.1.1 Sliding wear test with pin-on-plate test scheme

The spherical plain bearing used in helicopter's rotors is a typical application of the dry-lubricated bearings. In flight conditions, the spherical plain bearings in the rotors are driven through links by actuators, going through oscillating rotations. In the tail rotor, the oscillating rotations are basically single-axis (so called 'swivelling rotation'), along the circumferential direction of the sleeve like shown in **Figure 21** (a), while in the main rotor, the motion may be composed of multi-axis rotations. For instance, the rotation within the pitch-control-bearings under cyclic operations are usually regarded as a combination of the main swivelling rotation and the a subsidiary tilting rotation [183], like illustrated in **Figure 21** (a) (kinematics will be updated later in chapter 5). Normally, the resultant nominal contact pressure ranges from around 10 and 40 MPa, and sliding velocity is between 0.03 to 0.15 m/s (with oscillating frequency of around 3Hz) in common bearing configurations (information provided by SKF).

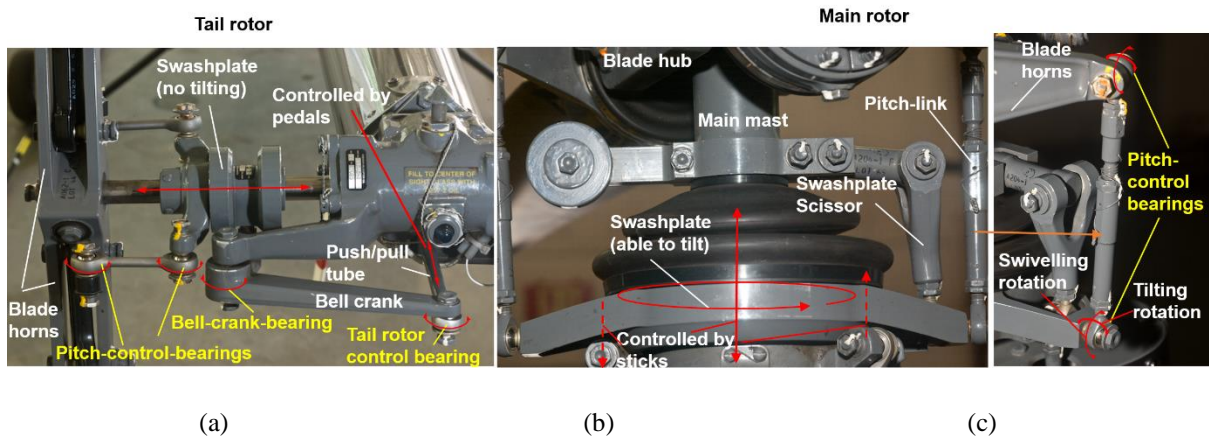


*Figure 21. The mechanism and component motions in (a) a tail rotor, (b) a main rotor and (c) pitch-controlling part of a main rotor of a helicopter*

With the working conditions considered, the pin-on-plate sliding wear tests were conducted to reproducing the sliding contact conditions, as the generated reciprocating test condition can reveal the oscillating nature of the motion. The tests were performed on a BICERI universal wear test machine, whose original set-up is as shown in **Figure 22**, and the relevant modifications made are introduced later in section 3.1.3. The driving motor has a rotating speed range of 20 to 240 RPM, leading to the reciprocating frequency of slider varying from 1/3 to 4 Hz, and the load applied through the weights and fulcrum can reach up to around 2450 N (250 kilogram-force). To simulate the contact in real bearings, the composite liner should serve as the pin specimen, fixed on the loading lever, and steel counterface should act as the plate specimen, carried by the slider block. This arrangement can reflect that in the real bearing configurations the spherical counterface has a larger surface area for the bearing liner to slide on, as illustrated in **Figure 23**. Together with the arrangement of samples, the loading and driving system can reproduce the representative operation condition ( $P = 40\text{MPa}$ ,  $V = 0.12\text{m/s}$  as selected later in 4.2.1) of spherical plain bearings in a helicopter.

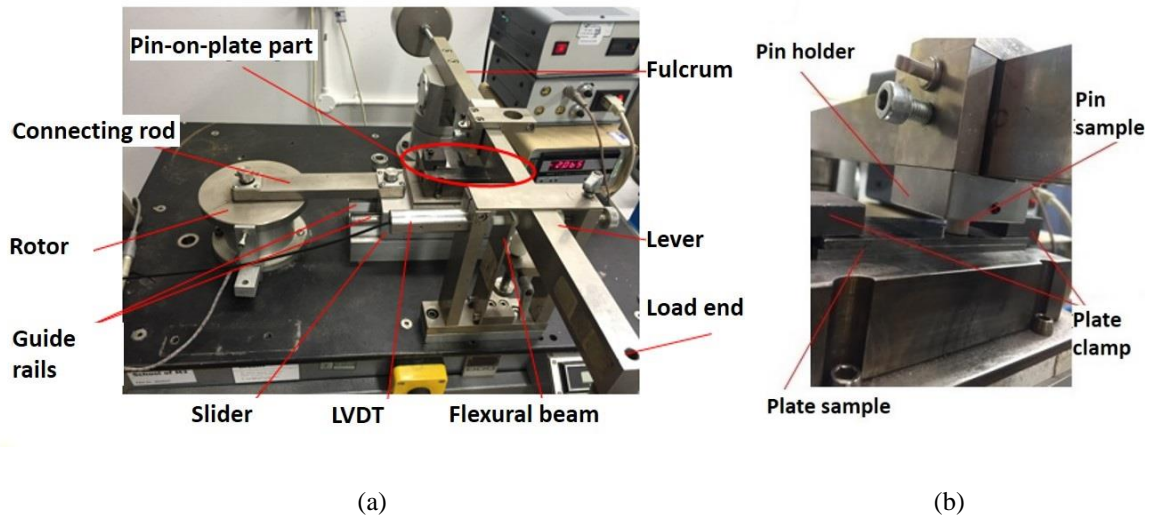


*Figure 22. (a) The original set-up of the reciprocating sliding wear test rig and (b) detailed view of the contact parts*

Moreover, under the constant rotating speed of the driving motor, the relative sliding displacement of the reciprocating plate is a sinusoidal function of time, relating well with the displacement-time relationship under single-axis oscillating rotation occurring in spherical bearings. Although the linear reciprocating could not perfectly replicate the multi-axis rotation under cyclic operation of a main rotor (in fact also proven as an effective approximation later in the case study in Chapter 5.2), this test approach can still reflect the operation condition in a sufficient application regime.

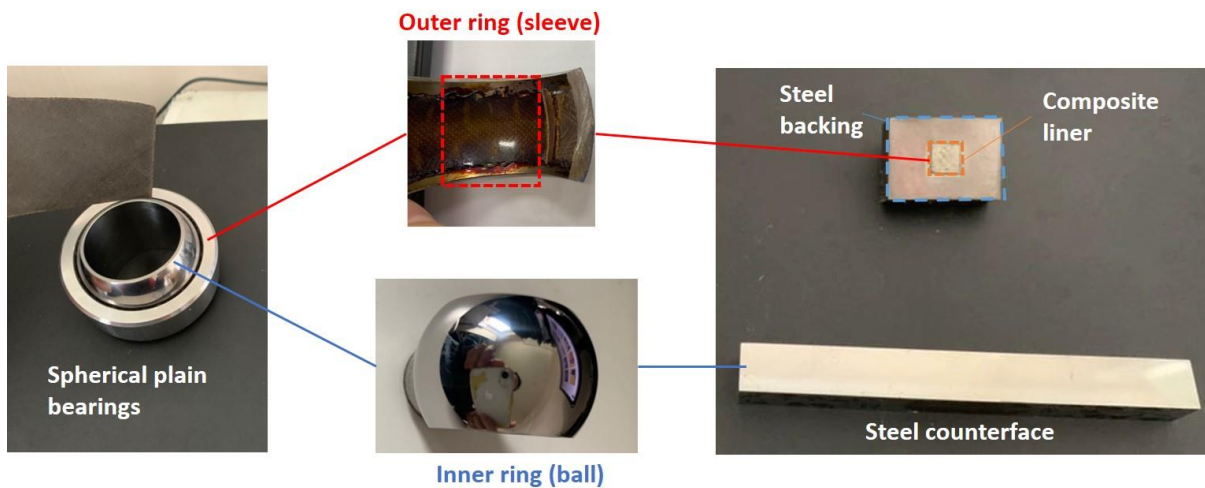


*Figure 23. Arrangement of pin-on-plate mimicking the contact in real spherical bearings*

On this test basis, aiming at revealing the influence of the counterface texturing on the tribological performance, procedures to prepare the samples, the sensory system for monitoring the signals and relevant analysis methods were developed, as described in detail in the following sections.

### 3.1.2 Sample preparation

#### 3.1.2.1 Pin sample

The liner in a spherical plain bearing is bonded on the steel backing to serve as the pin sample, as shown in **Figure 24** (a). This woven fabric composite of PTFE and glass fibre supplied by SKF Ltd is a typical liner in modern helicopter rotor-head bearings. Each sample has the same thickness of 280 $\mu$ m and square surface area of 7 mm $\times$ 7 mm. The bonding process (completed in SKF Ltd) followed the standard procedures used for the real bearings.

Screwed on the back of the steel block, like shown in **Figure 24** (b), the spherical dome nut enables freedom to tilt during fixing and facilitates self-alignment between the two flat surfaces in initial set-up. Meanwhile, a slot for thermal couple cable was manufactured on the block, with a small hole guiding all the way to the very back of the composite liner for temperature measurement.

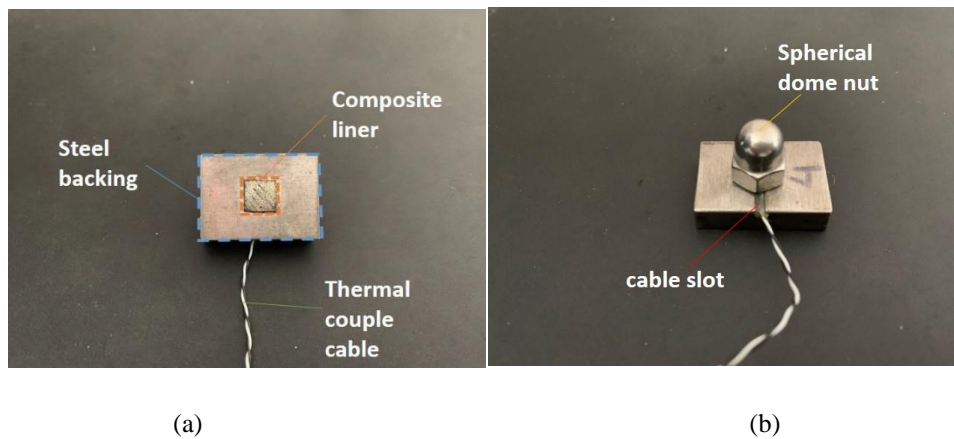


*Figure 24. (a)Front view and (b) back view of the pin sample and the holding block*

#### 3.1.2.2 Plate sample

The counterface plate, correspondingly, uses the same material widely used for the counterface ball in the spherical plain bearings - the AMS5630 440C stainless steel, with the hardness of 56 HRC. In its supplied state (polished), the average surface roughness is  $R_q$  0.02  $\mu$ m. To generate designated textured surfaces for investigation, the following texturing and polishing process were adopted.

##### - Counterface texturing

To generate bespoke texturing patterns on the counterface, the Ekspla AtlanticHE 1064 picosecond pulsed laser was employed together with the Aerotech multi-Axis high-precision positioning system. As shown in **Figure 25**, through mirror arrays, the laser was led into a 2D galvanometer head and then on the sample on a 4-axis stage (X, Y, Z and A as depicted) with

positioning precision of  $\pm 0.1\mu\text{m}$  for ablation of the designated texture pattern on the plate counterface.

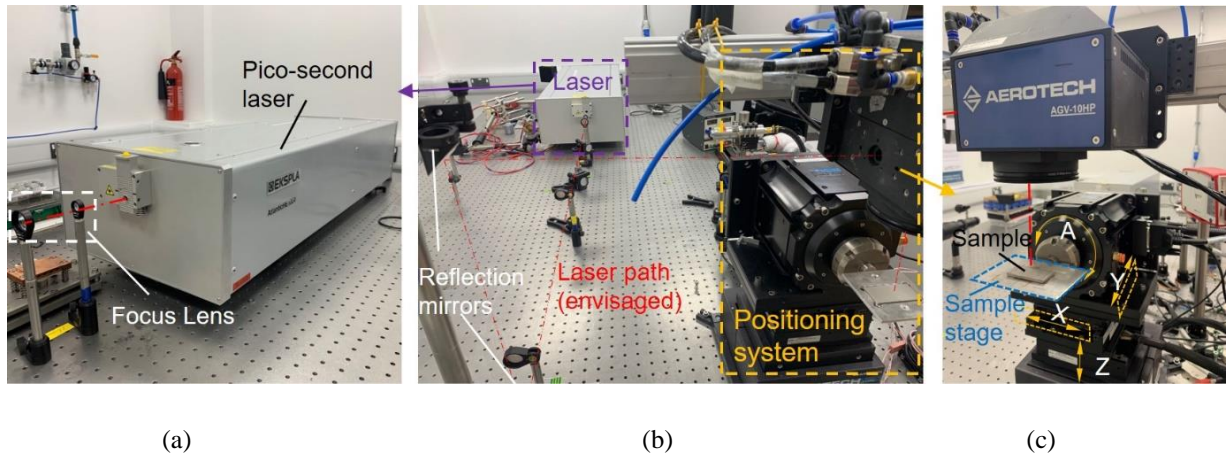


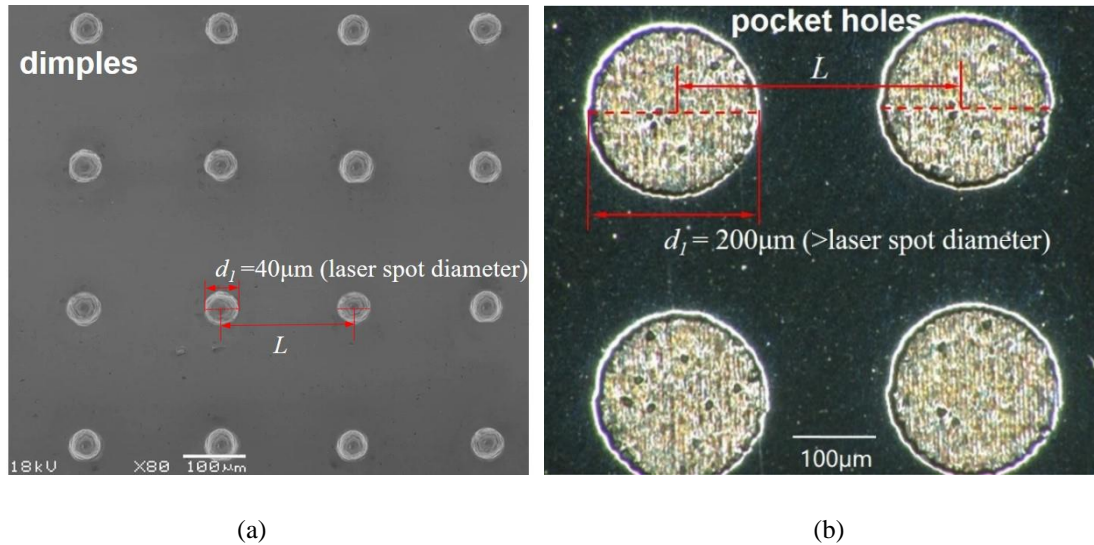
Figure 25. (a)The pico-second laser, (b) the whole view for laser system(c) the precision positioning system

Table 5. Main specifications of the Ekspla AtlanticHE 1064 pico-second pulsed laser

Parameter	Specification
Laser medium	Nd: YVO
Laser Diode	808 nm; max power 140W
Pulse duration	~50 ps
Wavelength	1064 nm
Repetition rate range	4 kHz
Average output power	~ 4 W
Pulse energy	~ 1 mJ
Beam diameter at $1/e^2$	$1.5\pm 0.3$ mm
Beam divergence	$< 2.5$ mrad
Focal diameter (spot diameter)	~40 $\mu\text{m}$

With the facilities, the laser is capable of producing various complex texturing forms, such as grooves (linear or curved), polygons and elliptical holes. However, these listed textures all have many specific parameters for the geometry and arrangement (like trench orientation, skewness of a polygon and aspect ratio of an ellipse). This would introduce excessive influencing factors when analysing the effects of texturing, such as the anisotropy caused by directional characteristics (e.g. when grooves or elliptical holes are aligned in varied orientations). In this thesis, however, the focus is not on the optimization of the textures' shapes, but revealing how the general parameters (texture dimensions and density) of surface textures may alter the

tribological phenomenon and friction and wear behaviour in the dry-lubricated contact. Therefore, textures with geometric features that may introduce too many influencing factors was not adopted in this study (e.g. direction and aspect ratios have to be considered for elliptical concavities and trenches to understand the anisotropic performance). Instead, the surface textures generated are confined to circular concavities uniformly distributed on the counterface, like shown in **Figure 26**, to avoid extra influencing factors like texture orientation and aspect ratio.



*Figure 26. Designed texture pattern with (a) dimples and (b) pocket holes*

For the fabrication for a type of circular concavity, like shown in **Figure 26**, depending on the designated diameter ( $d$ ), it is achieved either through applying the laser shot with single laser shots (for ‘dimples’) or controlled ablation paths (for ‘pocket holes’). It should be noted that, the smallest diameter would not be restricted by the focal diameter (spot diameter) of the laser (around  $40\mu\text{m}$ ), since diameters smaller than that can be achieved through polishing off a top layer of the counterface, as will be introduced later. As for the controlling of the ablation depth, firstly a calibration process relating the resultant depth with applied dwell-time (for dimples) or scanning velocity (for holes) was conducted prior to the manufacturing process as a guidance, like presented in **Figure 27**. Then, the relationship between the ablated depth  $Dep$  of the original texture and the parameters of the laser (power  $P_l$  and dwell time  $t_l$ , step 1 in **Figure 33**) can be found with the help of interpolation. For example, based on **Figure 27** (a), under  $3.6\text{ W}$  output power (90% of maximum) to fabricate a dimple with  $8\mu\text{m}$  depth, the dwell time should be set to 9 milliseconds.

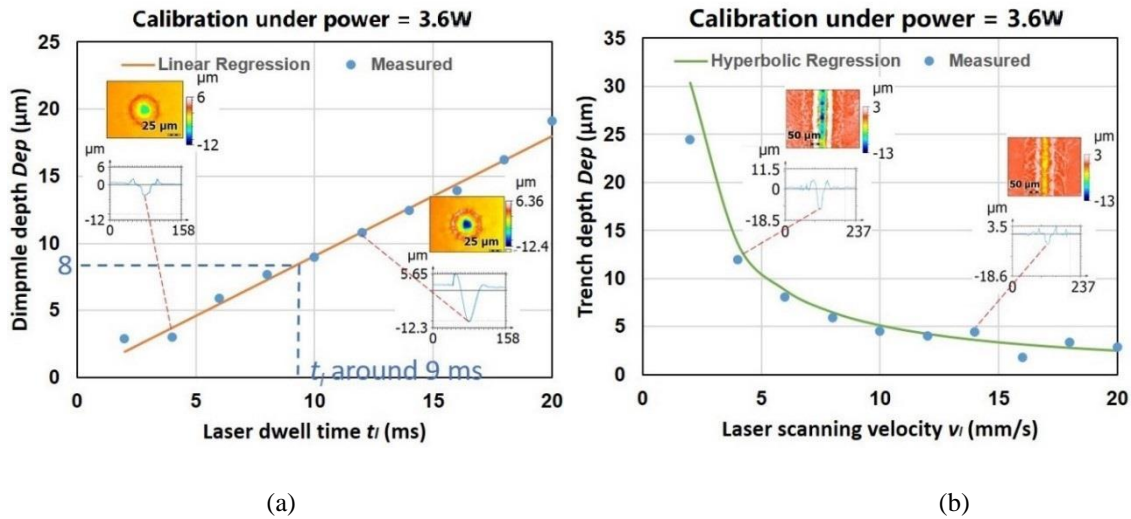


**Figure 27.** Linear interpolation of the (a) dimple depths versus dwell time of the laser and (c) trench depth versus scanning velocity of the laser under the output power 3.6 W

During laser ablation, in the central area where the energy is most focused (often defined as  $1/e^2$  of the laser beam), the material would be melted, evaporated, or directly converted into plasma under an depending on the energy flux input [184]. Adjacent to this area, due to heat-diffusion, a recast layer would emerge featuring occasionally oxide inclusions and micro-cracks, as well as a further heat-affected-zone (HAZ), in which grain refinement and hardening would occur as a result of rapid local quenching, like demonstrated in **Figure 28(a)** [185]. The increase the counterface micro-hardness can possibly influence that micro-abrasion of the PTFE, which was observed later on the edges of the dimples after in the wear tests (section 4.2 and 4.4). However, when the micro-hardness on part of the counterface is increased, the interaction between the glass fibres and the counterface can also be affected. In a word, the effect of the increase in micro-hardness is complex. However, despite the possible influence induced from the increase in micro-hardness, the thermal effect is reduced with lasers with shorter pulses. Compared with long-pulse-lasers (millisecond and nanosecond laser), the short-pulse-lasers (picosecond and femtosecond laser) can have a laser-matter interaction time considerably shorter than heat dissipation from the ablated region. Therefore, the heat effects are substantially localized and suppressed, like illustrated in **Figure 28 (b)** [185]. This is also why the short-pulse-lasers are often referred as ‘cold laser’.

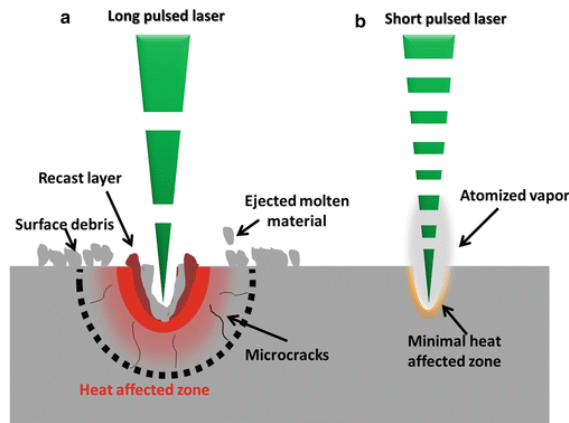


Figure 28 Comparison of thermal effects with (a) long pulsed laser and (b) short pulsed laser ablation process [185]

Judging by the theoretical estimation, which indicates how the size of the HAZ is influenced by the thermal properties of the material and pulse duration of the laser [186], the diffusion length in our application would be in nano-meters level. In addition, the observations on similar conditions (machining on stainless steels with pico-second laser) [187] also indicates a minimal HAZ. Therefore, the influence from the HAZ with the employed laser texturing can be considered minor. Comparing the re-deposition with the one created by a SP-100C-0013 nanosecond second (later used for roughening sleeve surface), as shown in **Figure 29**, it can be seen how the pico-second laser is advantageous in this aspect.

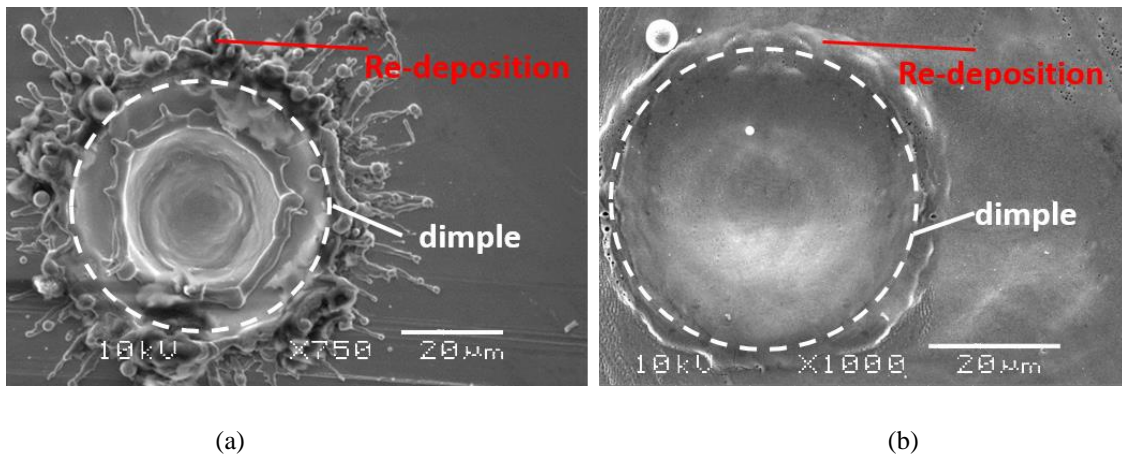


Figure 29. SEM image of a dimple region created by (a) the nano-second laser and (b) the pico-second laser

### - Counterface polishing

As has been pointed out, small as it is with pico-second laser, the re-deposition may still occur. This re-deposition need to be removed as the spikes and asperities may cause lead to extra abrasion during sliding contact. With this considered, a polishing process is essential for processing the surface to the desired state.

For the goal of generating the desired textured counterface, considered together with the texturing step, the polishing process was proposed to follow the two main steps (step 2 and 3 illustrated in **Figure 33**). The first polishing step (lubricated with water) aims at removing the inherent material re-deposition, and the final polishing (lubricated with 0.05  $\mu\text{m}$  silica suspension) should round the dimple edges. The polishing was conducted on the Struers LaboSystem Tegramin machine, as shown in **Figure 30**, and the details for these processing are discussed as following.



*Figure 30. Basic structure of the Struers LaboSystem Tegramin machine*

As has been described, circular concavities in different diameters can be produced using either ‘dimpling’ or ‘holing’ strategy, so for a type of dimples with a certain diameter ( $d_1$ ), to achieve the different coverages ( $p_c$ ) designated, the distance  $L$  between the adjacent dimples need to be set before the texturing step following the equation:

$$L = \sqrt{\frac{\pi d_1^2}{4p_c}} \quad (3.2)$$

What should be noticed is that for dimple texture,  $d_1$  should be the diameter of the dimples after the final step. Therefore,  $d_1$  is determined by both the original diameter  $d_0$  (40  $\mu\text{m}$ , determined by the laser beam) of the dimple, and the reduction in diameter as the texture gets shallower during the first polishing step. Using the calibration for the polished depth under different sets of polishing parameters (normal force  $F_N$ , rotating speed  $\omega$  and time  $t_p$ ), like shown in **Figure 31**, the diameter  $d_1$ , as well as the dimple depth  $Dep$  in the final state (influence from the later final polishing is negligible) could be controlled by selecting corresponding parameters for processing. For example, in the later section, dimples with 20  $\mu\text{m}$  diameter and 2 $\mu\text{m}$  were wanted, meaning that the diameter needs to be reduced by 20  $\mu\text{m}$  from the original 40  $\mu\text{m}$ . To achieve this, utilizing both the calibration **Figure 27** and **Figure 31**, dimples with diameter 40

$\mu\text{m}$  and depth  $4\ \mu\text{m}$  were firstly created by laser shots with output power  $3.6\ \text{W}$  and dwell time  $4.5\ \text{milliseconds}$ , then polished under  $40\text{N}$  normal force at  $200\ \text{RPM}$  rotational speed for around  $350\ \text{seconds}$  to remove the top  $2\ \mu\text{m}$ , reaching the designated state. The difference of dimple depth and diameter before and after polishing was measured using profilometer (Bruker Contour GT-I 3D Optical interferometer).

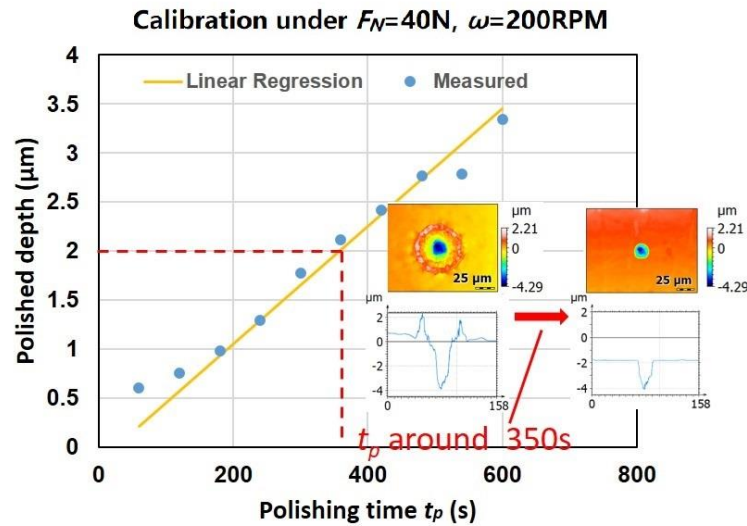


Figure 31. Measured data and the liner regression for polished depth versus polishing time ( $40\text{N}$  normal force and  $200\text{RPM}$  rotating speed)

After the first polishing step, the concavities would often be left with sharp edges. In the preliminary trials on counterface samples just after the first polishing step, the sharp edges may act as micro-cutting edges during sliding which leads to accelerated wear of the PTFE counterpart composite. To prevent this, the sample surfaces were then polished on the automated polishing machine (Struers LaboSystem Tegramin) for  $10\ \text{seconds}$ . In this process, a MetPrep final polishing cloth and  $0.05\ \mu\text{m}$  silica suspension were adopted to round the dimple edges with texture dimensions kept almost uninfluenced, like the transformation of profiles in the last step shown in **Figure 33**. During the polishing process, controlled normal force ( $40\text{N}$ ) were applied on the back of the samples by the automated polishing machine to minimize the change induced on the surface flatness. Similarly, the un-textured counterface samples, which would be used as the reference smooth surfaces, were also put through the two polishing steps in the same batch with the textured samples, so that the same surface roughness ( $R_q\ 0.015\ \mu\text{m}$ , excluding the textured areas) can be obtained. Comparing the tribological performance with counterface with and without each step polishing (with the wear test condition determined later in chapter 4.2.1), like shown in Figure 32, it can be seen that both polishing steps are essential

to the tribological performance, since the wear life would be substantially shorter (reduced by at least around 30%) without either of the steps.

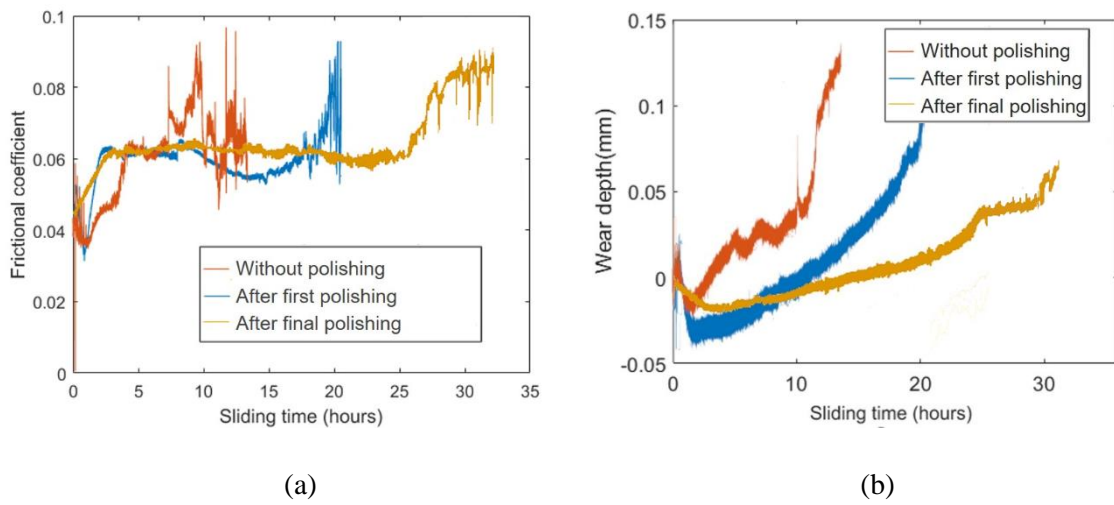


Figure 32. (a) Frictional coefficient and (b) wear depth versus sliding time with dimpled counterface (6.4% coverage of dimples with  $40\mu\text{m}$  diameter and  $2\mu\text{m}$  depth) in a wear test (normal pressure  $40\text{MPa}$ , reciprocating frequency  $3\text{Hz}$  and stroke length  $20\text{mm}$ ) before and after each step of polishing

Overall, the laser surface texturing and the two-step polishing compose the preparation process for the counterface samples- the main variant in this study, as illustrated in **Figure 33**.

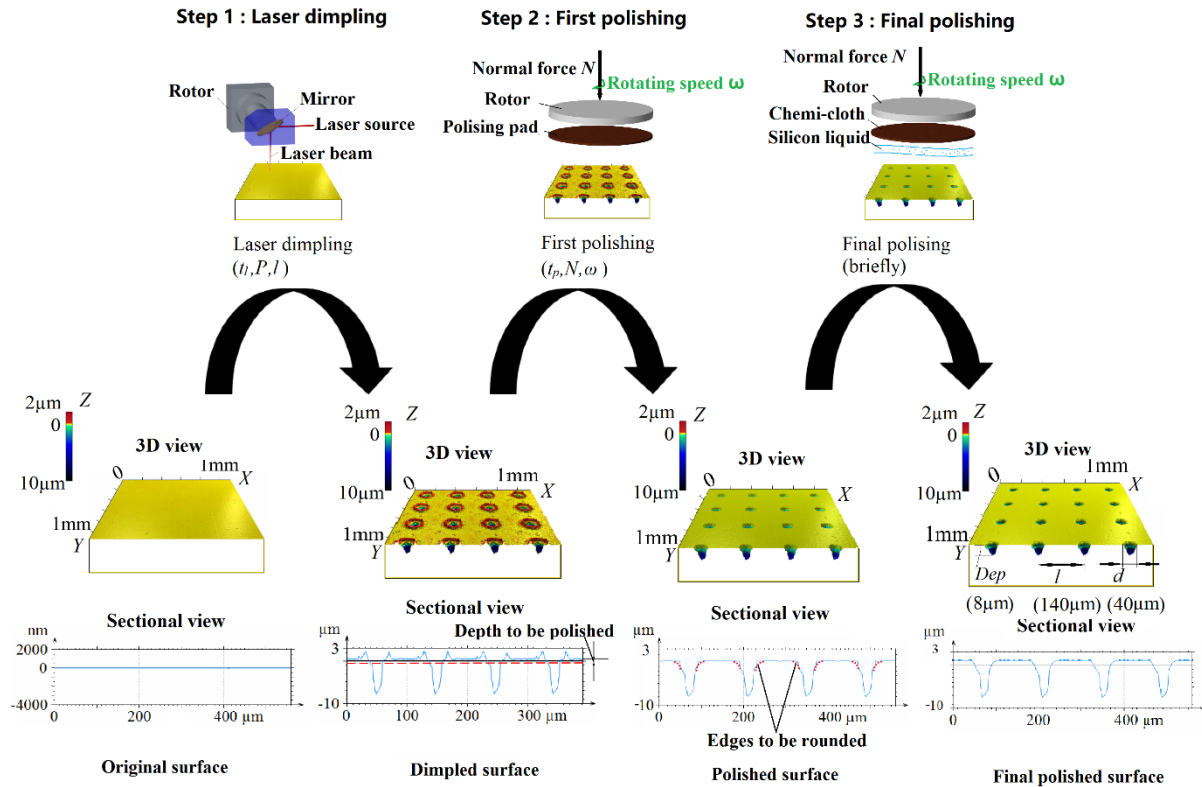


Figure 33. Processing scheme for manufacturing the textured surface

### 3.1.3 Test monitoring and signal analysis

#### - Friction monitoring

The frictional force is a key index for evaluating and analysing the overall tribological performance. In dry-lubricated contact, the friction can be sensitive to the lubrication state (e.g. how well is the transfer film formed), and the occurrence of different wear phenomenon (e.g. occurrence of abrasion and third-body particles). For the multi-layer composite studied in this thesis, the evolution of friction can also be a reflection what stage the wear process is in. Therefore, it is essential to acquire an accurate and reliable monitoring of friction.

For the wear tests, with the original set-up of the Biceri wear test rig, erratic chattering (reflected in the deflection curve of the flexure beam as in **Figure 34**) occurred under the high load (around 500N) on the load arm and the flexure-beam (previously shown in **Figure 22**), which was used to measure the frictional force. Because of the significant oscillation movement along with the pin sample (composite), the designated full-sliding operation between the pin and plate could not be fulfilled, and the measured deflection would not reveal the sliding friction under the real operation. In order to solve this problem, it is proposed that the loading arm should be constrained for its horizontal movement (as shown later in **Figure 40** (a)), and a force sensor should be placed on the pin side to measure the experienced friction. For the force sensor, the strain gauge measuring system was selected considering its simplicity and robustness.

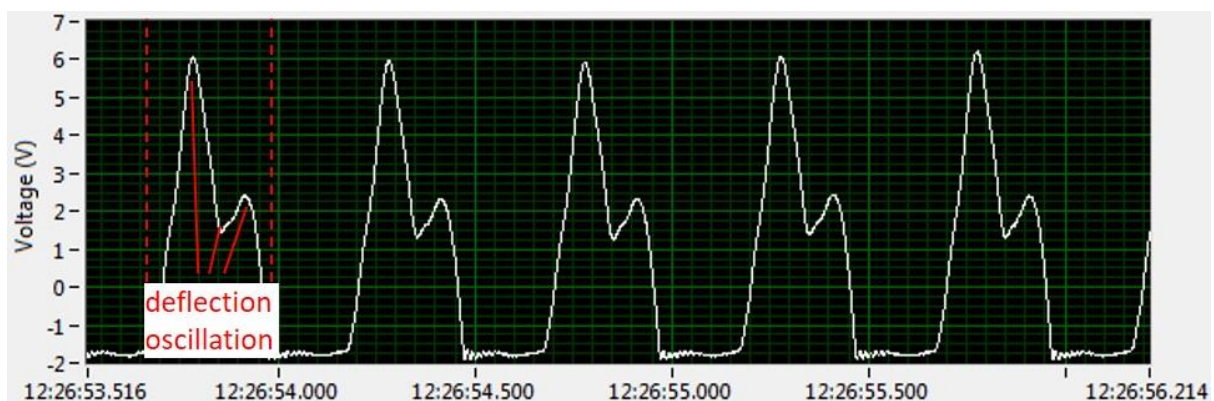


**Figure 34.** Friction force signal measured with flexure beam and LVDT for a wear test on the self-lubricating liner sliding against a smooth counterface (normal pressure 40MPa, reciprocating frequency 2Hz, stroke length 20mm)

A strain gauge is a metallic foil pattern with an insulating backing, which can be bonded to the designated work-piece by adhesives such as super glue. Under the external force, the metallic foil will deform along with the work-piece, and its electrical resistance will change accordingly. Using an electric bridge, usually Wheatstone bridge[188], the change in resistance will be

amplified and converted to voltage, and therefore, the corresponding strain value and external force can be determined.

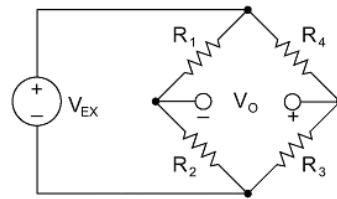


**Figure 35.** A Wheatstone bridge circuit[188]

As demonstrated in **Figure 35**, in a Wheatstone bridge circuit, the output voltage  $V_0$ , measured between the middle nodes of the two voltage dividers is represented as [188]:

$$V_0 = \left[ \frac{R_3}{R_3 + R_4} - \frac{R_2}{R_1 + R_2} \right] V_{EX} \quad (3.3)$$

where  $R_i$  ( $i = 1, 2, 3, 4$ ) are the resistance of each strain gauge, and  $V_{EX}$  is the excitation voltage.

It can be seen from the equation 3.5 that if four strain gauges have the same resistance, the output  $V_0$  would be 0. However, if a small disturbance is incurred on one strain gauge by bonding it to a deforming structure (referred as ‘Quarter-Bridge’), the change will incur unbalance of the bridge and an alteration in the output  $V_0$ . Moreover, arranged in a certain pattern, a pair of gauges, or all four gauges can be bonded on the structure (referred as ‘half-bridge’ and ‘full-bridge’) to double or quadruple the signal.

Due to the restriction of the sample dimensions (only 0.28mm thick), the strain gauges could not be installed directly on the sample like in some applications [189]. Instead, a specifically built shearing frame was designed for the sample to be fixed and the strain gauges to be arranged, as shown in **Figure 36**. To tailor the strain-gauge-frame to the wear test rig, like shown in **Figure 36** (a), on the top end, the rectangular aluminium frame is fixed to the loading lever by screws, and on the bottom, the slot accommodates the sample block of the composite liner.

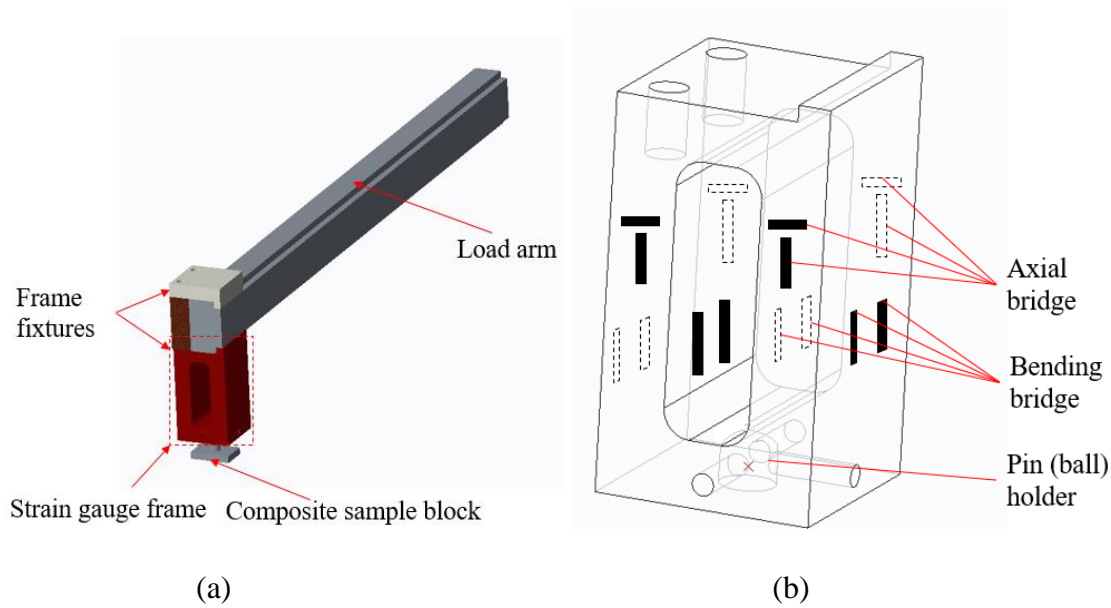


**Figure 36.** (a) Conceptual design of the friction measurement set-up using the strain gauge frame; b) arrangement of strain gauge bridges on the strain gauge frame

With the help of a series of Finite Element (FE) analysis on the shear deformation, the frame dimensions were determined together with the strain gauge selection. The designing principle was that the frame should be thin enough to give sufficient measurement sensitivity (i.e. resultant voltage signals considerably larger than the inherent noise of the system), while plastic deformation must be prevented. From the analysis and trials, the beam thickness of the frame was finalized to 5 mm. Meanwhile, considering sensitivity and dimension restrictions, Vishay L2A-06-062LW-120 general-use strain gauges were selected to incorporate with the strain frame. The strain gauge's resistance is 120 ohms ( $\pm 0.6\%$ ), and the gauge factor is 2.177.

Then, as displayed in **Figure 36** (b), type-1 full bridges (parallel pairs on the front and back of a beam) [188] were bonded on the side faces for friction measurement, utilizing the strain/voltage difference between the tensile side the compressive side caused by a shear force, while type-3 full bridges (perpendicular pairs on the front and back of a beam) were bonded vertically for normal load monitoring, functioning by the Poisson effect (the difference between  $\epsilon$  in orthogonal directions). The bridge circuits was fulfilled on the National Instrument SCXI-1314 Universal Strain Terminal Block, and the output voltage signal was processed with SCXI-1520 data acquisition (DAQ) module (achieved equivalent resolution  $4\mu\epsilon$  [190]). The analysis of the signal data was conducted on the PC console for analysing with NI Signal Express 2015 software.

Consequently, the raw signals of the output voltages were improved with the strain gauge system, as shown in **Figure 37**. In each half-cycle (sliding 'forward' or 'backward'), the output

voltages transformed smoothly with a small degree of oscillation, sufficiently providing a sampling region for friction measurement (smaller sampling frequency with full wear test). As the friction values can be converted by sampling the gap between the peak cycle and valley cycle, the influences from drifting of the sensor can also be minimized. It is required though, that a calibration process to be conducted prior to each test to correlate the output voltages with the frictional force (by measuring the output voltage with different known loads applied horizontally on the pin block through weights and a pulley).

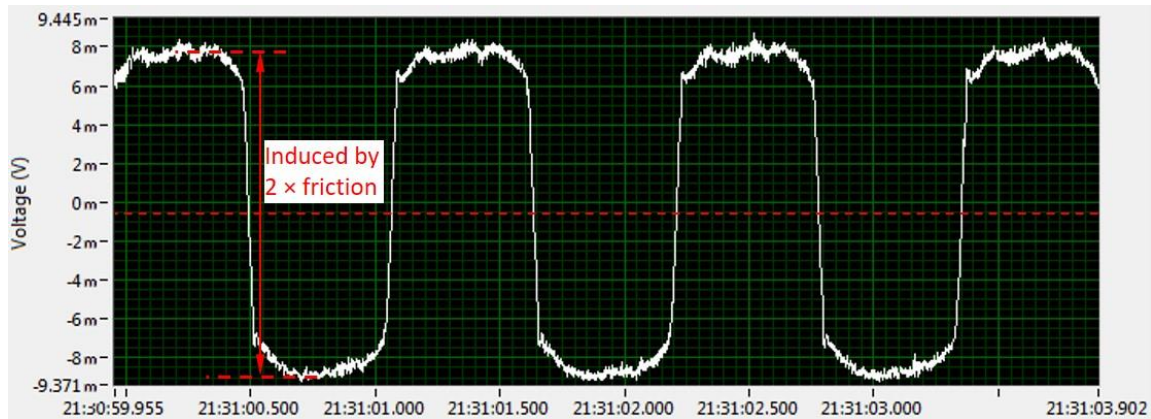


**Figure 37.** Friction signal measured from the dynamometer for a wear test on the self-lubricating liner sliding against a smooth counterface (normal pressure 40MPa, reciprocating frequency 1Hz, stroke length 20mm)

To evaluate the validity and reliability of the new friction measurement methods, a series of measurements was compared with that acquired with a calibrated dynamometer (Kistler 9317b as shown in **Figure 38**) under representative test conditions (e.g. normal pressure 40MPa, reciprocating frequency 3Hz, stroke length 20mm). The utilized Kistler 9317b is a preloaded 3-component dynamometer, capable of measuring normal force ( $F_z$ ) up to 2000N and shear force ( $F_{x,y}$ ) up to 200N. Under a load, the piezo element (quartz) yields an electric charge proportional to the force. The sensitivity is around 26 pC/N for normal force and around 11 pC/N for shear force. Then, with the Kistler 5011B charge amplifier (Sensitivity 0.01-9990 pC/M.U., scale 0.001-9.99E6 M.U/v), the charge signal was converted into voltage and sent to the NI USB-6009 I/O Device, and then PC console for analysing. In the test condition (normal force around 1960N, and frictional coefficient around 0.05 to 0.07 for most of the time), the force sensor is able to measure the frictional force whilst capturing its variation.

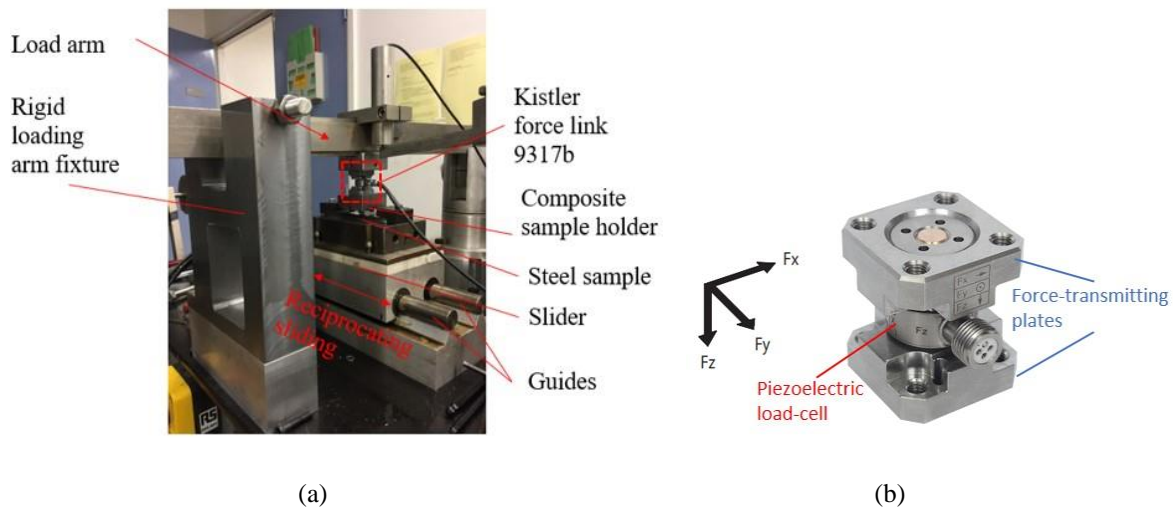


**Figure 38.** (a) The set-up for friction measurement using Kistler 9317b dynamometer and (b) the Kistler 9317b dynamometer

In the representative cases demonstrated in **Figure 39**, it can be seen that with all measurements with different durations, similar fluctuating pattern for the CoF in the run-in stage were captured by both measurement methods, even the exact values varied. More importantly, for comparison of the 8-hour sessions between both measuring techniques, it can also be seen that the similar entrances into the relative steady stage (after around 4.5 to 6 hours) were indicated, and the steady CoF were close, at around 0.07. These stable-stage features are crucial, particularly for the later full-wear tests. Therefore, despite that differences still existed between the two measurements (such as the fluctuating degree measured in run-in stage); the similarity stated above has already proved the credibility of the friction measurement using strain gauges.

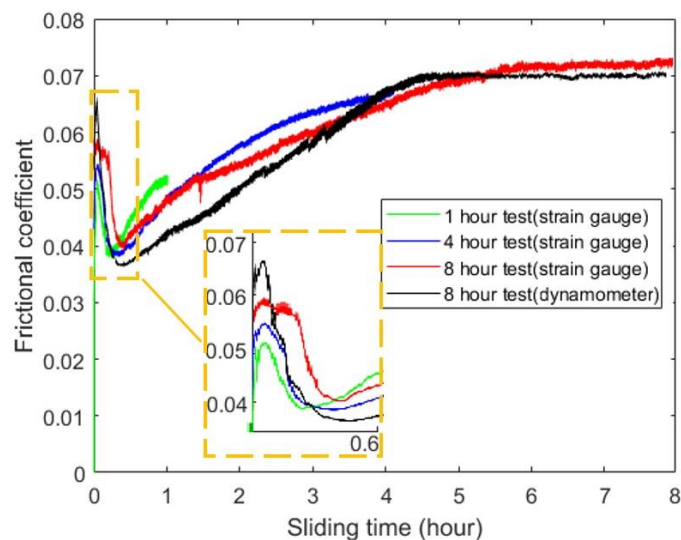


**Figure 39.** Comparison of frictional coefficient measured using strain gauges and dynamometer for a wear test on the self-lubricating liner sliding against a smooth counterface (normal pressure 40MPa, reciprocating frequency 2Hz, stroke length 20mm)

Overall, the developed strain-gauge system has an improved capability and sufficient validity in friction measuring. Considering that it has even higher robustness than the commercial dynamometer, whose functioning range was sometimes exceeded in final wear-out stage, the strain-gauge system was used for all the full wear test sessions conducted later in this thesis.

#### **- Real-time wear and temperature monitoring**

Since the commonly used gravimetric measurement of the wear volume needs interruption of the wear test and thus jeopardising the continuity, it is proposed to use a LVDT fixed vertically on the load arm to measure the real-time wear depth of the composite sample, as shown in **Figure 40**. With the set-up, the probe tip of the LVDT should be in contact with a fixed horizontal reference plane, so the sinking of the load arm can be continuously measured as wear progresses. The analogue signal (voltage) incurred by the displacement change in the LVDT was processed by the NI USB-6009 I/O Device (analogue input resolution 14 bits, output resolution 12 bits) with acquisition rate 60 Hz (20 points sampled each reciprocating cycle), and sent to the PC console for analysing with NI Signal Express 2015 software.

Meanwhile, since the contact temperature is a key index for the thermal effect during the wear process, it needs special attention, particularly during preliminary selection of the test parameters. Real-time monitoring of the temperature was conducted by implementing the thermal couple (calibrated) through the slot of the steel backing of the composite liner, as has been described previously with the pin-sample design (**Figure 24**). The slot was fabricated as deep as possible to allow the thermal couple to reach as close as possible to the contact interface. The utilized thermal couple was the SE027 exposed junction Type K thermocouple (Pico Technology Inc.), which has the tip temperature range of -75 to +250 °C. The signal acquisition was processed with Pico TC-08 USB Thermocouple Data logger with acquisition frequency of 1 Hz (sufficient considering wear is a long-term process). Together, the temperature measurement precision of 0.025°C was acquired [191].

In summary, the acquisition system of the signals for friction, wear and temperature described above compose the monitoring for the conditions of the sliding contact, as demonstrated in **Figure 40**.

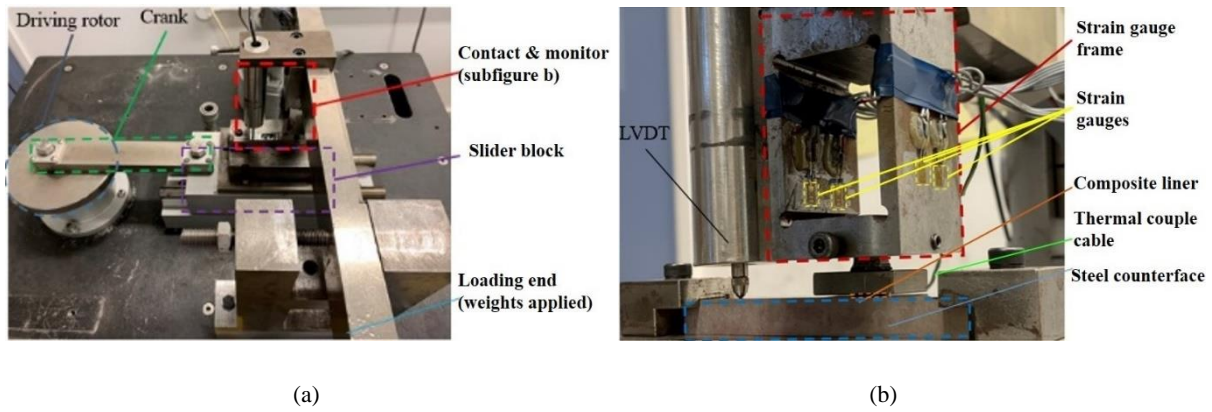


*Figure 40. Images of (a) set-up of the reciprocating sliding wear test rig and (b) detailed view of the contact & measurement*

### 3.1.4 Surface analysis and transfer film characterisation

To address the issues in observing and characterising the PTFE transfer film, and to develop a new method aiming at reliable observation and comprehensive characterisation the PTFE transfer film, varied techniques have been explored for their capability in this thesis. By their working principles, the surface analysing methods used in this thesis are in two categories: optical techniques, and analysis of emitted signals under an energy beam.

#### 3.1.4.1 Optical techniques

To acquire fast imaging of the surface, direct optical imaging method is the most economic and straightforward way. In this thesis, trials were done using the following techniques.

##### - High-speed-camera imaging

To explore the possibility of in-situ observation, a high-speed-camera imaging system was built to take photographic images of the counterface during operation.

The camera used is the MotionPro Y4-S2 High-Speed-Camera (Motion Pro, Inc.), which is capable of recording at 5100 frames per second with the resolution of 1024×1024. High density lux light is used to illuminate the objective as required for high speed cinematography. Besides, a lens assembly composed of the K2 Infinity videos lens, the CF amplifier tube (×1.66), the NTX Tube (2x), and the microscopic objective CF-4 (×4.57~6.10) were equipped. Aligned parallel with the counterface, like displayed in **Figure 41**, the lens assembly can achieve magnification up to around 200 times.

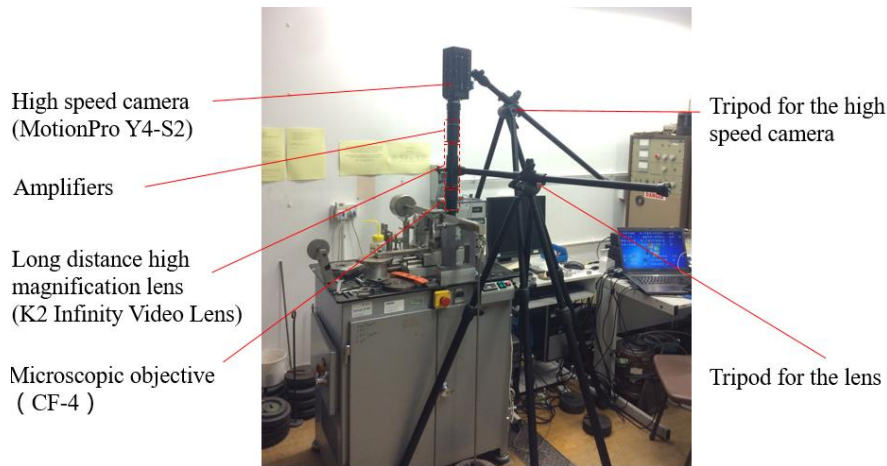


*Figure 41. Set-up for in-situ imaging of steel surface using high-speed camera*

With this set-up, the images of the counterface can be captured without ceasing the test. What is more, by setting the camera on the side (focusing on the section of the composite liner)**Error! Reference source not found.**

### - Optical microscopy

For in-situ microscopic imaging, the Keyence VH-7000 portable optical microscope (Keyence Ltd.) was used. It has a magnification range from 5 to 175 times, capable of generating coloured image with maximum view of 12mm × 12mm (at 5× magnification) and pixel numbers up to 4800 × 3600.

Incorporated with a portable lens stage, the portable microscope and the console PC shown **Figure 42** can be used on-site, enabling observation without removing the samples from the test set-up. It requires, however ceasing the test for each static picture to be taken.

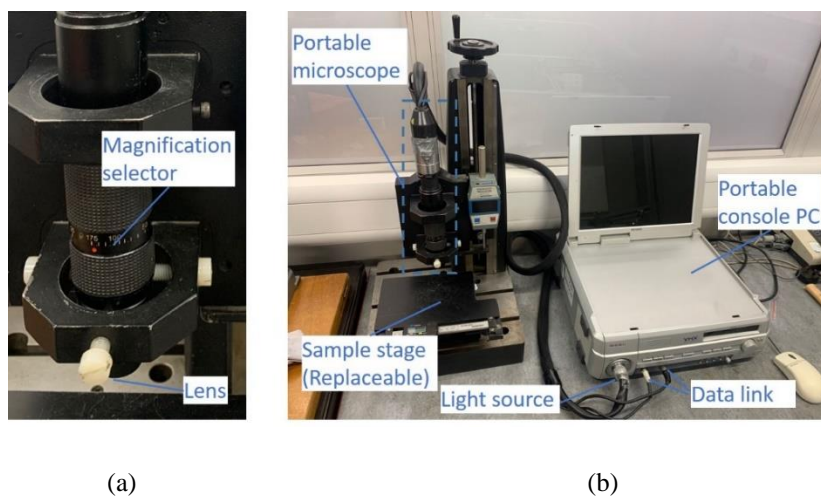


*Figure 42. (a)The portable optical microscope and (b) the overall system of the Keyence VH-7000 microscope*

## - Optical interferometry

To acquire information of the surface topography, the Bruker Contour GT-I 3D Optical interferometer (Bruker UK Ltd), as shown in **Figure 43** was utilized. The surface interferometer uses a charge-coupled device (CCD) image sensor to acquire the interference pattern caused by surface asperities, and therefore forming images of surface peaks and valleys. The lateral resolution acquired through the white light interferometry is around  $0.3\mu\text{m}$ .

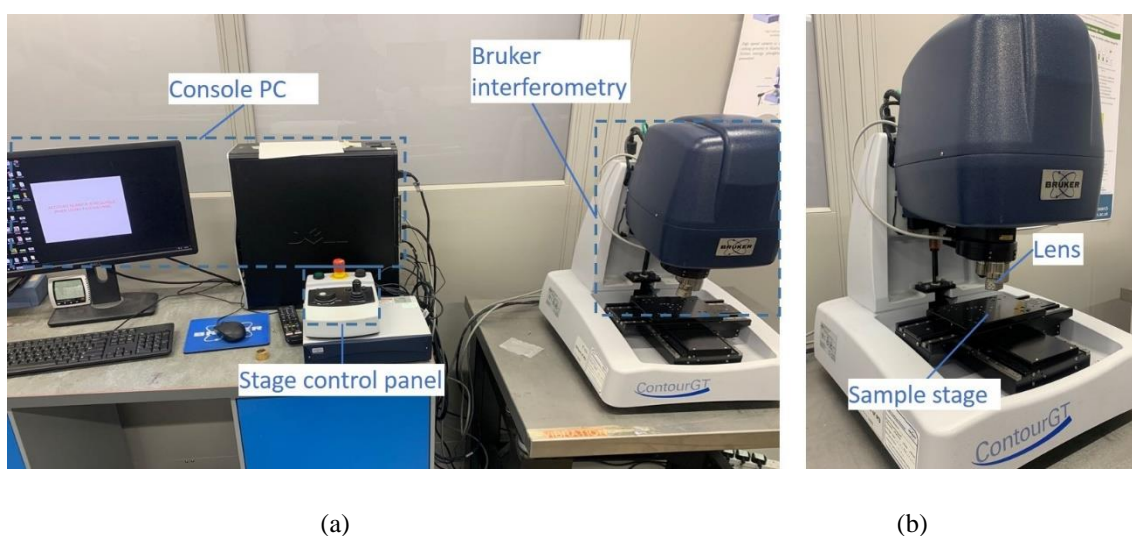


*Figure 43. (a) The overall system of the interferometry (b) the Bruker Contour GT-I 3D Optical interferometer*

### 3.1.4.2 Technology using emitted signal under energy beam

In many modern technologies of surface analysis, instead of light, a high-energy beam is used to interact with the surface material, and the surface properties were analysed using the emitted particles, such as electrons and ions. These types of surface analysis methods can all be categorised as one using energy beam and emitted signal. Since the emitted signals from different compositions on the surface would vary, some of these methods are capable of distinguishing the composition. Compared with the optical observations, these techniques may give a more reliable identification of the transfer film.

## - SEM analysis

SEM is one of the most commonly used technologies of this type. It scans a surface with a focused beam of electrons, and processes the emitted signals such as secondary electrons (SE) and back-scattered electrons (BSE), corresponding to its two basic imaging modes. The former mode has a higher surface imaging resolution since the SE are emitted from shallower locations of the surface compared with the BSE. The BSE imaging, however, is capable of distinguishing

the distribution of different material composition, as the signal is stronger with elements with larger atomic number. However, it could not identify the composition, while such a task needs to be achieved incorporated with another an element-analysis technique like Energy-dispersive X-ray spectroscopy (EDX).

In this thesis, the FEI Quanta 650 ESEM (FEI Company), as shown in **Figure 44**, was used to conduct surface analysis with an effort towards characterising transfer film. An Everhart-Thornley Detector (ETD) detector was used for SE analysis, and a Circular Backscatter Detector (CBS) was employed for BSE analysis. In addition, an Oxford Instruments X-Max - 150 EDX Detector was integrated with the instrument for chemical composition analysis.

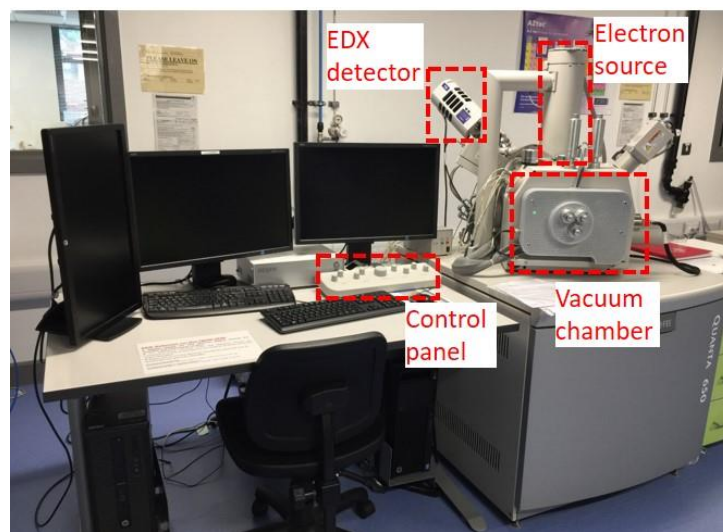


*Figure 44. The Quanta 650 SEM system*

Because the targeted subject – the transfer film was reported in varied thickness, it may need to vary the accelerating voltage to different ranges for exploration of characterising of the transfer film. To aid the analysis, CASINO v2.5, a commercial Monte-Carlo simulation software was used to simulate the stochastic paths of the electrons and compute the statistical distribution of penetration depth under each accelerating voltage tested.

#### **- ToF-SIMS analysis**

Time-of-Flight Secondary Ion Mass Spectrometry (ToF-SIMS) collects and analyses the secondary ions emitted when the surface is sputtered with a focused primary ion beam. The ions' time of flight in a 'flight tube' is measured to identify the ion type since the time is related with the ions' weight [192]. Because in this technique only the uppermost monolayers are sputtered, it is commonly believed to be a reliable technique to identify chemical composition in ultra-thin films. It is, however, a destructive test method as it removes the top molecule-

layers. Moreover it is also considerably more time-consuming than SEM (more than tenfold the time of SEM according to the author's experience).

Due to its capability of analysing the surface features to the degree of nano-meters, ToF-SIMS can be used for analysing the transfer layer on the counterface and serving as a benchmark for the improved SEM analysis.

In this thesis, the ToF-SIMS IV (ION-ToF GmbH) instrument, as demonstrated in **Figure 45** [193] was employed to analyse surface composition utilizing a Bismuth (Bi) primary ion source. With this mode, spectroscopy and imaging with spatial resolution around tens of nanometre can be achieved.

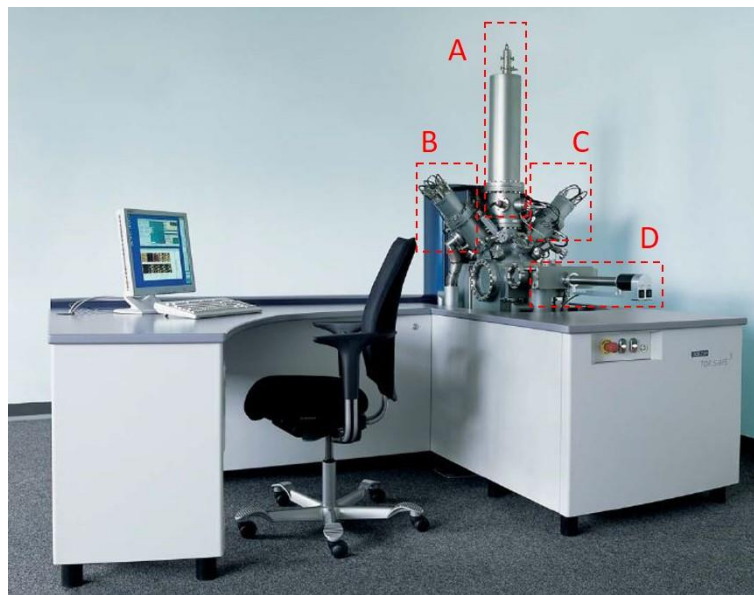


*Figure 45. ToF - SIMS IV (ION - ToF GmbH) instrument with key components labelled: (A) Time-of-flight mass analyser. (B) Bismuth cluster ion gun. (C) Cs+ and O2+ ion gun and (D) Load lock chamber and sample manipulator arm [193].*

### **3.1.5 Finite Element analysis for contact mechanics**

Introducing surface textures to the original 'smooth' surface can lead to stress concentration around the texture's edges. An extreme case is when the texture's edges are too sharp, a micro-cutting effect is created [44]. To evaluate this effect, particularly to link it with the dimensions and densities of the textures, a contact mechanics model was developed. The Finite Element (FE) software Abaqus/CAE 2016 was utilized to build the model.

#### **3.1.5.1 Governing equations**

To have an understanding of the theory and principles behind the model, the basic formulation used for modelling the contact problem in this thesis is presented.

##### **- Basic finite element equations**

According to the Abaqus theory manual [194], the standard displacement-based finite element analysis is applied, based on the virtual work statement. Basically, the physical interpretation for the virtual work statement is: the rate of work from the external forces under a virtual velocity field is equal to the rate of work from the equilibrating stresses on the rate of deformation under the same virtual velocity field. Therefore, the equilibrium equation for virtual work  $\Pi$  is:

$$\delta\Pi = \delta U - \delta W = 0 \quad (3.3)$$

where  $U$  is the work done by the external force and  $W$  is the work done by the equilibrating stresses, expressed as:

$$U = \int_V \tau^c : \delta\varepsilon dV \quad (3.4)$$

where  $\tau^c$  and  $\varepsilon$  are the conjugate pairing of material stress and strain measures, subjecting to fundamental constitutive relationships (e.g. elasticity), and

$$W = \int_S \mathbf{t}^T \cdot \delta\mathbf{v} dS + \int_V \mathbf{f}^T \cdot \delta\mathbf{v} dV \quad (3.5)$$

where  $\mathbf{t}$  is the unit surface force (e.g. frictional force and pressure force),  $S$  is the surface bounding the body volume  $V$ , and  $\mathbf{f}$  is the body force (e.g. gravity) for any point in the body. Hereby, equations 3.3 to 3.5 guide the solving of the internal stress/strain under the external force and enforced displacements – respectively the contact pressure and frictional sliding here.

### - Contact pressure

For the surface-to-surface contact between a deformable surface (composite) and a rigid surface (steel counterface), the contact pressure  $P$  at a surface node is related with the overclosure  $h$  (presumed deforming penetration to the mating surface):

$$\begin{cases} P = 0 \text{ for } h < 0 \text{ (open)} \\ h = 0 \text{ for } P > 0 \text{ (close)} \end{cases} \quad (3.6)$$

This illustrates that pressure would only be calculated if there is no gap between the adjacent surface nodes, and if it is calculated 0 it would set the overclosure back to 0. The virtual work contribution from the contact pressure is:

$$\delta\Pi = \delta P h + P \delta h \quad (3.7)$$

### - Sliding friction

In Abaqus, under the pre-defined sliding velocities, the slip velocity between two surfaces would follow from the prescribed motion and be independent of the displacement values. Consequently, the frictional stresses depends only on the local friction and the velocity field:

$$\tau_i = \tau_{eq} \frac{\dot{\gamma}_i}{\dot{\gamma}_{eq}} \quad (3.8)$$

Where the equivalent stress  $\tau_{eq}$  is equivalent with the local unit friction:

$$\tau_{eq} = \mu P \quad (3.9)$$

where  $\mu$  is the local coefficient of friction, which can be derived from the experimental data (section 4.2.1) as a function of the local contact pressure  $P$ . In addition, the equivalent velocity  $\dot{\gamma}_{eq}$  follows:

$$\dot{\gamma}_{eq} = \sqrt{\dot{\gamma}_1^2 + \dot{\gamma}_2^2} \quad (3.10)$$

where  $\dot{\gamma}_i$  are the tangential slip velocities of the implemented velocity fields ( $i = 1,2$ ).

### 3.1.5.2 Basic modelling strategies

#### - Full composition-cell model for the composite (with smooth counterface)

Firstly, in order to have an overall view of the contact condition between the composite and the steel counterface, a complete pattern-unit of the composite fabric was modelled with symmetrical and periodic boundary conditions applied according to the repetitiveness. In it, all the composition (i.e. PTFE, glass fibres and phenolic resin) were modelled as cubic cells according to their geometric distribution, as shown in Figure 46. Meanwhile, the counterface was modelled as a rigid-body considering it is much stiffer than the composite components (much higher elastic modulus- around 200GPa). With this model, the overall distribution of the contact pressure and stress distribution in different parts of the composite surfaces can be revealed.

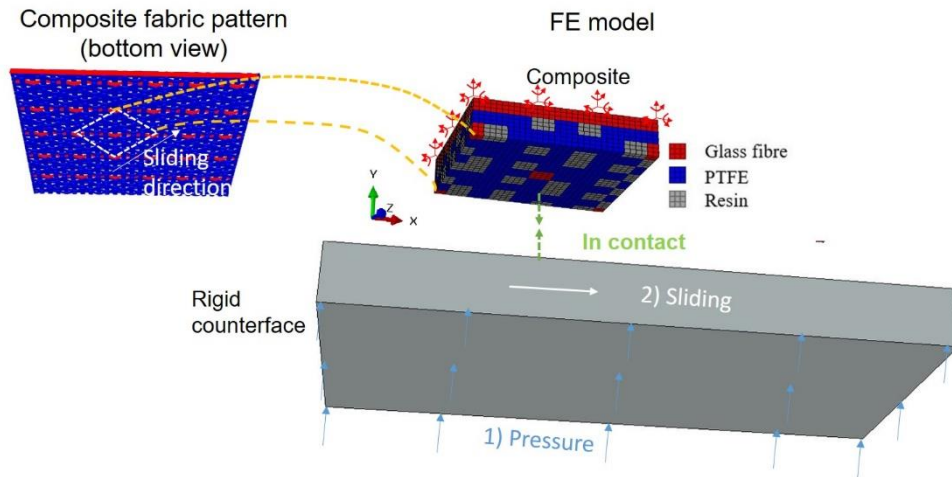


Figure 46. Full composition-cell model for the composite based on the fabric pattern

### - Simplified uniform-section model of the composite (with textured counterface)

Due to the high requirement in the meshing of composite in the cases of textured counterface (i.e. element size need to be sufficiently smaller than the dimples), even the composite unit described above would be too big to simulate. To solve this, it is proposed that a small section of the pattern-unit excluding surface glass-fibres, like shown in **Figure 47**, can be extracted as a simplified model with reduced size for adaption onto the textured counterface. The justification and the modifications for this approach is based on the preliminary finding that the contact pressure is similar in these sections, as will be discussed later in chapter 4.5. With this approach, a detailed indication of the contact pressure and stress condition influenced by counterface textures can be generated.

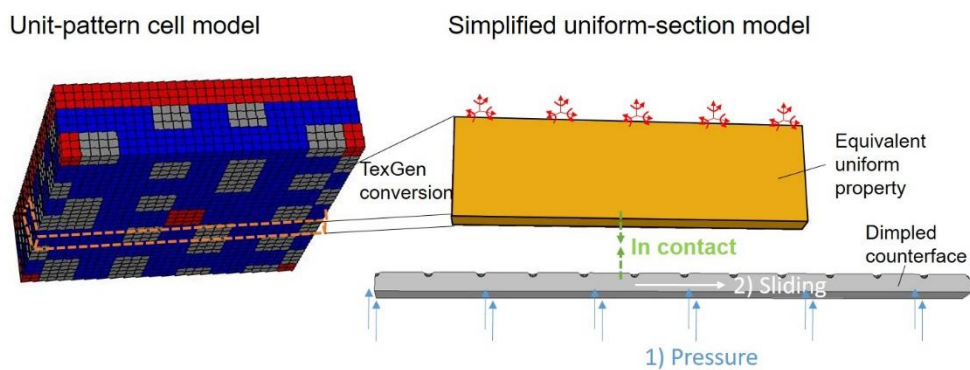


Figure 47. Extraction of composite section excluding surface glass-fibres to obtain the simplified uniform-section model

For the textured counterface, the modelled dimple shapes and dimensions correspond to those adopted on the real surfaces used in the wear tests. Moreover, one rows of dimples (instead of single one dimple) were modelled, and by varying the spacing distance between the adjacent dimples, different dimpling densities (corresponding to the values adopted in the wear tests) is

reflected. With this approach, the difference between the level of stress concentration with different dimple dimensions and coverages can be revealed.

### **- Loads and boundary conditions**

Firstly, for the normal load, a uniform pressure was applied from the bottom of the counterface, with the top surface of composite constrained, like has been demonstrated in Figure 46 and **Figure 47**. The reason behind this approach instead of applying the load on the top of the composite is to avoid the unrealistic sinking on the top to surface be simulated when the counterface is textured. In reality, be it in a real bearing, or in the pin-on-plate contact, the realistic situation is that the composite top (bonded to the rigid backing) is always un-displaced (like shown later in **Figure 77**).

After the compressing step, a shear load was facilitated automatically with a sliding motion applied. The amplitude of the load was determined by the frictional properties derived from experiments (in test section 4.2.1) and implemented in the surface-contact interaction.

For boundary conditions, as has been pointed out, symmetrical boundary conditions were applied on the sides of the composite part considering the symmetricity and repetitiveness of the modelled section and the textures, as well as the uniformity of the loads.

## **3.2 Bonding strength test for bearing liner on sleeve surface**

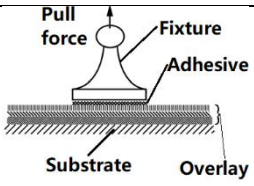
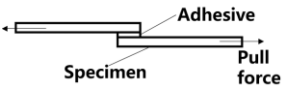
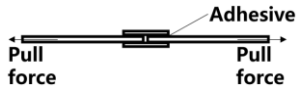
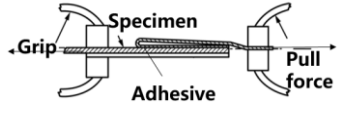
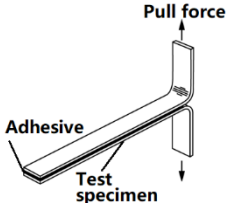
Bonding strength of the composite liner is crucial for the reliability of the bearing, as well as the fulfilment of the tribological performance. To explore the possibility of improving bonding strength with varied surface texturing, the following techniques were used.

### **3.2.1 Basic test methods for bonding strength**

#### **3.2.1.1 Single lap shear tests - for quantification analysis**

Many quantification methods for bonding strength have been established as standard tests. As summarised in **Table 6**, the main test types for measuring the strength of adhesive bonds include pull test, lap shear test and peel test, focusing at different aspects of the bond.

*Table 6. Summary of common test methods to quantify the bonding strength of an adhesive assembly*

	Schematic diagram	Representative standards/reference	Measurement focus
Pull test		[195]	Unit tensile load required to break the adhesive assembly
Lap shear test	<p>Single lap shear</p> 	[196]	Unit shear load required to break the adhesive assembly
	<p>Double lap shear</p> 	[197]	
Peel test	<p>180° peel</p> 	[198]	Unit peel force required to separate two surfaces at a certain angle
	<p>T-peel test</p> 	[199]	

In the dry-lubricated bearings, the concerned situation is that the shear force (friction) acting on the liner surface may cause high shear rate of the liner as well as the adhesive layer, leading to bond failure. Therefore, the second category- lap shear tests (in Table 6) test should be adopted since as it reveals the failure of bond under shear loading. Moreover, even though it seems the double lap shear is a more realistic representation, as the liner can be included (to connect the two lap specimen), in the initial trials the failure always occurred on the liner itself, leaving the bonding performance not distinguished. Considering this, single lap shear test was selected as the test method to quantifying the bonding strength.

For the single lap shear test, the Mecmesin 10-i tensile test machine (10 kN test capacity, speed range 1-1000 mm/min) was used to pull the bonded lap shear specimen, and the Mecmesin ILC-T load cell (measuring range 10 kN; resolution around 2N) was used to monitor the applied force during the pulling process, as shown in **Figure 48** (a). The pulling rate (0.127 mm/min), and the plate specimens' dimensions (101.6 mm×25.4 mm×1.62mm; overlapping length 12.7mm) are as recommended in test standard [196]. The built-in software of the tensile test machine can record data while plotting the curves of the applied pulling force during the tests.

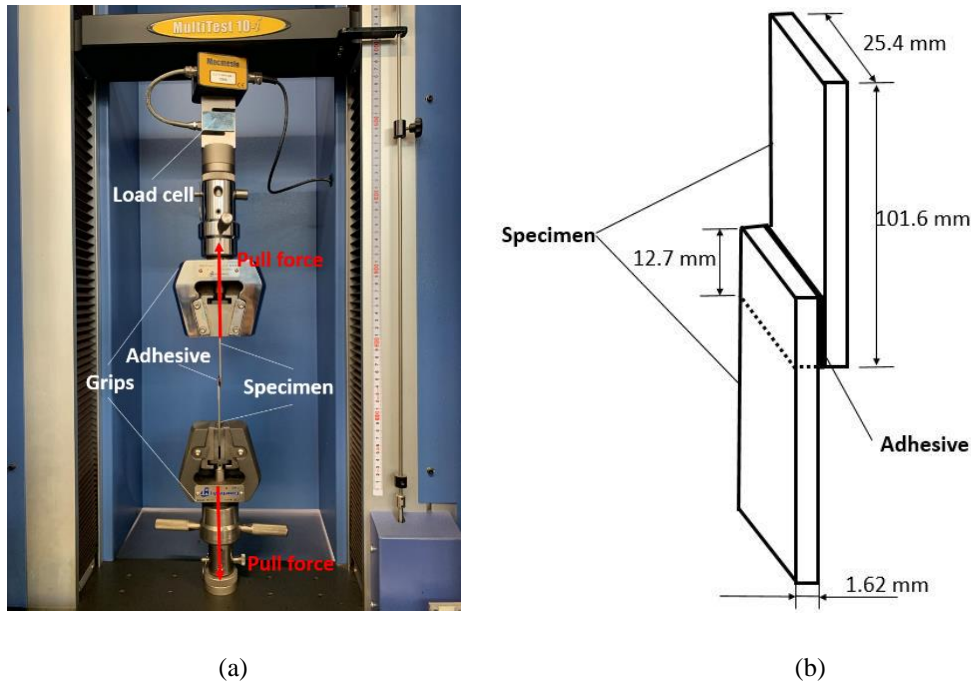


**Figure 48.** (a) Set-up of the measurement for bonding strength (single lap shear); (b) Dimensions of the lap shear specimen

For each pair of lap shear specimens, the applying of the adhesive, the clamping of the specimens and the curing of the adhesives would follow the same standard procedures by the bearing manufacturer (SKF Ltd).

### 3.2.1.2 Bearing liner peel tests- for final check

In bearing industry, to have a final check whether the bond between the liner and the sleeve surface is sufficiently enough, a typical test used for qualification is the peel test for bearing liners. As demonstrated in **Figure 49**, from a completely detachment initiated by a scalpel on the tip, the peeling will be proceeded by pulling the outer ring (sleeve) with the bearing liner firmly clamped on a fixture. During the process, the pulling should be kept at a moderate and steady speed. After the test, the inner surface of the outer ring should be observed (visually or by microscopy if necessary) to check the remaining liner material. Given the rationale that if the bond is strong enough, the peeling will not occur between the adhesive layer and the sleeve

surface, but only within the composite layers (difference displayed in **Figure 49**), the proportion of the liner material left on the surface can assist evaluating the bonding performance.

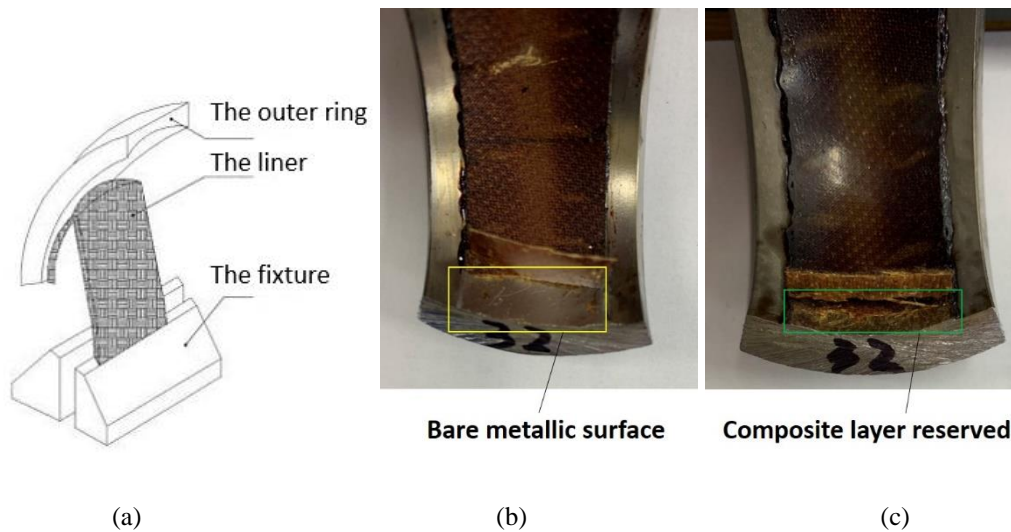


**Figure 49.** Qualification test method for the bonding strength of the spherical plain bearing liner

Through the qualification method, depending on whether a bottom layer of the composite liner can still be reserved on the sleeve surface, this approach can essentially provide a direct answer whether the worst scenario – the complete detachment of the liner can be prevented.

### 3.2.2 Sample preparation

In the bearing industry, prior to bonding the liner, a classical process for the sleeve surface is grit-blasting for surface roughening. Therefore, un-blasted smooth specimen (grinding finish,  $R_a$  around  $0.3\mu\text{m}$ ) and specimen having gone through standard grit-blasting process in SKF Ltd were provided as references. Meanwhile, since grit-blasting still poses issues like environmental ones (noise, waste and energy demands) [119], new texturing/roughening methods, like the ones introduced in the following sections are proposed as substitutes.

#### 3.2.2.1 Surface texturing by conventional machining processes

To explore whether commonly used processes for machining bearing surfaces may have the potential in improving bonding strength, some of the conventional machining processes were used to create surface textures on the bearing samples for the qualification test described above (section 3.2.1.2). Turning, honing and dimpling process using conventional machining tools were employed to fabricate trenches, cross-hatch grooves and dimples on the sleeve surfaces.

Moreover, since these machining methods have not been adopted to machining flat surfaces, laser surface texturing (the same pico-second laser introduced in section 3.1.2) was used to

produce resembling textures on the lap shear specimen surfaces. Through controlling the processing parameters (power, translating speed, dwell time, paths etc.) of the laser and applying post-texturing polishing, like described in 3.1.2, the generated texture pattern, dimensions and coverages should mimic those created by the conventional machining processes (further presented in section 6.2).

### 3.2.2.2 Surface texturing by novel processes - laser roughening

Firstly, the incentive of using laser to create micro-roughness on the surface comes from the observation of the re-deposition. Compared with the pico-second laser used for surface texturing, the re-deposition with nano-second laser is more prominent, like has been shown in **Figure 29**. Therefore, the SP-100C-0013 nano-second laser (SPI Laser UK Ltd.), which shares the same stage and positioning system with the pico-second laser presented in section 3.1.2.2, was used for roughening the sample surfaces as shown in in **Figure 50**. This laser is Nd: YAG fibre laser, with 18.8w ( $\pm 5\%$ ) maximum output power, 1062.0 ( $\pm 3.0$ ) nm wavelength and repetition rate from 1 to 100kHz. The beam diameter is around 0.90 – 1.20 mm with less than 2.8 mrad divergence. With the lens and mirror array, the resultant diameter at beam waist (spot diameter/ focal diameter) on the focal plane is around 50  $\mu\text{m}$ .

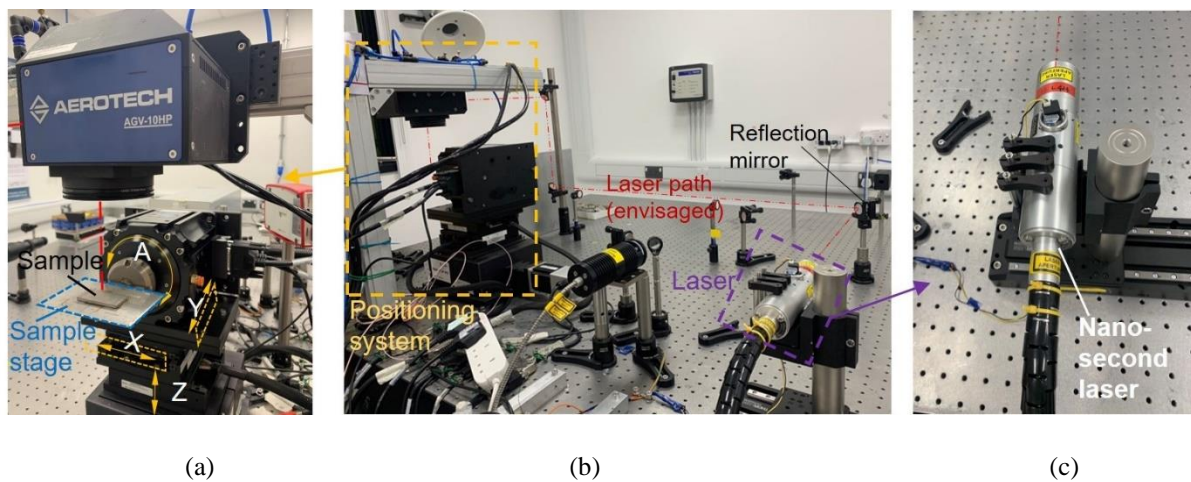


*Figure 50. (a) The precision positioning system, (b) The overall view for laser system (c) The nano-second laser*

To create micro-irregularities covering the whole surfaces, it is proposed that the dimpled area should be overlapped so that re-deposition can stand out. With this aim, like demonstrated in **Figure 51** (a), dimples were firstly produced in lines with different parameters (input power, laser dwell time and distance) for evaluating the uniformity and compactness of the micro-asperities. Through brief prototyping series like this, it was found that a dimpling spacing of 25 $\mu\text{m}$  (half of the dimple diameter) is small enough to ensure a compact coverage of the

artificial roughness. Meanwhile, under different input powers tested, by 0.001 second, the roughness seems to be the finest, as shown in **Figure 51** (b). Therefore, to manufacture the laser roughened specimens for lap shear tests, the whole areas for overlapping were roughened using laser with 25 $\mu$ m dimpling distance and 0.001 second laser dwell time.

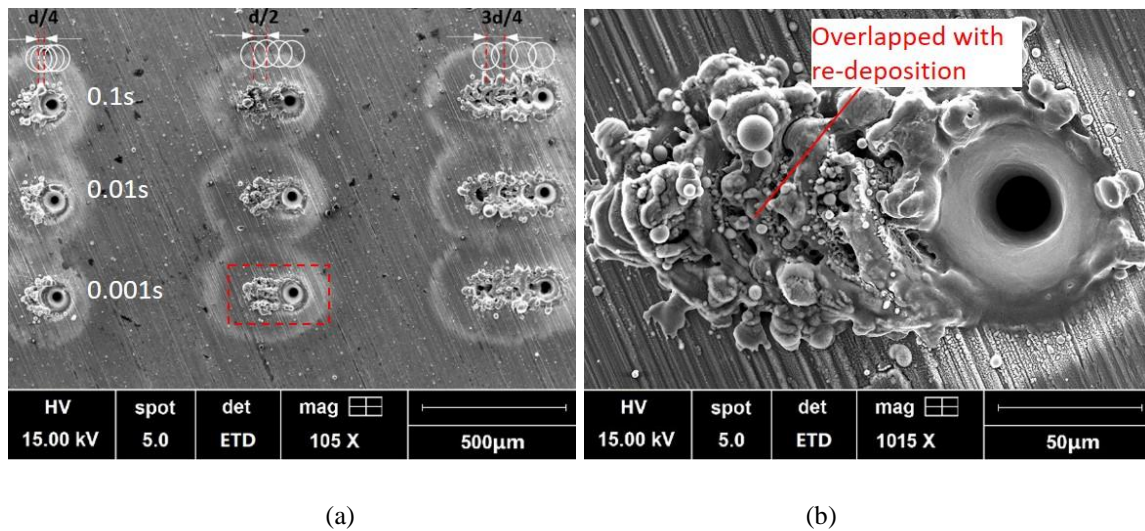


**Figure 51.** (a) Trials with different overlapping ratio and dwell time for laser roughening, (b) Magnified view of the overlapped re-deposition created with 25 $\mu$ m dimpling distance and 0.001 second laser dwell time

### 3.2.3 Post-test analysis methods

#### 3.2.3.1 Surface analysis techniques

For surface analysis on the specimen after the lap shear test and the peel test for bearing liner, the FEI Quanta 650 ESEM (the same one in section 3.1.4) was employed. The focus was on analysing the preserved material on the surfaces after the tests, in order to identifying features such as the ratios of reserved material (adhesives or layers of bearing liner) and the occurrence of failure modes (cohesive or adhesive).

#### 3.2.3.2 Wetting angle measurement

As apparent contact angle of a liquid droplet on a surface reflects the extent the liquid can wet the surface, it is often regarded as an indicator for adhesion [200] and even guiding tool for bonding surface preparation [201]. To assess whether it has the association with bonding performance and the capability of serving as an index for future texturing design, the contact angles were measured on the developed textured/roughened surfaces, and evaluated for its link with the bonding performance.

The flat steel samples used were the same with the ones used in the bonding strength. Before contact angle measurement, the smooth and varied textured sample surface were cleaned using

acetone and distilled water, and then dried by a heat-fun-drier. The measurement was conducted on a contact angle goniometer (FTA200, First Ten Angstroms, Inc.), as in **Figure 52**. Under room temperature (24°C), each time a water droplet (distilled water) with volume around of 15 $\mu$ L was pumped out through the syringe, and the contact angle was quantified on the video image using the built-in software which has an ‘edge finder algorithm’ [202].

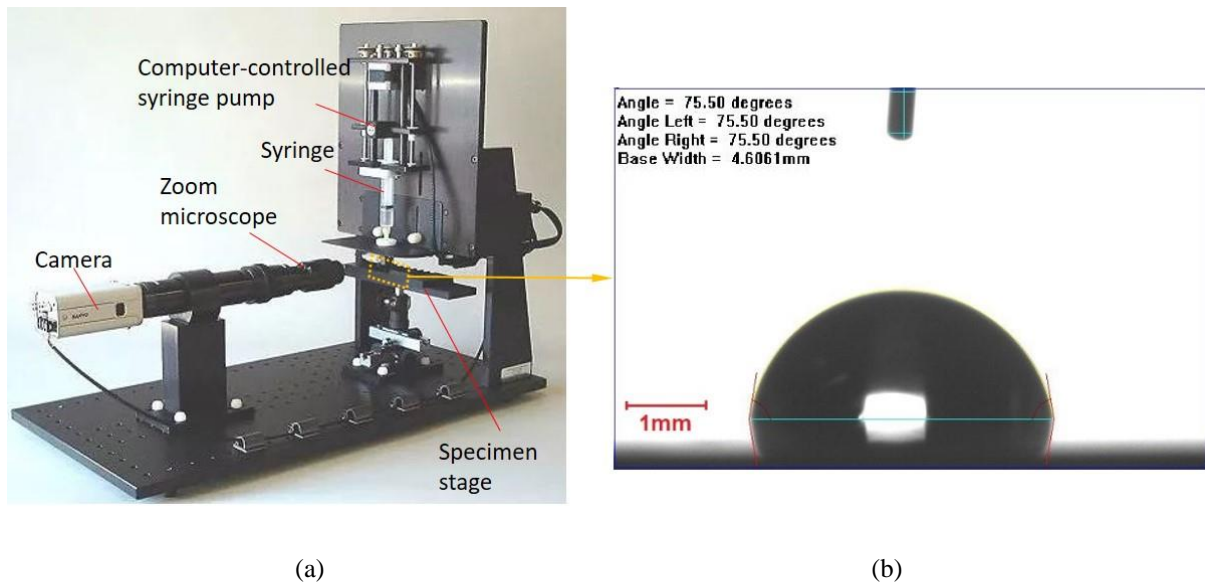


*Figure 52. (a) FTA200 video goniometer system [202]; (b) software interface for automatic contact angle measurement*

## Chapter 4

# The effects of surface texturing on the tribological performance and transfer film formation of dry-lubricated bearings

### 4.1 Introduction

Incited by the successful application of surface texturing in fluid-lubrication regime, and aiming at filling the knowledge gap in surface texturing under dry-lubricated condition, a wide range of the texture (dimples) dimensions and coverages were tested for their influence on the tribological performance of the dry-lubricated contact.

For the dry-lubricated bearings, it has been proven that, the self-lubricating property of the liner is fulfilled by the formation of PTFE transfer film on the metallic counterface during sliding contact [33,48,203]. The formation and functioning of the transfer film are then found to be influenced by the topography [3] and physical properties[87] of the counterface. Therefore, to study the influence of counterface textures, it is essential to reveal the characteristics of the transfer film formed on different counterface. Nonetheless, as has been addressed in the literature review (section 2.1.2), the characterising methods adopted in the previous researches were often incomprehensive, being only applicable in ideal conditions (perfectly smooth counterface), or delivering partial information of the transfer film. However, in the real engineering contact investigated in this chapter, factors like relatively high loading and counterface abrasion would inevitably increase the difficulty in characterising the transfer film, requiring surface analysis method with higher capability and reliability.

To meet these challenges, this chapter proposes to develop a systematic observation and characterisation method for transfer film of dry-lubricant, while special attention was given to the measurement of the transfer film thickness, whose relation with texture dimensions is critical for the benefiting effect of lubricant reservation to be achieved. Applying this method on the tested surfaces, the effects be induced by surface texturing on the transfer film formation and tribological performance were investigated.

In addition, in the limited number of previous studies on surface texturing in dry-sliding-contact, the effect of stress distribution alteration was identified [204,205]. This phenomenon also needs special attention as this effect was always reported as beneficial in low loading condition [155,206,207]. In the real engineering contact investigated in this chapter, the

influence may be different as the adverse effects induced by stress concentration such as hysteresis resistance [88] and micro-cutting [44] may be magnified under relative high load. Considering this, even though the established surface analysis on wear debris and transfer film can provide an indication for the occurring tribological phenomenon, a contact mechanics model is needed to give theoretical analysis for the influence on contact pressure and stress.

With the tests and analysis conducted, the physical phenomenon observed and the theories formulated for surface texturing under dry-lubricated contact are reported in this chapter.

## 4.2 Preliminary trials

### 4.2.1 Trials for test condition benchmarking

In order to set references and give guidance to the further test series, first benchmarking trials were done with smooth counterface under pressure lifted by steps, obtaining the relationship between the loading condition and the tribological performance as well as the Limiting-Pressure-Velocity (*LPV*). In polymer tribology, the *PV* factor is a crucial parameter as it reflects the load condition and denotes the thermal input (frictional heating =  $\mu PV$ , where  $\mu$  is the coefficient of friction). As for *LPV*, it is the threshold of applied *PV*, above which the thermal input would exceed a critical point and lead to accelerated wear due to possibly thermal effects like softening and melting [52]. Therefore, in further full-wear tests, where a short test duration is desired while the test condition should also be maintained representative, the *LPV* can guide the selection of the test parameters. In addition, for counterface texturing, the *LPV* can also help set an initial limit for the texturing area, as the reduction in contact area would lead to lifted contact pressure.

At first, the *LPV* test was performed with the normal wear test set-up, while the normal force, frictional force, wear depth and liner back temperature were monitored. The rotational speed of the driving rotor was set at and the 180 rpm and the reciprocating stroke length was set at 20 mm, leading to average sliding velocity of 0.12m/s. The normal pressure, starting at 10MPa (through applying 20kg weight), was lifted by 10MPa each time when a considerable duration of steady state has been reached. Finally, the test session ended with the load limit of the rig (50MPa, i.e. with 100kg weight applied).

As has been acquired in **Figure 53** (a) and (c), the frictional force increased with the lifted normal load, but since the enlarging magnitude was not as high as the normal load, the *CoF* dropped with the increasing normal load (an important feature of the PTFE). Meanwhile, the

temperature (measured on the liner back) went hand in hand with the frictional force, which should be because the temperature rise in this condition was basically from frictional heating. As for the wear rate, firstly it should be noted that at the initial period, negative wear depth was indicated. This should be caused by the thermal expansion of the test rig, which could influence the measurement of the wear rate in run-in stage but not the comparison of the steady-state wear rate between different groups [208]. Then, for each step of a pressure-lifting, a similar degree of increase was induced on the slope of wear depth (i.e. wear rate), except that it seems greater at the maximum load (50MPa), as shown in **Figure 53** (b). However, using linear progressing for the wear rate points versus the *PV* factors, the calculated probability-value (*p*-value) was merely  $5.73e-4$ , denoting a very good fit as shown in **Figure 54**. Considering this, it is not safe to say that at 50MPa the *LPV* is reached, so the *PV* factor needs to be lifted further to check for the real threshold value.

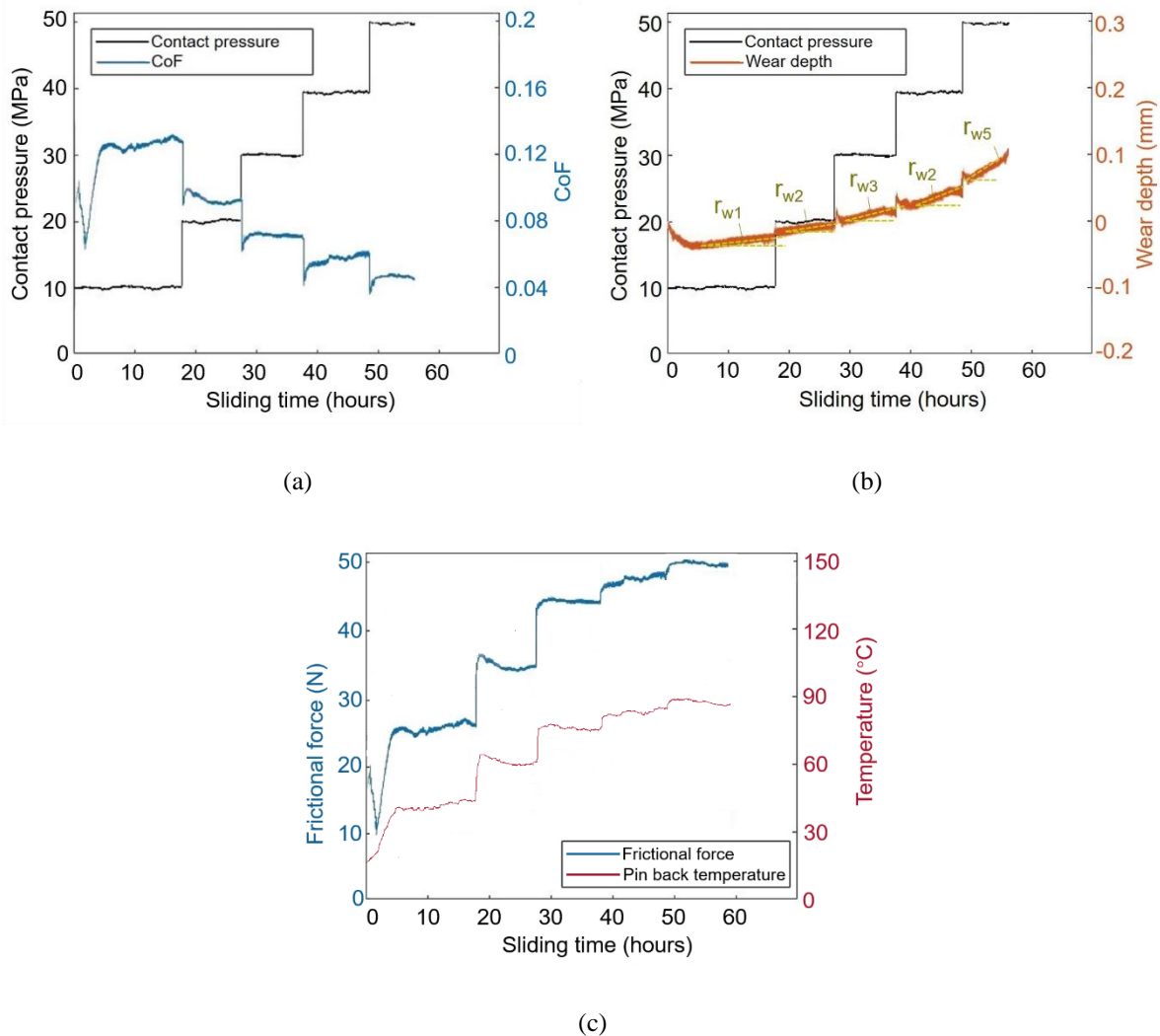


**Figure 53.** The (a) evolution of CoF with pressure lifting, (b) evolution of wear with pressure lifting and (c) evolution of frictional force and liner back temperature in LPV test 1 (average sliding velocity 0.12m/s)

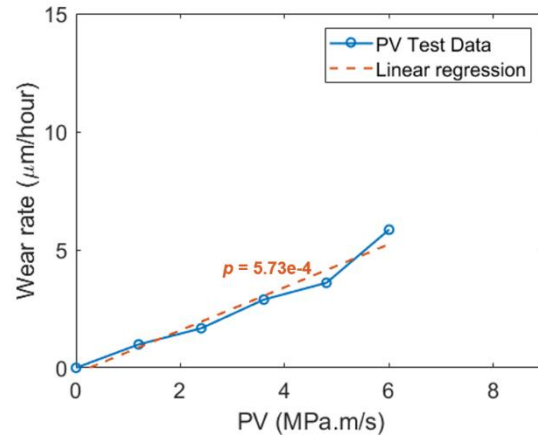


**Figure 54.** Linear progression for the wear rate versus PV value in PV test1

To further explore the *LPV*, since the pressure  $P$  could not be lifted anymore since the applied load has reached limit on the rig, a higher sliding velocity (0.24m/s) was applied to achieving larger  $PV$  values.

Consequently, in the second *LPV* test, as indicated in **Figure 55** (only the points with higher  $PV$  that the test 1 shown), when the pressure increased from 40 to 50 MPa, another prominent increase in wear rate seems to occur (note that the dramatic oscillations in the end should not be included). As summarised in **Figure 56**, the p-value for the linear fitting of all seven  $PV$  point (in both tests) became 0.0014. Even though in many occasions this value is still considered indicating good fitting credibility ( $<0.5\%$ ), it is considerably larger the p-value for the linear fitting with the last point excluded ( $p = 1.3e-4$ ), meaning that the linearity was greatly affected by this point. Moreover, contrary to that in previous steps of pressure-lifting, with which the rise in frictional force and temperature gradually damped, in the last step these increases were as dramatic, like shown **Figure 55** (c). Correspondingly, the dropping of CoF value with lifted pressure also entered a plateau phase at  $PV = 12 \text{ MPa} \cdot \text{m/s}$ , like demonstrated in **Figure 55** (c) was basically in the same level as when  $PV = 9.6 \text{ MPa} \cdot \text{m/s}$ . Overall, it can be concluded that at the point  $PV = 12 \text{ MPa} \cdot \text{m/s}$ , the *LPV* has been reached.

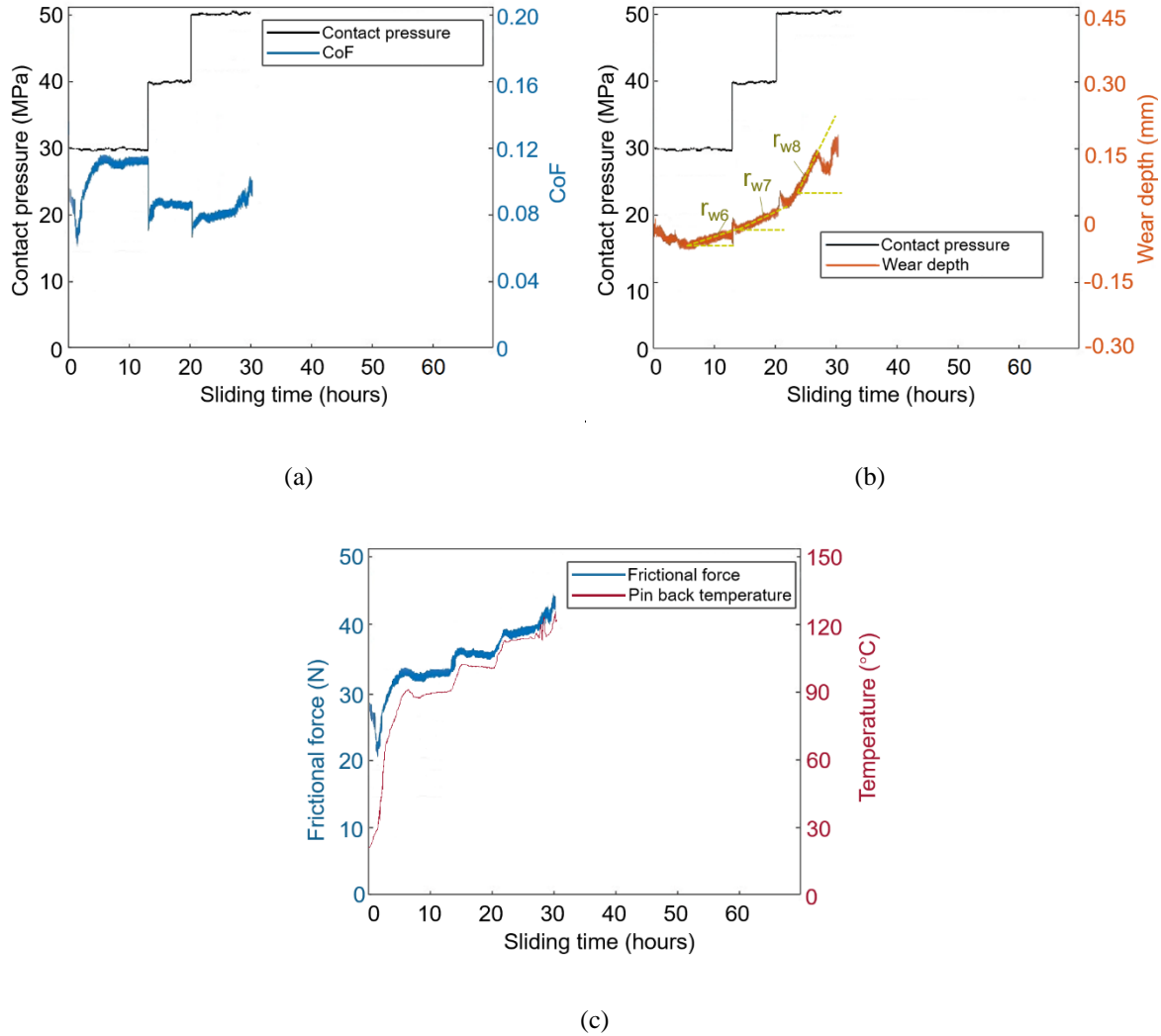


**Figure 55.** The (a) evolution of CoF with pressure lifting, (b) evolution of wear with pressure lifting and (c) evolution of frictional force and liner back temperature in LPV test 1 (average sliding velocity 0.24m/s)

Due to the size of the step-load, the critical  $PV$  of 12 MPa· m/s may not be the exact threshold value, but should still pose as a good indication. Corresponding to this  $LPV$  value, with 0.12m/s sliding velocity (near limit in helicopter rotor application), the limiting normal pressure is at 100 MPa. Nevertheless, for the full-wear test, the applied pressure was still kept at 40MPa. First of all this is already near the limit of the load range in helicopter rotor application. Then, by this setting, theoretically a considerable proportion (more than 50%) of space can be left for surface texturing, without lifting the nominal contact pressure and corresponding  $PV$  factor above  $LPV$ .

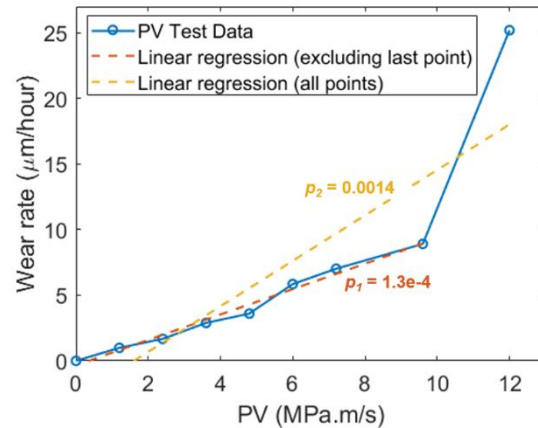


Figure 56. Linear progression for PV test2 for the PTFE composite liner using pressing lifting method

#### 4.2.2 Trials for texturing parameters selection

Using the tribological performance with the smooth counterface as the benchmark, a preliminary series of comparison tests was performed to have a view of influence from counterface textures.

The texture coverages adopted were 40%, 30%, 20% and 10%, and the circular concavities (around 8μm deep) manufactured have diameter of 200μm, 100 μm (pockets) and 40 μm (dimples). With this selection of parameters, a considerably wide span of texture coverages and dimensions can be covered, giving basis for further optimization, while the texturing limit still follow the guidance using *LPV* (discussed in chapter 4.2.1).

However, it was observed that almost all the wear tests finished dramatically fast – in the worst cases, with 40% coverage, the wear-out of liner and metal-metal contact occurred within an hour. Moreover, lower the coverage and smaller the texture diameter was, better the situation was. For example, when the coverage was reduced to 10%, as shown in **Figure 57** (b), the wear tests can last around 10 hours with the largest diameter (200μm), and around 20 hours with the smallest diameter (40μm), although still significantly lower than the smooth counterface. Similarly, with the trend observed in *LPV* tests (section 4.2.1), the *CoF* and the indicating temperature went almost simultaneously. What should be noticed is that for all the textured surface, the *CoF* and temperature never had a plateau phase like the smooth surface, but would rise continuously from below the steady state *CoF* values for smooth counterface to above them. The initial lower level was expectable, since the *CoF* should theoretically be smaller with lower nominal contact pressure achieved on textured counterface, but judging by the rise later on, it can be postulated that certain phenomenon must have led to continuously increasing friction, suppressing the *CoF* reduction effect expected.

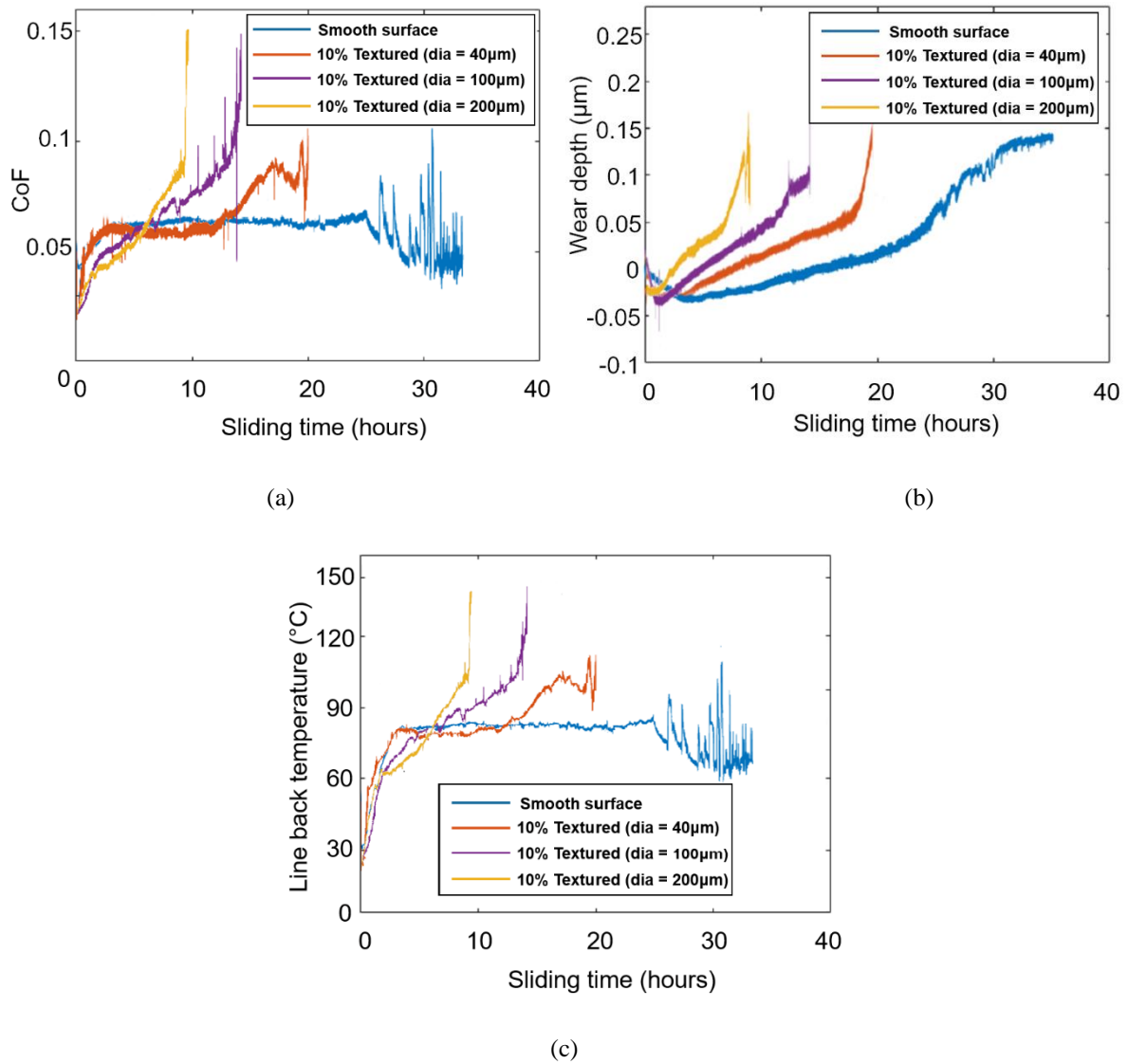


**Figure 57.** Measured (a) friction coefficient and (b) wear depth versus sliding time for three repeats of wear tests (normal pressure 40MPa, reciprocating frequency 3Hz, stroke 20mm) for smooth counterface and counterface with 10% coverage of circular concavities in different diameters

From the observations on the counterface, it has been confirmed that material was scrapped off the composite liner on the edges/sides of the concavities even though the edges had been rounded (stated in chapter 3.1.2), while on the non-textured areas transferred material was rarely seen, like shown in **Figure 58**. With observations on both surfaces considered, it is likely that the initially tested textures would cause severe scratching and abrasion, which would lead to excessive wear and rise in friction as observed.

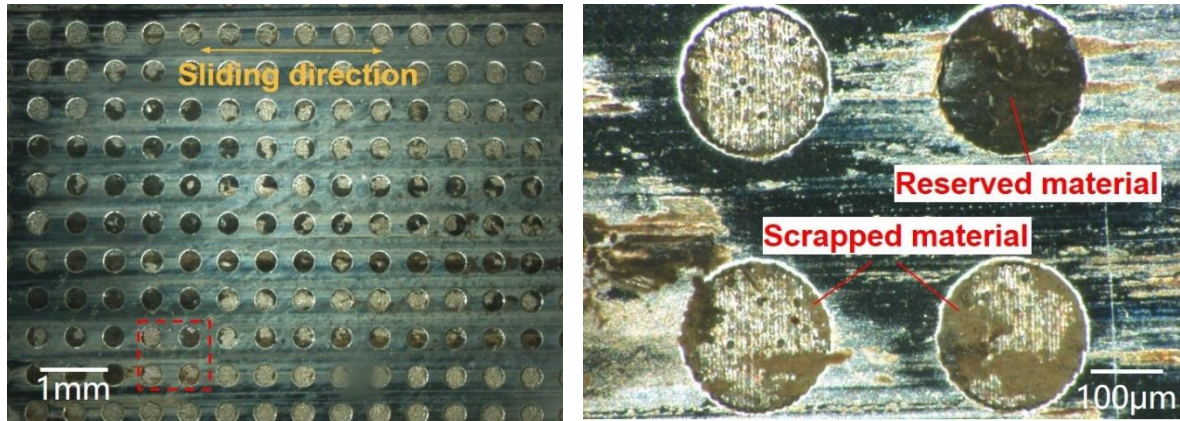


*Figure 58. The (a) whole view and (b) detailed view of a magnified area on the counterface with 10% coverage of pocket holes with 200µm diameter*

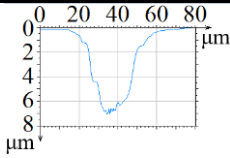
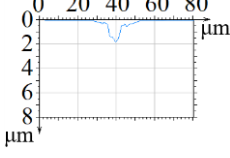
To summarise, preliminary as the trials and the observations were, they provide a basic indication that counterface textures could easily lead to a detriment overall tribological performance. This influence was less severe with smaller texture dimensions and coverages, and may be connected with abrasion caused by texture edges. Because of this, even though consideration had been given to nominal pressure limit (under LPV criteria) and edge sharpness, an inferior frictional and wear performance would be resulted. However, the potential of transfer reservation was also seen. Therefore, to explore whether improve performance can be achieved with optimized texture parameters, a more comprehensive test and analysis series needs to be done on textures with more confined coverages (well below 10%) and dimensions (only with dimples, i.e. diameter  $\leq 40 \mu\text{m}$ ). Meanwhile, a more sophisticated surface analysis needs to be developed for instructing transfer film reservation (depth determination) and identifying the tribological phenomena.

### **4.3 Friction and wear tests for the effects of textured counterface**

To study the effects of dimple depth, particularly its relation with the transfer film's thickness (later revealed in Section 4.4.1), a dimple depth considerably larger than the maximum film thickness is adopted in Type A, while a depth shallower than the maximum thickness is proposed for dimple B and C for comparison. Meanwhile, for Type B dimples, the diameter is reduced to half of the original dimples created by the laser, so that its comparison with Type A and C can include influences of dimples' diameters. Consequently, from Type A to C, the three types of dimples constitute relatively the 'wide & deep' (A), 'narrow & shallow' (B) and 'wide & shallow' (C) textures. Since the Type B dimple's diameter is half of A and C's, the settings of the coverage percentages can lead to that the distance for Type B dimples at a certain coverage (e.g. 0.4%) can equalise with that of Type A or C dimples in the higher coverage (e.g.

1.6%). Benefiting from it, in later analysis of the influence from dimples' spacing densities, whether it attributes to distance or area coverage can be recognised. For a more straightforward presentation, the three levels of texture coverage are later referred as 'low' (0.4%), 'medium' (1.6 %) and 'high' (6.4 %).

*Table 7. Matrix of dimensions and texturing coverage percentage of surface textures to test*

Dimple type		Coverage $p_c$ (Percentage of dimpled area)		
<b>A - Wide &amp; deep</b> ( $d=40\mu\text{m}$ , $Dep=8\mu\text{m}$ )		Low	Medium	High
		(0.4%)	(1.6%)	(6.4%)
<b>B - Narrow &amp; shallow</b> ( $d=20\mu\text{m}$ , $Dep=2\mu\text{m}$ )		Low	Medium	High
		(0.4%)	(1.6%)	(6.4%)
<b>C - Wide &amp; shallow</b> ( $d=40\mu\text{m}$ , $Dep=2\mu\text{m}$ )		Low	Medium	High
		(0.4%)	(1.6%)	(6.4%)

The influence of textures with different dimensions and densities were then tested while the smooth surface (40 MPa) is used as reference. For each counterface, at least three repeats were performed. As the deviations between repeats are relatively small and variations between different types of counterface are distinguishable, for each type only a representative repeat is presented in the graphs for comparison. Moreover, the measured liner back temperature is not presented here as the trend has been simultaneously reflected by  $CoF$ , and unlike the preliminary test, the differences between cases were minimal (all around  $75^{\circ}\text{C}$  -  $80^{\circ}\text{C}$  in steady state) with only one exception ( $90^{\circ}\text{C}$  -  $110^{\circ}\text{C}$  with high coverage of Type A wide & deep dimples).

To begin with, Type A (wide & deep) dimples incur no benefit on frictional performance at any coverage, as shown in **Figure 59** (a), but almost doubled the steady-state  $CoF$  with the highest coverage (6.4%). As for the wear performance, it is indicated in **Figure 59** (b) that with all but the lowest coverage (0.4%) would a remarkably worse wear performance (higher steady-state wear rate and a shorter wear life) be resulted. However, as has been indicated in the *LPV* test (section 4.2.1), theoretically under the elevated nominal contact pressure caused by the texturing coverages can lead to (maximum  $2.74\text{MPa}$  with 6.4% coverage), and the deterioration

of wear performance should be marginal. Therefore, the inferior performance of the texturing patterns can only be explained by the existence of another effect, which can increase the friction and jeopardises the wear performance further.

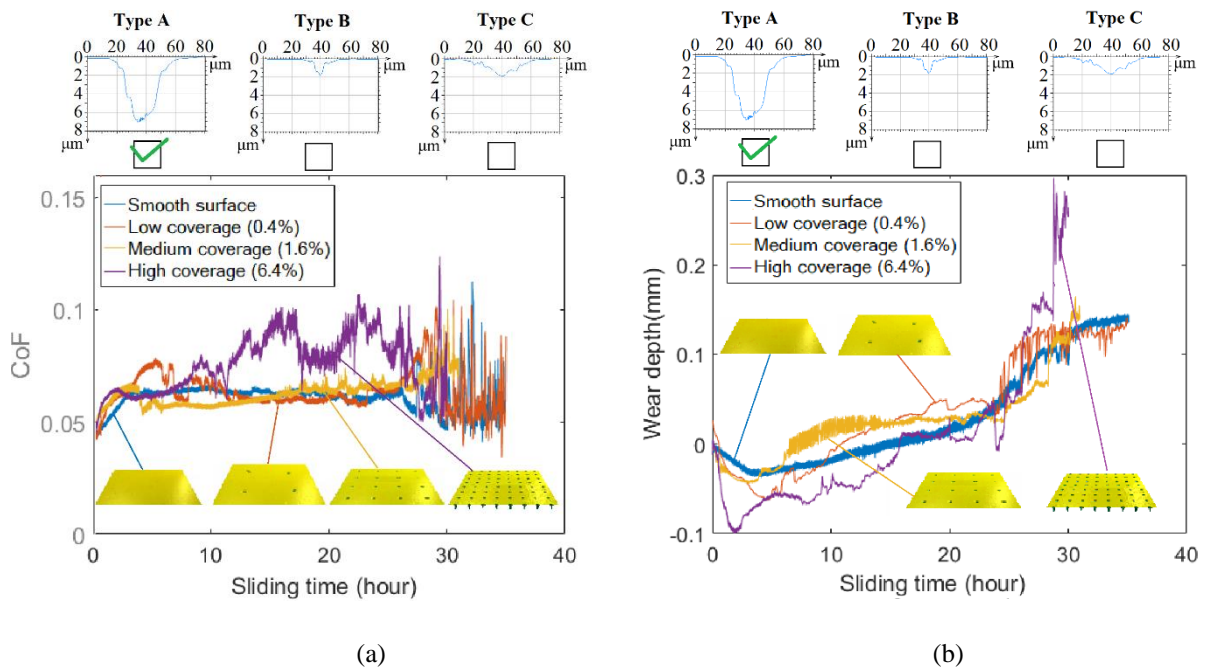


**Figure 59** Measured (a) friction coefficient and (b) wear depth versus sliding time for three repeats of wear tests (normal pressure 40MPa, reciprocating frequency 3Hz, stroke 20mm) for smooth counterface and counterface with different coverages of Type A (wide & deep) dimples

In comparison, with the Type B dimples (narrow & shallow), improvements have been observed in both frictional and wear performance compared with the smooth surface, particularly with the medium coverage (1.6%). For example, as shown in **Figure 60** (a), the steady-stage *CoF* was reduced by around 7% (0.005) with both the medium and high coverage. In terms of wear performance, both the low and medium coverages prolonged the wear life by around 14% (5 hours), while only the medium coverage outperformed the smooth surface in terms of the wear rate at the steady stage. Therefore, it can be seen that Type B dimples (narrow & shallow) in medium coverage (1.6%) generated the most outstanding improvements in both frictional and wear performance. Since the drops in *CoF* is prominent considering the minor increase in nominal contact pressure, and that the adverse influence on wear performance (as revealed in the *LPV* test) has been reversed, the texturing pattern, particularly the beneficial ones (low and medium coverage) must have induced another effect other than rising contact pressure that contributes to the improvement in *CoF* and wear rate.

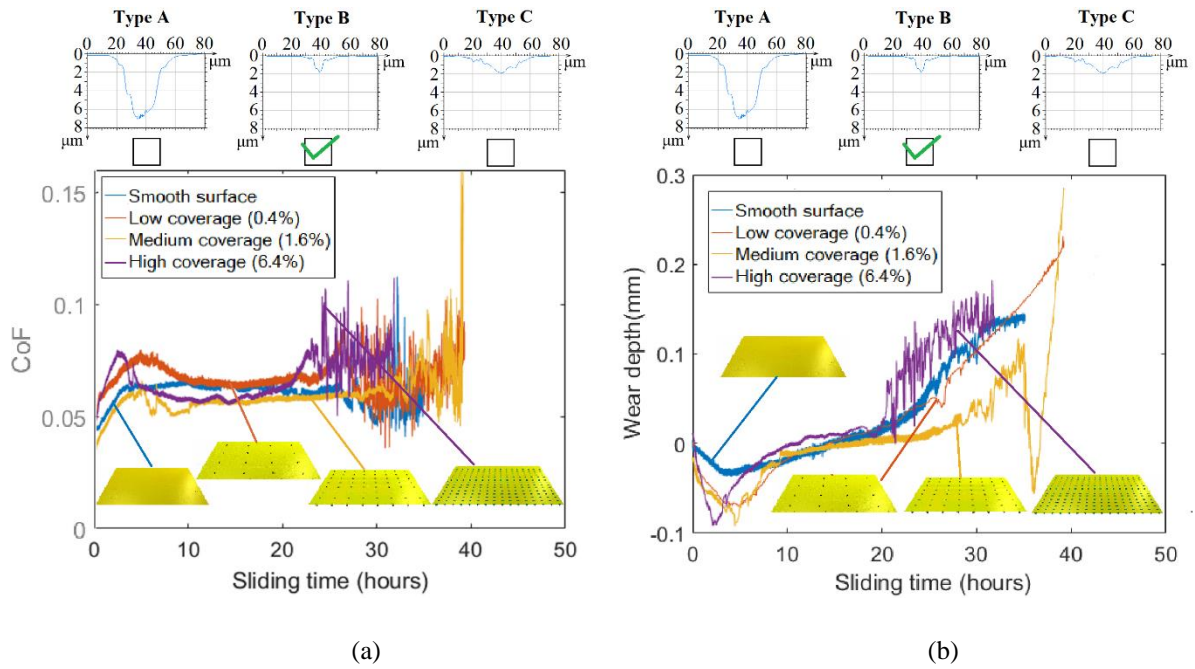


**Figure 60.** Measured (a) friction coefficient and (b) wear depth versus sliding time (normal pressure 40MPa, reciprocating frequency 3Hz, stroke 20mm) for smooth and dimpled counterface ( different coverages of Type B narrow & shallow dimples)

Finally, with the Type C dimples ( wide & shallow), the low (0.4%) and high (6.4%) coverages exhibited no improvement on frictional performance, but incurred a small degree of detriment on the wear rate and wear life, as demonstrated in **Figure 61** (a) and (b). Similar with the Type B dimples (narrow & shallow), with medium coverage (1.6%) the Type C dimples (wide & shallow) can improve the wear performance compared with the smooth counterface, even though in comparison the improvement is slighter - the steady-stage wear rate is around 6% lower than the smooth surface and the wear life is 5% longer.

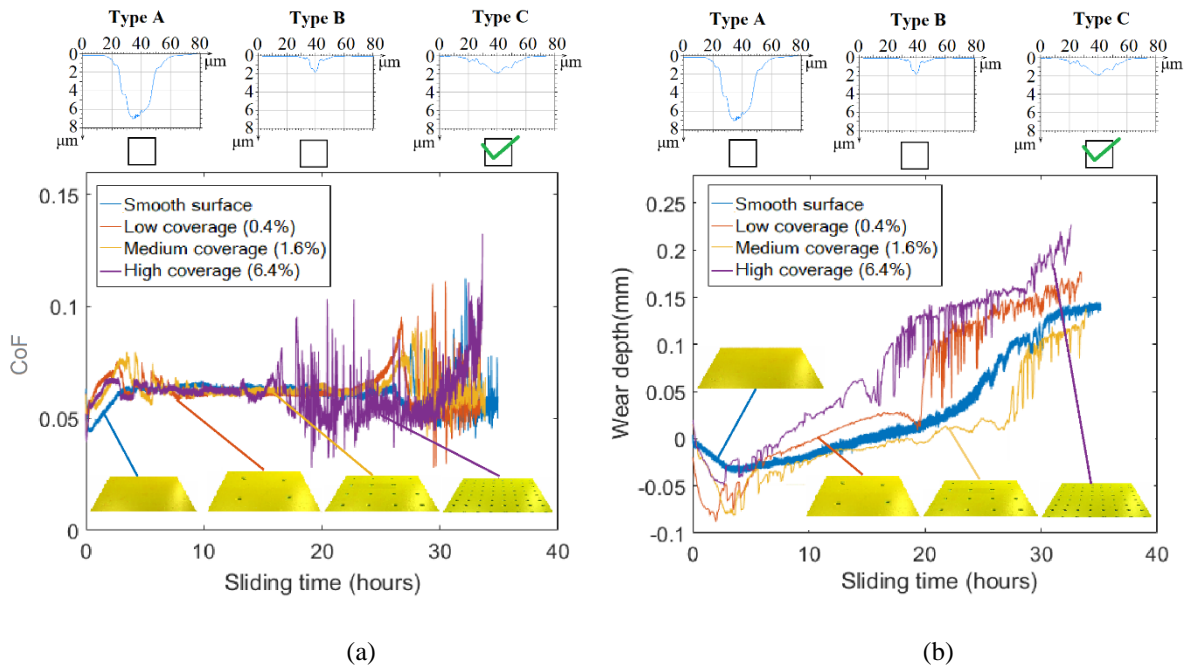


**Figure 61.** Measured (a) friction coefficient and (b) wear depth versus sliding time (normal pressure 40MPa, reciprocating frequency 3Hz, stroke 20mm) for smooth and dimpled counterface with different coverages of Type C (wide & shallow) dimples

In **Figure 59** to **Figure 61**, for each type of surface, results from only a representative repeat are presented in the graphs for comparison, while at least three repeats were conducted for each case. Like the examples shown in **Figure 62**, the deviations between repeats for each surface type are relatively small, and crucial index such as the wear life is distinguishable between the smooth surfaces (around 35 hours) and the dimpled surface (around 40 hours, for 1.4% coverage of type B dimples). Moreover, the wear performance index such as steady-state wear rate and onset time of wear-out (i.e. end of steady-wear stage) can also be distinguished. To obtain these parameters, at first, sample points were obtained from the raw data of the wear depth starting from sliding time at 10-hour (to ensure the running-in period is excluded) with a constant sampling interval. In the example shown in **Figure 62**, the sampling interval was 1 hour, as it is reasonable fine to distinguish the performance considering the overall wear life is around 30- 40 hours. Then, linear regression analysis was conducted on the first two, three, four points and so on, and the first point after which a bad fitting credibility (much larger probability-value  $p$  than former points) was resultant would be defined as the onset of wear-out, since the wear rate after it could not be regarded as steady anymore. Mathematically, this process is the same with the one to find the critical  $PV$  value illustrated in 4.2.1. Finally, as the onset point of wear-out was found, the slope of the linear regression for all the points before the critical point can be redeemed as the steady-state wear rate (correspondingly the mean value of  $CoF$  in the identified steady-state period can be regarded as the steady state  $CoF$ ).

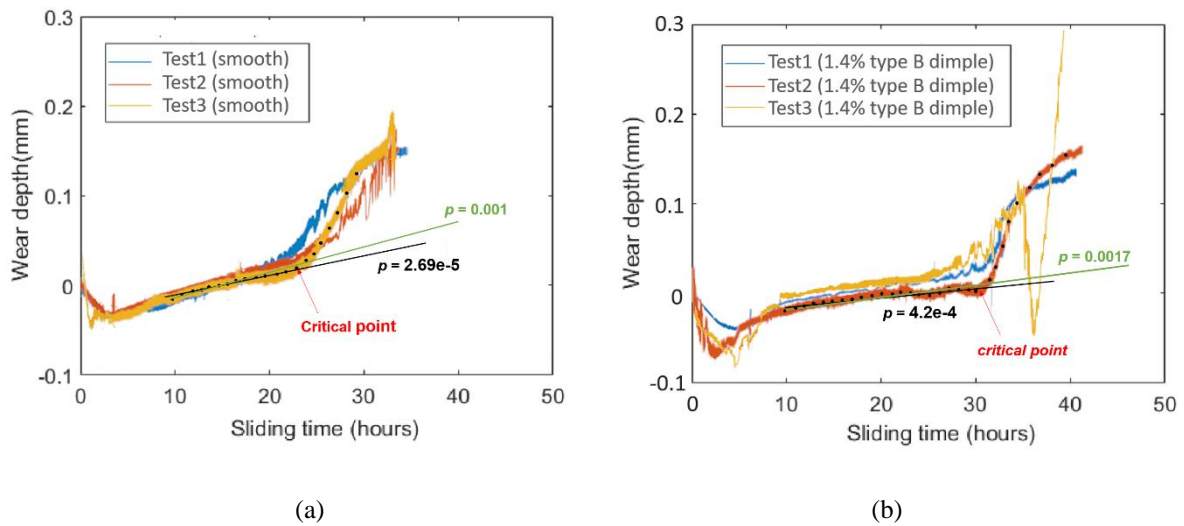


**Figure 62.** Measured wear depth versus sliding time for three repeats of wear tests (normal pressure 40MPa, reciprocating frequency 3Hz, stroke 20mm) with (a) smooth counterface and (b) counterface with 1.4 % coverage of Type B shallow & narrow dimples, with determination method for the onset time of wear-out demonstrated

To summarise the results, the frictional and wear performance indexes are presented in **Figure 63**, with the information of the repeats for each tested surfaces, including the smooth surfaces, which correspond to zero texture coverage in the graphs. As can be seen, the Type A dimples (wide & deep) always bring detrimental, if not no influence on the frictional and wear performance. However, for Type B dimples (narrow & shallow) or Type C dimples (wide & shallow), there is an outstanding trend that both frictional and wear performance improve when the coverage increases from the low to the medium, but then worsened when rising further to the high. It is only with this ‘optimal’ medium coverage (1.6%) of Type B dimples (narrow & shallow), considerable improvements in frictional coefficient, wear rate and wear life can be observed.

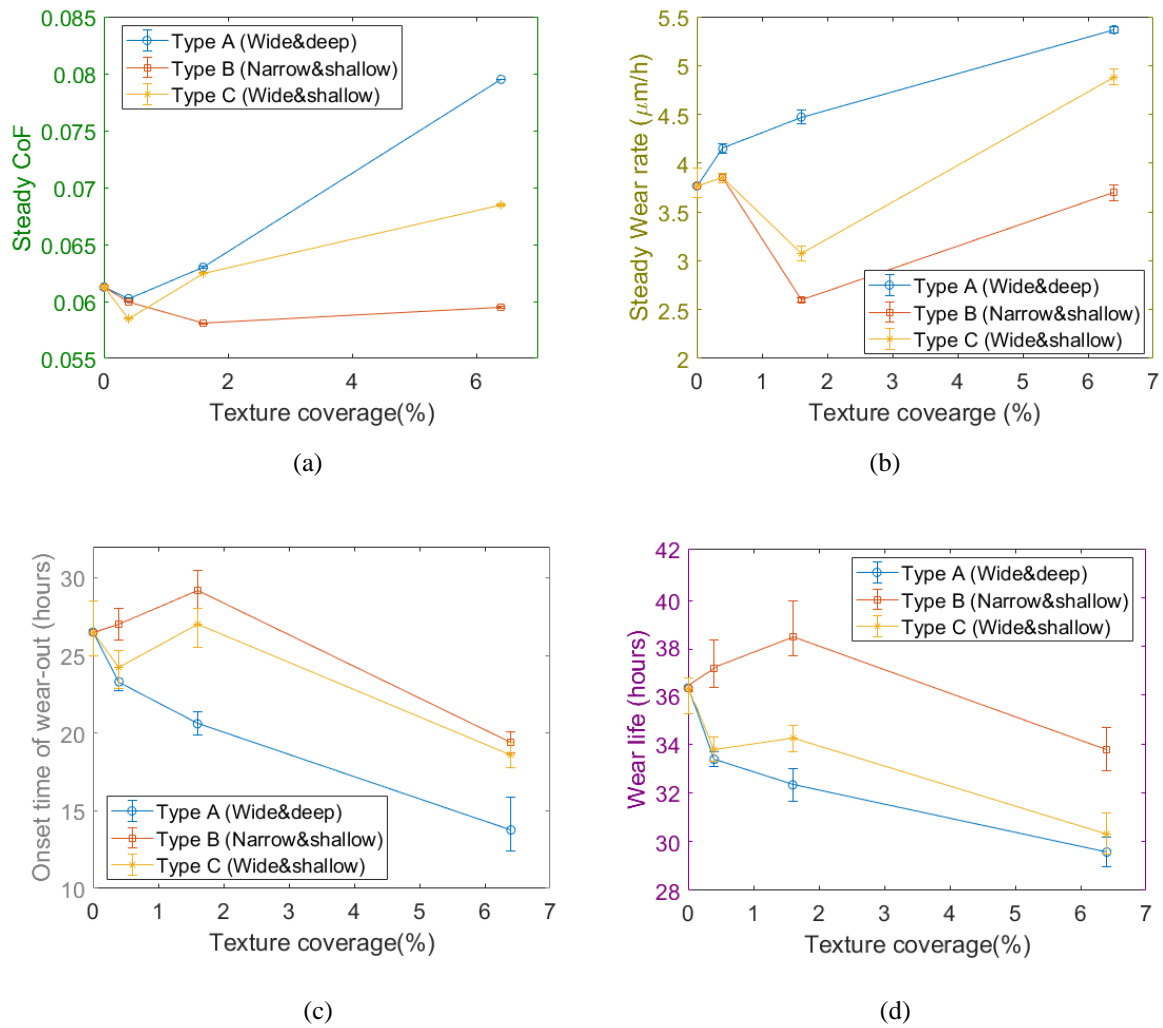


**Figure 63.** Summary of (a) Steady state frictional coefficients, (b) Steady state wear rates, (c) Onset time of wear-out stage and (d) Wear life for surfaces with different texture dimensions and coverages tested with 40 MPa normal pressure, 3 Hz reciprocating frequency and 20mm stroke length

The comments related to **Figure 59** - **Figure 63** reveal the observational influences from surface texturing on the tribological performance. Nevertheless, the physical phenomena inducing these different performance are the key to generate general principles analysing contact between dry-lubricating composite and textured counterface, and would be explored in the following sections.

#### 4.4 Surface analysis results

A thorough analysis on the counterface and the transfer film formation can give a good indication of the wear behaviour, assisting identification of the causes of the influence (beneficial or detrimental) found in the section above (4.3). To achieve these issues and build

a reliable characterising method, a novel analysis approach of the transfer film is firstly developed and then applied on the tested counterface.

#### **4.4.1 Transfer film characterisation: Benchmark on smooth counterface - Benchmarking observation methods**

In this section, an in-depth surface analysis to identify and characterise transfer film is presented with an emphasis on the new characterisation technique (SEM analysis with varying accelerating voltages and SIMS calibration), which has been introduced in the methodology section. The surface analysis presented in this section was performed on a smooth counterface that has been half-way through a full wear test, to ensure a substantial formation of PTFE transfer film.

Common practice for examining PTFE transfer films with optical images (from high-speed camera or microscopy) like Figure 64 (a), is to distinguish the PTFE simply by darkness. The areas darker than a subjective ‘threshold’ value is marked as black and identified as PTFE transfer film when the image is converted into binary, as shown in Figure 64(b). From the binary image, it can be seen that a large proportion of the dark area are long, thin strips along the sliding direction. However, from the surface topographic image Figure 64 (c), it can also be seen that along the sliding direction, many scratches were also created on the counterface, which in practice can create the ‘dark’ optical effects as well. Consequently, the optical imaging would lead to exaggerated estimation of the film coverage. Meanwhile, the surface topographic image (Figure 64(c)) is unable to reveal the transfer film accurately neither, since the topographic change is no longer just the result of transfer film, but its combination with surface wear, which in this case can be a few micrometres in depth. Overall, the methods using optical effects to identify the transfer film can be unreliable due to the presence of the wear on the counterface.

As proposed in the methodology section 3.1.4, BSE imaging in SEM analysis is a promising candidate to eliminate the uncertainties in optical methods, given that it can be validated by a reliable calibration method. To reveal its capability to detect thin film (sub-micron level), we test the BSE imaging of the transfer film on steel surface using low accelerating voltages (under 10 keV). As displayed in **Figure 65** (a) and (b), some distinctive dark areas appear, indicating the composition with lower atomic weight in BSE images. As the accelerating voltages used for the two images differed (10 keV to 5 keV), the dark areas also varied, indicating that the layers of this low-weight material can be of different thickness. In all the elemental composition

of the contact samples, apart from fluorine (F) in PTFE, elements from glass fibres (Si, O) and phenolic resin (C, H, O) are also lighter elements compared with iron (Fe), the dominant element of the steel. Moreover, if oxidation of iron manifests as a film on the surface, its overall atomic weight is also considerably smaller than iron itself. Therefore, it needs to use a chemical composition analysis to identify the composition of the dark areas becomes essential.

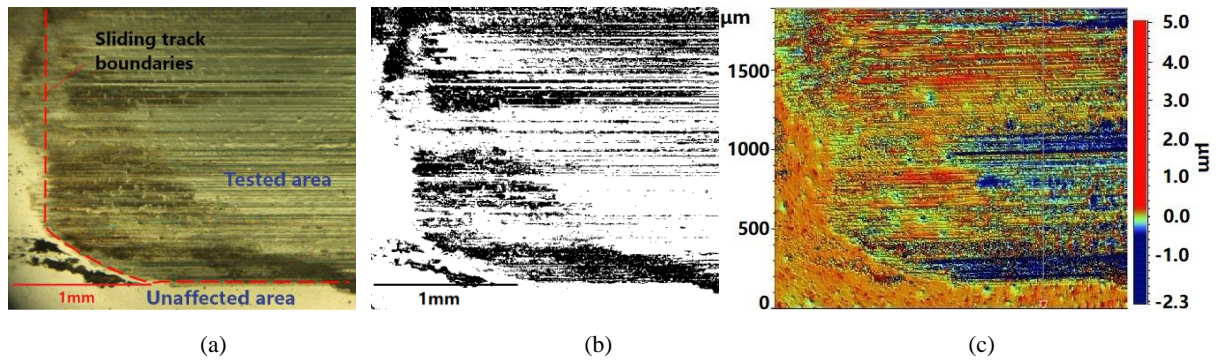


**Figure 64.** Observation of the smooth (non-textured) steel counterface using (a) optical microscopic image, (b) binary image converted from microscopic image, and (c) surface topographic image.

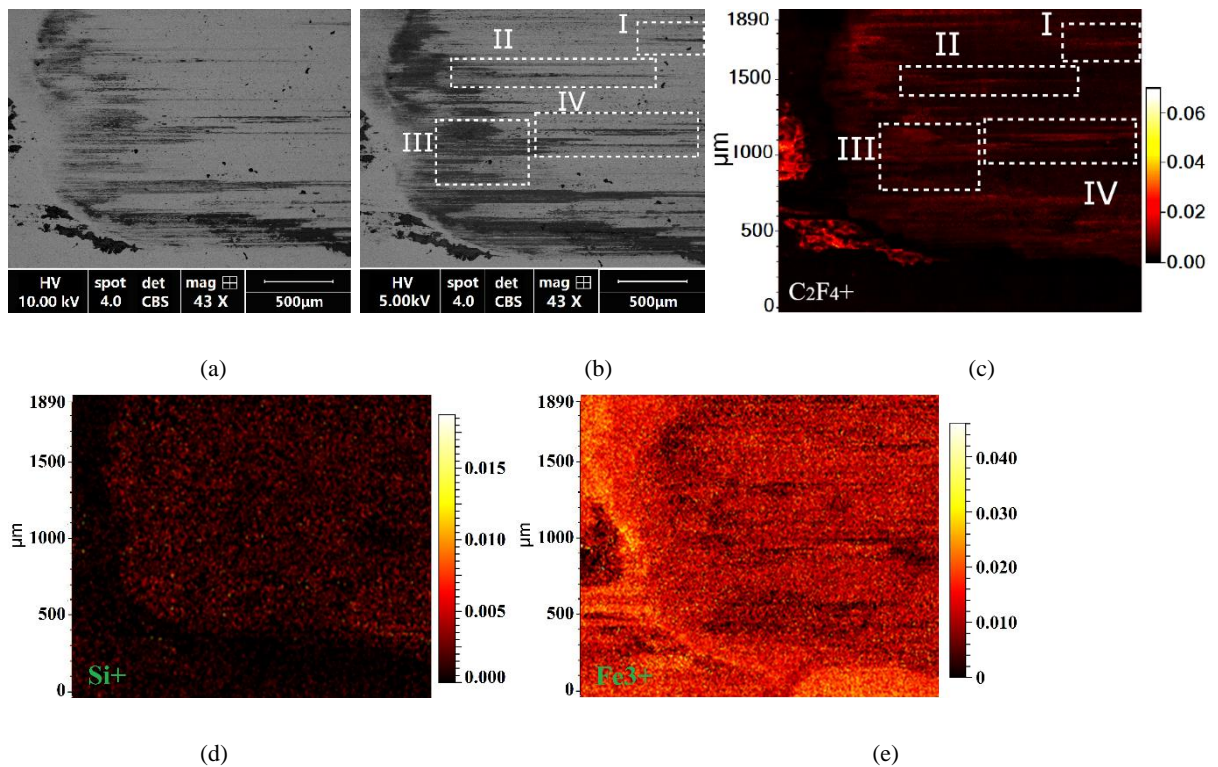


**Figure 65.** Observation of smooth (non-textured) counterface using (a) BSE image (accelerating voltage = 10keV), (b) BSE image (accelerating voltage = 5keV), (c) SIMS image of  $\text{C}_2\text{F}_4^+$  (counts normalized), (d) SIMS image of  $\text{Si}^+$  (counts normalized), (e) SIMS image of  $\text{Fe}^{3+}$  (counts normalized).

To clarify the identity of the dark areas, the mappings of the ions containing fluorine and other possible elements are generated for calibration using SIMS. Firstly, it can be seen that the areas

with high concentration of  $C_2F_4^+$  ions (bright spots in **Figure 65(c)**) resemble well with the dark areas in BSE image, particularly in marked details I-IV in **Figure 65(b)**. Other fluorine-ions such as  $F^-$  and  $C_6F_9^+$ , although not shown here, have a very similar pattern. As for the mapping of other possible ion sources, such as  $Si^+$  and  $Fe^{3+}$ , it could not relate with the BSE images at all, like shown in **Figure 65** (d) and (e). To conclude, the BSE images' resemblance with exclusively the Fluorine ions' mapping confirms that the dark areas in the BSE images represent the transfer of PTFE. Moreover, we can postulate that this technique should not be restricted to only PTFE transfer film, and can work for identification of other thin transfer film with featuring elements (e.g Mo in  $MoS_2$ ).

In comparison, some of the PTFE coverages detected by SIMS image of  $C_2F_4^+$  can be missing in the optical microscopic image and its binary version. For instance, areas I, V and IV in **Figure 65** (b) were 'flooded' by the surface scratches and consequently the coverages are not sufficiently presented in **Figure 65(a)**.

#### **- Film thickness characterisation with CASINO**

As has been revealed from **Figure 65**, under different accelerating voltage, the transfer film that can be observed under SEM (BSE mode) varied. In order to characterise the PTFE transfer film by its coverage and thickness, CASINO (v 2.51) - a commercial software for Monte-Carlo simulation was used to simulate the electron beam interaction under different accelerating voltages. In the software, the trajectories of the absorbed electrons and backscattered electrons can be simulated using selected models, once the elemental composition of the solid material (or material layers) and the properties of the electron beam are defined. With this function, the information depth of the backscattered electrons can be acquired for the steel surfaces with PTFE film transferred on it, providing theoretical guidance on the thickness of the PTFE transfer film observed under different accelerating voltages with the SEM.

To fulfil the film thickness calculation under a certain accelerating voltage, iterations of computing the Depth Distribution Function (DDF) of the backscattered electrons need to be done to find out the threshold PTFE film thickness, like shown in **Figure 66**. At first, assuming that a very thin (100 nm) PTFE film is atop of the steel surface, like demonstrated in **Figure 66** (a) and (b), most of the interacting backscattered electrons would be distributed below the film under the 30 keV accelerating voltage of the scanning electrons. In this case, the information from the steel substrate would overwhelm that from the PTFE film, namely the film is too thin to be detected. Then, if the film is sufficiently thick ( $6\mu m$ ), like shown in **Figure**

66 (a) and (b), all the interacting backscattered electrons would be distributed within the film, so the information about the film can definitely be revealed. However, in order to understand what is the minimum thickness of film that can be detected, iterations need to be done to find out the critical film thickness leading a threshold proportion (e.g. around 92% according to [209]) of the interacting backscattered electrons within the film thickness, so that the information from the PTFE film is dominating. After a few iterations, it was found that under 30 keV accelerating voltage, this threshold film thickness is  $3.9\mu\text{m}$ , as shown in **Figure 66** (f).

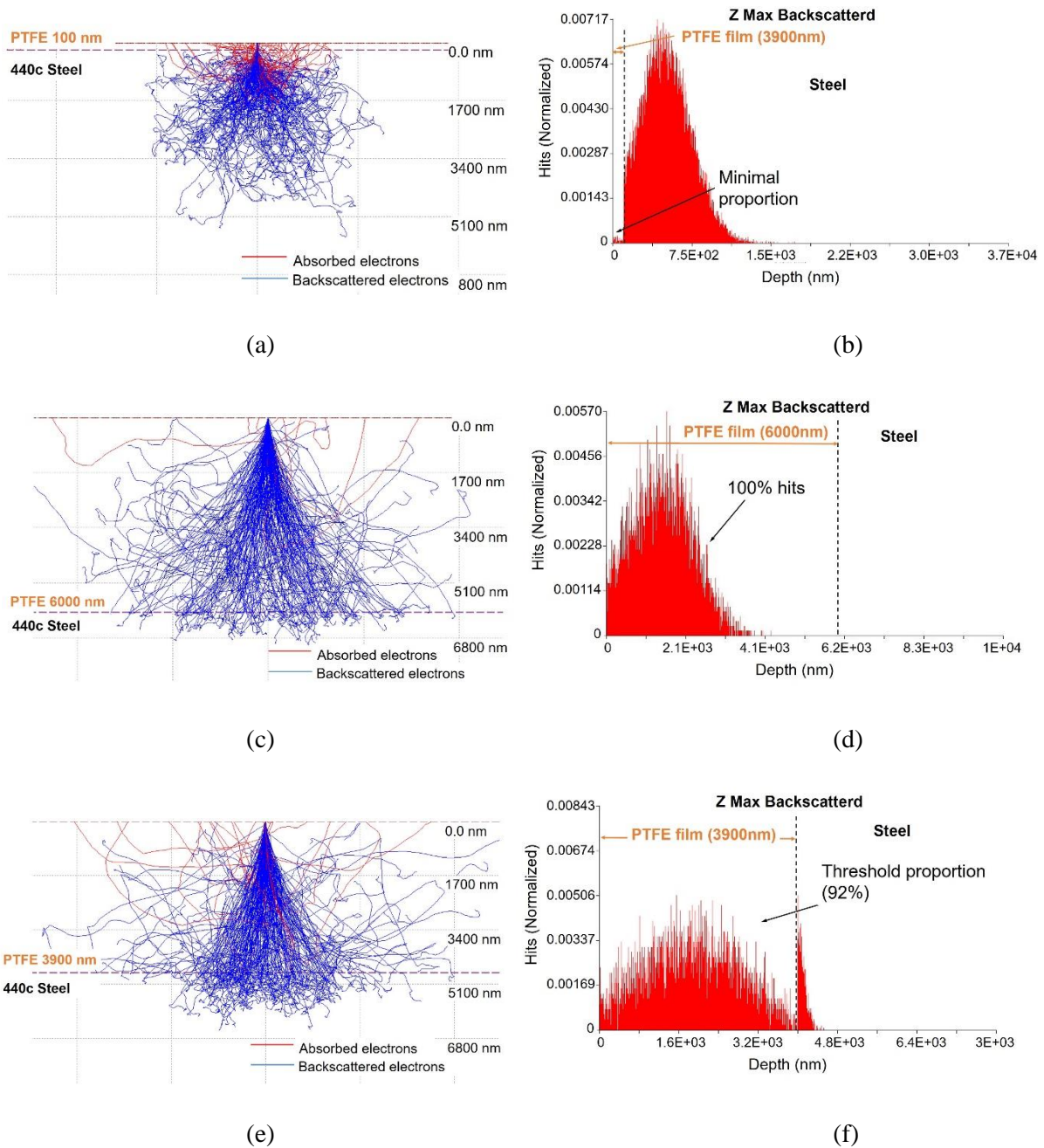


*Figure 66. CASINO output graphs for (a) Backscattered electrons distribution and (b) Depth Distribution Function graph of the Backscattered electrons with 6000 nm thick PTFE transfer film, and (c) and (d) corresponding graphs with 100 nm thick*

PTFE transfer film and (e) and (f) corresponding graphs with 3900 nm thick PTFE transfer film under 30 keV accelerating voltage

To evaluate the validity of the characterising method, the PTFE film thickness characterised in SEM image was compared with the topographic measurements (under relatively high accelerating voltages as the films detected were thicker and thus measurable by the interferometer). For instance, as shown in **Figure 67**, the thick transferred layer that can still be observed with 30 keV accelerating voltage (but not with higher voltages) was measured around 3.7  $\mu\text{m}$  thick, close to the threshold film thickness estimated using CASINO. Moreover, when the accelerating voltage is reduced to 5 keV and below, the computed information depth drop to tens of nanometres and under (as will be illustrated in **Figure 68**). Relating this with the much improved consistence between the observed PTFE transfer film in BSE image under 5 keV and by SIMS (which also reveals information on nanometre scale), as has been demonstrated in **Figure 65**, the validity of the method is further supported.

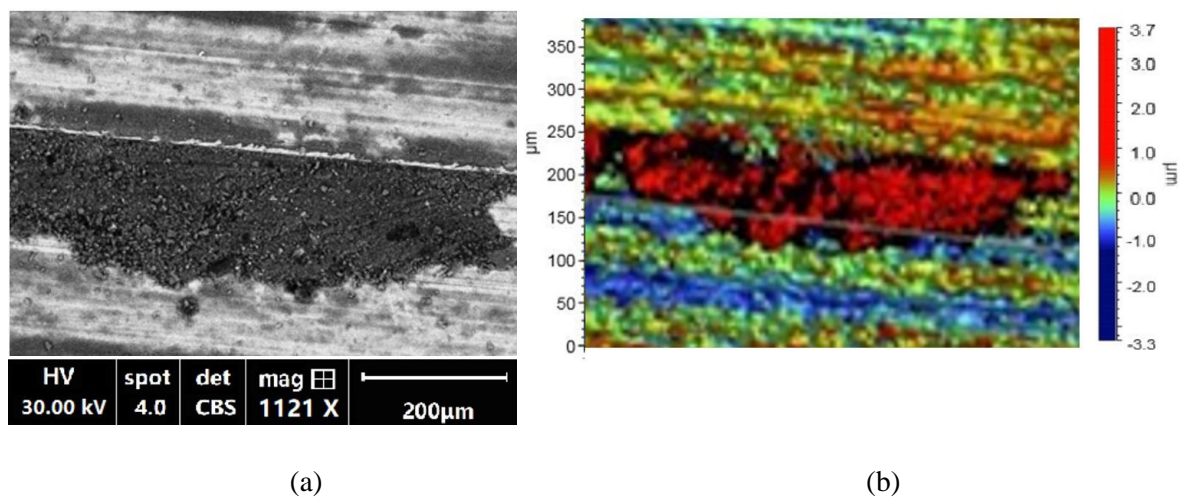


**Figure 67.** Comparison between the (a) SEM image (BSE mode) and (b) Topographic image of the surface area with a thick PTFE transfer film

With SEM investigation conducted on another location on the smooth counterface, the acquired images **Figure 68(a)-(d)** give a good example how the revealed coverage of PTFE transfer film changes with accelerating voltages. Comparing **Figure 68(a)** and (b), it can be seen that from 20 keV to 10 keV, the PTFE transfer film revealed by BSE image does not change significantly, with a long-strip-morphology along the sliding direction as the main morphology. However, when the accelerating voltage decreases to 5 keV, the detected film coverage increases dramatically, almost occupying the whole tested steel area, as shown in **Figure 68(c)**. This means that there is a step-change in the transfer film's thickness (computed through CASINO v2.5), from around 1 micrometre or above, to only tens of nanometres considering the

simulated distributions of the electrons' penetration depth (**Figure 68**(e)-(g)). There is, however, not much transfer film existing in-between these thicknesses. Finally, when the accelerating voltages dropped to 1 keV, the entire tested area appears dark, but the contrast could not be built effectively for distinguishing the un-affected area. In this case, even though it is possible that the transfer film can be present in the form of a few nanometres thick and less, the identification is beyond the capability of SEM. The 5 keV therefore can be regarded as an 'optimal' accelerating voltage for analysing the tested surface in this study as it unveils most of the PTFE transfer film with sufficient contrast.

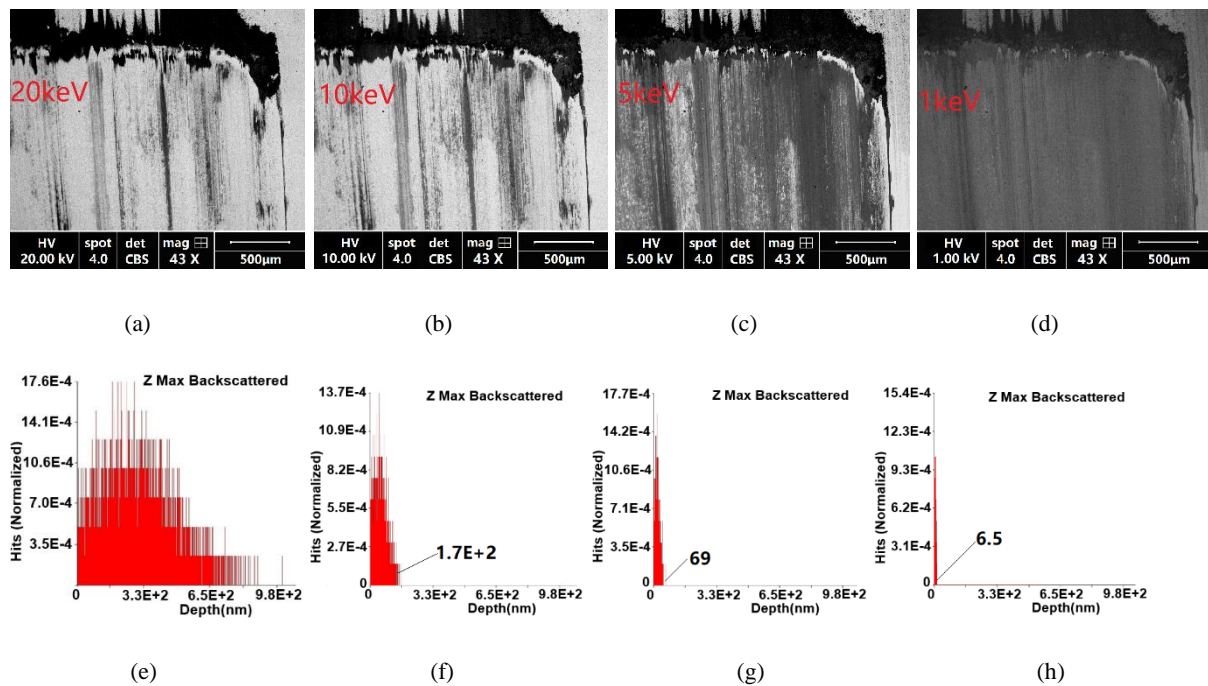


**Figure 68.** BSE images of smooth (non-textured) steel counterface using accelerating voltage (a) 20keV, (b) 10keV, (c) 5keV, and (d) 1keV; the Depth Distribution Function graph of the BSE images using accelerating voltage (e) 20keV, (f) 10keV, (g) 5keV, and (h) 1keV

With the two series of analysis on the PTFE transfer film above, our new method of characterising transfer film reveals two distinctive forms of PTFE transfer film on the counterface: one at micro-meters level the other in tens of nanometres and below. Because of the importance of matching the topographic variations of the counterface with the dimensions of the transfer film, this finding opens up a new prospect: improving transfer film formation by using micrometre-scale surface textures, while massive research has already be done in modifying surface roughness (nanometre degree in engineering surfaces).

#### 4.4.2 Transfer film analysis: Towards understanding of textured counterface

Taking advantage of the new method to characterise the transfer film, SEM analysis using the optimised voltage (5 keV) were used to evaluate transfer film's formation, including its

coverage, thickness and morphology, aspects which are strongly linked with the performance of dry-lubrication.

First of all, for all the tested surfaces with Type A (wide & deep) dimples, the SEM analysis revealed that they posed a negative influence on the transfer film's coverage, like presented in **Figure 69(a)**. Taking the one with medium coverage (1.6%) as an example, from the run-in to the steady stage, the dimples always created blank strips (area 1 and area 2 in **Figure 69**) among the film-covered area, exposing the metallic surface. This obstruction on transfer film formation appeared along the sliding direction and was common in all different dimple coverages. Such an observation was in line with that Type A (wide & deep) dimples in all coverages generates negative influence on the wear performance as stated in the section 4.3.

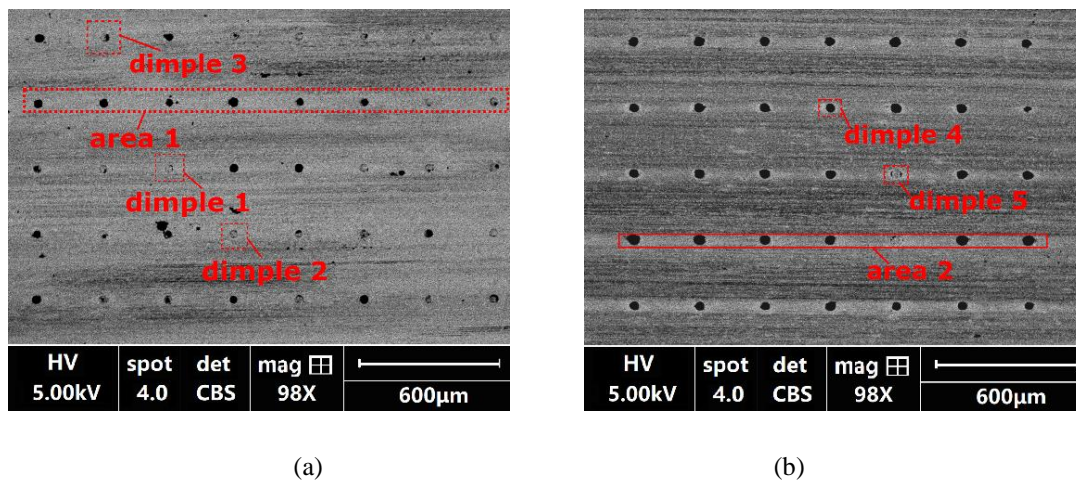


**Figure 69.** BSE images of the textured counterface with medium coverage (1.6%) of Type A (wide & deep) dimples in (a) run-in stage and (b) steady wear stage.

With a higher magnification on the dimples 1, 2 and 3 marked in **Figure 69**, it can be seen that the transferred PTFE was firstly obtained on the dimple edges, as shown in **Figure 70(e)-(g)**. The transferred debris' morphology, which was more distinguishable in SE images (**Figure 70**), was one of rough, irregular-shaped smears- a typical indication of abrasion wear. In the steady wear stage, in most dimples the 'reserved PTFE' (the PTFE wear debris or transferred PTFE contained within the dimples) had seemingly filled them, as the marked dimple 4 shown in **Figure 70(d)** and (h). Nevertheless, in the end it could not form an integrated transfer layer outside the dimple (might be because they were never entirely filled as examined separately with profilometer), thus still leaving the blank strips. Moreover, small amounts of un-filled dimples still can be found, with noticeable scratched debris on the edges, such as the dimple 5 marked in **Figure 69**.

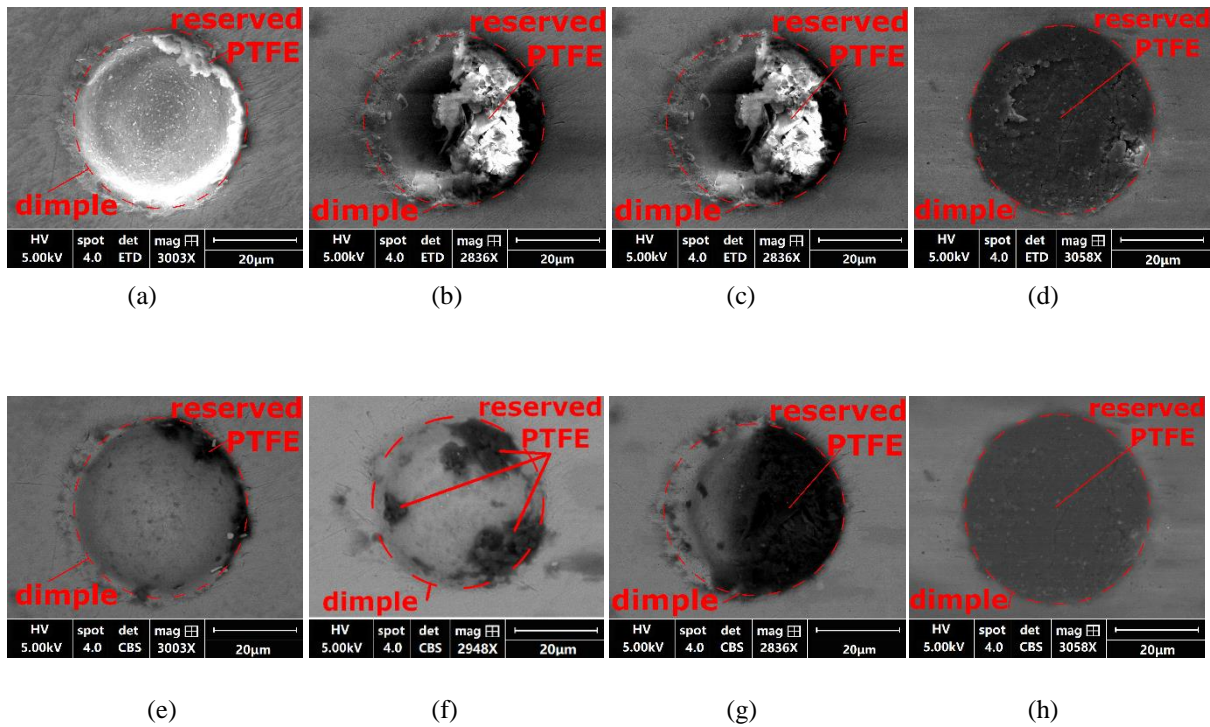


**Figure 70.** (a)- (d) SE images of Type A (wide & deep) dimples from run-in to steady stage (area 1-4 marked in Figure 69), (e)-(h) BSE images of Type A (wide & deep) dimples from run-in to steady stage (area 1-4 marked in Figure 69).

In comparison, with the same medium coverage (1.6%), the Type B (narrow & shallow) dimples increased the film-covered area as they created dark strips like shown in the boxed areas 1-4 in **Figure 71**. Besides, the reserved debris were no longer rough irregular particles peeled by the edges, but smooth flakes contained on the bottom of the dimples initially, as shown in **Figure 72** (a) and (b). This morphology feature could either be from the adhesion wear of the PTFE dragged from outside the dimples, or from delamination of the composite asperities intruding into the dimple. In later stage, the reserved debris accumulated and formed a transfer sheet layer. Different from the one in the wide, deep dimples, the accumulated debris was able to actually fill out the dimple and integrate with the transfer film formed outside the textured area in the later stage, as shown **Figure 72** (c) and (d).

These observations indicated that the dimples were able to act as dry-lubricants' reservoirs. More importantly, the reserved debris of dry-lubricant was capable of replenishing the non-textured part of the steel surface, benefiting both the coverage and the thickness of the dry-lubricant transfer film. This phenomenon should be able to reduce the direct contact between the metallic surface with the composite liner surface, reducing both the friction and wear. Overall, it can explain the superior performance of the narrow & shallow dimples under certain coverages.

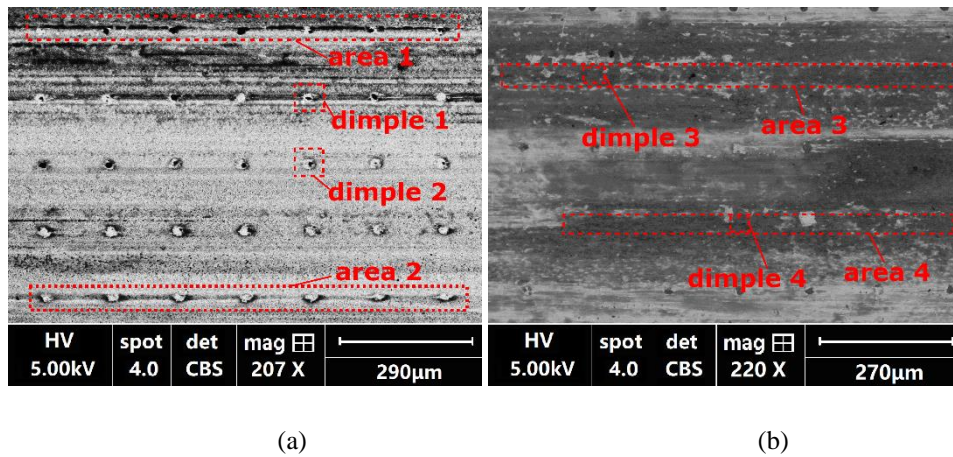


**Figure 71.** BSE images of the steel counterface textured with medium coverage (1.6%) of Type B (narrow & shallow) dimples in (a) run-in stage and (b) steady wear stage.

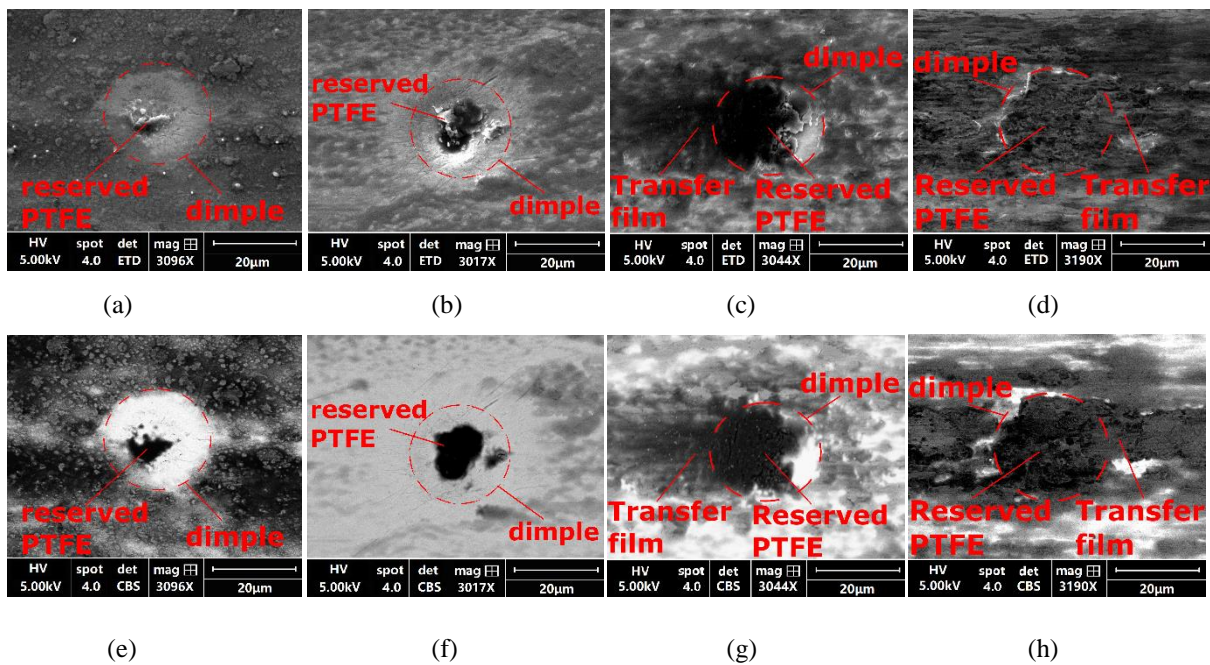


**Figure 72.** (a)- (d) SE images of Type B (narrow & shallow) dimples from run-in to steady stage (area 1-4 marked in Figure 71); (e)-(h) BSE images of Type B (narrow & shallow) dimples from run-in to steady stage (area 1-4 marked in Figure 71).

Similarly, when the dimples were shallow yet wider (Type C) these enhanced transfer strips could also be incurred as shown in the area 1, 2 and 4 in **Figure 73** (a) and (b). However, the appearance was less common than with Type B (narrow & shallow) dimples. From the images focusing on single dimples (Figure 74(a) and (b)), it was found that the Type C (wide & shallow) dimples resemble the Type A (wide & deep) dimples during the initiation of the wear process but the debris was again firstly collected on the dimples' edges. However, because the dimples had a lower depth, which was within the range which transfer layer could form naturally on a smooth surface, the accumulated debris was able to build up a transfer sheet covering the dimple's depth as shown in Figure 74(c) and (d) in the steady stage. Similar with the Type B

(narrow & shallow) dimples, the reserved debris in these micro-holes was also able to form a layer integrated with the transfer film formed outside the dimple. Meanwhile, the obstruction of the transfer film, which was similar with the ones with Type A (wide & deep) dimples would also occur, such as the area 2 marked in Figure 73(b). Since both the film-thickening effect and micro-abrasion effect were considerable under these conditions, they may offset each other, and this may explain why it did not create the advantages like narrow & shallow dimples, but would not lead to apparent disadvantage like wide & deep dimples.

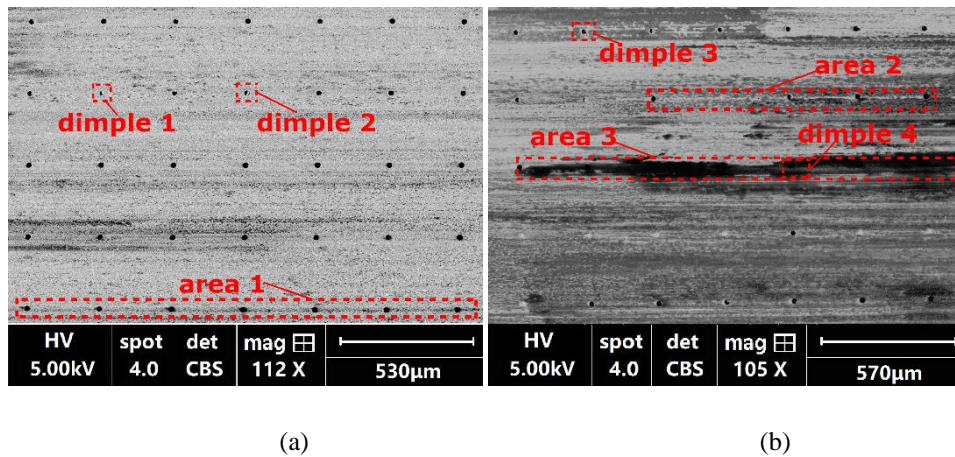


Figure 73. BSE images of the steel counterface textured with medium coverage (1.6%) of Type C (wide & shallow) dimples in (a) run-in stage and (b) steady wear stage.

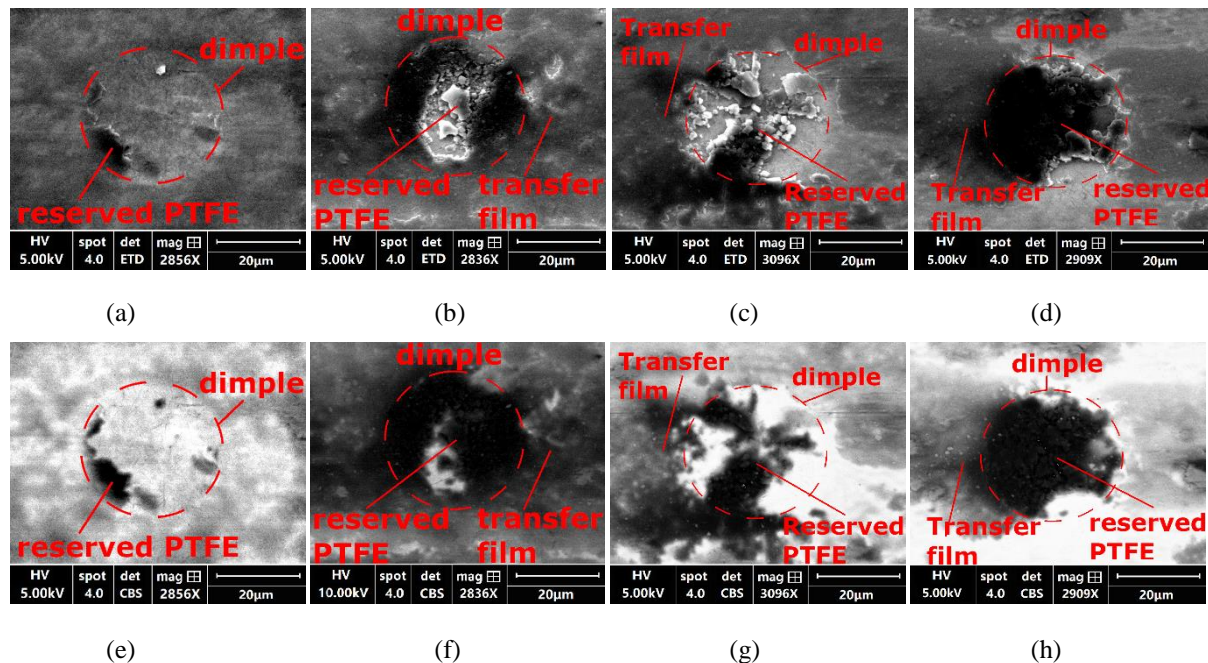
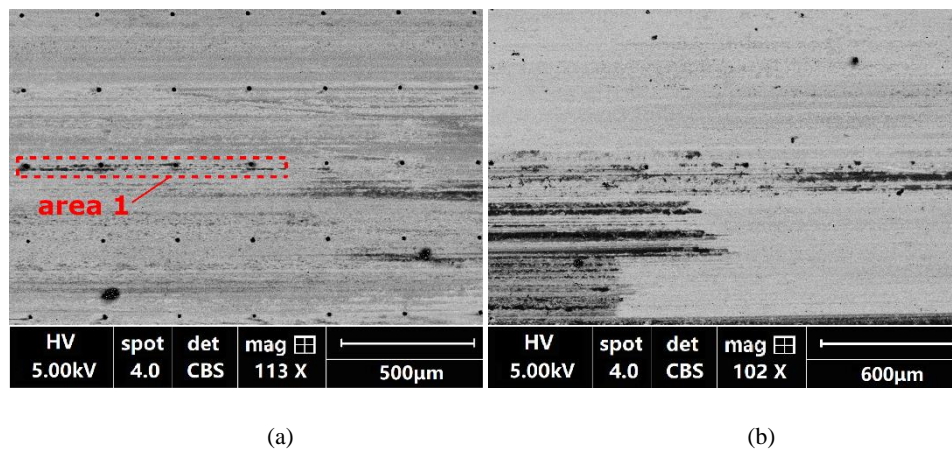


Figure 74. (a)- (d) SE images of Type B (narrow & shallow) dimples from run-in to steady stage (area 1-4 marked in Figure 73); (e)-(h) BSE images of Type B (narrow & shallow) dimples from run-in to steady stage (area 1-4 marked in Figure 73).

Both of the effects summarised above are also dependent on the coverage of the dimples. For instance, with the low coverage (0.4%) of Type B (narrow & shallow) dimples, the strips of

transfer film formed by dimples along sliding direction occur less occasionally. The only strip (area 1) observed in **Figure 75** is also dis-continuous, indicating that the adjacent dimples are arranged too far apart ( $280\ \mu\text{m}$  for low (0.4%) coverage) for the retained PTFE in the reservoirs (dimples) to travel and cover the whole distance. Moreover, with the low coverage (0.4%) of wide & shallow dimples, such a strip almost never appear (**Figure 75** (b)). This difference should be explained by the even longer distance ( $560\ \mu\text{m}$ ) between adjacent dimples for Type C (wide & shallow) under the same coverage in comparison with the Type B (narrow & shallow).



**Figure 75.** BSE images of the steel counterface textured with low coverage (0.4%) of (a) Type B (narrow & shallow) and (b) Type C (wide & shallow) dimples in steady wear stage.

When the coverage is set as high (6.4%), however, the micro-abrasion effect becomes more dominating for both Type B (narrow & shallow) and Type C (wide & shallow) dimples, like shown in **Figure 76** (a) and (b). As a result, the overall influence on transfer film is similar with the Type A (wide & deep) dimples. Therefore, it can be seen that both the coverage and dimensions of the dimples need to be on the lower side to avoid this abrasion effect. Moreover, this phenomenon is likely to be related with a more prominent increase in contact stress with higher coverage or larger size of texturing. To give a more detailed analysis of the relationship between the dimple dimensions and this effect, a finite element (FE) analysis is performed in the next section.

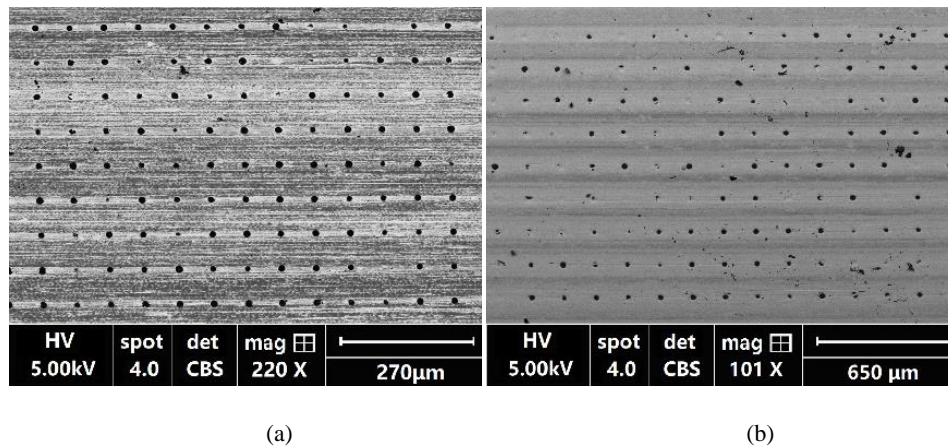


**Figure 76.** BSE images of the steel counterface textured with high coverage (6.4%) of (a) Type B (narrow & shallow) and (b) Type C (wide & shallow) dimples in steady wear stage.

To summarize, only with low (0.4%) and medium coverage (1.6%) of Type B (narrow & shallow) dimples would the benefit from texturing on the transfer film formation reach the high level, while the detrimental abrasion effect maintained at a lower degree, as shown in Table 8. Given that the observed phenomenon (wear debris and transfer film’s formation) was in line with the wear and frictional performance shown in the section 4.3, it can be deduced that both the benefiting effect on transfer film and the abrasion effect need to be considered when the coverage and dimensions of the surface textures are to be designed.

**Table 8.** Summary of dimple’s effects in different dimensions and densities

	Type A (Wide & deep)			Type B (Narrow & shallow)			Type C (Wide & shallow)		
	Low (0.4%)	Medium (1.6%)	High (6.4%)	Low (0.4%)	Medium (1.6%)	High (6.4%)	Low (0.4%)	Medium (1.6%)	High (6.4%)
<b>Enhancing film formation *</b>	+	+	+	++	+++	+	+	+++	+
<b>Micro-abrasion *</b>	++	+++	+++	+	++	+++	+	+++	+++

\*: “+” means very low and “+++” means very significant effect

## 4.5 Finite element analysis for the contact mechanics

The contact pressure and stress are crucial indexes for evaluating the wear condition in a sliding contact, since contact pressure is a component in *PV* factor and stress is directly related to the material failure. In this thesis, particularly, for the surface textures introduced (dimples) a possible contact phenomenon is the stress concentration caused by the dimple edges. To quantify this effect and to generate theoretical explanations of the wear performance with

different textured counterface, the contact mechanics analysis was performed with the Finite Element (FE) model built.

#### 4.5.1 Model evaluation and relevant adaptations

##### - Material properties

An accurate modelling of the material properties is vital for realistic reflection of the contact pressure and stress condition.

For the mechanical properties of the composite, firstly the data provided by the bearing manufacture (SKF Ltd) was used as the basis. Then, for calibration, a designed contact condition was created by pressing a specially-made pin sample (reduced area - 3 mm × 3 mm & liner section on the side) against the counterface with an exaggerated pocket hole (1 mm × 0.5 mm), like shown in **Figure 77** (the contour map of vertical deformation of the composite).

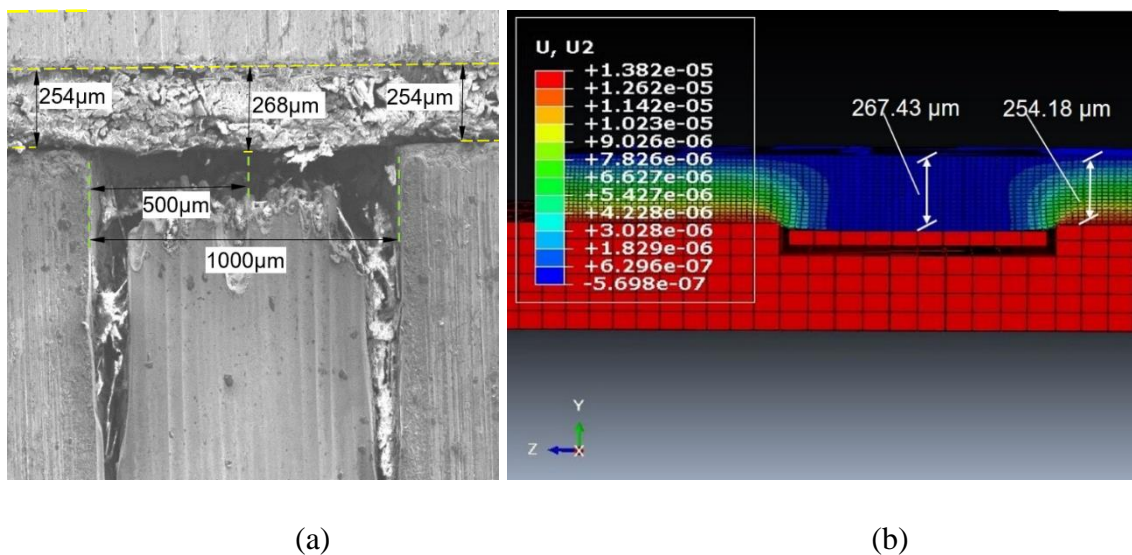


**Figure 77.** An example of calibration of the model using (a) Measured deformation of the composite line under a static pressing force; (b) Modelled contour map of deformation (vertical) on the composite liner under a static pressing force (normal pressure 40 MPa)

During this calibration process, special attention was given to two points. Firstly, the liner was placed in a specific position (i.e. pocket hole placed in the mid-position between two glass fibres on the section) to establish a representative state for calibration (later shown in section 4.5.1). Then, the model aims at reflecting the condition in steady stage, so the real measurement should be made on a liner which has just gone through a wear test session till the steady wear stage, to ensure that consistency in temperature (influencer on material properties). For example, in the case for **Figure 77**, before the rig was stopped for the picture to be taken, the liner had just gone through a wear test session passing the run-in stage (12 μm top layer of the

composite had worn off). Then, adjustments on the property values (such as elastic modulus) were made based on the deformations measured from the pictures obtained with the high-speed-camera shooting from the side. Finally, after consistency in displacement had been achieved between the tested and simulated condition, as shown in **Figure 77**, the calibrated mechanical properties were outputted, including the basic properties listed in Table 9. It should be noted that the PTFE wefts and warps (correspondingly the cells modelled) are stiffer than pure PTFE as the fibres are also impregnated with the phenolic resin. Besides, a plasticity model and data from a series of compression tests for the composite liner was also provided by SKF UK Ltd, contributing to modelling the mechanical properties of the composite liner.

*Table 9. Material properties for modelling the composing components of the composite*

	<b>Modulus of Elasticity (GPa)</b>	<b>Density (<math>\times 10^3</math> kg/m<sup>3</sup>)</b>	<b>Poisson ratio</b>	<b>Yield strength (MPa)</b>
<b>PTFE (impregnated)</b>	3.3	2.2	0.45	75
<b>Glass fibre</b>	72.0	2.55	0.22	4000
<b>Phenolic resin</b>	3.5	1.2	0.34	105

As for the further simplified model with assuming a uniform section, the integrated material properties were obtained using the textile modelling software TexGen (version 3.10) with its computation module for integrating properties of composite components (adopted by researchers such as Russel [4], like in **Figure 9**). As will be introduced later in section 4.5.1, the integrated material properties were also calibrated against the established model with different composition parts.

#### **- Discretization**

To ensure an economical yet accurate computation, a gradient mesh scheme was adopted for simulation with textured counterface, like shown in **Figure 78**. Taking **Figure 78(b)** as an example, fine grids (1.25 $\mu$ m) were meshed near the interface (bottom of the composite), which is the area of key importance for the contact problem. Going upwards, the grids were gradually transited (by doubling) to coarser ones (around 20 $\mu$ m on the very top).

Moreover, structural mesh was always employed, featured with hexahedra volume element for discretization. This meshing strategy not only has the advantage in memory saving and computation efficiency over unstructured mesh (tetrahedral element), but also enables easier control of the element size and number for grid-independence test.

Benefiting from the easy control of the element, the grid-independence was evaluated by comparing the results with varied element sizes. In the examples shown in **Figure 78**, by refining the grid size from  $1.67\mu\text{m}$  to  $0.91\mu\text{m}$ , number used for describing the region neighbouring the texture ( $20\mu\text{m}$  diameter,  $2\mu\text{m}$  depth) increased from 12 to 22. Correspondingly, the computed maximum stress value increased from  $94.28\text{MPa}$  to  $103.4\text{MPa}$ , while the basic pattern of the stress distribution maximum stress kept similar.

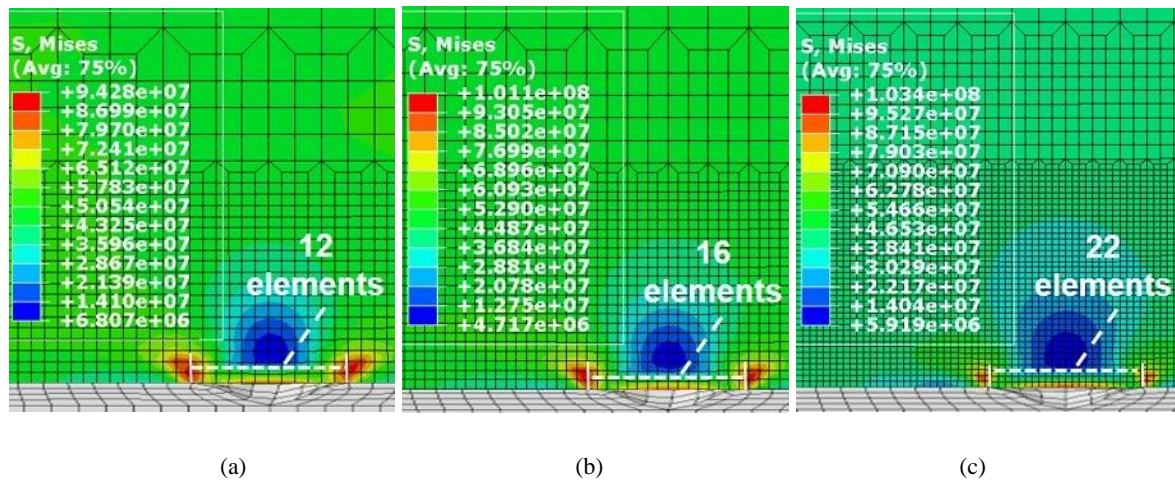


**Figure 78.** Stress distribution in PTFE composite against counterface with textures ( $20\mu\text{m}$  diameter,  $2\mu\text{m}$  depth) with (a)  $1.67\mu\text{m}$  grid length, (b)  $1.25\mu\text{m}$  grid length and (c)  $0.91\mu\text{m}$  grid length on the bottom

However, as summarised in **Figure 79**, the rising rate of the output maximum stress was damping. Apart from the three cases shown above (the first three points), it can be seen that if the element number is increased further to around  $7 \times 10^5$  (the fourth point), the incurred increase in maximum stress was considerably small (less than  $2\text{MPa}$  - 2% discrepancy). Using commonly-used evaluating method for mesh convergence like Richardson extrapolation [210], it can be estimated with the third point the error has already been sufficiently small (less than 3%). Therefore, considering the computational cost, the third meshing scheme (around  $0.91\mu\text{m}$  grid length on the bottom) was chosen for the FE analysis series. It is also adopted on modelling with smooth counterface in each condition for consistency.

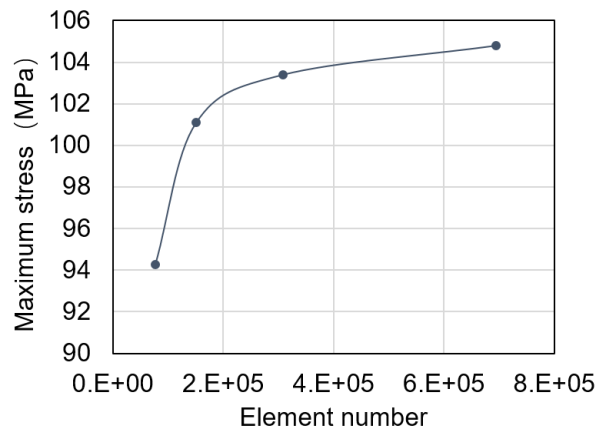


**Figure 79.** Mesh independence test using maximum stress computed through different element size set

### - Evolution of the contact condition

To start with, the varying of the contact condition under dynamic (i.e. with sliding) simulation was analysed to give an initial understanding of the evolution of the contact condition.

Firstly, a primary finding was that even though the dimples introduced are now micro-level, and the indentation into the dimple is minimal (nano-meter level as computed), severe pressure-lifting and stress concentration can still occur. For example, as shown in **Figure 80** (a), even with narrow & shallow (Type B) dimples, the peak stress can reach to 92.55 MPa (circled zones) on the surface in static condition (without sliding simulated), while with the smooth counterface, this value is only around 55 MPa (revealed in full-composition model, **Figure 82**). Succeeding with the static condition, the maximum stress increased to 98.42 MPa at the start-up (reaching to sub-surface) of the sliding as shown in **Figure 80** (b), then it oscillated and gradually stabilised at a lower level (96.52 MPa), as presented in **Figure 80** (c).

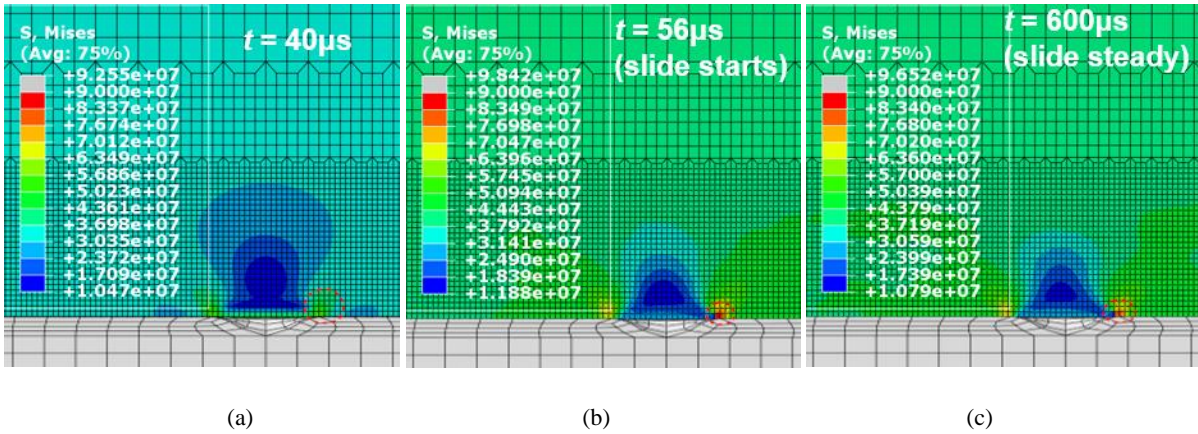


Figure 80. Stress distribution in PTFE composite in the case of counterface with medium coverage (1.6%) of Type B (narrow & shallow) dimples at (a) static state (b) first step of sliding (c) after 600 $\mu$ s of sliding.

Apart from the evolution of the stress distribution on the composite, the curve of the total strain energy (*ALLSE*) generated by the Abaqus built-in function can reveal the evolution of the overall contact condition, as shown in **Figure 81**. From the curve it can be seen that the strain level first saw a major rise upon the start of the sliding, but then dropped back moderately and oscillated with gradually decreasing amplitude. After around 550 $\mu$ s, a relatively stable state was reached (less than 2% of oscillation for the total strain energy value). Therefore, it is reasonable to utilize the stress/strain results obtained then to represent the simulated contact condition.

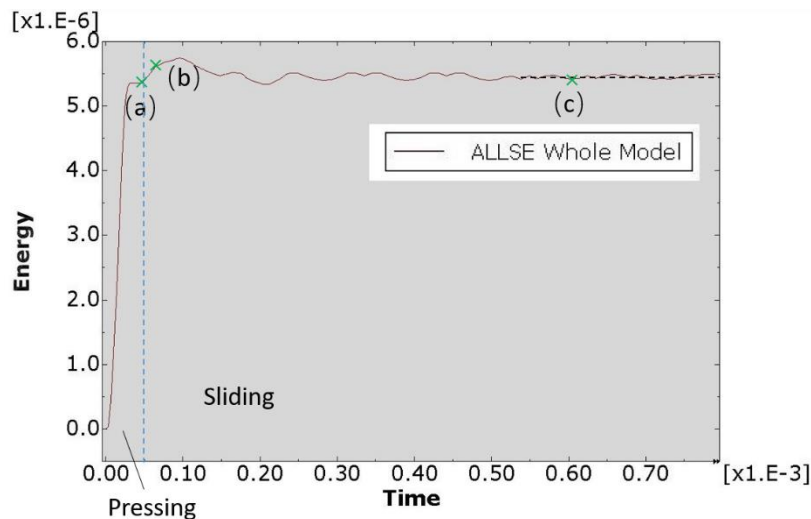


Figure 81. The total- strain-energy curve versus time output in Abaqus in the case of counterface with medium coverage (1.6%) of Type B (narrow & shallow) dimples

## - Preliminary simulation and basic findings

Firstly, to gain an overall view on the contact pressure and stress distribution on the composite during the contact, simulation was performed using the composition-cell model of the composite (presented in chapter 3.1.5). For contact pressure, the pressure distribution under the normal load (normal pressure) was computed aiming to show the variation in different parts of the surface, while for the stress, Von Mises stress was used as the index for evaluating the stress condition in sliding contact as it is related to failure of material under uniaxial loads.

As obtained, under the normal load (40 MPa), the resultant contact pressure on the composite surface was drastically higher at the glass-fibre areas (reaching 278.9 MPa), but at a similarly low level at most of the other areas (around 26.7 to 37 MPa), like shown in **Figure 82** (a). This reflected that the glass fibres as the stiffeners took much more load, relieving the pressure on the other parts. Then, in the dynamic simulation (sliding motion included), when the analysis reached a relative stable state, as shown in **Figure 82** (b), the stress also peaked at the glass-fibre areas, but with variations between glass-fibre locations due to sliding. As for the other areas, the surface stress was not as uniform as in the static contact pressure, but overall had similar stress distribution patterns along the direction of sliding (e.g. between the two boxed sections).

With the results obtained, it can be seen that a pressure-relieving phenomenon was incurred on the PTFE/resin parts by the glass fibres, leading to lower contact pressure and consequently stress in these components. Moreover, the uniformity of contact pressure and similarity of the stress-distribution on these relieved parts also incite the simplification and modification of the model, so that it can be adapted to the textured condition as described in the following sections.

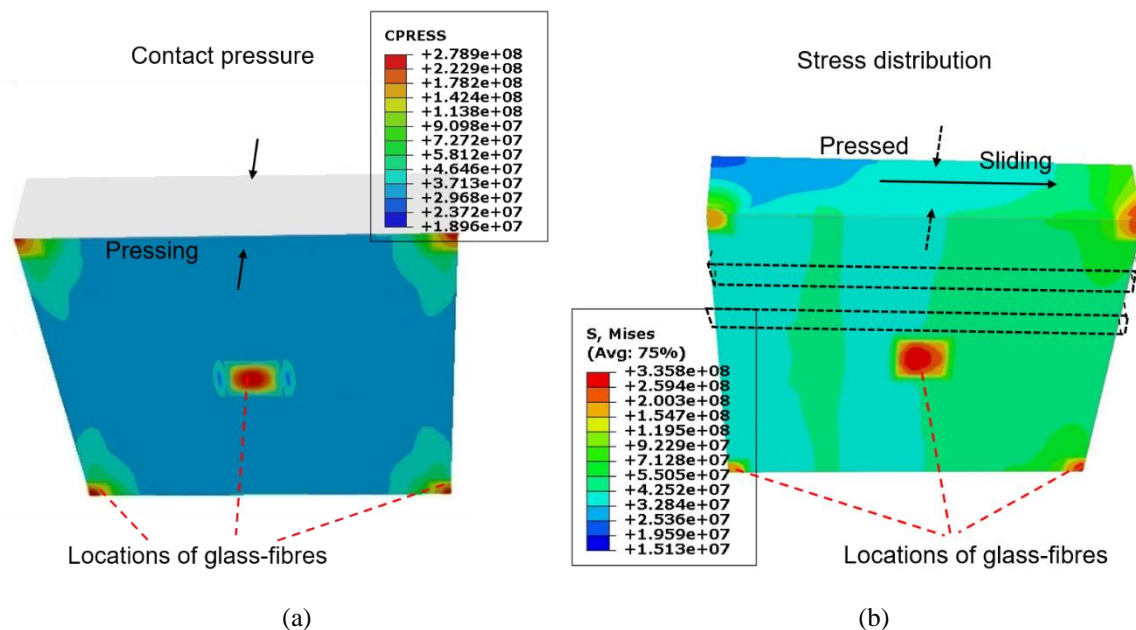


Figure 82. FE results of stress condition of the composite with (a) static analysis and (b) dynamic analysis (stable state)

Moreover, using this simulation, the resultant contact conditions under the load of *PV* limit (derived from the *LPV* test in chapter 4.2.1) were also computed, with the information for the pressure-relieved parts (areas excluding glass-fibres) extracted and listed in **Table 10**. Since the polymer components are the main bodies affected by the *PV* factor and contact stress and thus prone to wear, the reduced *P* (contact pressure) on these parts should lead to a new ‘real *LPV*’ standard targeting at the polymer parts. In further analysis focusing on the contact condition on the parts excluding glass fibres, this information would give a more related reference on the critical state for the composite.

Table 10. Summary of simulated results for contact pressure and stress under standard test condition and *PV* limit

Load condition	Normal pressure (MPa)	<i>P</i> (MPa) - excluding glass fibres	$\sigma$ (MPa) - excluding glass fibres
Standard test	40	29.68 – 37.13	32.84 – 55.05
Equivalent to <i>LPV</i>	100	66.26 - 93.52	70.82 - 109.7

#### - Adaptions and calibration for modelling with textured conditions

Comprehensive as the approach of modelling all the composition cells is, it is not realistic to directly apply the model on the situation of textured counterface – elements near the interface need to be sufficiently smaller than the dimple (i.e. at least around 20 elements per dimple diameter as tested in section) to reveal the stress condition adjacent to the dimpled region, so the element number would be excessively huge (estimated at least 50 million nodes, beyond the limit of the solver as tested) if a complete model is to be modelled on the dimpled surface in this thesis. Moreover, given the observations of the counterface during tests (in chapter 4.4), after certain sliding time the contact between the glass-fibres and the counterface, leading to complexity (e.g. counterface abrasion and possibly abrasive third-body) beyond the scope of this contact mechanics model. Therefore, considering that the impregnated PTFE fibres and phenolic resin have similar mechanical properties (as stated previously in Table 9) and experience similar contact pressure and stresses as found through preliminary simulations, it is proposed that the simulation focuses only on the sections excluding the glass fibres, and the mechanical properties are simplified to be uniform within these sections, as shown in **Figure 83** (a) and (c). With this approach, a model with reduced size and complexity can be established and adapted onto the cases with textured counterface.

To establish the uniform mechanical properties of the extracted section, the composition structure of the extracted section was modelled in TexGen (version 3.10) – a textile structure modelling software. With the built-in computation module [211], an equivalent mechanical properties of the structure can be derived from the input constitutive geometry with individual mechanical properties (from Table 9) and imported to Abaqus.

To reassure that the converted mechanical properties are representative, the contact condition computed with the simplified section was compared with the original full composition model on the calibrated case (with test in chapter 3.1.5). To give an example, for the stress distribution comparison, as shown in **Figure 83** (b) and (d), even though naturally the simplified model could not reveal the stress condition in the excluded parts (for glass-fibres), but the revealed stress distribution is close to that of the original part, particularly near the interface. Moreover, the stress concentration adjacent to the dimple edges is similar (e.g. maximum stress at around 320MPa). Therefore, it is reasonable to say that the simplified model has the similar capability of revealing the contact condition of the composite surface like the full-composition model. More importantly, benefiting from the uniformity, given adaptive boundary conditions (symmetricity and periodicity), the model can be further reduced to a designated size, meeting the mesh requirement with textured counterface. Correspondingly, the detailed analysis with textured counterface are presented in the following section.

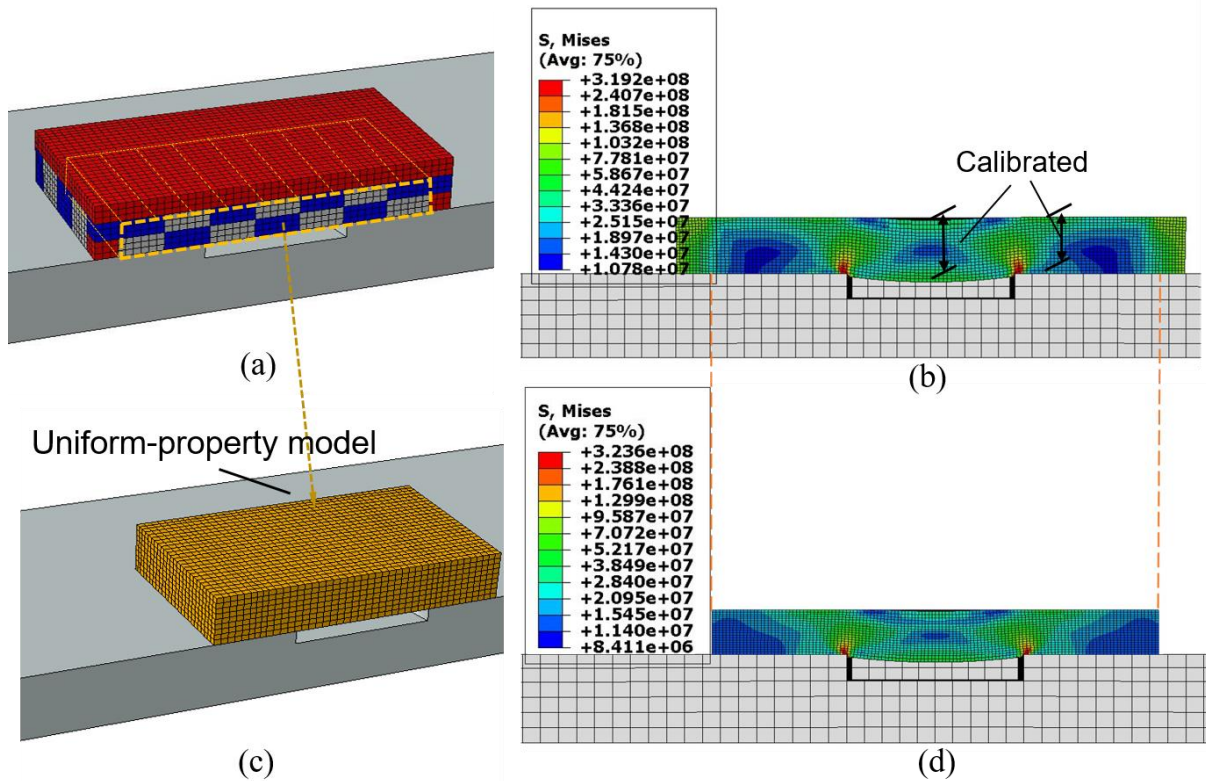
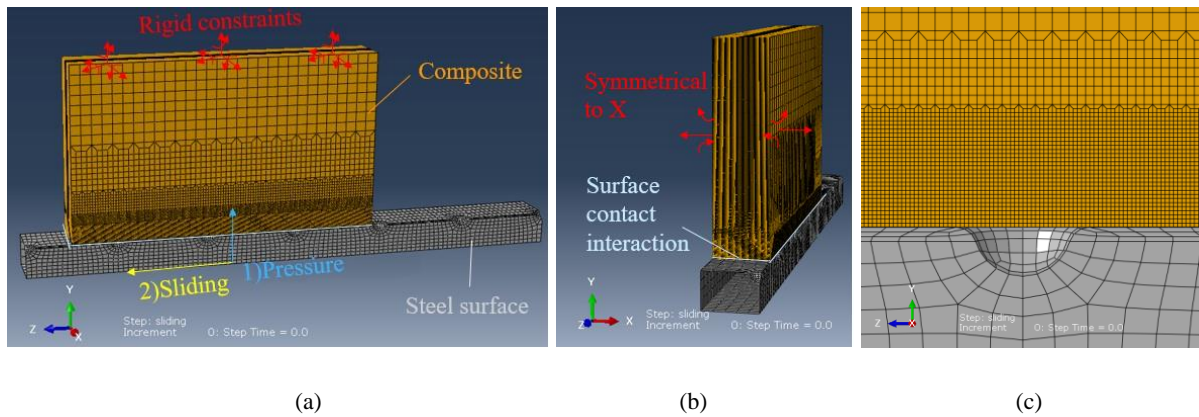


Figure 83. (a) The original model and (b) the output stress distribution and (c) the simplified model and (d) the output stress distribution for the calibration case

#### 4.5.2 Analysis of the contact condition with different textured counterface

To study the stress condition of the PTFE parts in the composite sliding against the dimpled surfaces, the following FE analysis was done using the uniform-section model developed, covering all tested dimple dimensions and coverages to relate the observed effects with the theoretical analysis.

For the simplified section, as shown in **Figure 83** (a) and (b), only a single row of dimples (along the sliding direction) and the corresponding composite section were modelled, with symmetrical boundary condition applied on the sides considering the symmetry in the geometry and uniformity of pressure load. By doing this, the scale of the model was reduced to the smallest possible, while the computation force can focus on interpreting the variation of contact condition induced near the dimpled areas, where a gradient mesh was employed as in **Figure 83** (c).



**Figure 84.** Demonstration of (a) geometric models, loading conditions and boundary conditions (b) interactions applied; (c) transition of the grid size (magnified view)

### - Influence of dimple dimensions

Using the steady-state results in the dynamic simulation, the influence of the dimple dimensions were analysed. Through comparison between different dimple types, it was found that dimples with higher diameter would incur more severe pressure-elevation and stress concentration, while the influence of dimple depth is minimal.

For example, at low coverage (0.4%), as shown in **Figure 85**, the maximum contact pressure with Type A (wide & deep) dimples and Type C (wide & shallow) dimples reached 108.8 MPa and 101.8 MPa, more than 15% higher than the (Type B) narrow & shallow dimples. Comparing with the real contact pressure of smooth counterface (maximum 37.13MPa), these values are substantially higher, leading to the ‘local *PV* factor’ more than doubled. More importantly, for both ‘wide dimples’ (Type A and C), the value exceeded the real contact pressure under *LPV* condition (91.72 MPa in **Table 10**), meaning the local thermal effect may have already exceeded the critical state. Therefore, even though the experimental set-up for temperature measurement is not sophisticated enough, the FE model has indirectly revealed the possibility of local softening and melting of the composite near the dimpled areas.

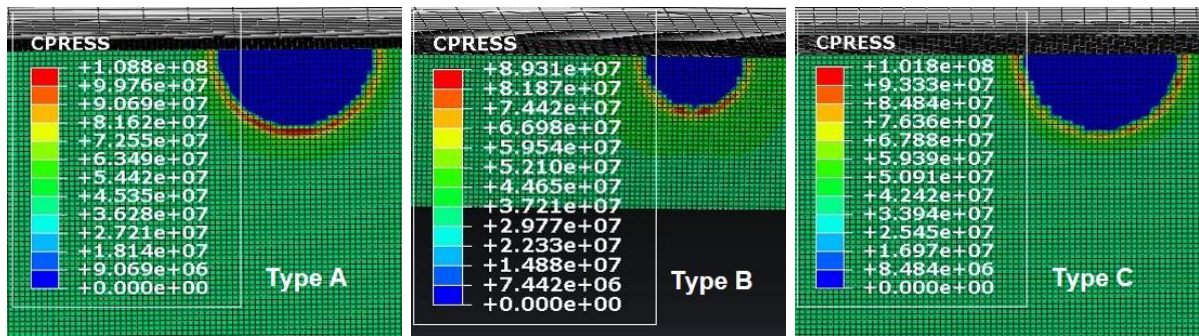


Figure 85. Bottom view of the PTFE composite for the pressure distribution on the surface sliding against steel surface with medium coverage (1.6%) of (a) Type A (wide & deep) dimples, (b) Type B (narrow & shallow) dimples and (c) Type C (wide & shallow) dimples under normal pressure 40MPa from the top

Similarly, for the stress condition, as shown in **Figure 86**, the maximum contact stress with wide dimples (Type A and Type C) would reach to over 110 MPa, dramatically higher than 96.52 MPa with the narrow (Type B) dimples.

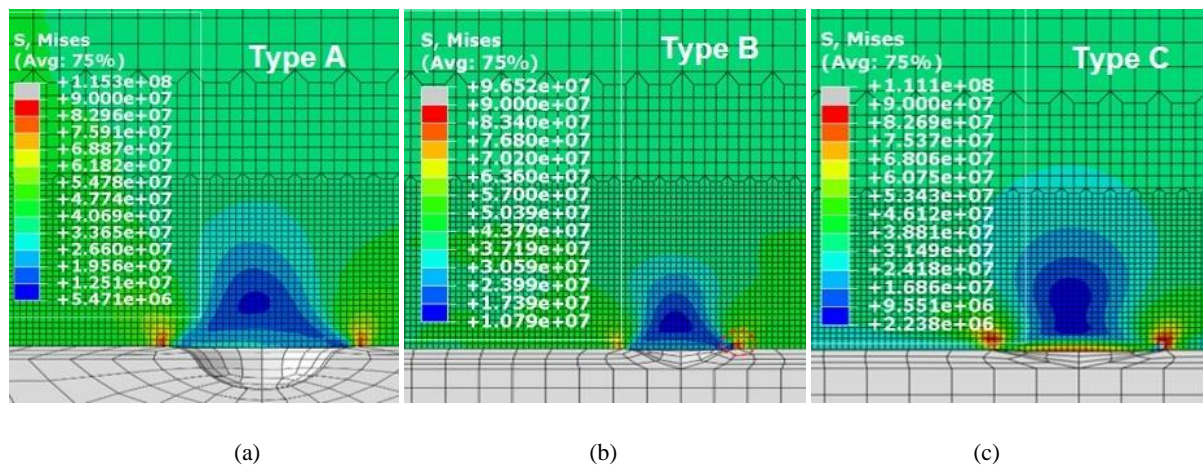
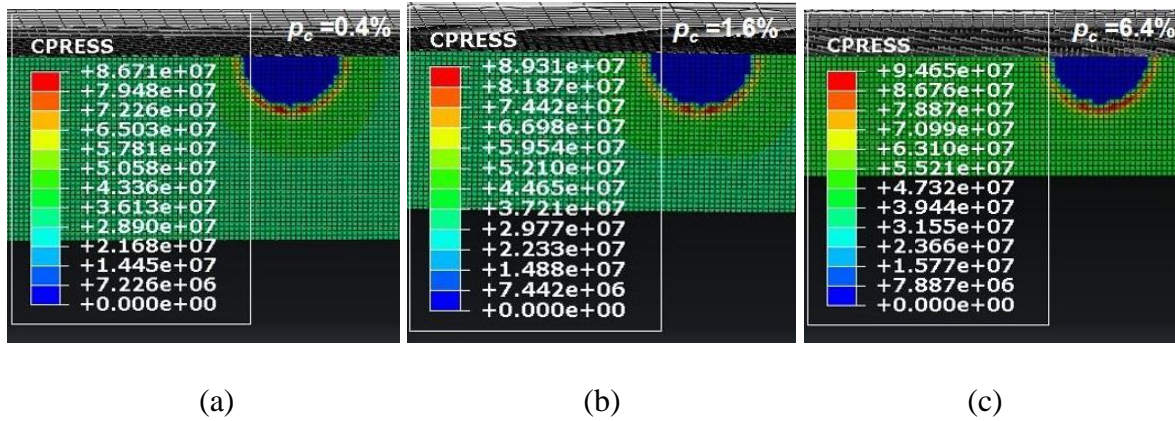


Figure 86. Stress distribution in the cross-sections of PTFE composite sliding against steel counterface with medium coverage (1.6%) of (a) Type A (wide & deep) dimples, (b) Type B (narrow & shallow) dimples and (c) Type C (wide & shallow) dimples under normal pressure 40MPa from the top and sliding velocity 0.12 m/s

### - Influence of texture coverages

Furthermore, higher the dimple coverage was, higher the elevated pressure and stress concentration were near the edges of the micro-cavities. In the example presented in **Figure 87**, for the Type B dimples (narrow & shallow), in medium ( $p_c = 6.4\%$ ) and high coverage ( $p_c = 1.6\%$ ), the maximum stress was correspondingly 2.6 and 5.99 MPa higher than 86.71MPa with low coverage ( $p_c = 0.4\%$ ).



**Figure 87.** Bottom view of the PTFE composite for the pressure distribution on the surface sliding against steel surface with narrow & shallow dimples in (a) low coverage (0.4%), (b) medium coverage (1.6%) and (c) high coverage (6.4%) under normal pressure 40MPa from the top

Correspondingly, the stress distribution presented in **Figure 88** demonstrated that the maximum contact stress in medium ( $p_c = 6.4\%$ ) and high coverage ( $p_c = 1.6\%$ ) were correspondingly 1.49 and 5.68 MPa higher than the 95.03 MPa with low coverage ( $p_c = 0.4\%$ ).

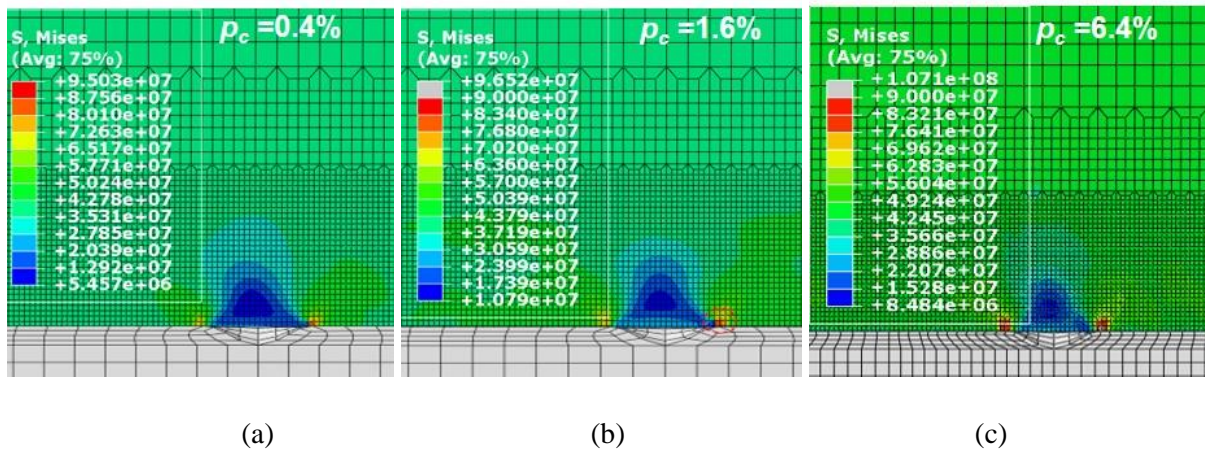


**Figure 88.** Stress distribution in the cross-sections of PTFE composite sliding against steel surface with narrow & shallow dimples in (a) low coverage (0.4%), (b) medium coverage (1.6%) and (c) high coverage (6.4%) under normal pressure 40MPa from the top and sliding velocity 0.12 m/s

With the results for all the tested surfaces summarised, it is proposed to relate these data with the observations in the tests to establish the criterion for estimating the micro-abrasion on the composite incurred by counterface textures. It should be noted that even though each obtained stress condition is only a transient result, since a relatively stable state has been reached, these outcomes can still give an overall representation of the condition.

At first, naturally, the proposition is to use the strength of the material as the estimation criteria, and micro-abrasion should be the result of the stress exceeding the strength of a constitutive component. With this principle, if the yield strength  $\sigma_y$  of the formulated section is adopted directly as the failing criteria, it seems to fail to give a useful indication, as under all conditions

the maximum stress has exceeded the yield strength  $\sigma_y$  like demonstrated in **Figure 90** (a). The main issue for this approach is that, considering the wear under the sliding contact as a form of material failure under multi-axis loading (i.e. compressing and frictional shearing), using the strength of the material acquired from single-axis testing (e.g. compressive / flexural strength) would be insufficient.

However, the stress under the critical condition (under *LPV*) with realistic multi-axis loading should be more representative. With this considered, the maximum stress under ‘real *LPV*’, as has been acquired in **Table 10** (section 4.5.1) is then proposed as the new criterion. As shown in **Figure 90** (a), the maximum stress under *LPV* ( $\sigma_{LPV}$ , obtained in section 4.5.1) may be effective, as those points above the  $\sigma_{LPV}$  line all correspond to those experiencing significant micro-abrasion during the tests. Nonetheless, it may miss some point, like the high coverage ( $p_c = 1.6\%$ ) of Type B dimples (narrow & shallow), which witnessed apparent micro-abrasion but still fall under the limit. Consequently, as shown in **Figure 90** (b), an over-optimistic estimation may be resultant for the ratio of failing elements indicated by this standard ( $r_{\sigma > \sigma_{LPV}}$ ), particularly for the point of high coverage ( $p_c = 1.6\%$ ) of Type B dimples (narrow & shallow). In other words, the value of the critical stress is overestimated.

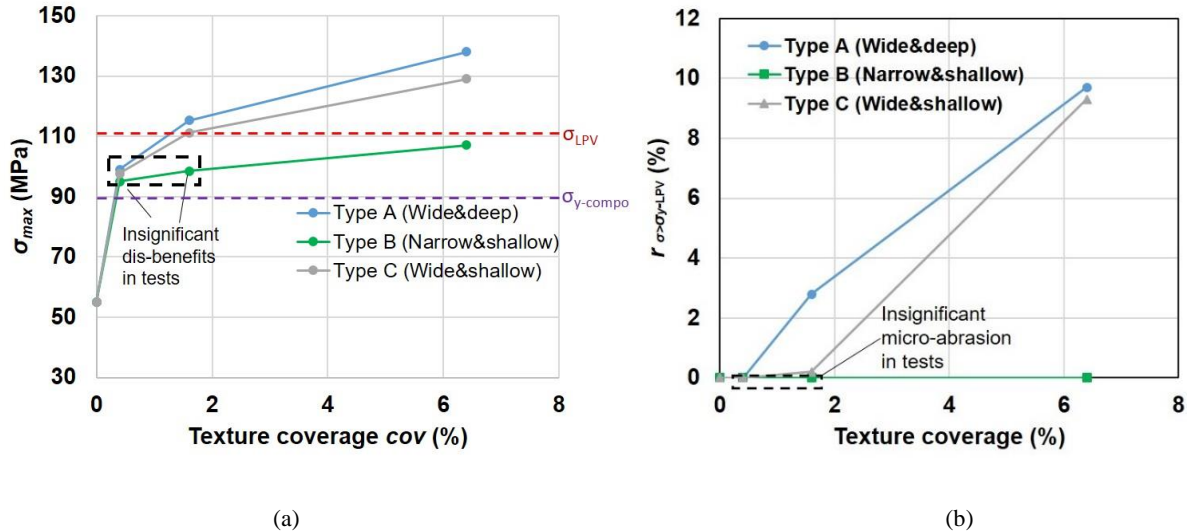


**Figure 89.** (a) Maximum stress and (b) percentage of surface elements exceeding  $\sigma_{LPV}$  on the composite surface against different textured counterface computed from the FE model under the same loading condition with the wear tests

A possible explanation for the insufficiency in using  $\sigma_{LPV}$  is that only stress is considered as the cause for accelerated failure and wear, while in fact the wear of polymer can be a complex phenomenon involving more factors such as the thermal effects (e.g. polymer softening and melting). This is also a limitation of the model as the thermal analysis has not been integrated. Considering that pressure  $P$  is related with the input of the contact, including both the

mechanical and thermal (frictional heating) aspects, other than stress  $\sigma$ , which only represents the mechanical response, it is proposed to use the real contact pressure under  $LPV$  as the improved critical criterion. As shown in **Figure 90**, with the implemented line of pressure ( $P_{LPV}$ ) corresponding to  $LPV$  (also computed in **Table 10**), not only those witnessed heavy micro-abrasion can be identified as above the line, but those saw minimal detrimental effect are separated as below this critical value. Therefore, the ‘real  $LPV$ ’ (in this condition equivalent to real pressure as the velocity was kept the same) is more effective than  $\sigma_{LPV}$  in indicating the occurrence of micro-abrasion. In other words, it is the better index for instructing the texture pattern to avoid micro-abrasion. Using this method, even though without explicitly modelling the thermal effects under frictional heating, a guidance based on  $LPV$  will be established.

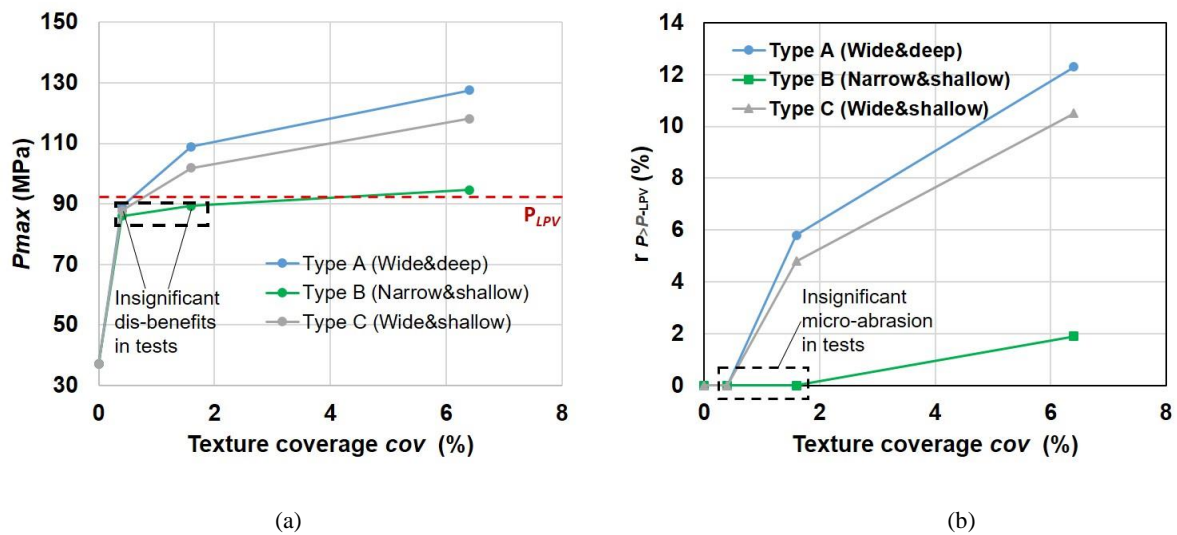


**Figure 90.** (a) Maximum contact pressure and (b) percentage of surface elements exceeding  $P_{LPV}$  on the composite surface against different textured counterface computed from the FE model under the same loading condition with the wear tests

Overall, through the whole analysis of contact mechanics, it can be seen two major phenomenon influences the identification of the real contact pressure: the pressure-relieving by the stiffeners/hard-fillers in the composite, and the stress concentration with surface textures. Therefore, when employing the  $LPV$  for instructing the texturing dimensions, considerations should be given to both phenomenon, so that ‘real  $LPV$ ’ can be obtained and utilized as a more comprehensive criterion for micro-abrasion, instead of simply using the nominal contact pressure.

## 4.6 Conclusions

This chapter reports on the understanding of the transfer film formation of dry lubricant with the presence of hard reinforcing fibres, and the micro-abrasion effect with textured counterface.

With the obtained knowledge, the phenomena governing the composite's frictional and wear performance sliding against textured counterface have been discovered, relating with the different wear mechanisms experienced with dimples in varied coverages and dimensions.

The main contributions findings and made in this chapter are:

*A comprehensive investigation on the transfer film characterisation in the self-lubricated contact was conducted, addressing the possible issues with previous methods. Aiming at solving the issues, a novel transfer film characterising technique was developed, based on multi-voltage SEM analysis, and calibration with SIMS analysis. In this investigation, the following points were found:*

- It was observed that due to the introduction of hard-stiffeners in polymer composite, abrasion tracks can occur on the counterface under dry-lubricated condition. This phenomenon can increase difficulty in characterising the transfer film on the counterface. The related issues on transfer film characterisation were addressed systematically for the first time, pointing out that previous methods applied in ideal condition may be insufficient in such real engineering contact.
- Through analysing the transfer film by layers with SEM in different accelerating voltages (with Tof-SIMS as an assisting technique), transfer film's dimensional properties is established
- two forms of transfer film can coexist on the steel counterface: the ultra-thin film (nano-meter degree) and the thicker transfer layer (micro-meter degree).

*The first systematic test series to investigate the influence of counterface textures on the tribological performance of dry-lubricated contact. Together with the assistance of the surface analysis method, the tests generate the following knowledge:*

- The dry-lubricated contact is very sensitive with the texture (circular concavities) coverages and dimensions. Under the test condition (typical in helicopter application), just a texture coverage higher than 10% of or diameter larger than 40 $\mu$ m would lead to rapid failure of the composite compared with when the counterface is smooth. However, these parameters would already lead to load index (*PV* factor) well under the threshold (*LPV*).
- The surface texturing may benefit the formation of the thicker form of transfer film, and the key is to constrain the dimple depth (*dep*) within the magnitude of the film thickness (2~3  $\mu$ m).

Moreover, there is an even narrower window of the dimple diameters and densities ( $d \leq 20 \mu\text{m}$ ,  $p_c \leq 1.6\%$  for the tested condition) for the effect to be achieved without incurring significant micro-abrasion, while the direct application of nominal contact pressure and *LPV* criterion may greatly overestimate this range.

*A contact mechanics model was developed to give theoretical explanation for the occurrence of micro-abrasion, and why direct application of nominal contact pressure/PV factor would fail to estimate the 'feasible range' for counterface textures. Through the simulation and analysis, it was found that:*

- Two phenomena would incur the difference in real contact pressure: the pressure-relieving by the stiffeners/hard-fillers in the composite, which is determined by the variation of mechanical properties of the composite components, and the pressure elevation induced by surface textures, which is determined by the dimple diameter and coverage. Therefore, the increase in real contact pressure may be highly non-linear, and thus requiring case-to-case consideration when employed to instruct texture design.
- Corresponding to the point above, it was found that the 'real stress' or 'real *PV*' (more comprehensive) on the polymer parts of the composite would serve as more realistic indexes for predicting the extent of micro-abrasion with textured counterface. Similarly, the threshold value should correspond to the 'real *LPV*' for the polymer parts.

Overall, two most important findings: consistency between texture depth and transfer film thickness should be kept for film reservation, and 'real *PV*' criterion should be used for avoiding micro-abrasion from the principles in surface texture design for tribological performance improvement in the self-lubricating bearings.

There are, however, limitations in the studies. For example, the approach of extracting the polymer section for simplified analysis may only be compatible the woven fabric of composite, since in other kinds the distribution of constitutive components may not be so well divided (by blocks). Moreover, the FE analysis has not included an explicit description of the thermal field, but only consideration of thermal effects using the *PV* indicator. With this said, the formulated methodology and knowledge can still give instructions for the designing of counterface textures in dry-lubricated condition, and the findings illustrated above can contribute to an advancement

in understanding of the physical phenomenon (e.g. transfer film formation, real contact pressure and stress) in this field.

## **Chapter 5**

### **The effect of surface texturing on the anisotropy of the tribological performance**

#### **5.1 Introduction**

As has been pointed out, the experimental study using pin-on-plate test scheme focused on applications with single-axis rotation like the tail-rotor bearings and some specific working conditions, and the composite liner is always aligned in a fixed orientation ( $45^\circ$  to the reciprocating line- a conservative balancing choice by the bearing manufacturer). However, as the composite is a heterogeneous material, it may possess anisotropic performance and may have optimal orientations. Moreover, in some occasions more complex kinematics would occur. As a typical example, the pitch-control-bearings in the main rotor-head need to perform multi-axis rotation accordingly to adjust the pitch angle of the blade. Normally to simulate the multi-direction sliding of a composite surface, the coupon test approaches include using pin-on-disk set-up (constant-speed rotation), circularly translating pin-on-disk (CTPOD) and introducing a self-spinning on the composite pin sample. However, the key in establishing the test method is whether it can reflect the kinematics in real operating conditions.

Given the criticality in interpreting the kinematics and reflect it in the experimental studies, the model to describe the motions of pitch-control bearings in helicopter rotor-heads needs to be updated, as the commonly-used ones are often rather empirical and not associated with the kinematics of the system. In this chapter it is proposed the kinematics of the pitch-control-bearings should be modelled with a strategy emphasizing the relationship with the real operation conditions, thus giving guidance for the experimental study of the anisotropic issue.

If the counterface is textured, the contact-pair may become one in which both components have heterogeneity (one in material composition and one in surface topography), so anisotropy of the contact system may be further influenced. To evaluate the effects of surface texturing in this aspect, the tests with textured counterface and related analysis are also conducted in this chapter.

## **5.2 Analysis of the kinematics of the pitch-control-bearings in helicopter main rotor**

### **5.2.1 Proposed modelling principle for the kinematics - output-oriented strategy**

Normally, a model to describe the kinematics of a mechanism can be categorized as either deterministic or stochastic, based on whether the output from the model with a certain input will be fixed or with randomness. However, in this study it is proposed that for the analysis of kinematic of sliding contact components, the model should be classified as input-determined and output-oriented based on the characteristics of the mechanism and the nature of the operation. The rationale for the modelling approaches is discussed here.

In many mechanical systems, the mechanical constraints would decisively lead to an exclusive sliding path. The journal bearing and the piston-cylinder assembly are typical examples, as the shaft would only follow the circular path conformal with the inner circumference of the bearing and the piston would only slide along the central axis of the cylinder like shown in **Figure 91**. Due to the simple pattern of sliding path (along one straight line or circle), in these two instances, the issue with the occurrence of an anisotropic surface comes down to whether the aligned surface orientation would provide sufficient tribological performance. In addition, piston-cylinder movement contains reciprocating, thus needing consideration in the non-centrosymmetric tribological behaviour of the surface, namely that the friction and wear may alter sliding forward and backward (i.e. 180° change in orientation). Naturally, this special type of anisotropy originates from the non-centrosymmetric distribution of constitutive material (e.g. random-woven composite), and non-centrosymmetric micro-structure (e.g. three-fold symmetric aluminium crystals [212]) or surface topography (e.g. video tape-head contact with interlocking skewing asperities [213]).

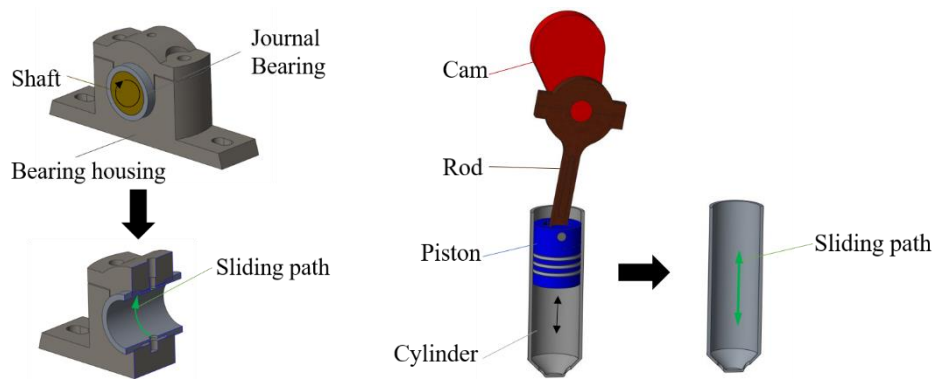


**Figure 91.** The schematic illustration of the operation and the sliding path of (a) a journal bearing and (b) a piston-cylinder assembly

Apart from those with rigid mechanical restraints, the sliding within some system with less strict geometrically directing can also be input-determined. In a milling process, for instance, no mechanical restriction is applied to hinder the sliding of the milling tool on the work-piece-surface. However, in working condition, the relative motion between the two surfaces is essentially the combination of the linear translating motion and the simultaneous self-rotating of the tool. Consequently, the resultant sliding path of points on the tool surface is a sinusoidal curve, varying with the ratio between the translating speed and the rotating speed of the tool [82]. Therefore, in real scenarios, the trajectories of contact points are conclusively determined by the operating rule and parameters set in prior. Therefore, the input-determined model would still apply well on this sliding motion. However, different from the two former examples, in this case the tribological performance is a reflection of all the sliding orientations combined.

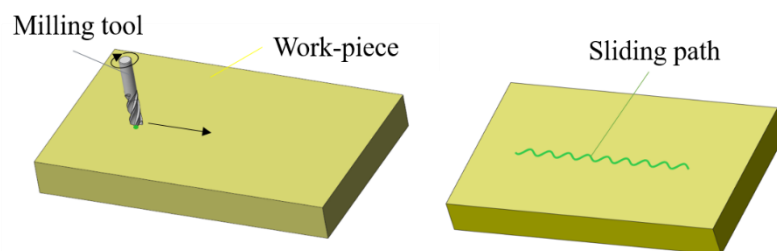


**Figure 92.** The motions involved in the milling process and the resultant sliding path of a point on the milling tool surface

Contrary to the examples stated above, in some systems containing sliding components, neither will the mechanical restrictions lead to an exclusive sliding path, nor should inputting operating parameters be the resources of defining sliding pattern. Instead, the variation of the output of the system would determinatively influence the sliding path, and the derivation of the model should therefore emerge from this perspective.

A representative example for the output-oriented cases is the prosthesis joint. Prosthesis joints are essentially socket-ball joints used in Total Hip Replacement (THR) or Total Knee Replacement (TKR). Due to the conformal spherical contact, universal rotation is enabled. Therefore, with the increasing use of polymer composites such as those of Ultra-high molecular weight polyethylene (UHMWPE) in the artificial joints, the attention on the anisotropic performance arises.

In the early laboratory studies (from late 1990s) on the effects of alteration in sliding direction (or surface orientation) within prosthetic joints, an extra motor was added to rotate the composite pin in the pin-on-plate (linear reciprocating) set-up to enforce a constant changing of orientation [83,85,214]. Using similar ideology, more approaches were developed to include the orientation change in standard coupon tests, including modifying the conventional pin-on-disk set-up into a circularly translating pin-on-disk (CTPOD) [84], and introducing an additional spinning and inclining on the ball sample in ball-on-disk tests[215]. However, in the authors' view, although these methods do facilitate the variation of sliding direction, yet with the whole-cycle rotation applied on the pin/ball, particularly with the constant rotation speed set in these examples, the resultant sliding angles (or surface orientation angle) would eventually have a uniform distribution from 0 to 360°. Such an outcome would contradict with the real output of the application – in human hip and knees the movements would have limitations, as well as a normal operation range during most of the daily activities. In fact, as early as 1970s, studies have pointed out the limits and frequent prosthetic ranges of motion[216,217]. In a word, these direct manipulations on surface orientation fail to recognize the realistic outputs.

The international standards, however, started addressing this issue from 2002. In test instructions for both hip joints (ISO 14242:1) and knee joints (ISO 14243:1), it is required that wear tests of a prosthesis joint should be conducted on multi-degree-of-freedom wear simulators before clinical use, and that the motion simulated should mimic that of joints in human gaits, like shown in **Figure 93(a)**. The modelled kinematics involve evolution of displacement in anterior-posterior (AP) direction and angles in abduction–adduction (AA) internal-external (IE) angle and flexion–extension (FE) rotation, like shown in **Figure 93(b)** and (c). It has been proved that using a more realistic representation of these output variables, not only would the predicted wear rate be more accurate, but the wear contour and depth would also be closer to reality [218].

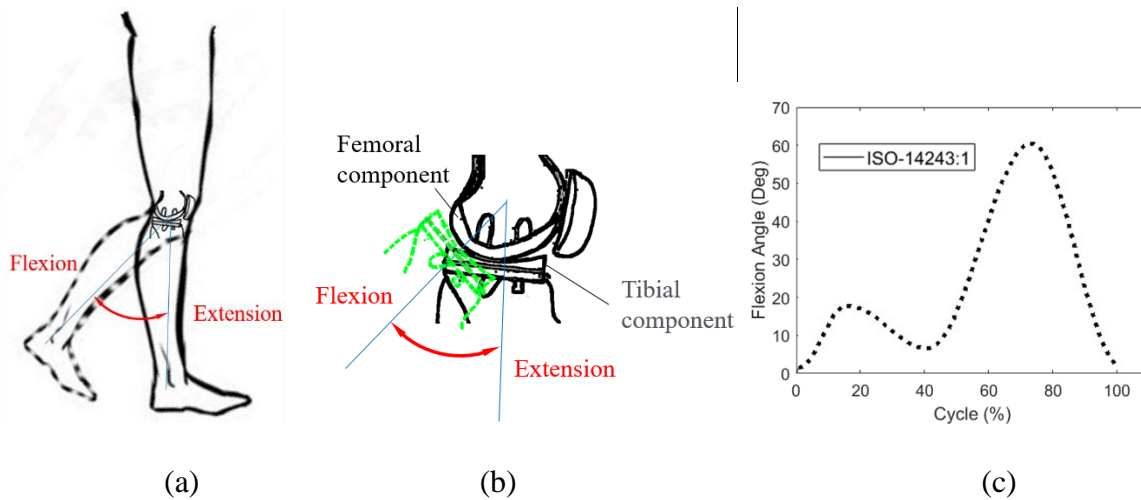


**Figure 93.** (a) Flexion-extension of a normal human gait, (b) Corresponding flexion angle range in the prosthesis joint and (c) the evolution of the flexion angle range in the prosthesis joint [218]

To summarise, for systems like prosthesis joints, where the freedom for sliding direction is still left within the mechanism, but clearly the requirement of the output (human postures and gaits) needs to be fulfilled, the kinematics should be derived from the output to establish a comprehensive model.

In this thesis, like prosthesis joints, the pitch-control-bearing (spherical plain bearing) for the helicopter main rotor-head should fall into the output-oriented catalogue. Meanwhile, misconceptions still exist in its kinematic model. Therefore, it is proposed that an analysis of the kinematics should be conducted following the output-oriented principle, thus guiding the investigation of anisotropy in friction and wear.

## 5.2.2 The kinematic model of helicopter pitch-control-bearings

### - Mechanism of pitch-control-bearings in a helicopter rotorhead

In a helicopter rotorhead, the pitch-angle of the blades need to be controlled to accommodate different operation demands. This is fulfilled by adjusting the extensions of different control rods (linked to the control-stick in cockpit) and consequently the position and posture of the swashplate assembly, which is composed of the swashplate bearing, the lower (stationary) swashplate and the upper (rotating) swashplate.

Since spherical plain bearings (with self-lubricating composite liner) are equipped on both ends of the pitch-control-rod, free rotation can be facilitated between the swashplate and pitch-control-rod (and between pitch-control-rod and blade-pitch-horn) as shown in **Figure 94**. Therefore, the movement of the swashplate, be it up-down-translation (for ‘collective control’) or self-tilting (for ‘cyclic control’), can be translated into evenly altering or flapping of pitch-

angles through pitch-control-rod (also referred as con-rod). In a word, the sliding within the pitch-control-bearings is an intermediate motion to link the output of pitch-angles with the controlling of swashplate.

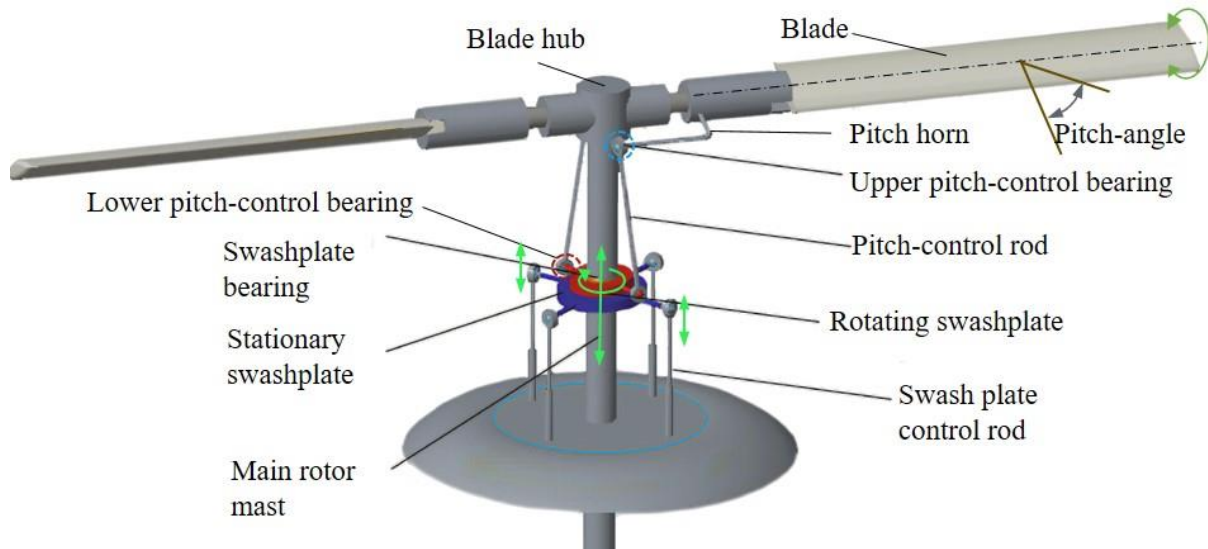


*Figure 94. CAD model of a helicopter main rotor (rigid-type) assembly*

Despite the connection between the sliding condition and the output, it seems that the models currently used in both industrial and academic studies fail to address this. Coupon tests on the bearing liner material include the circular rotation motion utilizing the pin/ring on disc set-up[44,219] would lead to the same misconception experienced in the prosthesis research: the orientation angle would go through 0-360° evenly during the sliding process. In the international standards for the tests of self-lubricating spherical plain bearings (e.g. AS81819 and AS81820 published by SAE International), simply one-axis rotation is required. The best effort to correlate with reality may be the development of multi-axis rotation simulators [43,220,221], but the motions applied is still based on an empirical model of two axis-rotation: swivelling and tilting (e.g. swivelling  $\pm 8^\circ$  and tilting  $\pm 8^\circ$  in [221]), like shown in **Figure 95**. The resultant sliding path is a spherical ellipse (or a circle when swivelling limits equal tilting limits) as modelled in **Figure 96(a)**, indicating a sliding angle distribution symmetrical at 90° as illustrated in **Figure 96(c)**, with the deviation depending on the ratio between the swivelling range and tilting range.

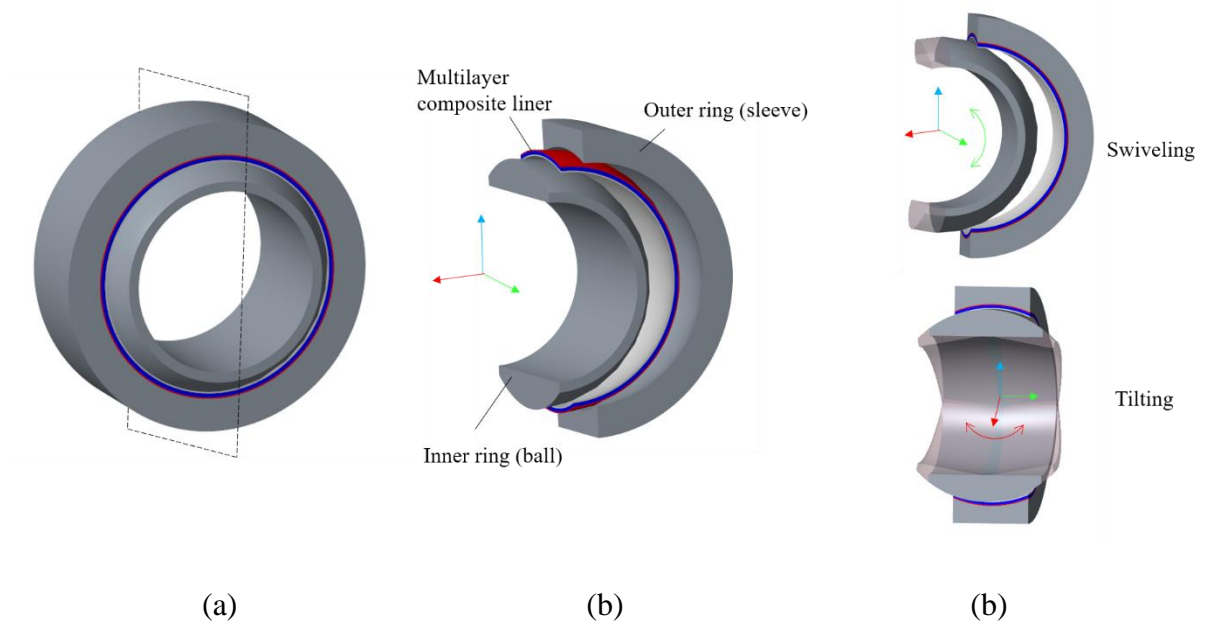


**Figure 95.** (a) The configuration of a dry-lubricated spherical plain bearing used in helicopter rotorhead and (b) the cut section view; (c) illustration of the swivelling and tilting motion of the bearing

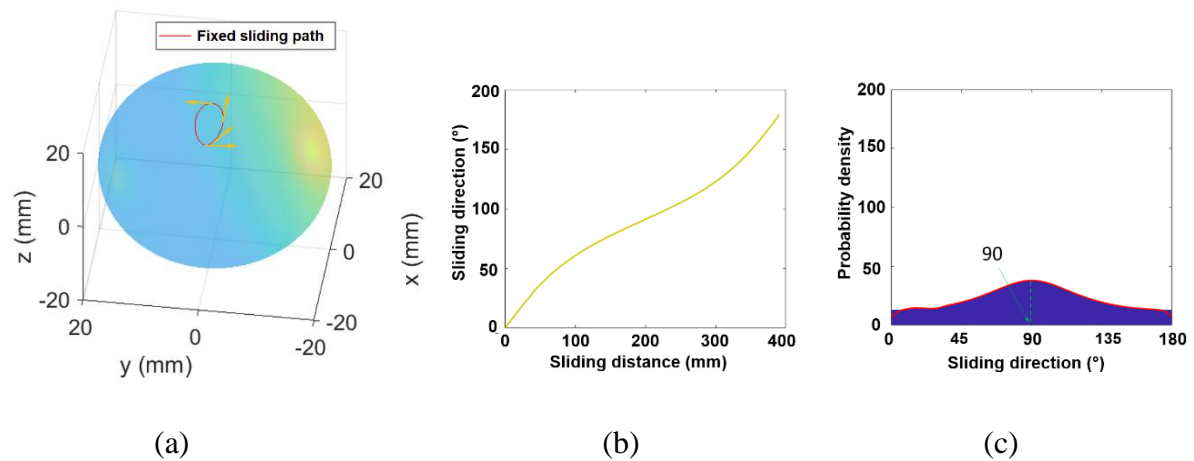


**Figure 96.** (a) The theoretical sliding path according to the empirical swivelling and tilting model, (b) the sliding angle experienced during a rotation cycle and (c) the probability density distribution of sliding angle experienced during the sliding process

In all these kinematic models of spherical bearing, the defining of the motion is empirical. More importantly, it is neither related to the kinematics of the mechanism in which the bearing is implemented, nor the realistic variation of system output (pitch-angle) that indicates the working condition. To improve this, the output-oriented model with consideration of the kinematics of the entire helicopter rotor system was derived as following.

**- Derivation and application of the output-oriented kinematic model**

At first, since a realistic reflection of the output is of crucial importance, a series of data in pitch-angle has been acquired by SKF Ltd through recording on an in-service helicopter using

angle-sensors over a long period of duty. Sorted in accordance with different operations (e.g. take-off, cruising, spot turn etc.), the static angle ( $\theta_0$ ) and dynamic angle ( $\Delta \theta_0$ ), together with the number of hours experienced for each condition have been collected.

Then, in order to produce a simplified yet representative geometric model of rotorhead, the mechanical configurations (as shown in **Figure 94**) are transformed into a model with representative basic geometric entities. For example, all the bar-shape linking components are simplified as its straight line axis (e.g. the pitch-control-rod is represented by the line AB) and the centres of the rotation mechanism are represented as points (e.g. point A stands for the centre of the pitch-control-bearing).

Apart from a global coordinate set at the centre of the swashplate bearing (at point O), a local coordinate system XYZ is also set at the centre of the pitch-control bearing (at point A), considering that the goal of the model is analysing the interfacial sliding within the bearing. By setting the X axis coinciding with  $\overline{OA}$  (radius vector from the swashplate centre to the bearing centre), and XY plane parallel with plane  $A_0OY_0$  (the upper-swashplate plane), the direction angles of the vector  $\overline{AB}$ , namely  $\varphi$  - its angle with the X axis, and  $\varepsilon$  - the angle between its projection on Z'OP plane and the Z axis can determine the position of a contact point on the bearing sleeve relative to the bearing bush.

In the annotated sketch of the system and the quadrilateral  $OABO_1$ , namely **Figure 97**(b) and (c), the variation of pitch-angle  $\theta_l$  goes along with changing in  $l_0$  - the distance between O (centre of swashplate) and O' the (centre of blade hub), and  $\alpha$  - the  $\angle A_0OA_0'$  (tilting angle of the swashplate). Given a fixed set of the two variables characterising the swashplate, the angle  $\delta$  ( $\angle A_0OA$ , marking the rotation of the pitch-control bearing from its initial position) is the tracking mark for the variation of other geometric variables.

Therefore, the model needs to solve the tracking of direction angles  $\varphi$  and  $\varepsilon$  through rotation cycles ( $\delta$  from 0 to  $360^\circ$ ), when swashplate position and posture parameters  $l_0$  and  $\alpha$  are controlled so that, the designated pitch-angle ( $\theta_0 \pm \Delta \theta_0$ ) can be output to achieve desired aerodynamics in different working conditions. Expressed mathematically, with known variables  $\theta_0$ ,  $\Delta \theta_0$  and  $\delta$ , the unknowns  $\varphi$ ,  $\varepsilon$ ,  $l_0$  and  $\alpha$  need to be solved under this mechanism.

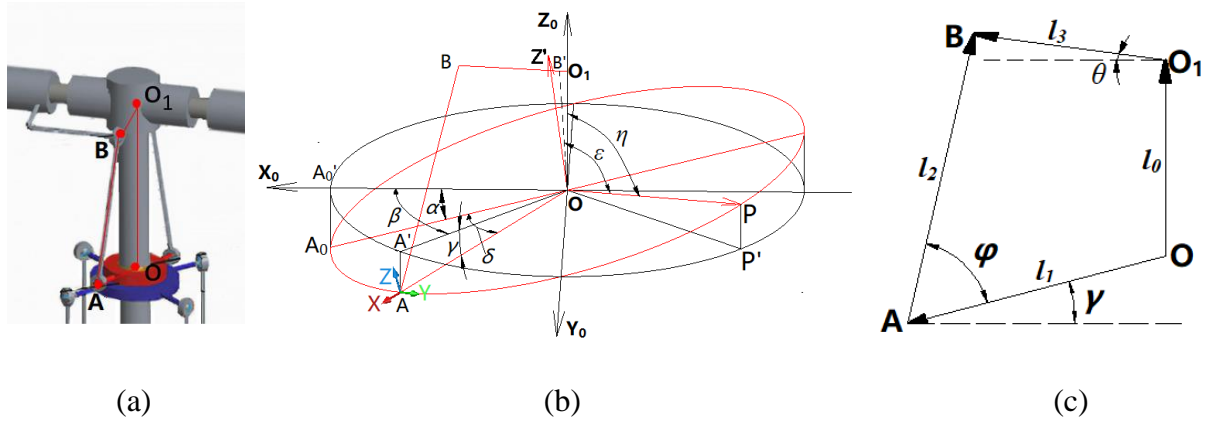


**Figure 97.** (a) Rotorhead model with rotating points annotated, (b) Simplified geometric model of the swash plate-conrod-bearing assembly and (c) the quadrilateral  $OABO_1$  representing the swashplate-conrod-horn-mast assembly

Apart from the CAD model, the mathematical representation (for the kinematics of the helicopter rotorhead) of the kinematics was also developed to facilitate an easier adjusting of the geometrical parameters (as this can be done with only changing the variable values in the computer program). Moreover, the credibility of the model can be tested by comparing the two methods. To establish the mathematical representation of mechanism, firstly, the unknown variable  $\varphi$  needs to be linked with the output - pitch-angle  $\theta_1$ . In the quadrilateral  $OABO_1$ , as shown in **Figure 97** (c), the following geometric relationship is found:

$$\left( \frac{\cos \gamma}{\sin(\varphi + \gamma)} - \frac{l_2}{l_1} \right) \cdot \sin(\varphi + \gamma + \theta) = \left( \cos \gamma \cdot \tan(\varphi + \gamma) - \frac{l_0}{l_1} - \sin \gamma \right) \cdot \cos(\theta) \quad (5.1)$$

where  $\gamma$  denotes the tilting angle of the swashplate ( $\angle AOA'$ ) at point A as demonstrated in **Figure 97** (b). Together with  $l_0$ , they denote the controlling parameter of the swashplate in respectively 'cyclic' and 'collective' position as has been described above.

Because when the pitch-control-bearing (with centre A) is at two extreme positions ( $A_0$  and  $A_1$ ) as in **Figure 97**,  $\theta_1$  has its maximum and the minimum value, two set of conditions can be applied on equation 5.1:

$$\theta_1 = \theta_0 + \Delta \theta_0, \text{ when } \gamma = \alpha$$

$$\theta_1 = \theta_0 - \Delta \theta_0, \text{ when } \gamma = -\alpha$$

Applying these two causes in equation 5.1, two governing equations can be obtained describing the association between the output ( $\theta_1$ ) and the three unknowns ( $\varphi, l_0, \alpha$ ) to solve.

Then, to define the kinematic constraint equation for the mechanism, the fixed length  $l_3$  of  $\overline{O_1B}$  is utilized:

$$\overline{O_1B}^T \overline{O_1B} = l_3^2 \quad (5.2)$$

Intrinsically,  $\overline{O_1B}$  can be expressed as follows:

$$\overline{O_1B} = \overline{OA} + \overline{AB} - \overline{OO_1} \quad (5.3)$$

while the three vectors on the right hand side can be represented by the angle:

$$\overline{OO_1} = l_0 \cdot C_0 \quad (5.4)$$

$$\overline{OA} = l_1 \cdot C_1 \quad (5.5)$$

$$\overline{OB} = l_2 \cdot C_2 \quad (5.6)$$

where  $c_0$ ,  $c_1$  and  $c_2$  are the direction vectors which can be explicitly expressed by the direction angles:

$$C_0 = [0,0,1]^T \quad (5.7)$$

$$C_1 = [\cos \gamma \cdot \cos \alpha, \cos \gamma \cdot \sin \alpha, \sin \gamma]^T \quad (5.8)$$

$$C_2 = [\cos(\varphi + \gamma) \cdot \cos \alpha, \cos(\varphi + \gamma) \cdot \sin \alpha, \sin \gamma]^T \quad (5.9)$$

After substituting  $\overline{O_1B}$  into equation 5.2 using equation 5.3 to 5.9, even though a new governing equation 5.2 emerges to describe the relationship between direction angle  $\varphi$  and other unknowns, the number of unknowns (four:  $\varphi$ ,  $\alpha$ ,  $\gamma$ ,  $l_0$ ) still exceeds that of governing equations as  $\gamma$  becomes a new unknown.

Therefore, to relate  $\gamma$  with the known variables, another intermediate variable  $\beta$  (denoting the angle  $\angle AOA_0$  as in **Figure 97**) is introduced. Based on the geometric relationship that the project of angle  $\angle AOA'$  on the  $XOZO$  plane is angle  $\angle A_0OA'_0$ , the following two supplemental equations can be derived:

$$\cos(\delta) = \cos(\gamma) \cdot \cos(\beta) / \cos(\alpha) \quad (5.10)$$

$$\cos^2(\gamma) = \cos^2(\alpha) / (\cos^2(\beta) + \cos^2(\alpha) \cdot \sin^2(\beta)) \quad (5.11)$$

Consequently, they governing equation group become five equations with five unknowns ( $\varphi$ ,  $l_0$ ,  $\alpha$ ,  $\beta$ ,  $\gamma$ ), and therefore can be solved analytically.

For the direction angle  $\varepsilon$ ,  $\overline{AB}$  (vector for pitch-control-link) is project on  $Z'OP$  plane (parallel with the  $ZAY$  plane in local coordinate) to generate an equivalent angle  $\angle B'OP$ . As  $\angle Z'OZ$  equals to the angle  $\gamma$ , a relationship can be derived with  $\varepsilon$  and an intermediate variable  $\eta$  ( $\angle Z_0OP$ ):

$$\cos\varepsilon = \cos\eta/\cos\gamma \quad (5.12)$$

To relate the intermediate variable  $\eta$  with the knowns, because the point P is what the centre of the ball (point A) rotates 90 degrees along the swashplate circumference, the following connection can be found:

$$\cos\eta = \sin\delta \cdot \sin\alpha \quad (5.13)$$

Therefore, since  $\delta$  and  $\gamma$  have been solved in the last step, solutions for  $\varepsilon$  and  $\eta$  can be found using governing equation 5.12 and 5.13. The computation of the two direction angles  $\varphi$  and  $\varepsilon$  is then conducted using software MATLAB 2018a.

To evaluate the validity of the mathematic model, the computed sliding path was compared with the one tracked in the CAD model (using Mechanism-Measures module in CREO) for different operation conditions. From an example of the sliding path under a cyclic pitch control (**Figure 98**), it can be seen that the computed path matches well with the actual sliding path recorded from the CAD model. In fact, the errors between the computed coordinates and the recorded ones are calculated 0 for all points tracked, meaning that the computation error is smaller than the machine precision ( $2^{-53}$  for MATLAB 64-bit version). Such a high precision is achieved as this is an analytical solution of a deterministic model.

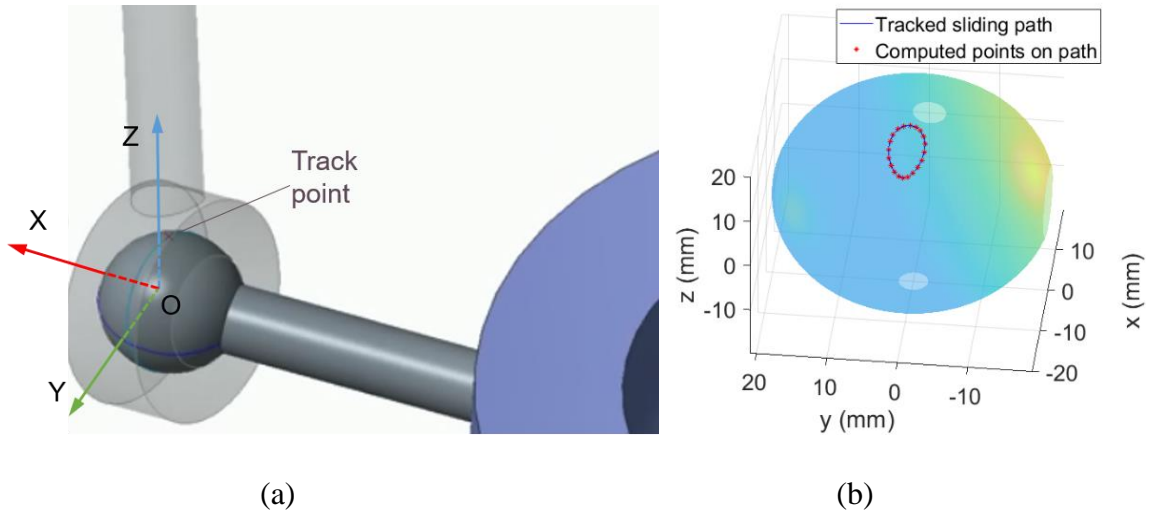


**Figure 98.** (a) The coordinate system and track point set in the CAD model (b) Comparison between the computed points (mathematical model) and the tracked sliding path (CAD model)

Till this step, in fact a deterministic model of the rotorhead mechanism with the capability to predict the sliding path within pitch-control bearings has been established. To investigate the variation of sliding direction, the sliding path in different operation conditions are computed, oriented from the pitch-angle data collected. The slopes of the tangent at discrete points with

small intervals ( $\Delta\delta = 0.1^\circ$ ) were also acquired along these curves, forming the probability density graphs of sliding angles, like demonstrated in **Figure 99**(d) to (f).

Through comparing different operation conditions, two main features of the sliding path curves need to be pointed out:

- a. In condition where pitch-angle is relatively low and stable (e.g. in cursing), the aspect ratio of the area closed by the curve is large, as shown in **Figure 99**(a), thus leading to the sliding close to linear-reciprocating. With operations require higher pitch-angle (e.g. spot turn **Figure 99**(b)), the area span of the curve is larger and the aspect ratio is close to 1 (closer to a circle), so the sliding is experiencing a wide span of alteration in direction during each cycle. However, in condition where pitch-angle is relatively low and stable (e.g. cursing in ), the aspect ratio of the area is larger, thus leading to the sliding close to a linear reciprocating movement.
- b. The transcendental spherical curve can be non-centrosymmetric. This behaviour can be observed in the cruising state, as well in other occasions where static angle is big and dynamic angle is moderate (e.g. landing/take-off as in **Figure 99**(c)). As a result, the spectrum of the sliding orientation in this situation has a skewness off  $90^\circ$ , like shown in **Figure 99**(d) and (f). This differs with the empirical expression, in which the  $\pm 5^\circ$  tilting angle would lead to a symmetrical distribution of sliding orientation, as demonstrated in **Figure 96**(c).

Through these observations, it can be seen that the sliding path is a closed curve without a fixed morphology. Moreover, by its nature, this sliding path is a curve tracing the footprint of a point moving continuously on a spherical surface with a set mechanism, with its defining equations containing more than algebraic functions. Therefore, the sliding path is a closed transcendental spherical curve[222].

After collecting the spectrums of sliding angles in all the working conditions, a weighted overall estimation of the probability density distribution is also generated, as shown in **Figure 99**(g) using the proportions of time duration for varied operation conditions as the weighted ratios. It can be seen that the overall spectrum is close to that of cruising and take/off, having an apparent peak slightly off  $90^\circ$  (at around  $85^\circ$ ). This is because cruising, as well as some other working conditions with similar output (e.g. steady state hovering) occupies the majority of the flight time while operations like spot turn occurs rarely (around 1% for spot turn).

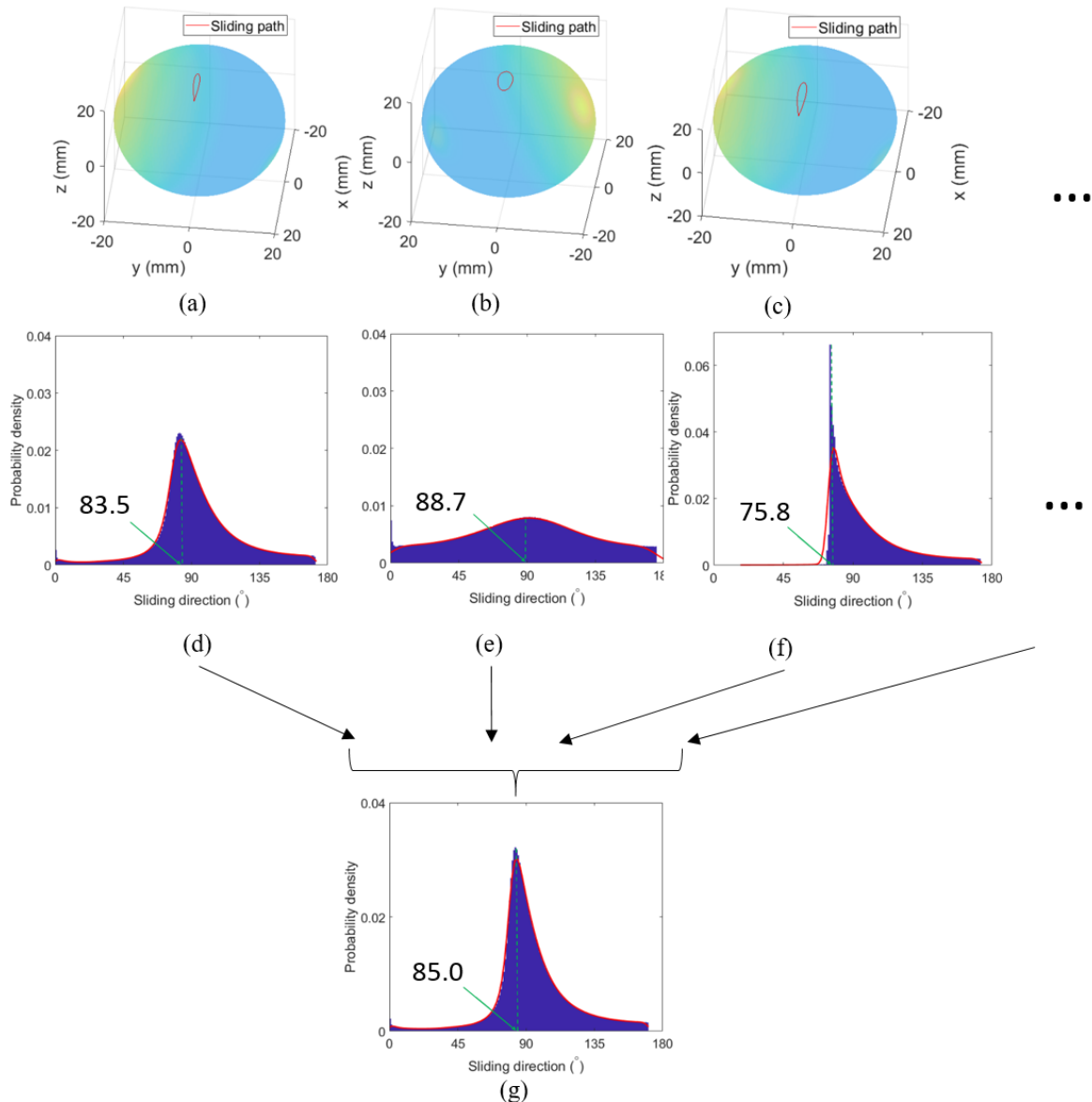


**Figure 99.** Curves of the sliding path on the sphere under (a) cruising state ( $\theta_0 = 4.73^\circ, \Delta\theta_0 = 1.66^\circ$ ), (b) spot turn with maximum gust ( $\theta_0 = 11.8^\circ, \Delta\theta_0 = 4.23^\circ$ ) and (c) landing/take-off ( $\theta_0 = 6.36^\circ, \Delta\theta_0 = 0.28^\circ$ ); Distribution graph of sliding angle in (d) cruising state, (e) spot turn with maximum gust, (f) landing/take-off and (g) overall weighted estimation

From the derivation of this output-oriented kinematic model, it can be seen that an output-oriented model should not be restricted as solely deterministic or stochastic. In the studied situation of helicopter main rotor-head, even though the pitch-angle is an output with stochastic nature, illustrated with statistical model, it needs to be integrated with the deterministic model for the rotor-head to generate the full picture of the variation in sliding within the pitch-control bearing.

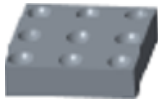
Considering the outcome of the model, it is reasonable to say that with the studied working condition, the focus of the tribological performance for the pitch-control-bearing can be put on a single direction (peak angle around  $85^\circ$ ). If an optimal orientation exists on an anisotropic

surface (i.e. the composite bearing liner), it should be aligned along this direction relative to the counterface in the pitch-control bearing. For the laboratory study, on this occasion, the linear-reciprocating test would suits better than other coupon test methods (pin-on-disc rotation, CTPOD etc.) as it is the most close to the real kinematics in terms of both sliding path and sliding angle distribution. However, it needs to be pointed out, this does not mean pin-on-plate test scheme suits all pitch-control-bearings. Instead, a case-by-case study using the output-oriented model is necessary for guidance of the investigation.

### 5.3 Wear test for the anisotropy in the tribological performance

As guided by the output-oriented model, to investigate the tribological performance of the anisotropic surface (composite) against a homogeneous smooth surface, four varied representative orientations ( $0^\circ$ ,  $45^\circ$ ,  $90^\circ$ ,  $135^\circ$ ) were selected to conduct reciprocating pin-on-plate tests. Then to study the influence on anisotropy from a heterogeneous counterface, the tests were also conducted with steel counterface with the preferred texture pattern selected in chapter 4 (1.6% coverage of dimples with diameter of  $20\mu\text{m}$  and depth of  $2\mu\text{m}$ ), as illustrated in **Table 11**.

*Table 11. Test matrix for wear tests on different counterface types and composite orientations*

Counterface type		Composite orientation			
		$0^\circ$	$45^\circ$	$90^\circ$	$135^\circ$
<b>Homogenous (smooth)</b>					
<b>Heterogeneous (dimpled)</b>					

The basic test setting was the same with the wear tests in Chapter 4: 3 Hz reciprocating frequency (i.e. 180 RPM rotating speed of the rotor), 20 mm reciprocating stroke length and 196 N normal force load was applied through the modified BICERI universal wear test machine. The measurement of the load and friction was performed using two full bridges of strain gauges (Vishay L2A-06-062LW-120) and the wear rate was recorded continuously with a Linear Variable Differential Transformer (LVDT) implemented vertically to a reference plane.

After the test, SEM analysis and FE analysis were conducted accordingly to help give theoretical explanation of the observed phenomenon.

### 5.3.1 Friction and wear measurements

To focus on the comparison of the performance between different composite orientations, the typical frictional and wear curves (selected from three repetitions for each condition) were plotted in two groups- with composites in varied orientation angles on smooth counterface (**Figure 100**) and with dimpled counterface. Firstly, with smooth counterface, using steady-state CoF and wear life as the evaluating indexes, an optimal angle -  $0^\circ$  and an undesirable orientation -  $90^\circ$  can be identified. The  $0^\circ$  had a wear life around 44 hours, exceeding the  $90^\circ$  (around 30 hours) by around a half. In addition, the steady-state CoF of  $0^\circ$  was around 0.053, considerably lower than that of  $90^\circ$  (around 0.062). Meanwhile, the other two tested orientations performed similarly in both frictional and wear, falling in-between the  $0^\circ$  and  $90^\circ$ .

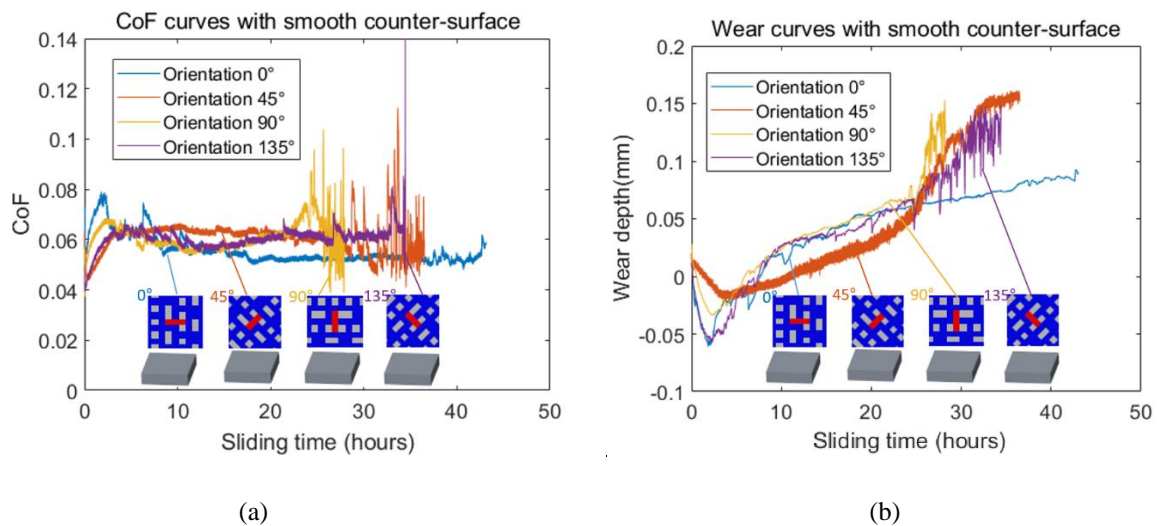


**Figure 100.** Measured (a) friction coefficient and (b) wear depth versus sliding time for three repeats of wear tests (normal pressure 40MPa, reciprocating frequency 3Hz, stroke 20mm) for PTFE/glass fibre composite sliding against smooth counterface with four different orientations

As for dimpled cases, the anisotropy had the same pattern among the four orientations. However, the performance was slightly lifted with each conditions while the difference between them was moderately reduced. On one hand, the steady-state frictional coefficient for all orientations met at around 0.055 despite the small difference (maximum around 0.003) in the earlier period (from 6 to 15 hours). On the other, all four orientations saw a small improvement, which should be attributed to the reformation of transfer-film by dimples according to the last (chapter 4). However, the extension on wear life with  $90^\circ$  orientation was a remarkable 3 to 5 hours (from the three repeated tests conducted), but the effect on the  $0^\circ$  case was marginal (no more than 1 hour), meaning the gap between different orientations was narrowed to some extent because of surface texturing.

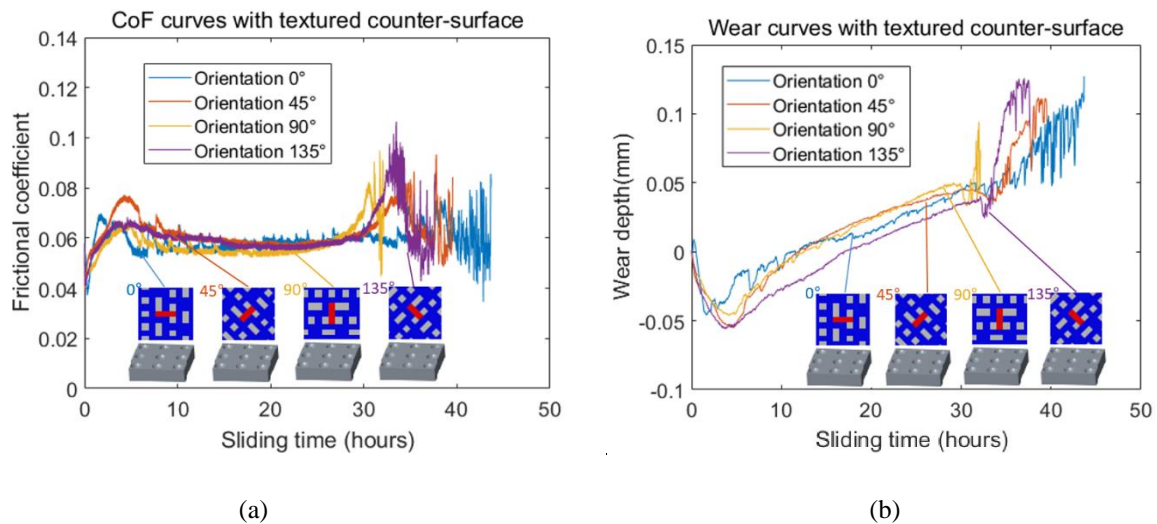


**Figure 101.** Measured (a) friction coefficient and (b) wear depth versus sliding time for three repeats of wear tests (normal pressure 40MPa, reciprocating frequency 3Hz, stroke 20mm) for PTFE/glass fibre composite sliding against dimpled counterface (dimple depth 2  $\mu\text{m}$ , diameter 20  $\mu\text{m}$ , coverage 1.6%) with four different orientations

To sum up, these test results indicated a connection between the tribological performance and the orientation of the composite, with 0° being the optimal and 90° being the least favourable. The ranking of the orientations did not vary when counterface textures were introduced, but the difference between them would be reduced. To explain the findings, the following analysis were conducted, aiming at relating these differences with the intrinsic feature of the composite - non-uniform material distribution, and the changes incurred by counterface textures.

### 5.3.2 Post-test surface analysis

In order to find the phenomenon leading to the anisotropy in tribological performance of the composite liner sliding against steel counterface, SEM analysis was and surface topographic imaging were conducted on the resultant surfaces acquired in tests around half-way through the steady-wear stage. Meanwhile, comparisons were also conducted between the conditions with the smooth and textured surfaces to investigate the influences from the surface texturing.

#### - Analysis for the causes of anisotropic tribological performance

First of all, as shown in **Figure 102** (a) and (b), on the counterface, not only transfer film was deposited as expected (dark areas in BSE images), wear tracks were also generated (as in the topographic image). Therefore, the counterface, which was originally homogeneous acquired certain heterogeneity in topography as the tests progress. From the consistency between the positions of the wear-track and the glass-fibres, it can be postulated that the tracks emerged from the abrasion of glass-fibres. Since by assigning the composite 0° or 90°, as shown in **Figure 102** (a) and (c), the shortest or the longest side of the glass-fibres would be imposed on

the sliding direction, correspondingly the minimal and the maximum area of wear-tracks would be generated among all different sliding directions. Since the abrasion wear tracks are drastically rougher ( $R_q > 0.4 \mu\text{m}$  as measured), they would cause a considerably higher wear rate and friction than the smooth counter-part. Even though as indicated by **Figure 102** (b) and (d), PTFE transfer were also contained in the wear-track-regions, the maintaining of it would be constantly affected by the scratching of glass fibres and the as well as the debris. Judging by the test results that orientation of  $90^\circ$  saw the worst wear performance and  $0^\circ$  had the best, the benefit in transfer film in wear-track-areas certainly had not exceeded the drawback of abrasion.

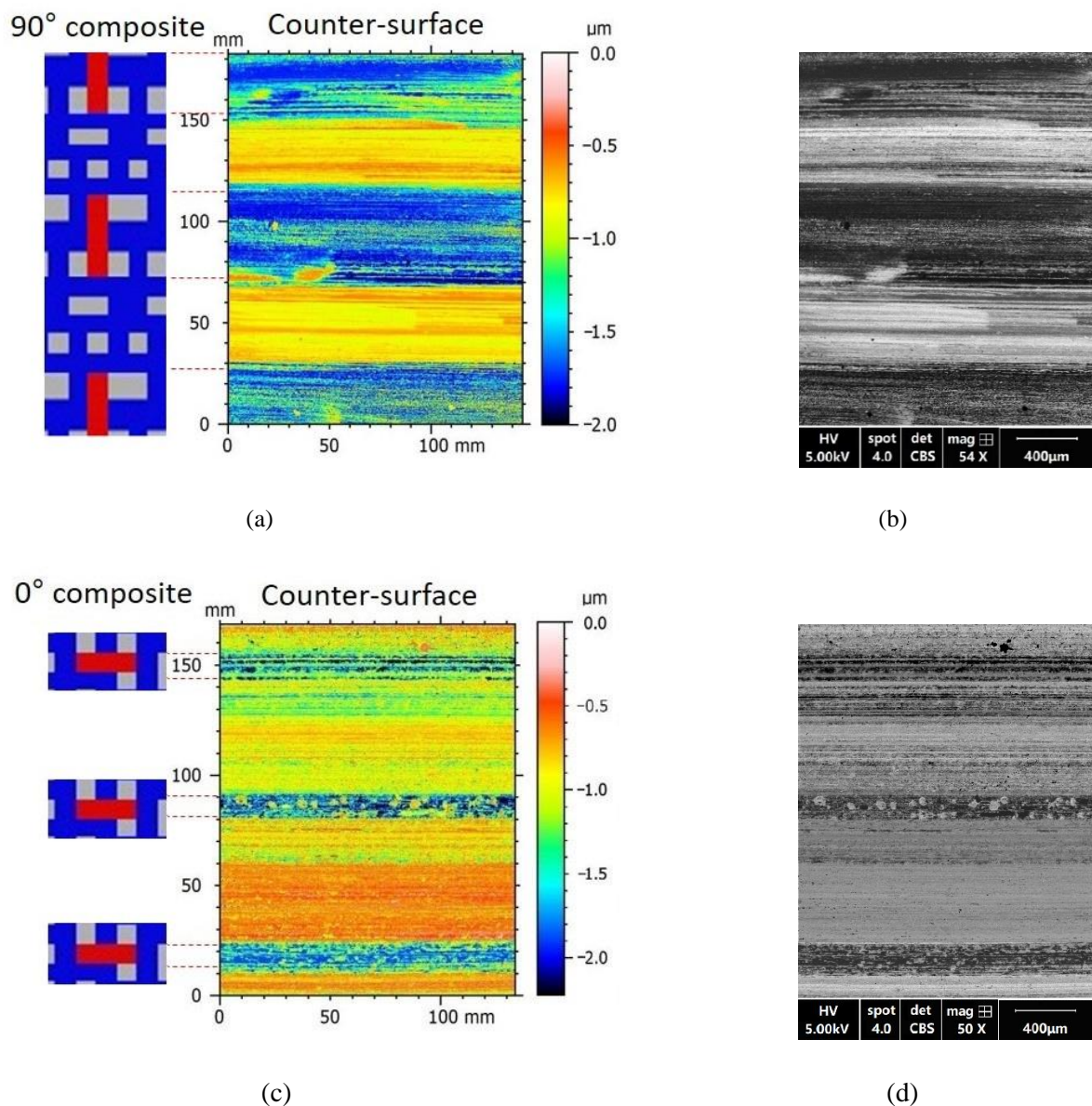


**Figure 102.** (a) Topographic image and (b) SEM image (BSE) of the counterface (initially smooth) half-way through the wear test (normal pressure 40MPa, average sliding velocity 0.12/s) with composite oriented at  $90^\circ$ ; (c) SEM image (BSE) and (d) topographic image of the counterface (initially smooth) half-way through the wear test with composite oriented at  $0^\circ$

As for the  $45^\circ$  and  $135^\circ$ , in spite of the  $90^\circ$  shift, the resultant wear track widths are theoretically the same (in-between two extremes under  $0^\circ$  and  $90^\circ$  conditions), like demonstrated in **Figure 103**, corresponding to their performance (in-between the performance of  $0^\circ$  and  $90^\circ$  conditions) in the wear tests.

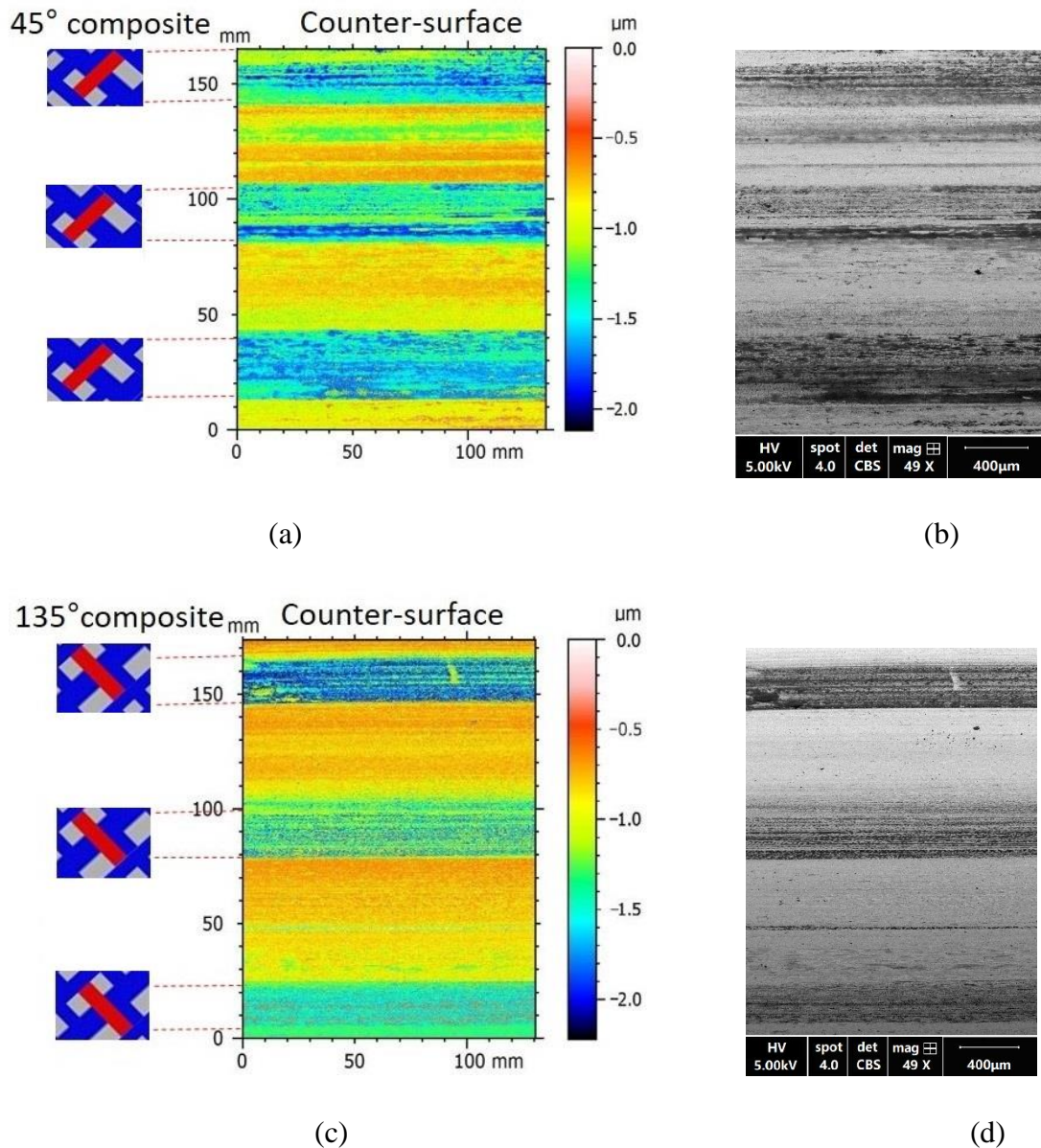


**Figure 103.** (a) Topographic image and (b) SEM image (BSE) of the counterface (initially smooth) half-way through the wear test (normal pressure 40MPa, average sliding velocity 0.12/s) with composite oriented at  $45^\circ$ ; (c) SEM image (BSE) and (d) topographic image of the counterface (initially smooth) half-way through the wear test with composite oriented at  $135^\circ$

Therefore, it can be concluded that the main contributor to the anisotropy was the orientation-dependent areas of the counterface wear tracks, as the width of the wear tracks is equivalent to the projected length of the glass fibre perpendicular to the sliding direction. This sequential effect deriving from the distribution of composing material should also be present on the cases

with textured counterface as well. However, how surface textures may create a difference will be discussed as following.

#### - Analysis for the influence from surface textures

First of all, for textured counterface, generally the wear-tracks and PTFE transfer film distribution resembled that on smooth counterface. However, differences on the wear track areas were also observed. With 90° composite orientation, on the counterface, certain areas within the wear-track-region appeared smooth (marked as ‘smoothened area’ in **Figure 104**), while some dimpled areas adjacent to the glass fibres saw extra wear tracks.

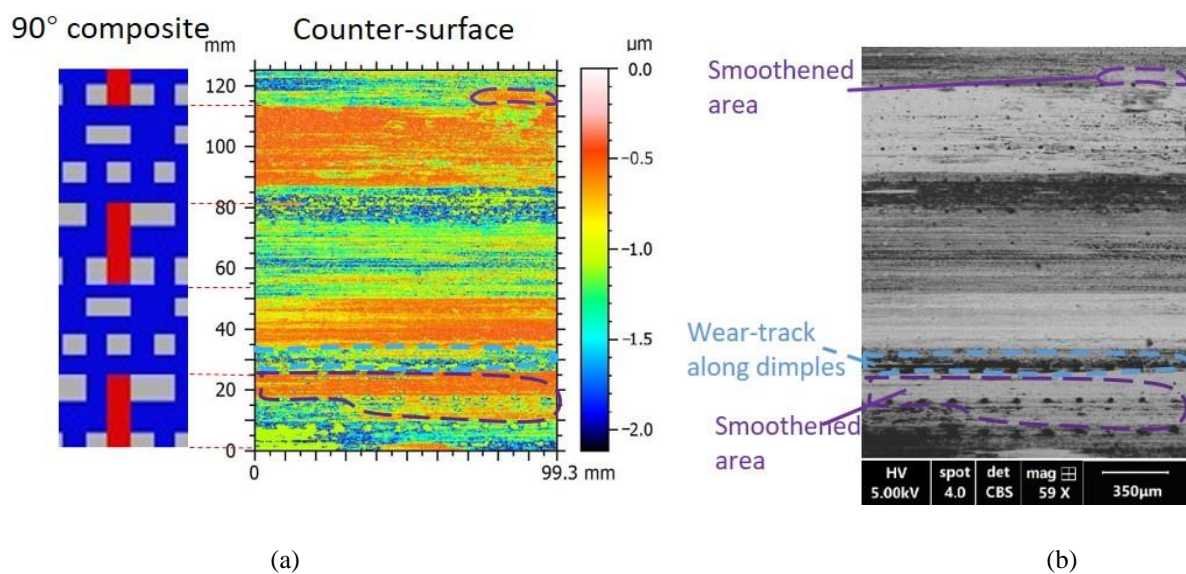


**Figure 104.** (a) Topographic image and (b) SEM image (BSE) of the counterface (initially smooth) half-way through the wear test (normal pressure 40MPa, average sliding velocity 0.12/s) with composite oriented at 90°

Moreover, similar phenomenon induced by textures can also be seen with 0° composite orientation, as shown in **Figure 105**, but since the wear track areas induced by glass fibres under 90° orientation would have been small at the first place, the smoothing effect was not prominent like in 0°. Instead, more wear tracks near the textured region on the counterface were observed. Consequently, the counterface wear tracks became more texture-dependent instead of glass-fibre dependent (analogous to the preliminary observations with the larger textures in section 4.2.2), and the resultant counterface in 0° and 90° appear more alike. This can be related to the relieving of anisotropic performance found in the test results (section 5.3.1).

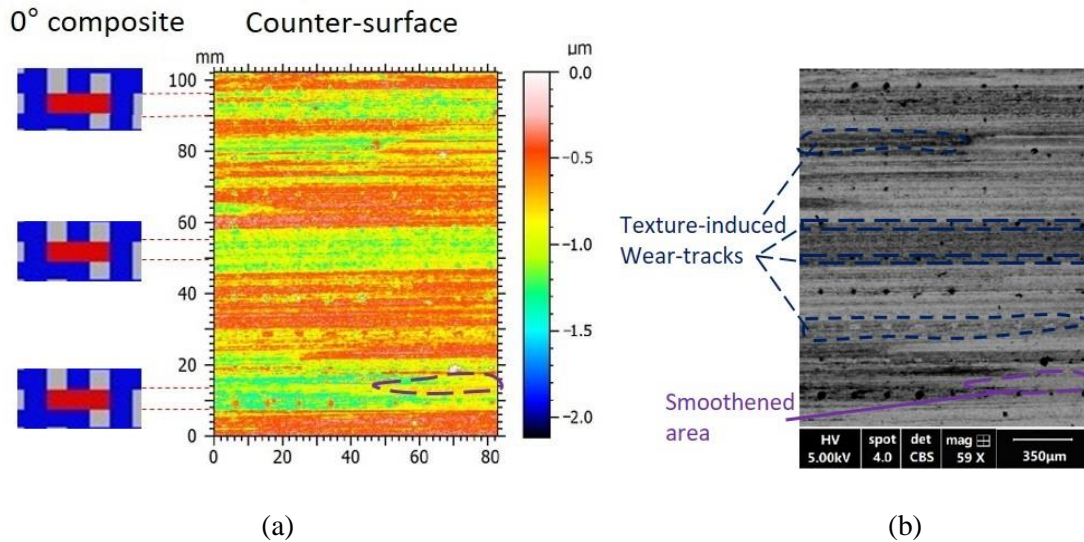


**Figure 105.** (a) Topographic image and (b) SEM image (BSE) of the counterface (initially smooth) half-way through the wear test with composite oriented at  $0^\circ$

On SEM images of the composite surfaces, a phenomenon that lead to the smoothing effect on the dimpled counterface was found. As shown in **Figure 106** (a) and (b), with dimpled counterface, strips of PTFE back-transfer (marked as ‘PTFE back-transfer’, verified by EDX analysis) were reserved on the composite surface ( $0^\circ$  orientation). However, for the case with smooth counterface, as shown in **Figure 106** (c) and (d), little back transfer was observed.

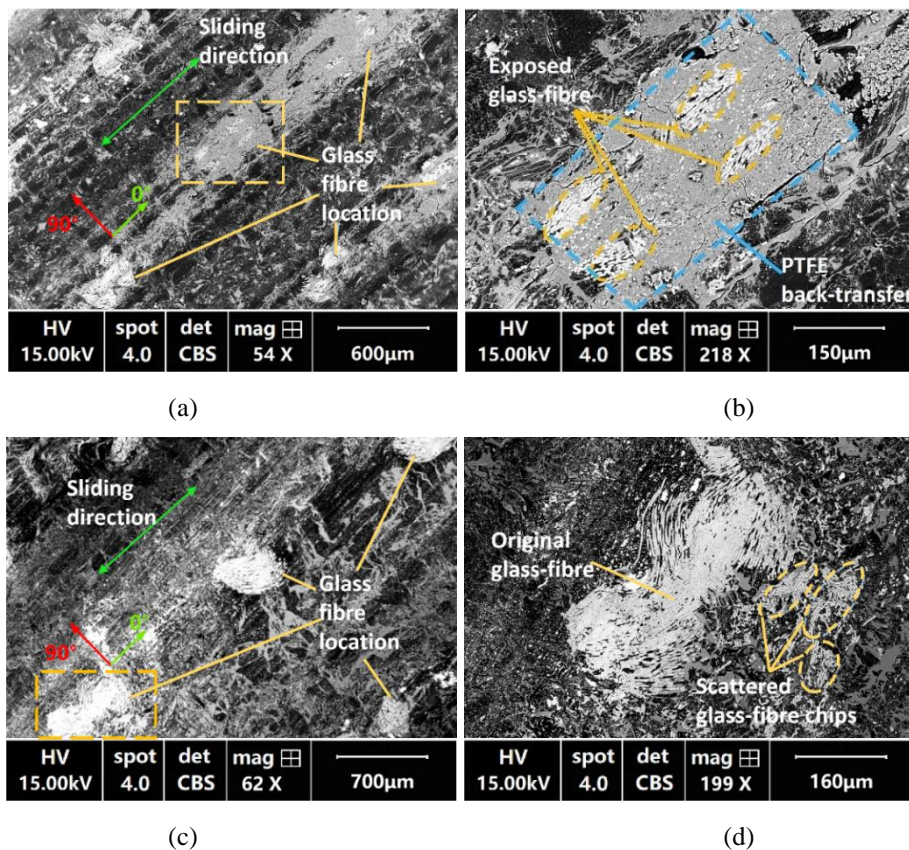


**Figure 106.** SEM image (BSE) of the composite surface (oriented at  $0^\circ$ ) sliding against (a) dimpled counterface and (b) a magnified view; against (c) initially smooth counterface and (d) a magnified view

Similarly, with 90° composite orientation, like shown in **Figure 107**, the back-transfer was also more prominent with dimple counterface. Theoretically, this back transfer can serve as a protective layer, containing the hard wear particles from glass fibres and alleviating the generation of counterface wear track and further abrasion.

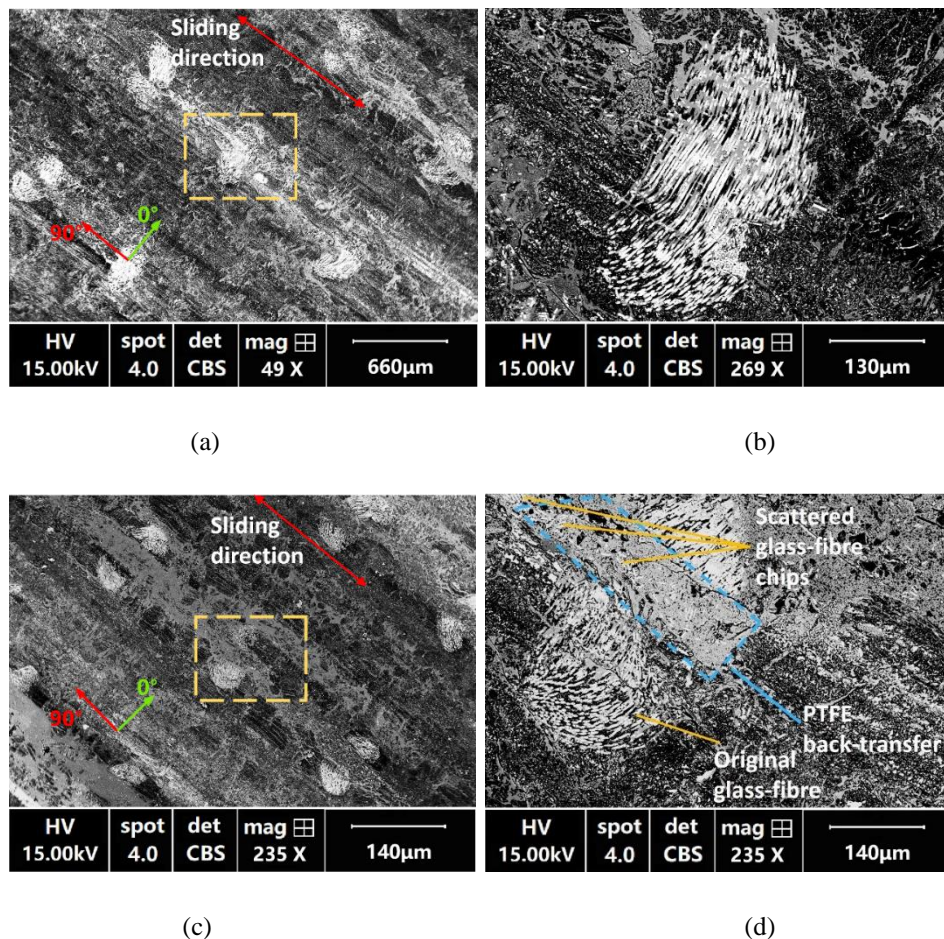


**Figure 107.** SEM image (BSE) of the composite surface (oriented at 90°) sliding against (a) initially smooth counterface and (b) a magnified view; against (c) dimpled counterface and (d) a magnified view

Overall, it has been observed that the dimples can reduce the roughening in wear tracks on the counterface created by glass fibres in the composite. This effect can be associated with the reservation of PTFE back-transfer, or the pressure//stress redistribution induced by textures (verified later). Due to the different widths of the wear tracks, which correspond to different orientations of the composite, the improvement would vary- those more affected by the glass fibre abrasion would be improved more, and vice versa. Moreover, the dimples can be regarded as a pre-deposited heterogeneity spreading all over the counterface, and the resultant influence on the counterface topography and tribological behaviour can suppress those induced by glass-fibres. Consequently, the tribological performance becomes more texture-dominant instead of composite-orientation-dominant; therefore, alleviation in anisotropy is achieved.

### 5.3.3 FE analysis of the stress re-distribution effect from counterface textures

To acquire a more detailed illustration on how the surface textures (dimples) influence the contact condition on this specific mixed surface of roughened (caused by glass-fibre abrasion) and smooth areas, the contact mechanics was analysed using the FE model developed in this thesis (see chapter 4.5).

To focus on the influence of surface textures and to reduce computation cost, the counterface is modelled as one pre-set with half roughened and half smooth (i.e. the state during the steady-wear stage), like shown in **Figure 108**. As for the roughened area, since to model the whole roughness morphology requires un-reasonable meshing and computation cost, while the effect of roughness is not the focus of the model, it is simply treated as an area with much larger  $CoF$  (0.3 – tested on counterface with high density of dimples, resembling roughened surface). For the material property, loading and so on, the modelling approaches totally follow that in chapter 4.5.

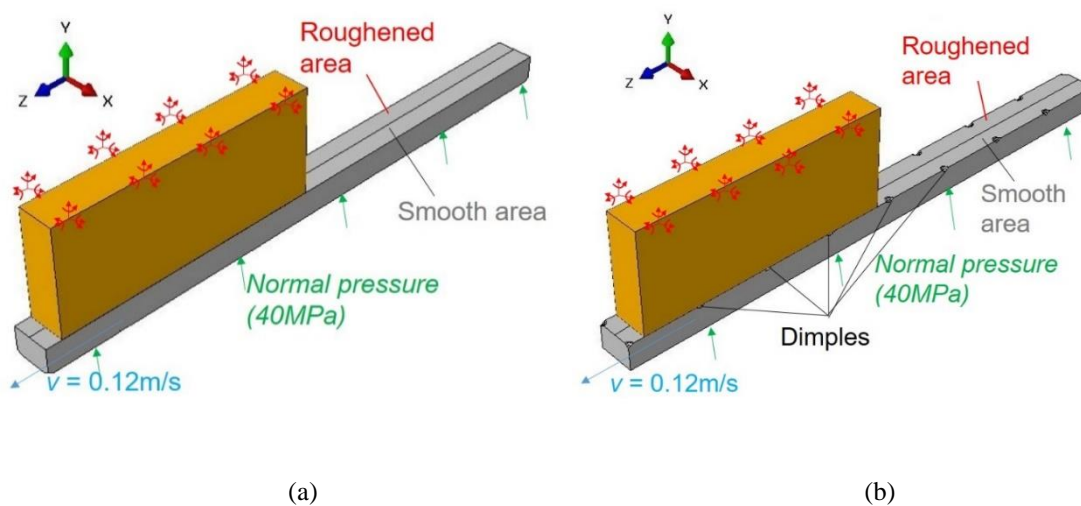


*Figure 108. The model of the contact pair with (a) un-textured counterface and (b) dimpled counterface considering the roughened areas with wear tracks*

The results from these two conditions modelled, as in **Figure 109**, show that the dimples induced a switch of ‘high-stress area’. For the un-textured case, as shown in **Figure 109** (a), the contact stress on the roughened area (majority between 67.0 and 71.2 MPa) was overall in a higher level than the smooth area (majority between 62.8 and 67.0 MPa). In comparison, on the dimpled case, as shown in **Figure 109** (b), the peaks of stress shifted to the areas near dimple edges. Even though the stress in the stress-concentration regions can reach to a dramatically higher level (more than 90 MPa), it was reduced to a certain degree in the non-textured areas (mostly in the 62-69.45MPa). Moreover, with the detailed view of the composite

area near the dimple edge, like shown in **Figure 109** (b), even a low-stress region around the dimple edge was observed. Revisiting the FE analysis conducted in the previous chapter (in section 4.5), it can be seen that this phenomenon is common among textured conditions. In **Figure 80** (a) and **Figure 86** (c), this effect was revealed most prominently, adjacent to the stress-concentration zones.

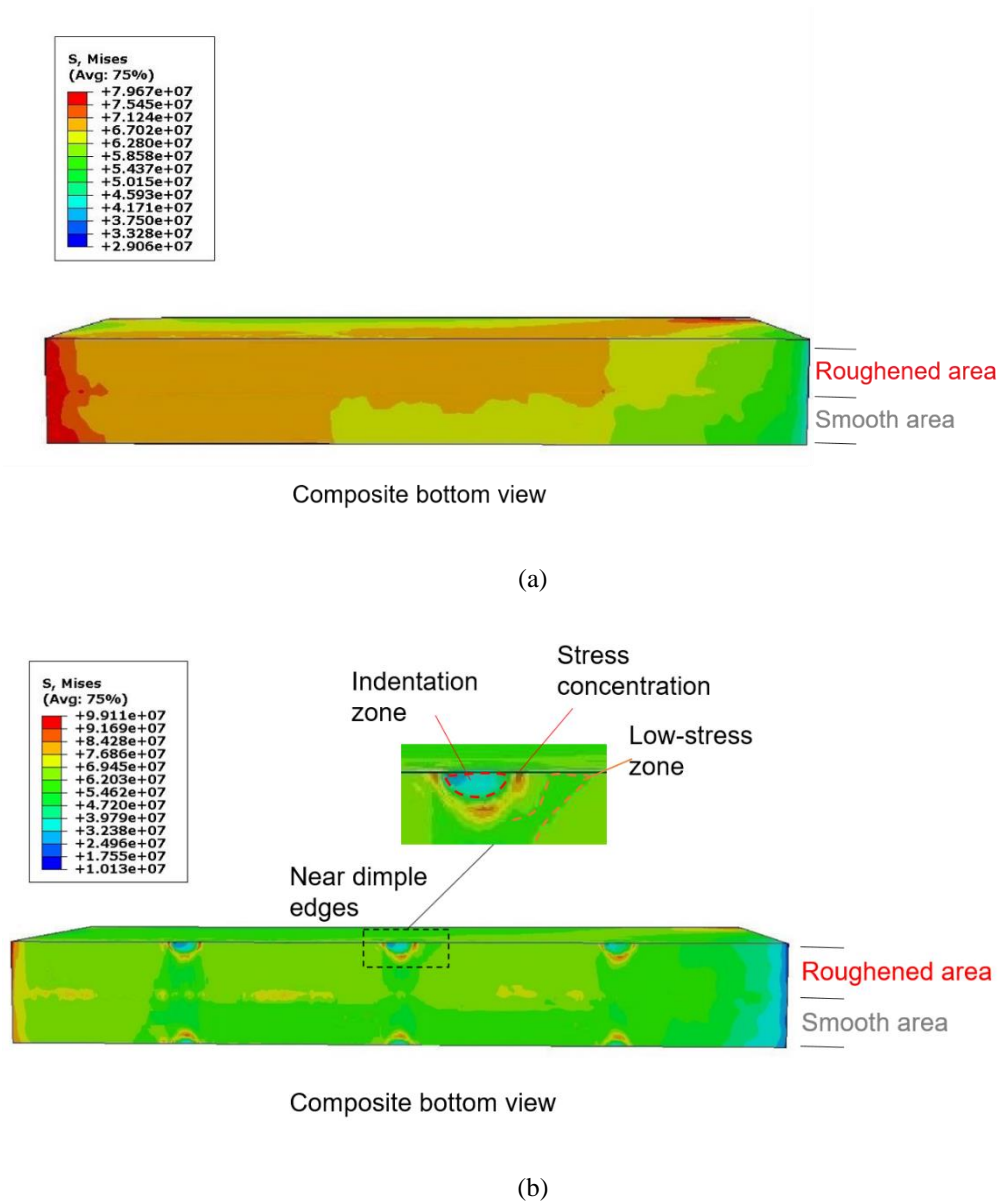


**Figure 109.** Contact surface (bottom surface) stress distribution on the composite liner with (a) un-textured and (b) dimpled counterface

Overall, apart from stress-concentration, the surface textures can also simultaneously lead to stress-relieving in other areas. This effect resembles that induced by hard fibre addition (glass-fibres) in the composite, as they both ‘sacrifice’ some areas while benefiting others. Solely considering the magnitude of the two changes incurred: the stress-relieving was relatively

moderate but the increase in the stress-concentration zones was huge (pushing it near the threshold value as revealed in section 4.5), the overall influence of this stress-shifting function may not even be beneficial. Nonetheless, in the condition where considerable counterface areas (half of the area modelled) were roughened, this effect can condense the stress-elevation areas to the regions neighbouring the edges of counterface textures. This should support the observation that with counterface textures, some counterface areas remain smooth among those abraded by the glass fibres (section 5.3.2).

With a more detailed analysis on the contact condition, how this stress relieving was incurred can be revealed. As shown in **Figure 110(a)** - the graph for vertical displacement ( $U_2$ ), under pressing, the part of the composite neighbouring the concavity would indent into it. This indentation should be smaller with ‘narrower’ dimples – in this case (dimple diameter  $20\ \mu\text{m}$ ) it was merely around  $0.2\ \mu\text{m}$  based on the extracted data shown in **Figure 110(b)**. In addition, a small degree of tilting on the contact line always occur along with this indent, like marked in **Figure 110(b)**. Judging by the direction of the tilting, it would essentially result in a smaller overclosure (i.e. less penetration /more interfacial gap between interfacial nodes) at the point. According to the complimentary relationship between the contact pressure and the overclosure in the theoretical formula (illustrated in section 3.1.5.1), this would cause the reduction in local contact pressure, and stress consequently - an extreme case is when the overclosure becomes negative (i.e. interfacial gap becomes positive), the contact pressure would be zero. In a word, the indenting in the dimpled area and the accompanying tilting outside the region can lead to the stress-relieving.

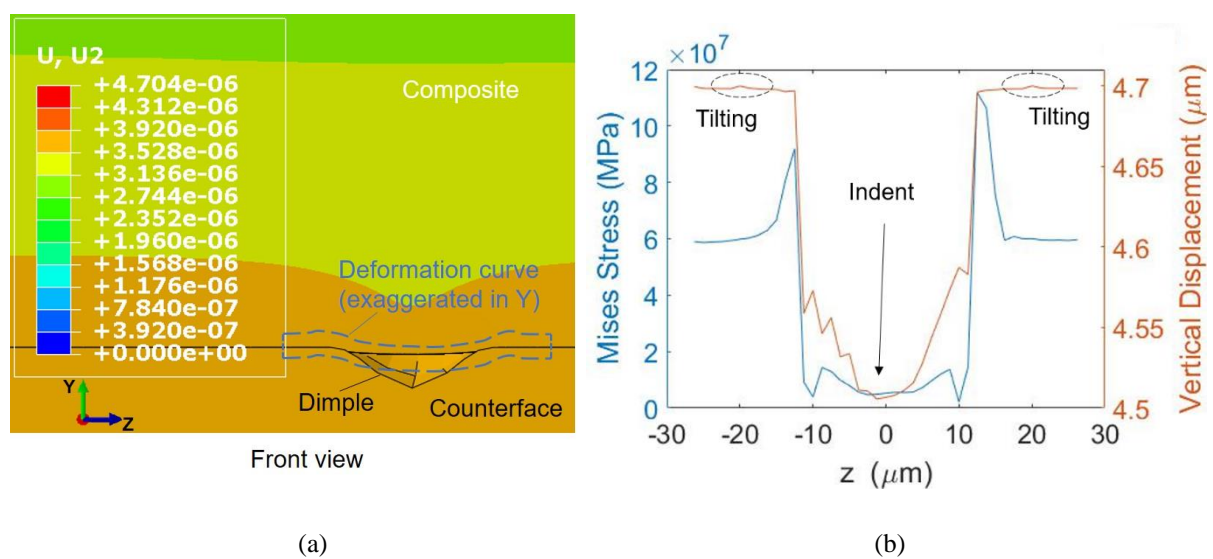


**Figure 110.** (a) Section view of the composite deformation with dimpled counterface (vertical displacement in a scale of 10 times), (b) The extracted stress and vertical displacement data versus  $z$  location (pressed under 40MPa.)

Overall, dimples textured on the counterface can alter the stress distribution by shifting the peak-stress region to near-dimple areas, which would experience stress concentration. Meanwhile stress in some other parts on the composite surface can be relieved as the composite indents into the dimple and forms a tilting effect outside the dimple. Even though this model only gives a simplified quantification analysis, this observation should be capable of revealing the basic phenomenon how surface textures would relieve the effects caused by abrasion wear tracks on the counterface (emerging from hard fibres in composite liner).

## 5.4 Conclusions

In this chapter, the output-oriented modelling principle is proposed for revealing the influence of kinematics on contact condition with anisotropic tribological performance. Based on this principle, the kinematic model for the pitch-control bearings in helicopter main rotor was developed, addressing the previous misconceptions in this constantly discussed application.

With the understanding on the kinematics, a series of wear tests was conducted to investigate the influence of material heterogeneity and counterface topographic heterogeneity on the tribological performance of a dry-lubricated bearing.

The main contributions and findings in this chapter are:

*A novel kinematic model for the pitch-control-bearings in helicopter main rotor was developed, based on the output-oriented principle proposed for modelling the kinematics of sliding contact involving possibly anisotropic tribological performance. The issues with the commonly used empirical model were addressed:*

- The real sliding path within the pitch-control-bearings follows a group of transcendental spherical curves, instead of the combination of swivelling and tiling like commonly perceived. Consequently, the resultant distribution of sliding directions is not symmetrical about  $90^\circ$  like in the conventional empirical model, and may have a prominent peak deviated from  $90^\circ$  instead of a considerably uniform distribution.

*Guided by the new kinematic model, a series of wear tests were conducted to reveal the anisotropic tribological performance of the self-lubricating bearing. The influence of counterface textures on the anisotropy was reported. Through the test and relevant surface analysis, the following findings were made:*

- The anisotropic tribological performance derives from the mutual interaction between the contact pair: the hard fibres (glass fibres) would cause counterface wear tracks, whose width depends on the projected length or the glass fibres perpendicular to the sliding direction, and the wear tracks would in turn lead to higher wear rate on the composite liner. Therefore, the optimal orientation becomes the one leading to the smaller side length perpendicular to the sliding direction.

- It was found that the anisotropy can be reduced when the counterface was textured with uniformly distributed dimples. This can be related to that the counterface abrasion caused by hard fibres have become relieved, through interfacial phenomenon including PTFE back-transfer and contact pressure/stress redistribution, which are more texture-dependent.

*The FE model developed previously was applied to correlate the influence of counterface textures and the contact mechanics. The following theoretical support was formulated:*

- The reason for the dominance of texture effect is that the stress elevation induced by the texture edges would surpass that from counterface abrasion tracks. Therefore, the further abrasion on the composite surface would become less dependent on the sliding direction, as it abrasion caused by texture edges is less affected by the orientation.

Overall, this study reports an interesting phenomenon. The root cause for anisotropy is heterogeneity, be it in material distribution, physical properties, topographic or some other sort. In this case, in the original form (composite against smooth counterface), the root cause of anisotropy is the heterogeneity in material distribution. However, the material distribution does not directly lead to anisotropy, but generate another heterogeneity (topographical one on counterface) that would further causes anisotropic tribological performance. From this view, the counterface texture is actually a type of pre-applied topographic heterogeneity, and the reason why it can relieve the anisotropy can be interpreted as that it is in a ‘more uniform’ fashion (as it spreads evenly all over the counterface) than the heterogeneity of material distribution in the composite.

It should be noted that the studies conducted still have some limitations. For examples, the observed anisotropy may be exclusive to this type of composite liners (woven fabric), since in other ones (e.g, laminar or particulate) the abrasive wear tracks may just be uniformly spread

over the counterface. Moreover, it should be noted that even though the developed principles and modelling of the kinematics is universal, the studied case was a unique condition based on real application. In other applications, if the distribution of the sliding direction is not so condensed within a small range, a test method simulating with the entire motion would be necessary. With this said, the established knowledge on the anisotropy in the tribological performance of self-lubricating bearings can still instruct the optimization of the composite alignment in certain applications, and the findings on the influence of counterface textures would form an advancement in the understanding of this field. For instance, since it has been identified that the anisotropic tribological performance of the self-lubricating PTFE composite was caused by the variation of counterface wear tracks (by the hard stiffener – the glass fibres), an important prospect of this knowledge is to adjust the composition of the composite. How much stiffener should be included in the composite, and what types of stiffener (e.g. any other kind of substitutive hard fibres such as polyesters) should be used, etc. should all be considered, leading to a new optimization problem for the composite.

## **Chapter 6**

# **The effects of surface texturing on the bonding strength of the bearing liner**

### **6.1 Introduction**

Due to the importance of achieving a strong bond between the liner and the outer-ring in the dry-lubricated bearing system, massive research and development have been put in adhesive, bonding process and surface processing. For the processing of the outer ring surface, effective as it is, the currently established grit-blasting method still poses many issues such as possible embedment of grits into the surfaces jeopardising surface integrity and environmental concerns (noise, waste and demands for electric power and consumables) [119]. Therefore, new efficient surface processing for bonding strength improvement are constantly being searched for.

In this chapter, different surface texturing techniques and novel surface roughening are proposed for the bonding strength purpose and evaluated for their performance. The mechanism of bonding performance improvement is investigated, and the theory behind the influence of different surface texturing/roughening is studied. Furthermore, considering the strong link found between the bonding strength and the wettability of the surface, the influence of the surface texturing on wettability of the surface is investigated. By introducing a new model for the contact angle with improved predicting capability with textured surfaces, this study provides the possibility of predicting the change on wettability and bonding strength by surface texturing in different forms and dimensions.

### **6.2 Experimental scheme and sample surface characterisation**

To explore the potential of surface texturing/roughening techniques in bonding strength improvement, a few novel processes were developed. These methods, together with the grit-blasting prototype were applied on flat sample surfaces for lap-shear test to obtain quantities analysis of the influence, and on outer-ring surfaces for liner peel test for a final qualitative check. Then, to identify the mechanism how surface texturing/roughening affects bonding strength, wettability test and post-test SEM analysis are conducted.

In the following, the developed surfaces are presented with characterisation using SEM and surface profilometer accordingly.

### - Conventional machined surfaces

To investigate whether conventional processes for machining bearing surfaces may have the potential in improving bonding strength, some of the commonly-used machining processes were used to create surface textures on the bearing outer-ring surfaces for the peeling test described in section 3.2.1.2. The surface textures include dimples by the modified hard-turning (HaT) process, the cross-hatch textures from a honing machine, and straight trenches using a turning machine. To minimize the influence of difference in texture dimensions and coverages between tested methods (since contact area is a key factor affecting bonding strength), as shown in **Figure 111**, the depths of three types of textures are controlled in a similar range (around 15  $\mu\text{m}$ ), and the coverages of the textured areas were all set at around 50%.

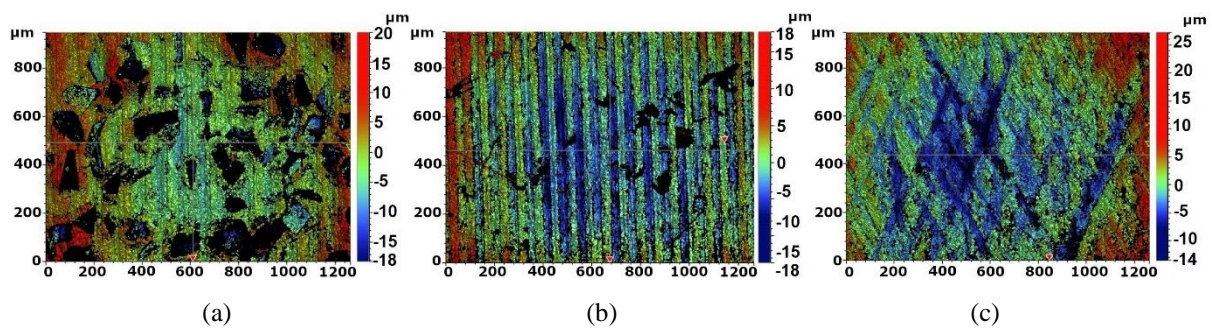


*Figure 111. Surface topography image (by Bruker) of surface machined by (a) hard-turning, (b) turning and (c) honing*

Then, when using the lap shear test (introduced in section 3.2.1.1) to conduct quantitative comparison of bonding strength, since these processes are not catered for machining flat surfaces, laser surface texturing was employed on the flat sample to mimic the textures of these conventional machining, as introduced in the following.

### - Laser textured surfaces (mimicking conventional machined surface)

Since the conventional manufacturing processes stated above are for the machining of bearing surface (spherical or cylindrical surfaces), but not compatible with the flat surfaces, laser surface texturing was applied on the flat specimen of lap shear test for quantifying bonding strength. On the steel plates, the generated surface topography mimic those from hard turning (dimple textures), turning (straight trench textures) and honing (cross-hatch textures). These three types of surfaces are later referred as ‘laser HaT’, ‘laser honed’ and ‘laser turned’ surfaces. Similar with those achieved on real bearings through conventional machining (**Figure 111**), the depth of the textures was controlled at 15 $\mu\text{m}$ , and the width of the trenches (or the dimple diameter) was set at 40 $\mu\text{m}$ . The controlling of the dimensions was fulfilled using the calibration between the texture depth with operating parameters (power, laser dwell time and moving

speed) in chapter 3.1.2.2. The coverage of the textures on the surfaces was kept consistent at 50% with different texturing. After the surfaces were textured (like shown in **Figure 112**), they were all polished on the Struers LaboSystem polishing machine to remove re-deposition.

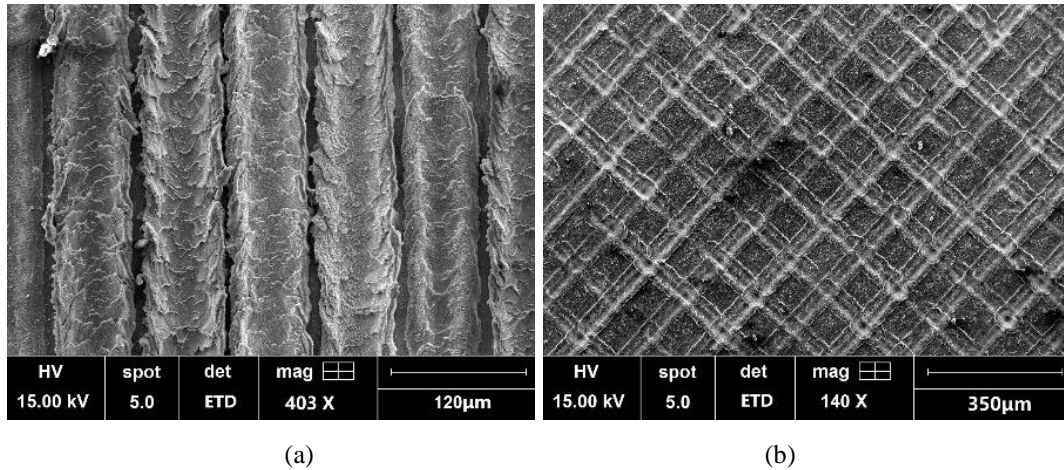


**Figure 112.** SEM images (SE mode) of (a) laser turned surface and (b) laser honed surface (before polishing)

It should be noted, because of the type of laser used (pico-second laser), on the textured surfaces, laser-induced periodic surface structures (LIPSS) appeared within the ablated areas. This ‘ripple’ structures, like shown in **Figure 113**, were also micro-level structures. Within the trenches, as shown in **Figure 113** (a), the ‘ripples’ all aligned perpendicular to the trenches. The spacing between ‘ripples’, like shown in **Figure 113** (b) and (d), is close to the wavelength of the laser (1064 nm), indicating that they were probably the type-1 LIPSS, caused by surface Plasmon polariton effect [223] under high energy flux (max power was used for this session).

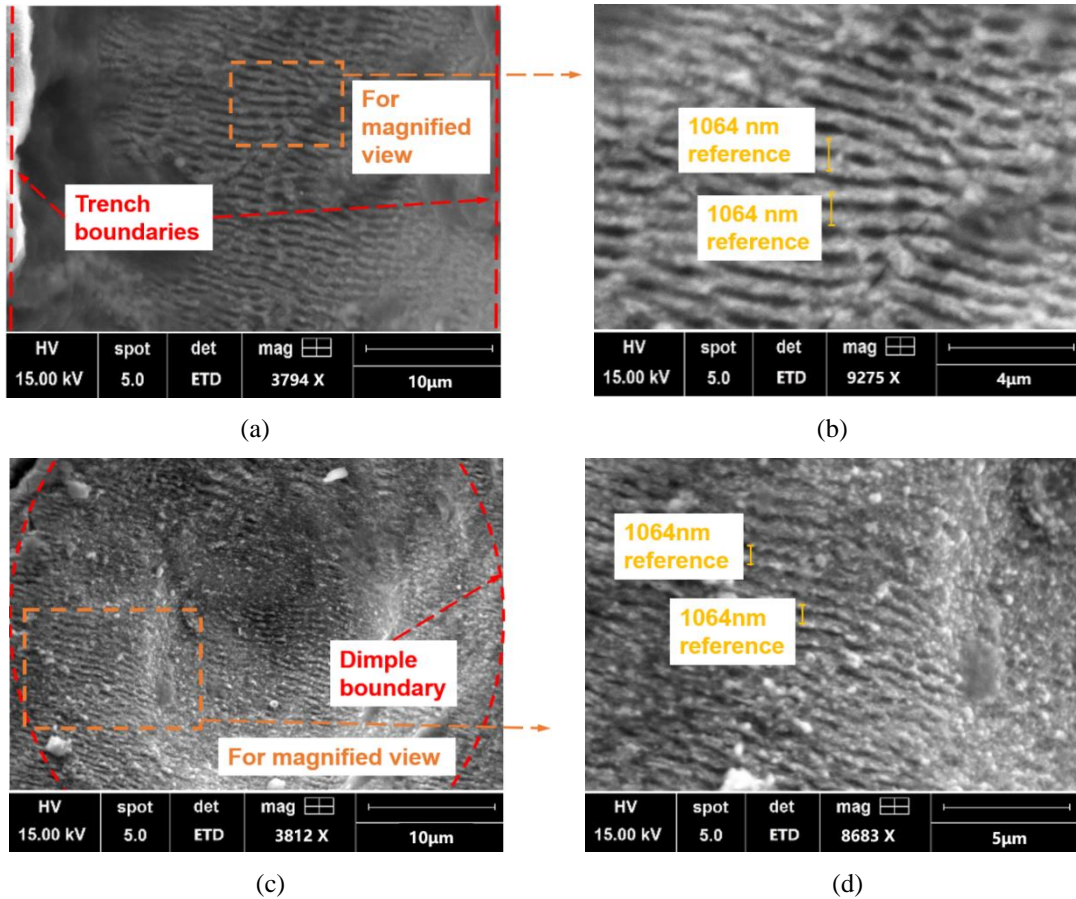


Figure 113. (a)(b)LIPPS within a trench of a laser-honed surface; (c)(d)LIPPS within a dimple of a laser-HaT surface

**- Grit-blasted surface**

Unlike the conventional processes stated above, grit blasting can produce irregular roughness in much smaller dimensions all over the surface, as demonstrated in **Figure 114**. This ‘fine’ roughness is from the continuing attacks on the entire surface from the sharp edges of the particles.

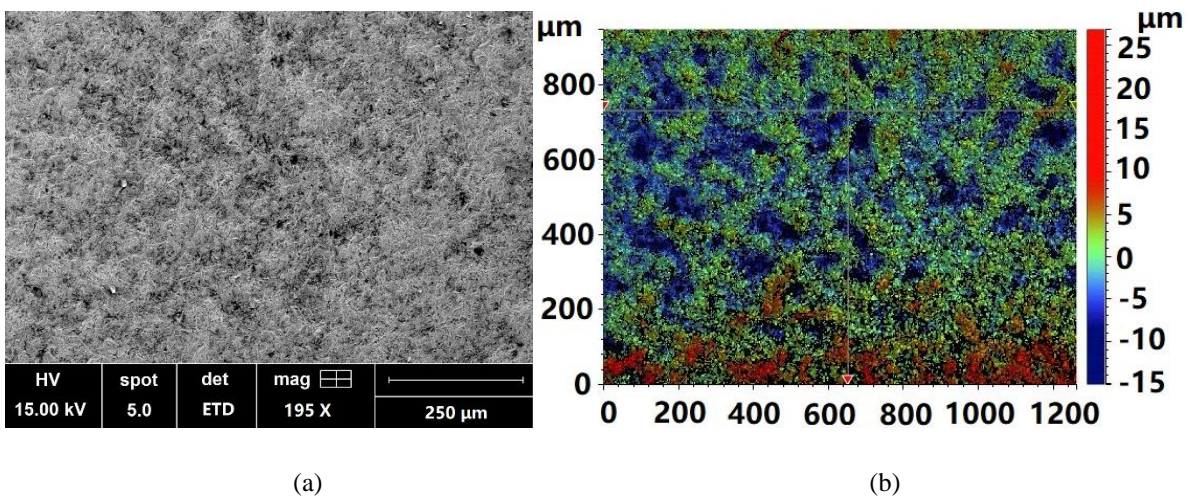
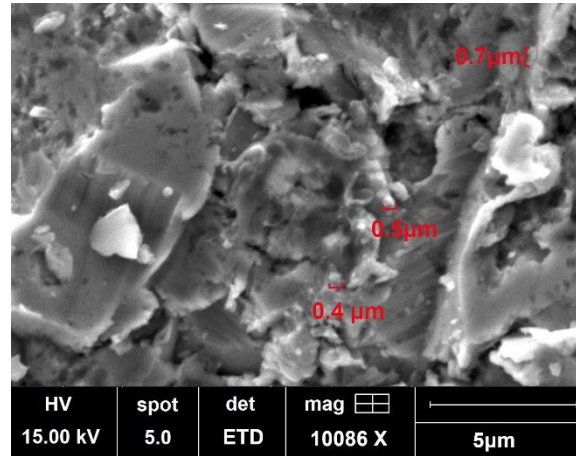


Figure 114. (a) SEM image of the grit-blasted bearing outer ring surface, (b) surface topographic image (obtained by Bruker interferometry) of the grit-blasted bearing outer ring surface

As indicated by **Figure 115**, the dimensions of the asperities generated on the surface can reach below a micron. Theoretically, this micro/nano-roughness feature adds contact area with the adhesive and assists better adhesion, so the novel roughening processes introduced later also aim at achieving similar structures.

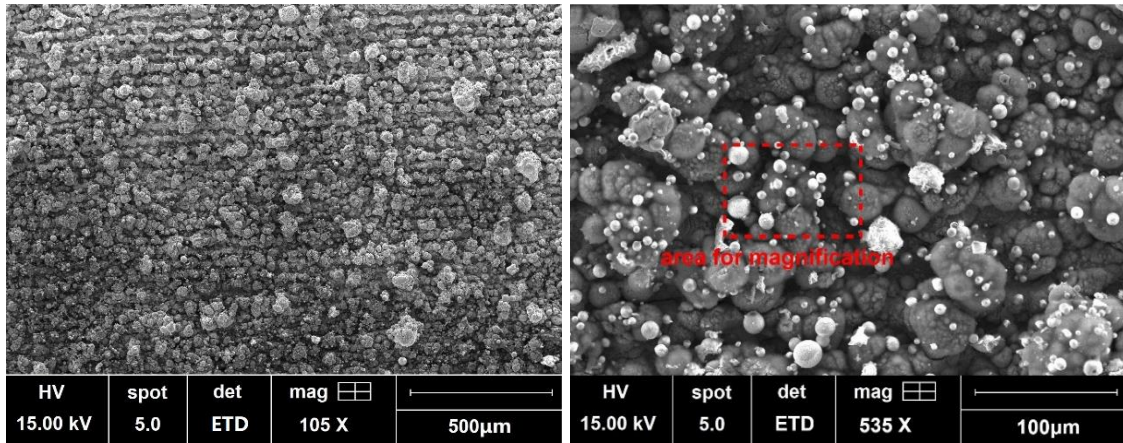


*Figure 115. Sub-micron level asperities generated on the grit-blasted surface*

#### - Laser-roughened surface

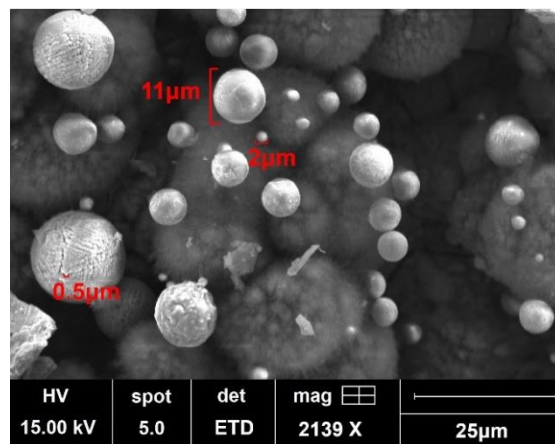
On contrary to laser texturing method, the proposed laser-roughening process did not get rid of the re-deposition but took advantage of it, considering its highly rough appearance.

Through applying the overlapped laser shots, the whole surface can be covered by the re-deposition, as shown in **Figure 116** (a). As indicated in **Figure 116** (b), the roughness generated are micro-level spherical molten deposits, on which sub-micro and even nano-scale strip-like structures affiliates, like in **Figure 116** (c). These are essentially desired features, since the induced multiplication of surface area and the porosity within the molten spheres may benefit adhesion.



(a)

(b)



(c)

Figure 116. SEM image of a laser-roughened surface with (a) 105× (b) 535× and (c) 2139 × magnification |

With the textured/roughened surfaces, the lap-shear tests and liner-peel test were arranged accordingly, as illustrated by **Table 12**.

Table 12. Test matrix for lap-shear tests on different roughened/textured surfaces

	Reference	Roughened		Textured		
<b>Lap-shear test (flat sample surface)</b>	Smooth	Grit- blasted	Laser- roughened	Laser- turned	Laser- honed	Laser- dimpled
<b>Liner-peel test (outer-ring sample surface)</b>	Smooth	Grit- blasted		Turned	Honed	Hard- turned

### 6.3 Lap shear tests – for quantification analysis

To achieve a quantitative comparison of bonding strength acquired through the different surface texturing/roughening technologies proposed, lap shear tests were performed. Like has been introduced in chapter 3.2.2.1. In each test, the bonded lap shear joint specimen were pulled till the failure, i.e. complete separation of the two surfaces.

From the obtained curves on the relationship between the applied pull-force and the displacement between the two gripped specimens, like shown in **Figure 117**, it can be seen that the curve shares certain similarities with a stress-strain curve of a tensile test. For example, it would start with a linear deformation stage until a yield point, after which the displacement can rise dramatically without much increase in the applied force. Then, another turning point would appear, and the pull force would increase again rapidly with the displacement, before it reaches the final failure point, corresponding to the complete separation of the two surfaces. Considering the characteristics of the curves, both the yield point and the failure point are recorded for assessing the bonding strength of the assembly. The former one denotes the initiation of the bonding failure, after which the two bonded surfaces may have a considerable relative sliding to each other under the shear load, and the lateral one denotes the complete detachment of the two surfaces. The corresponding stress value (pull force per area) at these two points are later referred as ‘yield bonding strength’ and ‘ultimate bonding strength’ (the conventionally defined bonding strength) in this work.

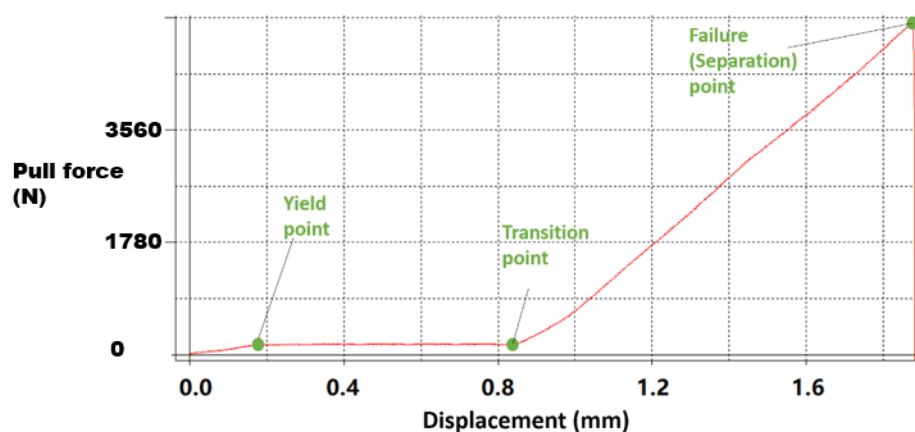


*Figure 117. Pull force – displacement curve generated from a single lap shear test (with grit-blasted surface) for measurement of the bonding strength*

All the lap shear tests conducted ended with the failure of bonding, while no failure of steel plate specimen occurred. Moreover, the maximum pull force applied (shown at bonding failure

point in **Figure 117**) does not exceed 1200 lbf (5338 N), which would lead to theoretically only around  $720\mu\epsilon$  of strain, namely 0.073mm of displacement on the steel specimen. Compared with the overall displacement at failure (mostly around 2.0mm), the deformation of specimen is minimal. Therefore, the influence from the deformation of the steel specimen is negligible, and the measured pull force is capable of representing the bonding strength.

### 6.3.1 Investigating the influence by surface texturing- comparison between surfaces with different texturing methods

To gain the knowledge of what different influence can be induced with different surface texturing, both ‘yield bonding strength’ and ‘ultimate bonding strength’ were recorded and compared in this section.

From the conducted lap shear tests, it is found that the mean values of measured yield bonding strength of different textured surfaces are all close to that of smooth (non-textured) surface (at 0.237MPa) as shown in **Figure 118**. The largest difference is only 3.38% (0.245MPa for laser roughened surface).

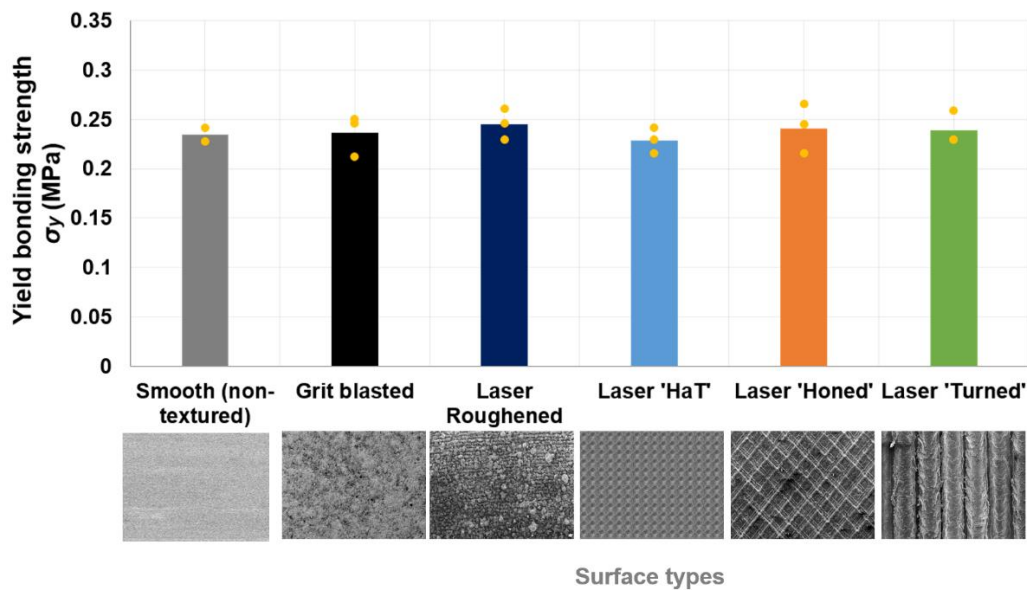


**Figure 118.** Measured yield bonding strength of bonded surfaces with different surface textures

Meanwhile, the ultimate bonding strength can be increased considerably, varying on the surface texturing applied. At most, this improvement on the mean value can be 56.45% (by grit- blasting) from the smooth surface (mean value of 10.22MPa) as displayed in **Figure 119**. Following grit-blasting, laser-roughening can increase the ultimate bonding strength by around 4.0 MPa. Meanwhile, all the laser surface texturing seem to create minimal improvement.

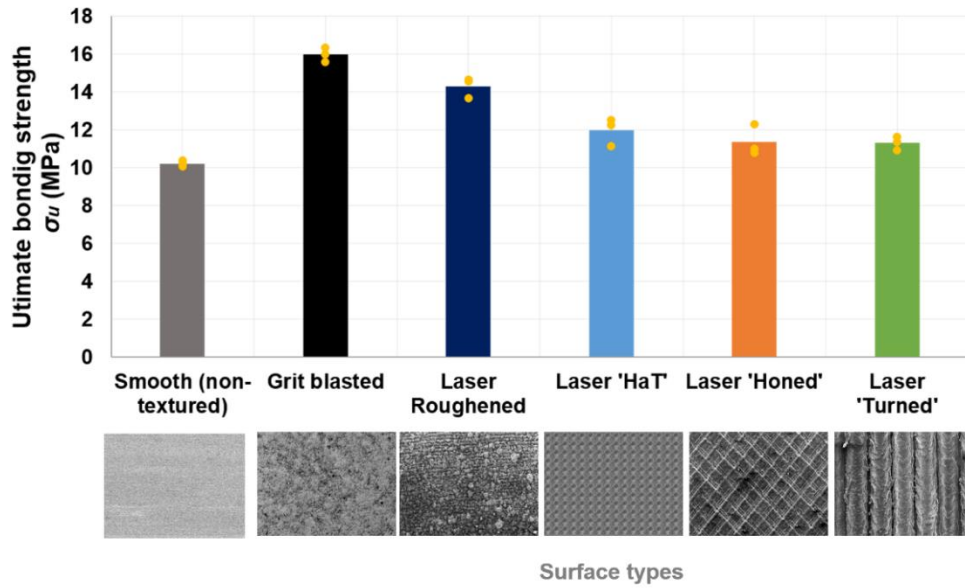


*Figure 119. Measured ultimate bonding strength of bonded surfaces with different surface textures*

To determine whether the difference brought by the surface texturing on bonding strength is significant, one-way analysis of variance (ANOVA) was performed by MATLAB 2017a. Based on ANOVA, to investigate which surface textures can incur significant influence, multiple pairwise comparison t-tests using Tukey's honesty significant difference criterion were conducted on MATLAB 2017a.

From the one-way ANOVA, it was derived that for the first dataset- the yield bonding strengths of different surfaces, the p-value (probability of that test statistic  $F$  is larger than computed statistic 0.19) is 0.9734, which is much larger than 0.05. Therefore the data for different surface types are not significant different, or in other words, the yield bonding strength is not effectively influenced by the surface textures.

As for the ultimate bonding strengths of varied surfaces, the p-value (probability of  $F > 32.32$ ) is  $4.39 \times 10^{-7}$  (much smaller than 0.05), indicating that for some of the surfaces the data are significantly different with each other. Then, from the results of pairwise t-tests (**Figure 120**), it can be seen that the three surface texturing that can credibly improve the ultimate bonding strength are grit blasting and laser roughening.

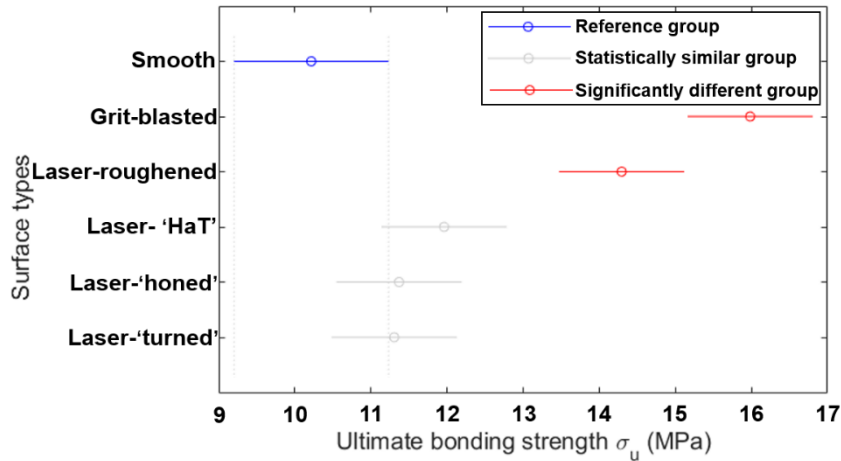


*Figure 120. Multiple pairwise comparison t-tests results- estimates of ultimate bonding strength with comparison intervals for different surface types*

Overall, both novel roughening processes generate significant boost to the ultimate bonding strength, matching that of the grit-blasting. Meanwhile the yield bonding strength is not statistically influenced. A possible explanation is that the yield bonding strength denotes phenomenon like non-texture-related phenomenon, such as adhesive bulk yielding, instead of adhesion failure.

### 6.3.2 Contact angle measurements

As the contact angle of a liquid droplet is often regarded as an indicator for adhesion [200] and bonding strength [201], it was measured on different textured surfaces to assess its association with the bonding performance achieved. With this evaluation, the capability of using it as an index for future texturing design is explored.

The contact angles of the water droplet on the different types of surfaces can be obtained using the automatic angle measuring function once the contact point is captured in the built-in software, like shown in **Figure 121**. (a). However, on some of the surfaces, for example, the laser-roughened surface, the water droplet spreads over immediately after being applied, like shown in **Figure 121**. (b). In this case the on contact point, the line tangential to the droplet profile is redeemed as parallel to the surface, leading to a near-zero wetting angle, and the surface is considered as super-hydrophilic.

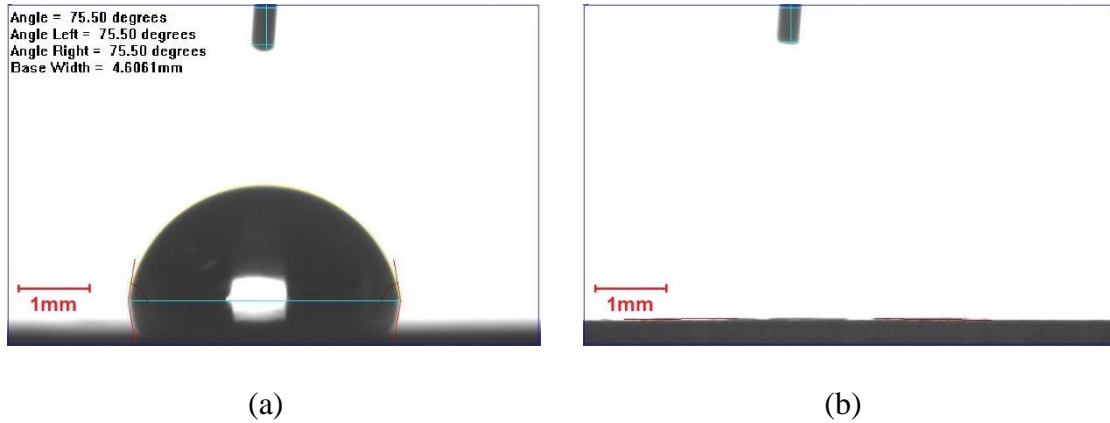


**Figure 121.** Contact angle measurement of a water droplet on (a) a smooth (non-textured) surface, (b) a laser-roughened surface.

As summarised in **Figure 122**, by grit blasting, and laser-roughening, the hydrophilicity of the original smooth (non-textured) surface (contact angle around  $76.13^\circ$ ) can be enhanced to super-hydrophilicity. Meanwhile, with the other three laser surface textures, the wettability can also be altered to a smaller degree. However, one thing needs attention is that, the contact angles measured on the laser-turned surface (with grooves) would differ greatly depending on the viewing angle – it is always higher when measured parallel to the grooves (around  $83^\circ$ ), and significantly lower when measured vertical to the grooves (around  $56^\circ$ ). Nevertheless, what really relates to the measured bonding strength angles should be the ones measured from vertical direction, since they reveal how the water droplet ‘spreads’ along the groove direction (also the shearing direction).

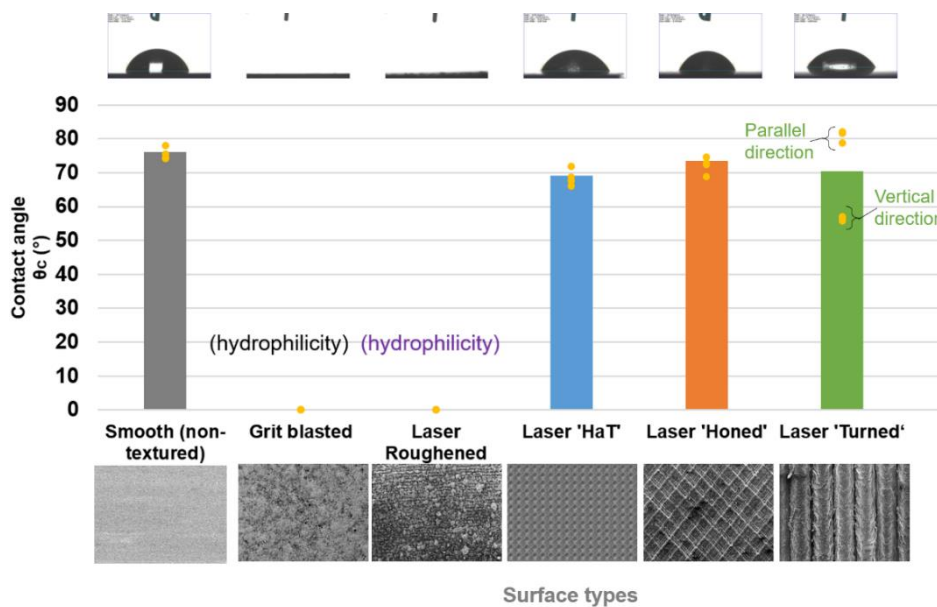


**Figure 122.** Measured contact angle of water droplet on different surface textures

Similarly, the significance of difference between the data were also analysed using one-way ANOVA and multiple pairwise t-tests. From the analysis, significant variance was found between measured contact angles of the different surfaces (with p-value  $3.90 \times 10^{-20} \ll 0.05$ ), and the groups that are statistically different from the smooth (non-textured) surfaces are surfaces textured by grit blasting, and laser roughening (demonstrated in **Figure 123**). This finding matches with the result from the last section (6.3) as the ultimate bonding strength can only be improved by these three surface texturing methods.

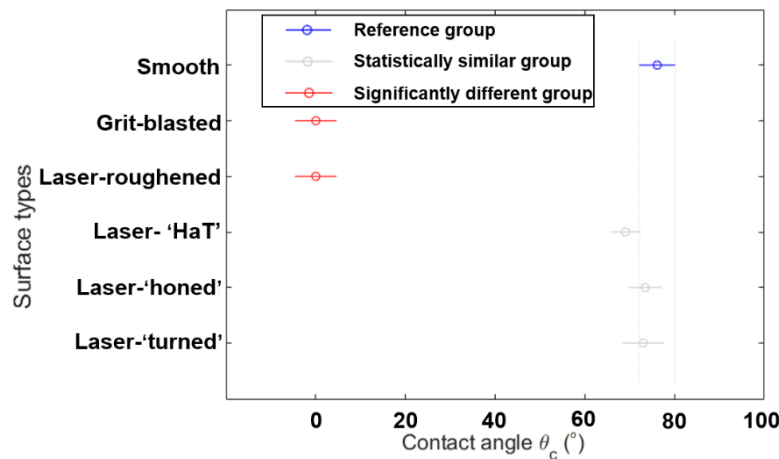


*Figure 123. Multiple pairwise comparison t-tests results- estimates of contact angles with comparison intervals for different surface types*

However, to determine whether the contact angle and the ultimate bonding strength are correlated, correlation analysis including Pearson correlation analysis and Spearman correlation analysis were performed using MATLAB 2017a. The former one test if the two variables are linearly correlated, while the lateral one analyse if monolithic relation (including non-linear) exists based on the rank of the variables. Moreover, since the surface tension between the solid and the liquid ( $\gamma_{sl}$ ) linearly related to the other surface tensions with the term  $\cos(\theta)$  in the young's formula (illustrated in **Figure 19**), the values of  $\cos(\theta_c)$  is also tested for its correlation with the ultimate bonding strength.

From the Pearson test, it was found that linear relations were found for both pair of variable with considerable high coefficient of correlation ( $r = -0.86$  and  $0.85$  respectively), as shown in **Figure 124**. However, the coefficients of correlation for Spearman analysis are even higher, as  $|\rho|$  is around  $0.91$  in both case, denoting significant correlation ( $>0.9$ ). Therefore, it is more probable that the contact angle and the ultimate bonding strength of a surface are correlated

with a non-linear relationship, and the relationship is monolithic- lower the contact angle, higher the bonding strength.

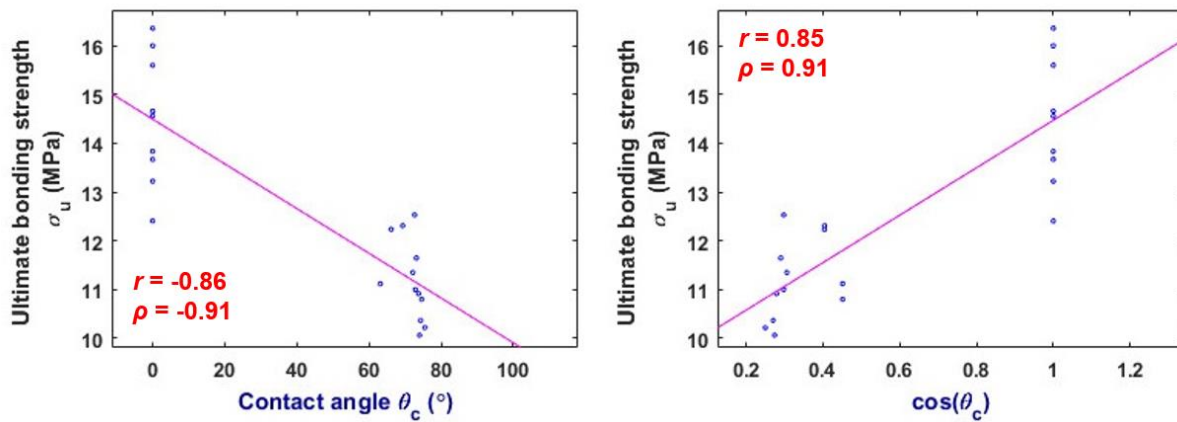


*Figure 124. Correlation graph between (a) ultimate bonding strength and contact angle, (b) ultimate bonding strength and cosine value of contact angle*

In a word, the improvement of wettability can serve as a criterion whether the introduced surface texturing/roughening process can improve the bonding strength.

### 6.3.3 Post-test SEM analysis

As the influences of the developed surface roughening/texturing techniques on the performance in lap-shear test have been determined, SEM analysis of the surfaces after the tests can help analyse the proportion of different types of failure (cohesive and adhesive) occurred during the tests, and identify possible mechanism in influencing bonding strength.

To identify cohesive and adhesive failures, the BSE mode was used in SEM analysis as contrast should be built between the reserved adhesive (phenolic) and the surfaces (steel). The adhesive failure in this case is the separation of the adhesive from the surface as a result of insufficient adhesion, while the cohesive failure reveals that the cohesive bond within the bulk of adhesive itself is prevailed by the adhesion. Therefore, considering a constant adhesive bulk cohesion, for the study conducted, less the adhesive failure / more the cohesive failure, better the adhesion performance the developed surfaces give.

For the analysis of the failure modes in lap-shear tests, data of percentage of reserved adhesive was collected using tools like imageJ software (as shown in **Figure 125**). One should notice that this needs to be done on both specimen surfaces in a lap-shear test. This is because the proportion of cohesive failure is not simply how much area on one surface the adhesive is not

ripped off, but a function of the statistics from both surfaces considering the scheme demonstrated in Figure 126.

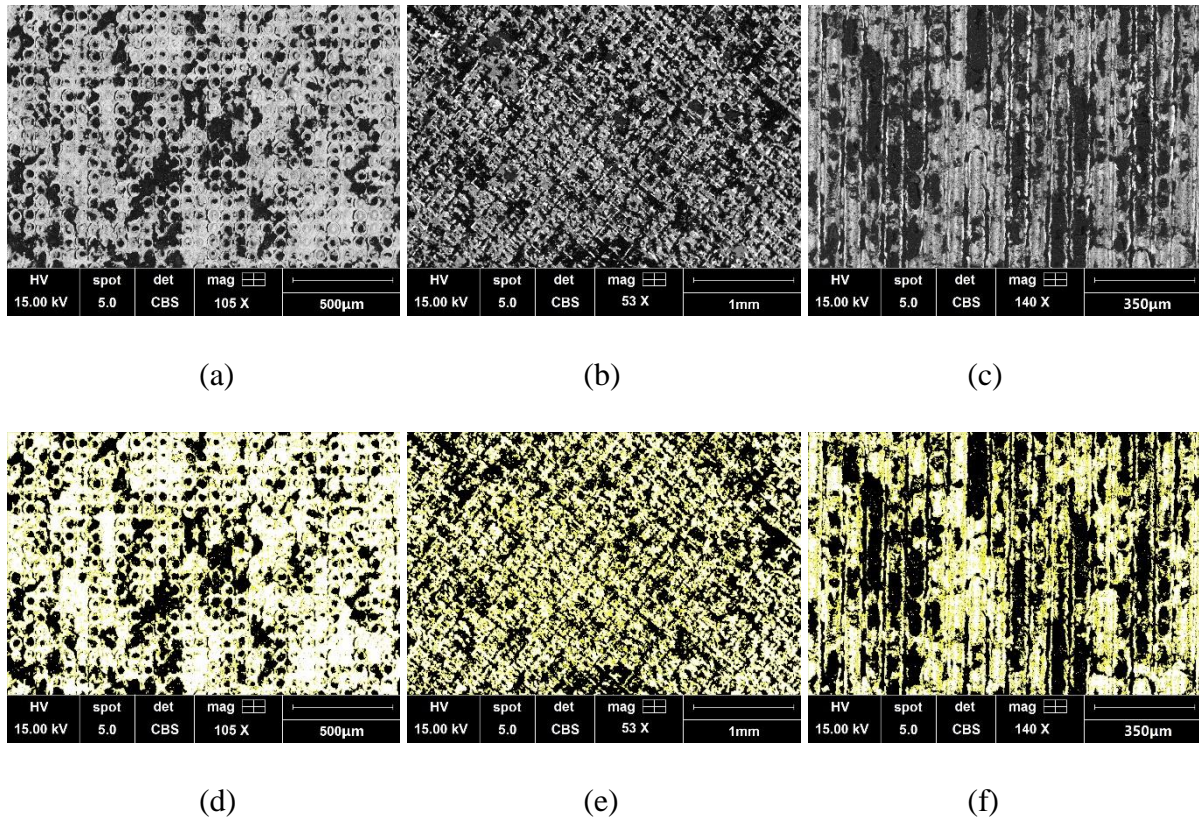


Figure 125. SEM image (BSE) of (a) Laser HaT surface, (b) Laser honed surface and (c) Laser turned surface; binary images (with separation areas highlighted) of (d) Laser HaT surface, (e) Laser honed surface and (f) Laser turned surface

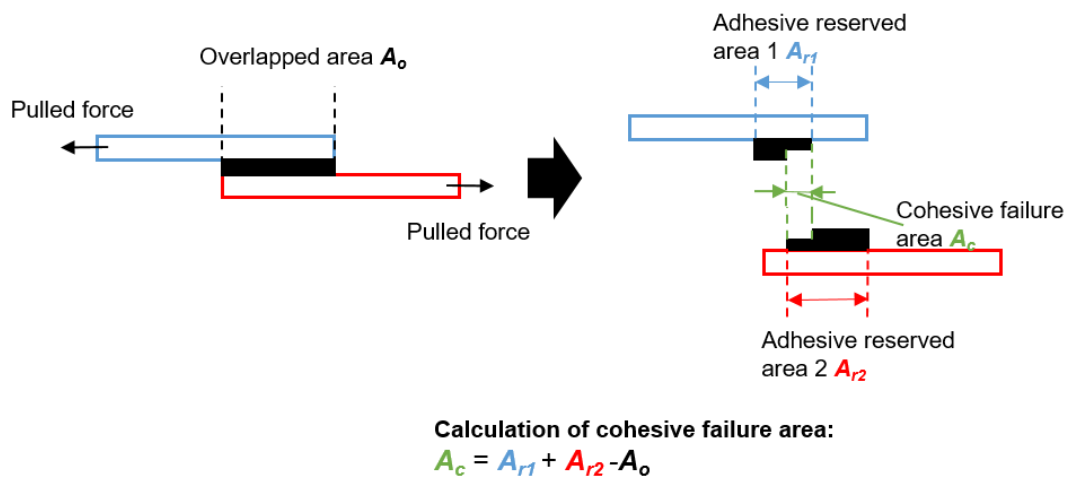
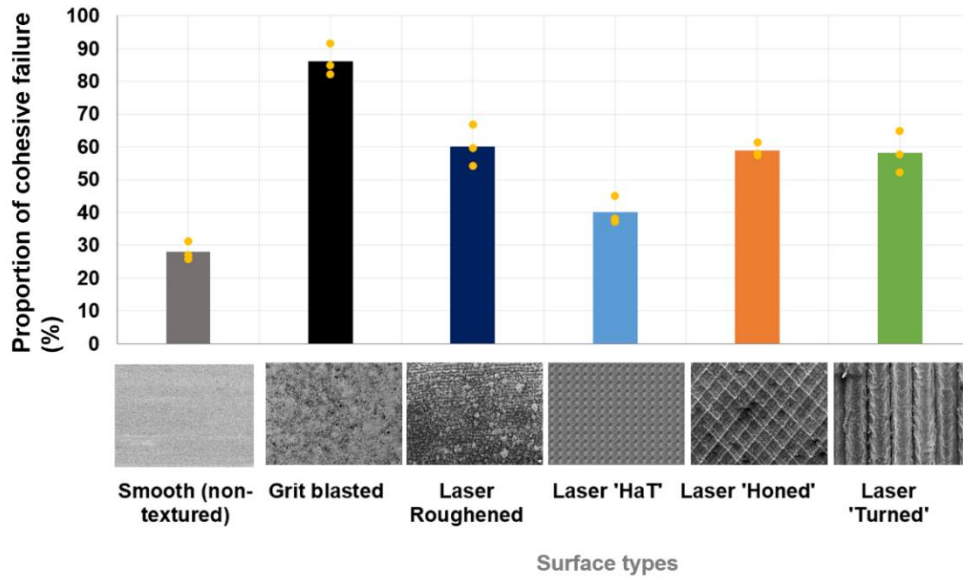


Figure 126. The principle for calculating cohesive failure area

With the calculating principle, the proportion of cohesive failure occurred in all lap-shear tests was obtained. As shown **Figure 127**, Grit-blasted surfaces saw the highest rate of cohesive failure of nearly 90% in average, meaning that with these two types of surfaces, adhesive failure rarely occurred. For all the laser-textured surfaces, this rate is around 40 to 60 percent, also

much higher the smooth surfaces (around 28%). Surprisingly, laser-roughened surfaces, which has much superior bonding performance (similar with grit-blasted), also have similar cohesion failure rate, at around 50%.



*Figure 127. Proportions of area with reserved adhesive after lap shear tests on surface with different textures*

With a higher magnification to analyse the surface, the answer was found: some of the delaminated counterface asperities were retained, as their flat delamination section were observed, like shown in **Figure 128** (a). During image processing, these areas would be automatically treated as adhesion failure area. Such a phenomenon, as illustrated in **Figure 129**, emerges from the intersecting and interlocking of the asperities from mating surfaces. In fact, the resultant failure should also be regarded as a cohesive failure, but should be called ‘adherent cohesive failure’, to distinguish it from the common cohesive failure referring the one for the adhesive bulk. The occurrence of this also implies that the adhesion between adhesive and solid surface is strong enough so delamination would emerge elsewhere, but it is worth noticing as it shows the micro/nano-structures created are just clusters of re-solidified deposits, and may not have sufficient bulk strength.

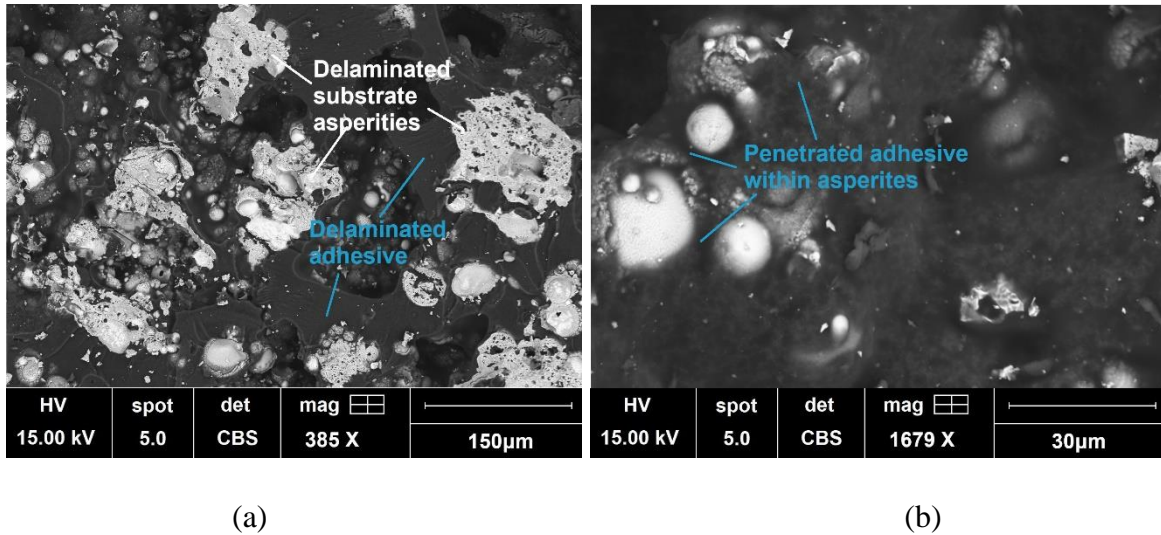


**Figure 128.** SEM image of a laser-roughened surface (after lap shear test) with (a) 385× magnification to analyse mainly the condition of remained resin and (b) 1679 × magnification to analyse mainly the surface topography of the steel

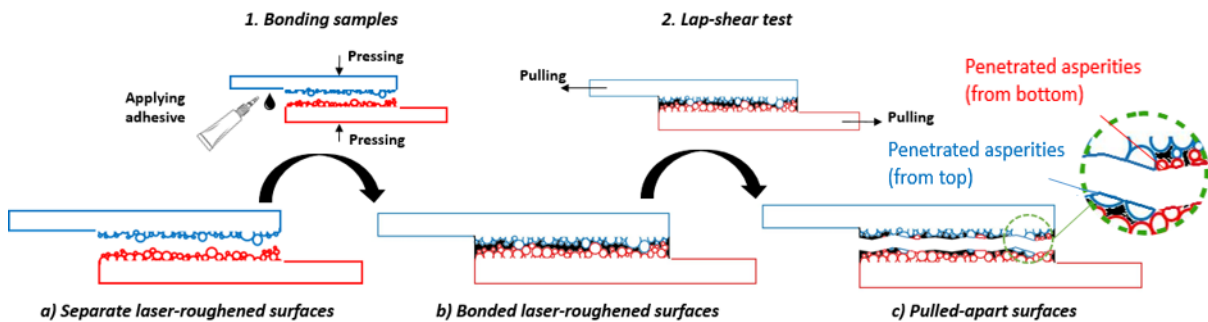


**Figure 129.** Schematic view of the formation of the cohesive failure of both the adhesive layer and the substrate asperities from lap-shear test of laser-roughened surfaces

On the grit-blasted surfaces, difference was observed between the rougher area and smoother area for their capability in reserving adhesive, like shown in **Figure 130**. Even in the laser textured surface, adhesive tends to be preserved more within the trenches/dimples, in which micro-level structure- LIPSS exist, as shown in **Figure 131**. However, it should be noticed that this does not prove the superiority of micro/nano-roughness in providing higher adhesion force, since it has been pointed out that adhesive remained on one surface does not guarantee adhesive failure did not occur on the counterface.

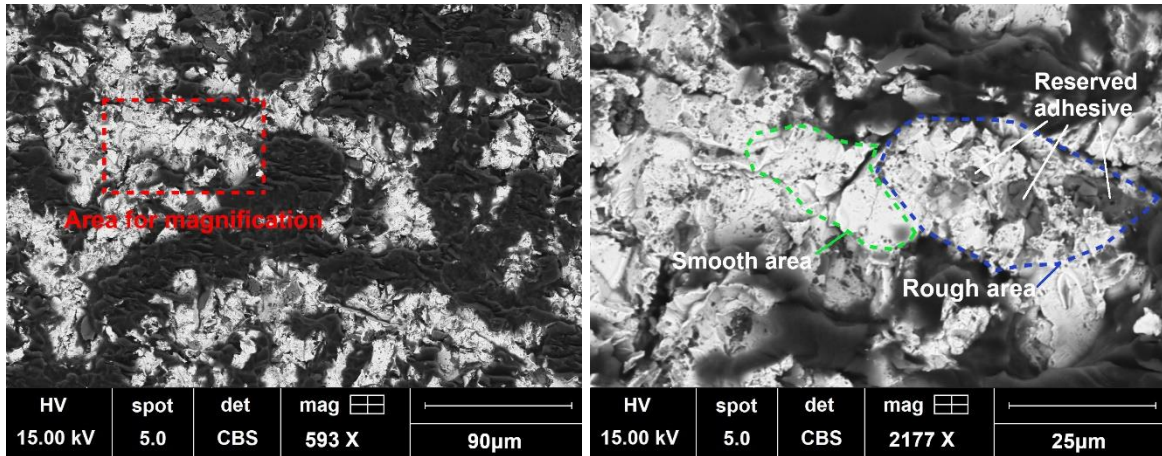


Figure 130. SEM image of a grit-blasted surface with (a) 593× magnification to analyse mainly the condition of remained resin and (b) 2177 × magnification to analyse mainly the surface topography of the steel substrate

For the surfaces textured by laser mimicking those conventional machining processes, the reserved adhesive on the surface mainly located within the trenches or dimples produced, as shown in **Figure 131**.

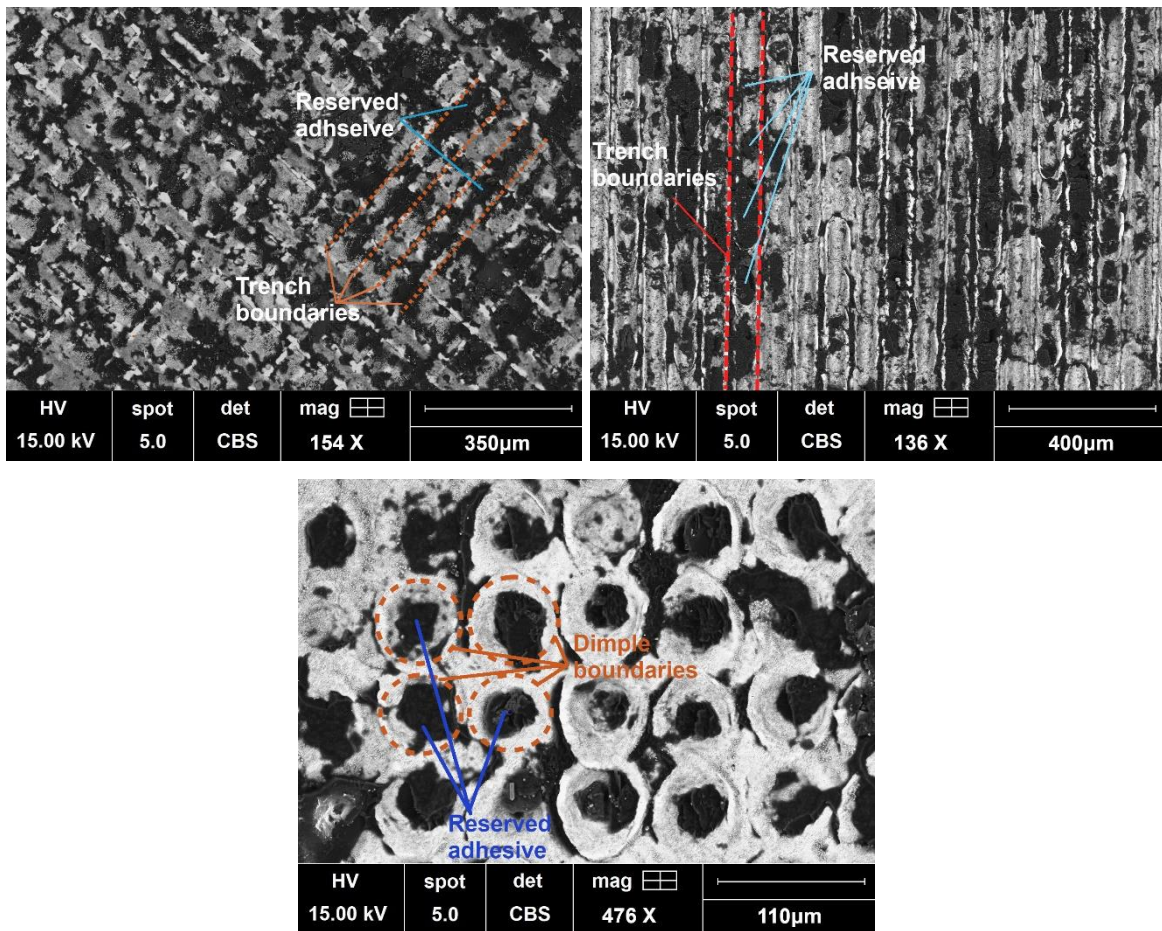


Figure 131. SEM images (BSE mode) of the (a) laser honed (b) laser turned and (c) laser HaT surfaces after lap-shear tests for indicating the distribution of reserved adhesive

Overall, the developed roughening processes generally lead to a substantially enhanced adhesion performance. Among them, laser-roughening also has a prominent inter-locking effect, even-though the surface structure's strength may not withhold this effect. The laser-textured surfaces, however, would still see considerable proportion of adhesive failure during lap-shear tests even if it has some advantage towards the smooth (non-textured) surface.

#### 6.4 Bearing liner peel tests – for qualitative final check

For a qualitative determination whether the bond with the liner on the real bearing sleeve can be sufficient, an empirical test method for bearing manufacturers is the peel test of the liner. After a small detachment initiated by a scalpel, the PTFE/glass fibre composite liner that was initially bonded on the sleeve surface (following the standard process from SKF Ltd) would be peeled along to check whether succeeding delamination would occur between the liner and the outer-ring surface (failure condition) or only within the composite layers (pass condition).

From the peel tests of the bearing liner, it was found that on the smooth surface (polished, non-textured) almost the whole was peeled off the outer ring surface, as shown in **Figure 132(a)**. From the SEM analysis, it can be seen that only smears of the resin- the dark spots in **Figure 132(c)** were still reserved on the surface. These observations indicated that the bond formed with the smooth surface is inferior to the strength of the liner itself, leading to a contact system more venerable to large shear force.

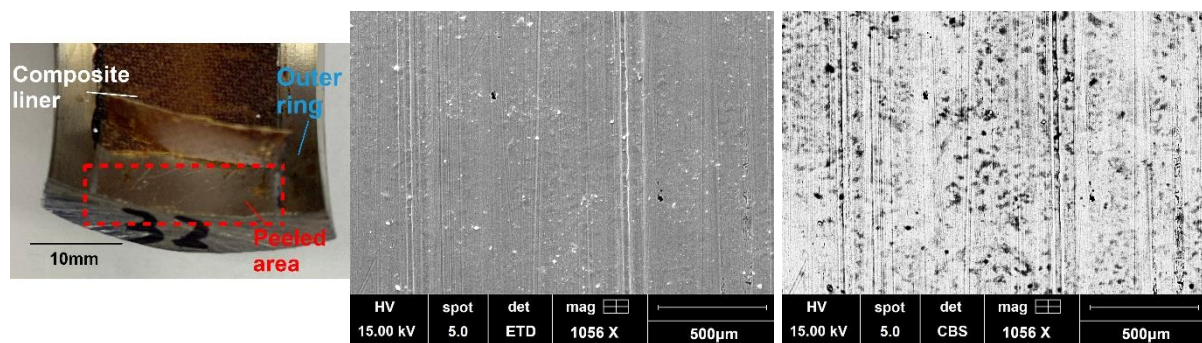


*Figure 132. (a) Photographic image, (b) SEM image (SE mode) and (c) SEM image (BSE mode) of the smooth inner surface of the outer ring after the peel test*

In comparison, the grit-blasted surface was able to avoid any interfacial separation and only lead to detachment within the liner. As shown in **Figure 133(a)** to (c), bottom layers of the liner were still preserved and no bare steel surface was exposed. From the EDX analysis in **Figure 134**, which indicated both the Fluorine-rich layer and the Silicon-rich layer, it can be postulated that the entire bottom layer (mainly glass fibres), and the majority of the middle

layer (mainly PTFE fibres) have been reserved. This indicated that both the resin-steel bond and the liner-resin bond were strong enough, that during peel the detachment could only progress from a weaker position - between the layers within the composite liner itself.

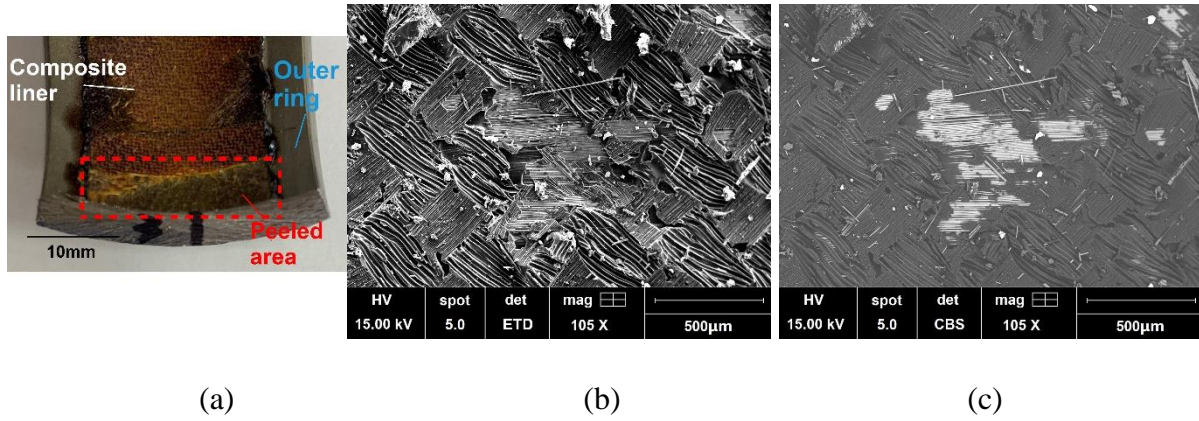


**Figure 133.** (a) Photographic image, (b) SEM image (SE mode) and (c) SEM image (BSE mode) of the grit-blasted surface of the outer ring after the peel test

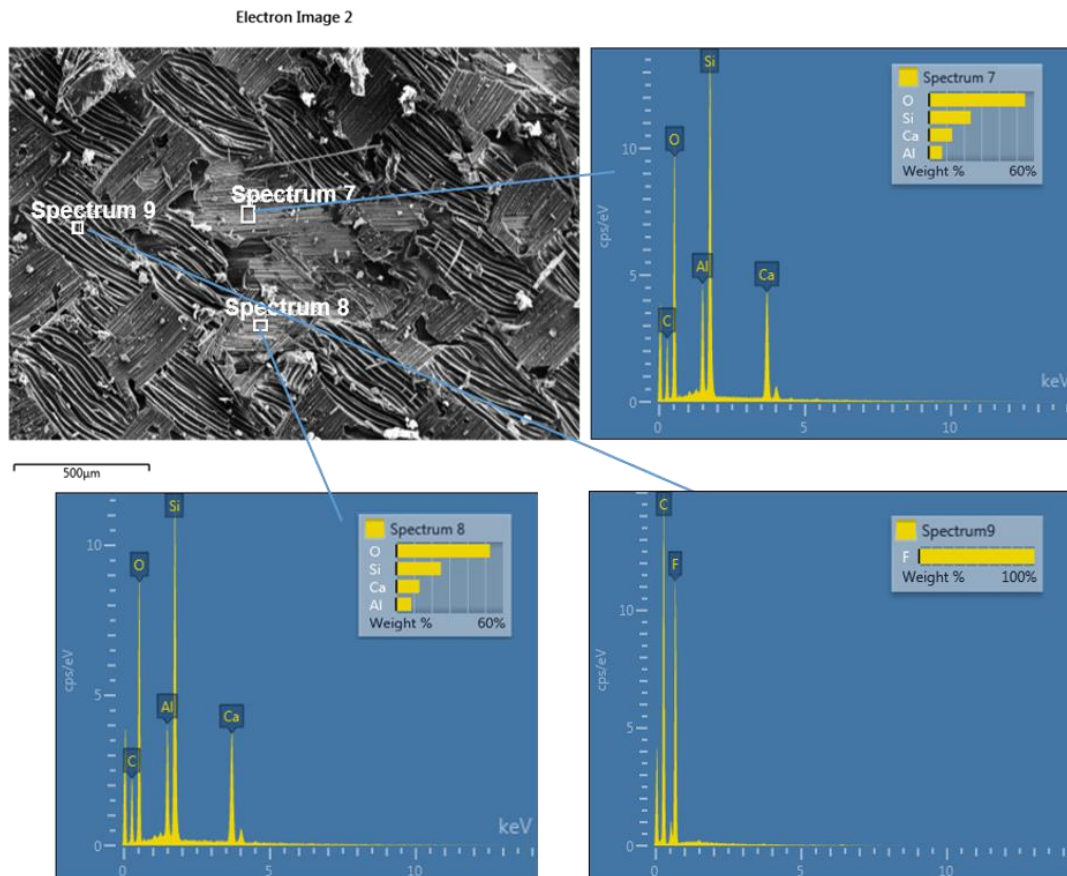


**Figure 134.** EDX analysis of the elemental composition of the glass fibre layer (spectrum 7 and 8) and the PTFE layer (spectrum 9) reserved on the outer ring surface after the liner peel test

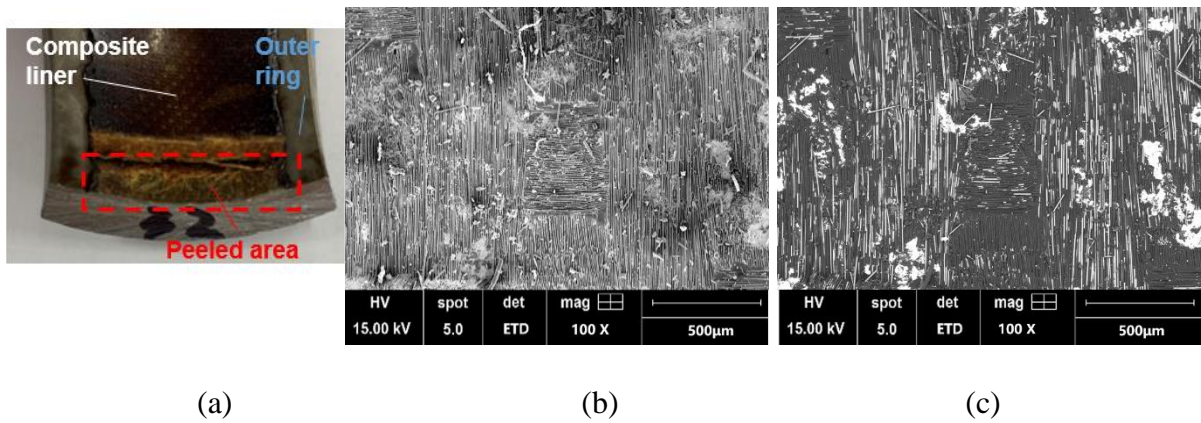


**Figure 135.** (a) Photographic image, (b) SEM image (SE mode) and (c) SEM image (BSE mode) of the laser-roughened surface of the outer ring after the peel test

As for the surface textures produced with conventional machining processes, the peeling would always result in a detachment of the majority of the liner from the sleeve surface, as displayed in the peeled area in **Figure 136** - **Figure 138**. Certain liner layers were preserved, but all in very small proportions. From the SEM analysis, it can be seen the reserved material was mainly bulk resin, while very limited amount of fibres were observed. On the hard-turned surface, as indicated in **Figure 138**, the resultant surface was almost just like that of the smooth surface.

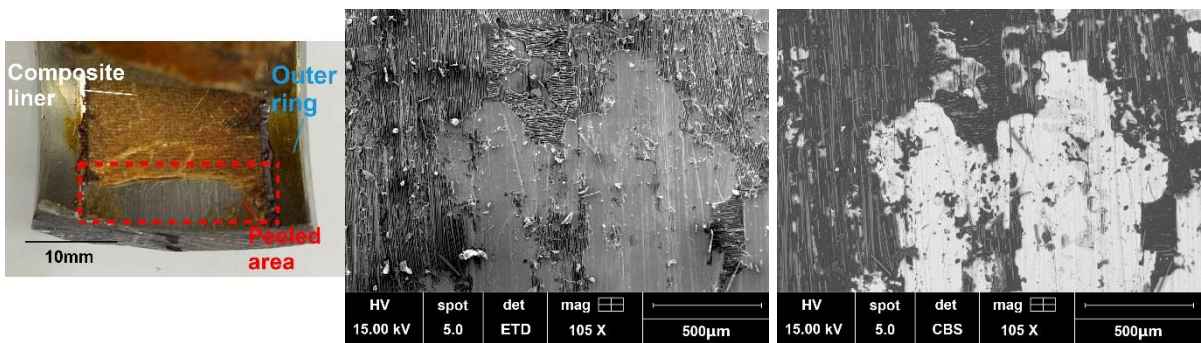


**Figure 136.** (a) Photographic image, (b) SEM image (SE mode) and (c) SEM image (BSE mode) of the turned inner surface of the outer ring after the peel test

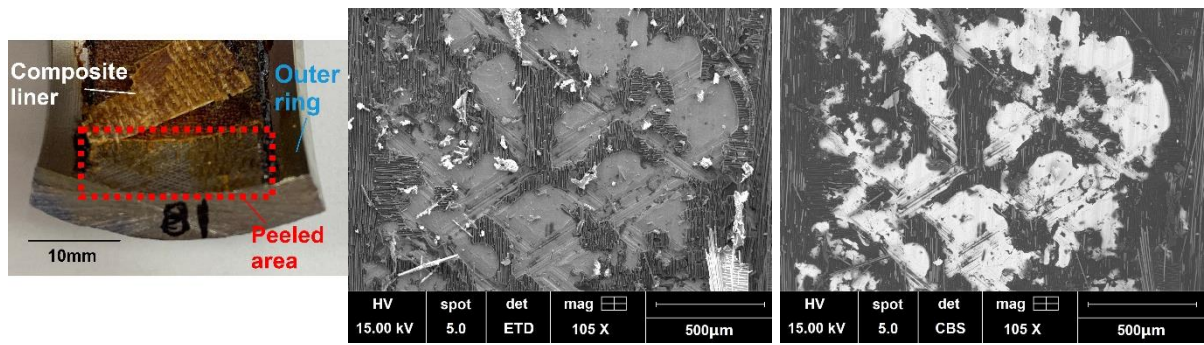


**Figure 137.** (a) Photographic image, (b) SEM image (SE mode) and (c) SEM image (BSE mode) of the honed inner surface of the outer ring after the peel test

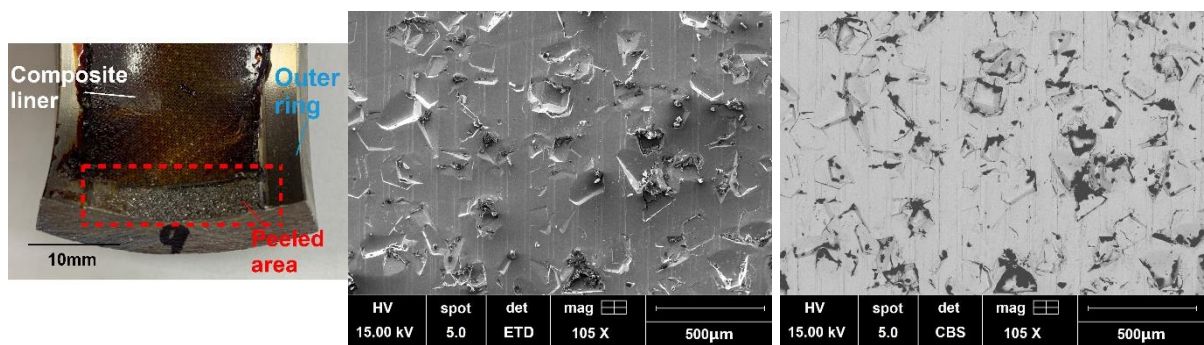


**Figure 138.** (a) Photographic image, (b) SEM image (SE mode) and (c) SEM image (BSE mode) of the HaT inner surface of the outer ring after the peel test

Overall, all the conventional machining process provided very limited increase in the resistance to peel for the bearing liner, while laser roughening can achieve similar liner-reserving capability like grit blasting. This ability can prevent catastrophic separation of the liner under the extreme case where certain detachment has been established.

## 6.5 Wettability analysis for the roughened/textured surfaces

Due to the significant correlation found between the bonding strength and the wettability of the surfaces, the contact angle should be a pertinent index for indicating the influence of surface roughness/textures on the bonding strength. Furthermore, to provide initial designing principles for fabrication of surface textures (possibly reducing experimental work), interpretation and theoretical models of the influence of topographic features on the formation of wetting angles are needed.

### 6.5.1 Interpretation using conventional models and the inefficiency

In order to explain the difference in measured contact angles on varied textured/roughened surface, the classical wettability model were employed at first.

The theories behind the improvement of bonding strength through roughening/texturing include the penetration of the adhesive into the micro surface structures, creating a multiplication of real contact area and even mechanical-interlocking[163]. As one of the classical theories of modelling contact angle, the Wenzel's model is in coherence with this theory. It illustrates the phenomenon that on a rough surface the asperities would be immersed by the liquid, adding more contact area and leading to further wetting than an ideally smooth surface. The consistency between the surfaces with super-hydrophilicity and those with significantly improved bonding strength presented in the chapter 6.3.2 proves this correlation. However, for other textured surface ('laser turned', 'laser honed' and 'laser HaT'), neither a similar improvement in wetting behaviour nor a considerable level of increase in bonding strength was observed, even though similarly micro-roughness (from LIPPS) were created on these surfaces. Provided that the LIPPS were generated only within the trenches or dimples created by the laser, CB's model may give an explanation of this difference – air-pockets may be trapped within the concavities to prevent immersion by the liquid droplet.

To evaluate the applicability of Wenzel's and CB's theory in modelling the contact angles for the roughened/textured surfaces, the contact angles computed with both models are compared with the measured ones as shown in **Figure 139**. In the Wenzel's model it is assumed contact occurred between the liquid and all the asperities and concavities, while in the CB's model the textured part of the surface is regarded as completely separated from the liquid surface. The estimation of the surface area with the roughened/textured surfaces is based on the surface characterisation in chapter 6.2, like shown in **Figure 114****Error! Reference source not found..**

From the comparison, it can be seen that for the roughened surfaces, the super-hydrophilicity can be accurately reflected by the Wenzel's model, but for the three types of laser textured surfaces, the predicted contact angles based on the CB's hypothesis are considerably lower than the measured data. In fact, the measured contact angles for laser textured surface are between the values predicted by Wenzel's model and CB's model. Moreover, for laser-turned surface, significant anisotropy in wettability was observed- the contact angle observed from parallel to the trenches is around  $82^\circ$ , but becomes around  $56^\circ$  when measured from the view vertical to the trenches (used in the last chapter as it indicates the wetting performance along the lap-shear direction), as demonstrated in **Figure 140**.

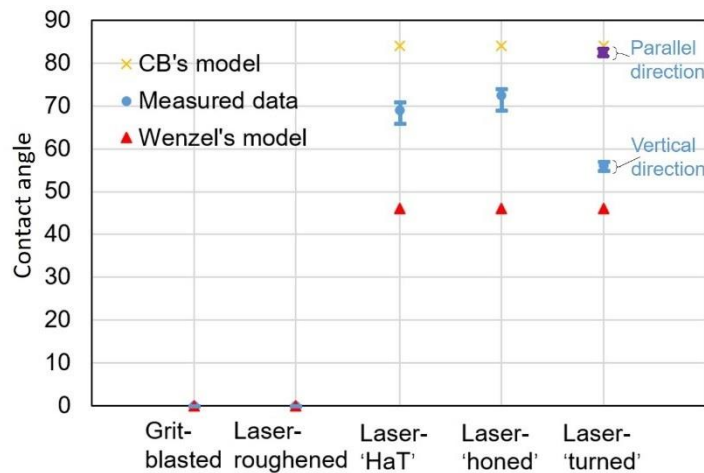


Figure 139. Comparison of measured contact angle data with predicted by classical models

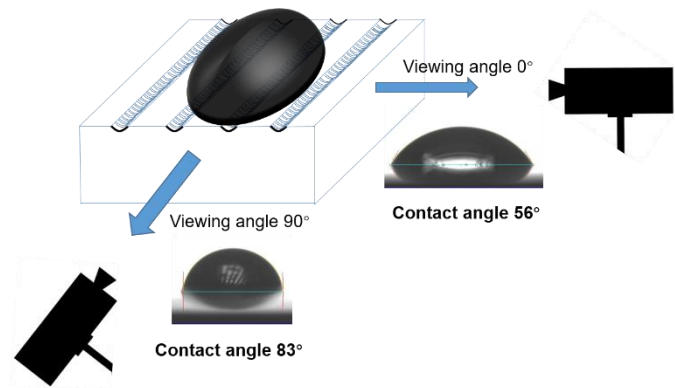


Figure 140. Anisotropy of contact angles for laser-turned surface

Judging from the deviance of both models, and that the laser textured surfaces in this thesis contain two types of textures (trench and micro-level LIPSS in it) which theoretically may lead to opposite wetting behaviour, it is reasonable to postulate the real condition of the wetting on the these surfaces may be mid-way between the Wenzel's and CB's model- the liquid may partially penetrated and wetted the textured concavities. Therefore, a new model is proposed to describe the generic condition of texture wetting (partial penetration) rather than the extremes posed by the two classical models. Meanwhile, the wetting behaviour in a three-dimensional regime should be included in the model to account for the anisotropy with the laser-turned surfaces in this thesis.

### 6.5.2 Derivation of the wettability model based on surface free energy analysis

As has been proposed, the model should take into consideration the in the 3D scheme, so direct modifications on the Young's model like Wenzel's model and CB's model could not be

sufficient. Therefore, the model is derived from the fundamental analysis of surface free energy so that a comprehensive consideration of the influence from surface topography can be included.

Firstly, the derivation of the basic form of free energy analysis is presented using fundamental conceptions illustrated in many previous literatures [224,225], providing basis for the contact angle model. Basically, the main principle of the surface energy analysis is that, the solid-liquid-gas system would only become equilibrium when the total free energy of the surfaces is minimized, otherwise it would have the tendency to fall to a lower state. In this three-phase system, the free energy is the summary of the products of the contact area and unit surface energy (surface tension  $\gamma$ ) in different medium pairs (solid-gas, solid-liquid and liquid-gas). Since the surface tension in different medium pairs is determined by their inherent nature, the minimising of free energy is through adjusting contact areas, i.e. by altering liquid morphology. For example, an ideally small volume of liquid droplet (gravity effect etc. neglected) in the gaseous atmosphere would form a spherical shape by itself to minimize the surface free energy, which would be:

$$W_l = A_{lg}\gamma_{lg} = 4\pi r^2\gamma_{lg} \quad (6.1)$$

where  $r$  is the radius of the droplet sphere, and  $\gamma_{lg}$  is the surface tension between the liquid and the atmospheric gas.

As for when the liquid gets into contact with a nominally flat solid surface, the droplet may or may not spread to a certain extent over the solid surface until it reaches a new equilibrium state. Despite the complexity of analysing the evolution of surface energy during this process, a two-state simplification is utilized to describe the phenomenon (referring to the approach used in [224]). Firstly, it is presumed the in the air the droplet has formed the shape with a spherical upper surface (to minimise liquid-gas interfacial area) and a flat bottom surface (as constrained by the solid surface), like shown in **Figure 141**. In the first step, the total free energy of the system is the combination of that with liquid-gas interface and solid-gas interface:

$$W_{total1} = \gamma_{lg}(A_{sl} + A_{lg}) + \gamma_{sg}A_s \quad (6.2)$$

where  $A_{sl}$ ,  $A_{lg}$  are the interfacial area of correspondingly solid-liquid interface liquid-gas interface,  $A_s$  is the overall surface area of the solid surface and  $\gamma_{sg}$  is the surface tension between solid and gas. Then in the second step, the bottom of the droplet gets into contact with the solid surface. In this process the area of liquid-gas interface on the bottom of the liquid, as well as



$$\cos \theta_Y = \frac{\gamma_{sg} - \gamma_{sl}}{\gamma_{lg}} \quad (6.7)$$

By introducing factors to modify the apparent contact area  $A_{sl}$  in equation 6.7 to real contact area considering the roughness and gas-pockets with rough/textured surfaces, Wenzel's equation and CB's equation can also be formed.

The free energy analysis, combined with the modelling strategies for 2D wetting system used by researchers like W Li [226] and Y Liang [178] and an improved geometric analysis to account for the 3D geometry formulate the model to predict the contact angles on the textured surfaces.

Firstly, resembling the two-step analysis for the surface free energy of the liquid droplet, a similar procedure is introduced for the condition with a textured surface: in the starting state, it is assumed that the liquid droplet is in the form of equilibrium on a smooth solid surface. Then, it 'spreads' (like the transformation from the starting state to transformed state in **Figure 142**) or 'shrinks' (reverse to the transformation in **Figure 142**) on the textured surface till the new real equilibrium state is reached. Since equilibrium state has been achieved on the first step, the key is to analyse the change of surface free energy in the second step.

With the introduced wetting behaviour, that the liquid would penetrate a top proportion of the trenches, the change in free energy can be expressed as:

$$\Delta W = \gamma_{lg} \cdot G(y) + (\gamma_{sl} - \gamma_{sg}) \cdot S(y) \quad (6.8)$$

where the first term is the increase of free energy caused by the increase of liquid-gas interfacial area-  $G(y)$ , including that from the upper surface of the droplet, and the addition from the formation of gas-pockets. The second term is the increase of free energy caused by the increase of liquid-solid interfacial area-  $S(y)$ , including that with the un-textured area and with the texture areas immersed by the liquid.

Combined with the Young's equation (equation 6.7), the change in free energy can be converted into

$$\Delta W = \gamma_{lg} \cdot [G(y) - \cos \theta_Y \cdot S(y)] \quad (6.9)$$

and then further normalized to

$$\Delta F = g(y) - \cos \theta_Y \cdot s(y) \quad (6.10)$$

where  $\Delta F$  is the surface energy alteration normalized to the unit of length, and  $g(x)$  and  $s(x)$  are the change in contact length corresponding to  $G(y)$  and  $S(y)$  when analysed under 2-D scenario.

Therefore, according to equation 6.10, the change in surface free energy is determined by the combined effect of the ‘spreading’ extent ( $y$ ), the geometric variation (influencing  $g$  and  $s$ ) and the intrinsic properties of the surface ( $\theta_Y$ ). Conceptually, the increase of gas-liquid interface -  $g(y)$  would lead to increase of free energy, while the increase of solid-liquid interface -  $s(y)$  would do the opposite, if the initial state is hydrophilic ( $\theta_Y < 90^\circ$ ). Normally, the ‘spreading’ would lead to the increase of both interfaces simultaneously but in different extent, so the equilibrium position is the threshold point after which no more drop of free energy can be incurred by further wetting. Moreover, in the two-tier textured surface in this thesis, the micro-roughness would magnify the increase of solid-liquid interface, while the occurrence of trapped gas pocket would contribute to additional gas-liquid interface. Therefore, a numerical analysis of the free energy evolution, taking into account of all the effects stated is needed to give comprehensive explanation of this complex condition.

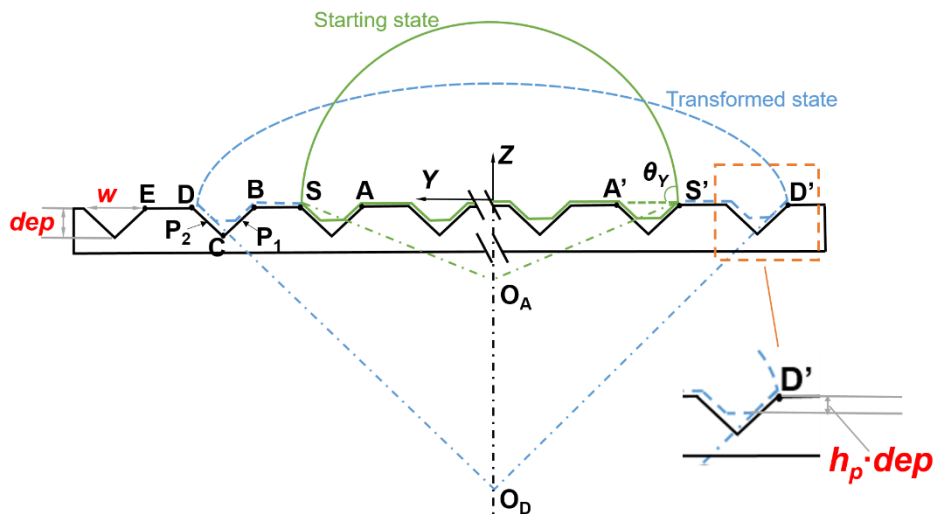


**Figure 142.** Proposed model of the wetting process viewed from  $90^\circ$  viewing angle (from direction parallel with the trenches)

Taking the transformation described in **Figure 142** as an example, the variable  $g(y)$  in equation 6.10 can be expressed as functions of wetting span  $y$ :

$$g(y) = g_u(y) + g_b(y) \quad (6.11)$$

where  $g_u(y)$  is

$$g_u(y)_{S \rightarrow D} = |\widehat{DD'}(y)| - |\widehat{SS'}(y)| \quad (6.12)$$

in which the curve lengths  $\widehat{DD'}(y)$  and  $\widehat{SS'}(y)$  can be computed on the assumption that the curve is a circular arc, and that the section area covered by it keeps constant during the wetting

process. Moreover, with the simplified geometric model for the trenches in **Figure 143**,  $g_b(y)$  can be obtained:

$$g_b(y) = \begin{cases} 0, & y_s \leq y \leq y_s + \frac{h_p \cdot w}{2} \\ y - \frac{h_p \cdot w}{2}, & y_s + \frac{h_p \cdot w}{2} < y \leq y_s + w - \frac{h_p \cdot w}{2} \\ w(1 - h_p), & y_s + w - \frac{h_p \cdot w}{2} < y \leq y_s + w + l \end{cases} \quad (6.13)$$

where  $y_s$  is the half base width of the droplet in the initial state (equilibrium on the smooth surface), and  $h_p$  is the introduced penetration ratio to represent the penetration of the fluid into the texture concavities ( $h_p = 1$  indicates complete wetting into the groove, and  $h_p = 0$  means non-wetting).

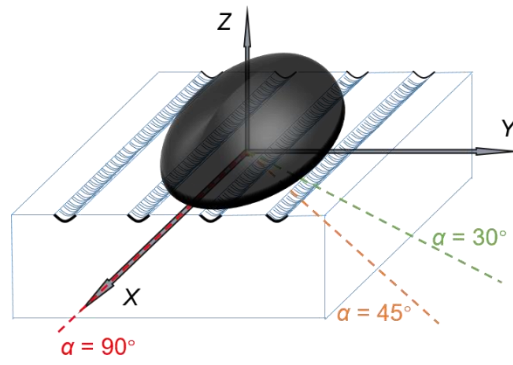
As for the  $s(y)$ :

$$s(y) = \begin{cases} \sqrt{4r_d^2 + 1} \cdot (y - y_s), & y_s \leq y \leq y_s + \frac{h_p \cdot w}{2} \\ \sqrt{4r_d^2 + 1} \frac{h_p \cdot w}{2}, & y_s + \frac{h_p \cdot w}{2} < y \leq y_s + w - \frac{h_p \cdot w}{2} \\ \sqrt{4r_d^2 + 1}(h_p \cdot w + y - w), & y_s + w - \frac{h_p \cdot w}{2} < y \leq y_s + w \\ \sqrt{4r_d^2 + 1} \cdot h_p \cdot w + y - w, & y_s + w < y \leq y_s + w + l \end{cases} \quad (6.14)$$

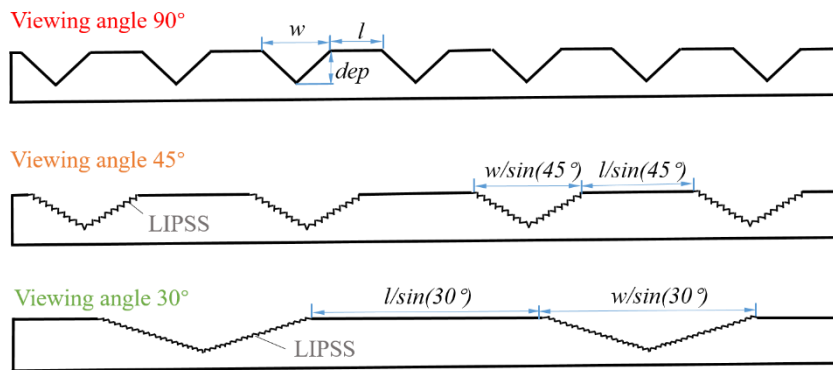
where  $r_d$  equals to  $dep/w$ , denoting the depth-width ratio of the texture.

What should be noticed that, the formulation presented above is only for a special 2D scenario represented by the surfaces with trenches/grooves (from viewing angle  $90^\circ$ ). However, the droplet is a three-dimensional entity and the equilibrium needs to be analysed from different direction, as it has been pointed out that the instabilities from any orientation would interfere the overall equilibrium, leading to further change of liquid morphology [227]. To fulfil this, it is necessary to extend the analysis to in different viewing angles [177].

With the laser-turned surface in this thesis, when viewed from another direction, apart from the extending of the texture width  $w$  and spacing  $l$  incurred by the viewing angle, like demonstrated in **Figure 143**, another modification needed is that when the viewing angle deviates from  $90^\circ$  (parallel with the trenches), the micro-roughness from LIPPS would appear, bringing additional increase on the contact length, as demonstrated in **Figure 143**.



(a)



(b)

**Figure 143.** (a) Different viewing angles for analysing the wettability; (b) the sectional views from different viewing angles

Correspondingly, under viewing angle different from 90°,  $g_b(y)$  should be modified as:

$$g_b(y) = \begin{cases} 0, & y_s \leq y \leq y_s + \frac{h_p \cdot w}{2} \\ (y - \frac{h_p \cdot w}{2}) / \sin \alpha_v, & y_s + \frac{h_p \cdot w}{2} < y \leq y_s + w - \frac{h_p \cdot w}{2} \\ w(1 - h_p) / \sin \alpha_v, & y_s + w - \frac{h_p w}{2} < y \leq y_s + w + l \end{cases} \quad (6.15)$$

where  $\alpha_v$  is the viewing angle as shown in **Figure 143** (a), and  $s(y)$  is updated as:

$$s(y) = \begin{cases} \sqrt{4r_d^2 + 1} \cdot (y - y_s) \cdot \frac{r_a}{\sin \alpha_v}, & y_s \leq y \leq y_s + \frac{h_p \cdot w}{2} \\ \sqrt{4r_d^2 + 1} \frac{h_p \cdot w}{2} \cdot \frac{r_a}{\sin \alpha_v}, & y_s + \frac{h_p \cdot w}{2} < y \leq y_s + w - \frac{h_p \cdot w}{2} \\ \sqrt{4r_d^2 + 1} (h_p \cdot w + y - w) \cdot \frac{r_a}{\sin \alpha_v}, & y_s + w - \frac{h_p \cdot w}{2} < y \leq y_s + w \\ \sqrt{4r_d^2 + 1} \cdot h_p \cdot w \cdot \frac{r_a}{\sin \alpha_v} + (y - w) \cdot \frac{r_a}{\sin \alpha_v}, & y_s + w < y \leq y_s + w + l \end{cases} \quad (6.16)$$

where  $r_a$  is multiplication factor for the real contact length created by the micro-roughness within the grooves- in this case the LIPSS as demonstrated in **Figure 113**.

Based on the model formulated, the curves for the free energy evolution under pre-set wetting process and given conditions (including initial wetting conditions and surface topography etc.) are computed using programming codes in MATLAB R2017a. In every ‘spreading’ (i.e. increased wetting span), or ‘shrinking’ step (i.e. reduced wetting span), the evolution of the droplet section geometry, along with the change in free energy are computed based on equation 6.10 -6.16.

### 6.5.3 Evaluation and application of the wettability model

#### - Evaluation of the basic analysis of surface free energy

At first, to conduct a preliminary evaluation of the developed model in revealing the realistic wetting performance, the model is firstly applied on a condition that has established results and theory - the roughened surfaces with micro-roughness. In this scenario, it is considered that as the micro/nano-asperities uniformly spread all over the surface, the geometric difference of the surface sections from different viewing angles is negligible, and a free energy from one viewing angle is representative. Then, to simulate micro-roughness that can ‘tenfold’ the real contact area, it is set the concavities have very small width and depth ( $w, dep = 0.5\mu\text{m}$ ), and high roughness factor ( $r_a = 10$ ). Applying these conditions, the evolution of free energy versus varying contact angles can be obtained. When plotting the free energy curves of various viewing angles, we artificially impose a gap between adjacent curves at the starting points (on which the  $\Delta F$  value should actually all be 0) for a better demonstration, like shown in **Figure 144**. As can be seen, except for  $h_p = 0$  (no- penetration), with which the free energy curve is almost flat, the free energy curves always monotonically decrease as the contact angle drops from starting point to 0 (i.e. as the droplet ‘spreads’). Moreover, when  $h_p = 1$  (full- penetration), the curve has the highest slope of falling, meaning that by this fashion the droplet would

achieve the utmost minimization of the surface free energy. Overall, the condition reflected by this analysis is consistent with the realistic observation, as well as the Wenzel's theory, that the liquid droplet would wet all the surface and spread over the surface with micro/nano-roughness and lead to an almost-zero contact angle.

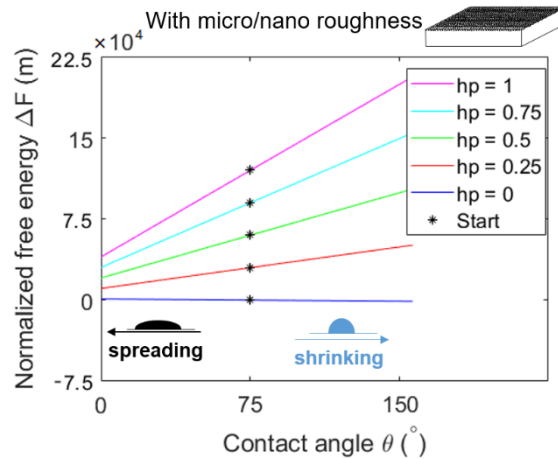


*Figure 144. Free energy curves for the water droplet on a surface with micro/nano roughness under different penetration depths*

As for when the analysis is applied on the laser-turned surfaces in the thesis, the analysis is more complex. As can be seen in **Figure 145** (a), viewed from  $90^\circ$  (from parallel direction to the trenches), the evolution of surface free energy is going through a zig-zag route when the contact angle varies (except for  $h_p = 1$ , full-penetration). Therefore, as demonstrated in detail in **Figure 145** (b), from the starting point S (corresponding to the geometry in **Figure 142**), the three-phase-intersection point would not move to A as there is an energy barrier, but would easily shift to B, and then D as these represent lower-energy states. Later on, at the position D, the point would not easily move either way, as free energy is higher at both B and E. However, since D is only the local minimal, not the global one, once there is a disturbance of the distance

(i.e. un-equilibrium of energy state in another orientation), it still tends to fall toward the D-E-F direction. In positions like D, the system is in a so-called ‘meta-stable’ state.

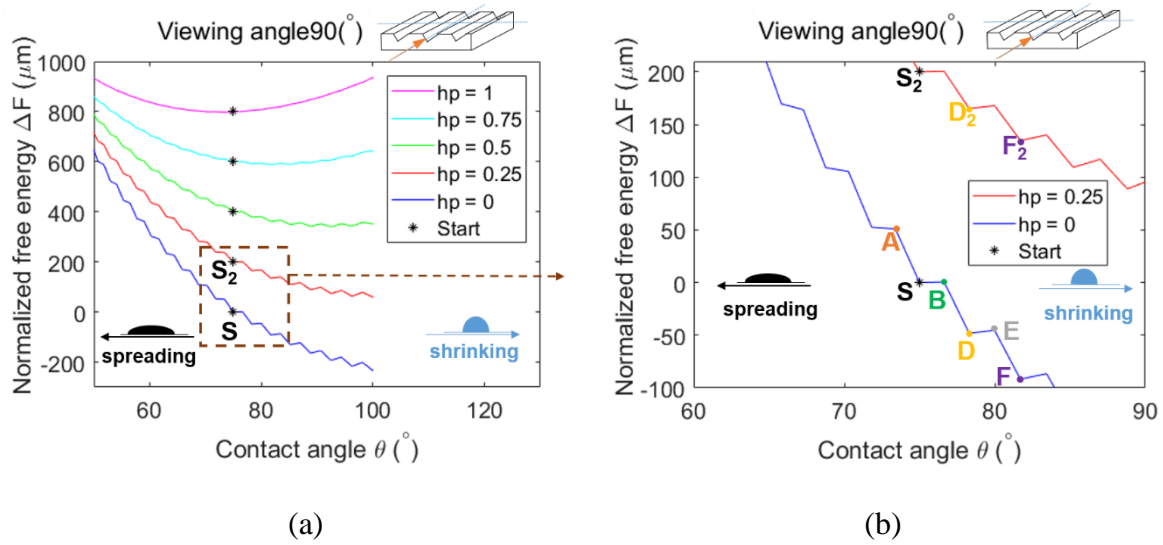


**Figure 145.** Free energy curves for the water droplet on the laser turned surface at viewing angle of  $90^\circ$

Then, to find out in which form the liquid morphology has to be so that the overall stability can be reached, free-energy analysis is therefore needed considering all different viewing angles, like the examples in **Figure 146**. When the viewing angle slightly deviates from  $90^\circ$  to  $85^\circ$ , as shown in **Figure 146** (a), a notable change of the free-energy curves can already be observed: along with the increase of the penetration depth, the free-energy curve has a higher extent of ‘tilting down’ on the ‘spreading’ side. Consequently, unlike under  $90^\circ$ , where meta-stable positions are almost always on the ‘shrinking’ side, the meta-stable positions under relative large penetration depth ( $h_p > 0.5$ ) are now located on the ‘spreading’ side, i.e. with tendency of further wetting. As the viewing direction revolves and approaches  $0^\circ$  (vertical to the trenches), this shifting of the free energy curves becomes more prominent. For example, at  $10^\circ$ , as shown in **Figure 146** (b), above  $h_p = 0.25$  the meta-stable points are all shifted to the ‘spreading’ side, and the overall dropping slopes of these curves are becoming increasingly larger. Overall, as the viewing angle swifts from  $0^\circ$  to  $90^\circ$ , the free energy curves, namely the wetting behaviour become more like one of a surface with micro/nano roughness, and vice versa. This trend is caused by that, like demonstrated in **Figure 143** (b), as viewing angle varies from  $90^\circ$  to  $0^\circ$ , the depth-width ratio of textures decreases, and the viewed section is becoming more like a flat surface with micro/nano- roughness (i.e. the LIPSS modelled) on it.

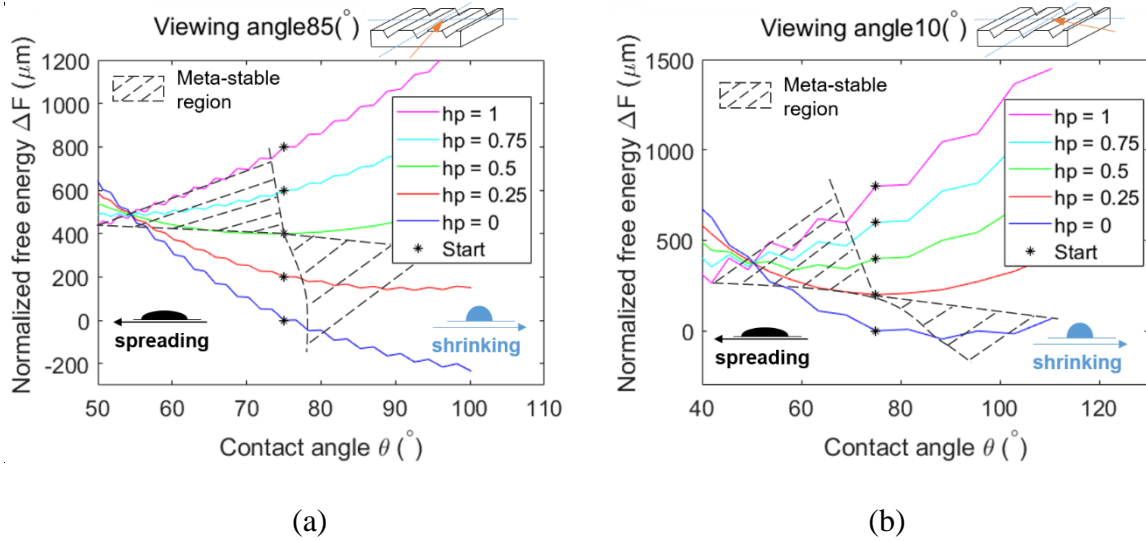


Figure 146. Free energy curves for the water droplet on the laser turned surface at viewing angle of (a) 85° and (b) 10°

Under no-penetration condition (i.e. CB’s model), when trying to search for the common contact angle for stabilities like shown in **Figure 147** (a), it is observed that no point satisfy the requirement: what for viewing angle 90° is a meta-stable position (contact angle 96.2°) is an unstable position for viewing angle 50° and below. Moreover, under the condition of a uniform penetration (e.g.  $h_p = 0.5$ ) among all wetting regime, as in **Figure 147** (b), it is impossible to find such a common contact angle: on the viewing direction approaching 90° the metastable points are on the ‘spreading’ side, while near 0° the points are in contrary on the ‘shrinking’ side. Overall, the overall equilibrium state and the solution of contact angles could not be obtained under this modelling scheme.

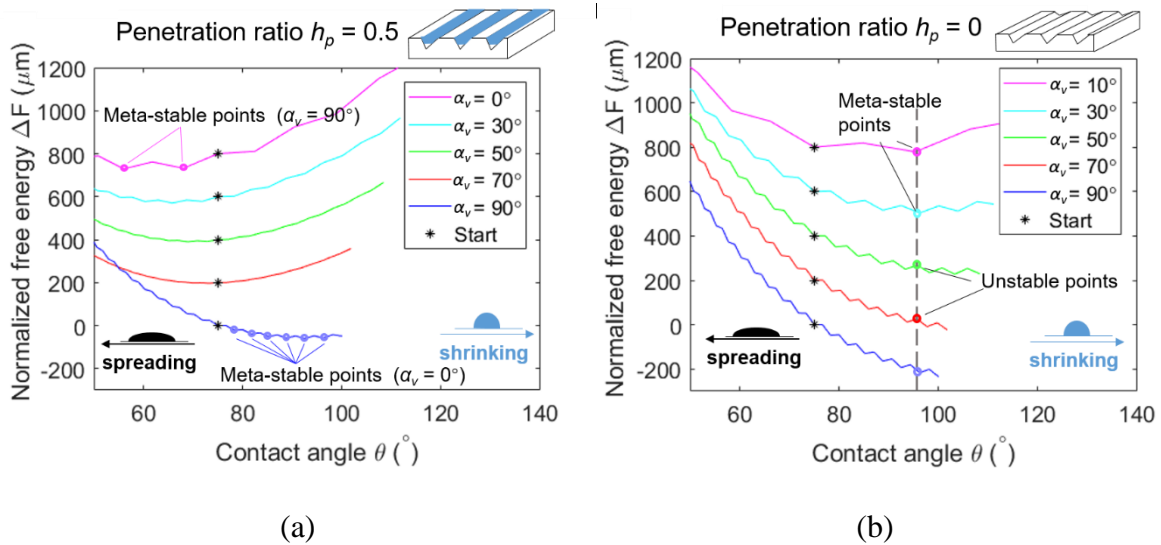
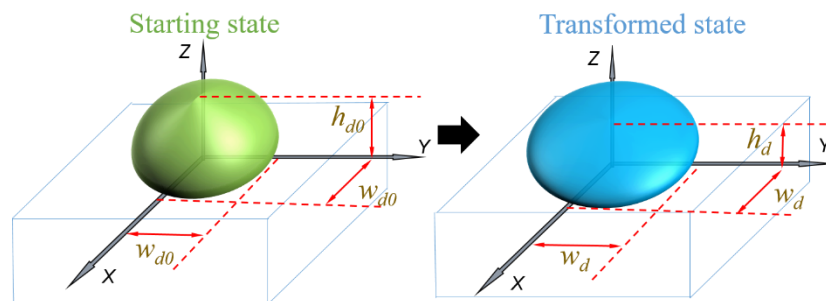


Figure 147. Free energy curves for water droplet on the laser turned surface at different viewing angle with relative penetration depth (a) 0 and (b) 0.5

In the step described above for searching the solution of the equilibrium state, what should be noted is that, since the search is for a common contact angle that leads to stability for all orientations, it pre-assumes that the change of the droplet morphology is identical in different orientations. Consequently, as long as it is found that overall equilibrium could not be achieved under this condition, the droplet could only deform in a fashion that the extent of ‘spreading’ (or ‘shrinking’) in different orientations would vary but all lead to equilibrium on their own, while the coherence of the overall morphology is still maintained. Therefore, it can be seen that the anisotropic wettability is induced by the different free energy paths in varied orientations.

### - Modification on the three-dimensional droplet morphology

As has been pointed out, the original modelled transformation of the droplet morphology, like shown in **Figure 148**, presumes uniform ‘spreading’ (or shrinking) of the droplet over the XY plane and thus, is only valid on an isotropic smooth surface. On a surface with non-negligible heterogeneity, such as the surface textures in this thesis, this model could not be compatible with the varied free energy in different orientations. To solve this issue, a new strategy of modelling the morphology transformation is proposed based on volume consistence as shown **Figure 150**.



**Figure 148.** Original droplet form transformation model: constant sectional area in every viewing angle

In the proposed modelling approach, based on the observations from the obtained droplet images and investigations on droplet morphology in previous research like [178,180,181,228], it is assumed that the droplet is the cap volume of an ellipsoid. Therefore, considering a main deforming orientation and a subsidiary deforming orientation in orthogonal relationship (e.g.  $0^\circ$  and  $90^\circ$ ), as shown in **Figure 149** and **Figure 150**, the volume consistence can be modelled:

$$V_0(h_{d0}, w_{d0}) = V_1(h_{d1}, w_{d1}, w_{d2}) + V_{pen} \quad (6.17)$$

where  $V_0$  is the volume of the original spherical cap and  $V_1$  is the assumed ellipsoid cap volume, which are functions of the droplet dimensions [181].  $h_{d0}$  and  $w_{d0}$  the height and half base-width of the droplet in the initial simulation state (same as equilibrium state on smooth surface).  $h_{d1}$

is the height of the droplet in the final equilibrium state.  $w_{d1}$  and  $w_{d2}$  are the half base-width at main axis and minor axis of the elliptical contact line, and  $V_{pen}$  is the volume of liquid penetrated into the textured concavities.

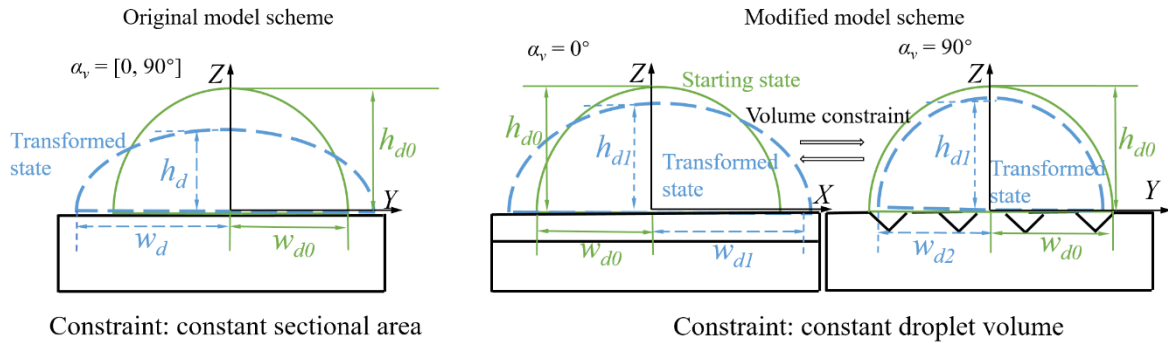


Figure 149. Sectional view of the droplet morphology evolution in (a) original model scheme; (b) modified model scheme

Therefore, given how in the main deforming orientation the ‘spreading’ (or ‘shrinking’) and ‘penetration’ condition is, simultaneously the half base-width ( $w_{d2}$ ) in the subsidiary orientation can be determined. Then on the bottom surface, considering the elliptical contact line (perimeter of the contact area), the half base-width in any viewing angle can also be obtained:

$$w_{\alpha} = \sqrt{(w_{d1} \cdot \sin \alpha_v)^2 + (w_{d2} \cdot \cos \alpha_v)^2} \quad (6.18)$$

where  $w_{\alpha}$  is the half base-width in viewing angle  $\alpha_v$ .

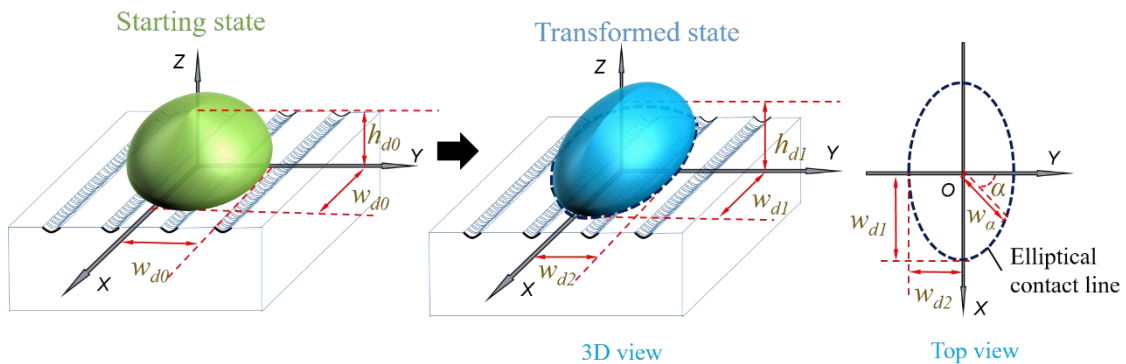


Figure 150. Proposed droplet form transformation model: constant droplet volume constraint

Moreover, from all viewing angles, the sections of droplet should share the same height ( $h_{d1}$ ), like shown in Figure 149 (b). Therefore, how the overall morphology of the droplet should evolve with the change of wetting state in the main deforming orientation can be acquired, while the volume consistency and morphology coherence are maintained.

It should be noted, this assumption also covers the special condition: when the base-width values are equal in the main and subsidiary orientation ( $w_{d1} = w_{d2}$ ), the contact line will be a circle and this condition should correspond to the original model.

After the volumetric morphology constraints are established (equation 6.17 and 6.18), with coordinates-conversion accordingly, they can be integrated into the free energy analysis (equation 6.10 to 6.16). Then, theoretically free-energy maps can be obtained along with the morphology change. However, solving all the possible cases of morphology change is unrealistic since each condition already requires numerous iterations when the constraints are integrated. Therefore, for simplification:

- Based on the meta-stable positions from the main orientation ( $0^\circ$ ), a morphology would be firstly obtained
- Then a small step of volumetric morphology alteration initiated from a small ‘spreading’ (and ‘shrinking’) disturbance at the  $90^\circ$  orientation is simulated and the resultant changes of free energy in different orientations are computed.

Through this approach, whether the system has reached overall equilibrium can be determined with considerably reduced computation, by just checking whether resultant condition after disturbance are in a higher or lower state.

In order to find out the overall equilibrium state, the proposed analysis was performed with assumed penetration ratios by trial. Through this testing process, it is found that with either no-penetration or a high penetration ratio, like shown in **Figure 151** (a) and (b), no equilibrium state can be reached, as only a few viewing angles (particularly those close to  $90^\circ$ ) experience meta-stable state in the ‘base morphologies’. As demonstrated, the volumetric morphology constraints reflected by the constraint curves fulfil the adjustment of the points to concern for free energy in viewing angles. However, it should be noted when trying to solve the base form 2 under ‘no-penetration’, like shown in **Figure 151** (a), an issue occurred as the subsidiary orientation could not ‘spread’ any more to compensate the huge ‘shrinking step ( $\theta$  exceeds  $90^\circ$ )’ in the main orientation. This should be caused by the inefficiency of describing the volume as a top ellipsoid cap, as the volume to be simulated exceeds half of an ellipsoid (when the contact angles are larger than  $90^\circ$ ). Therefore, it should be pointed out the current morphology model

may have the limitation in dealing with huge alteration of wetting performance (e.g. switching from hydrophilic to hydrophobic).

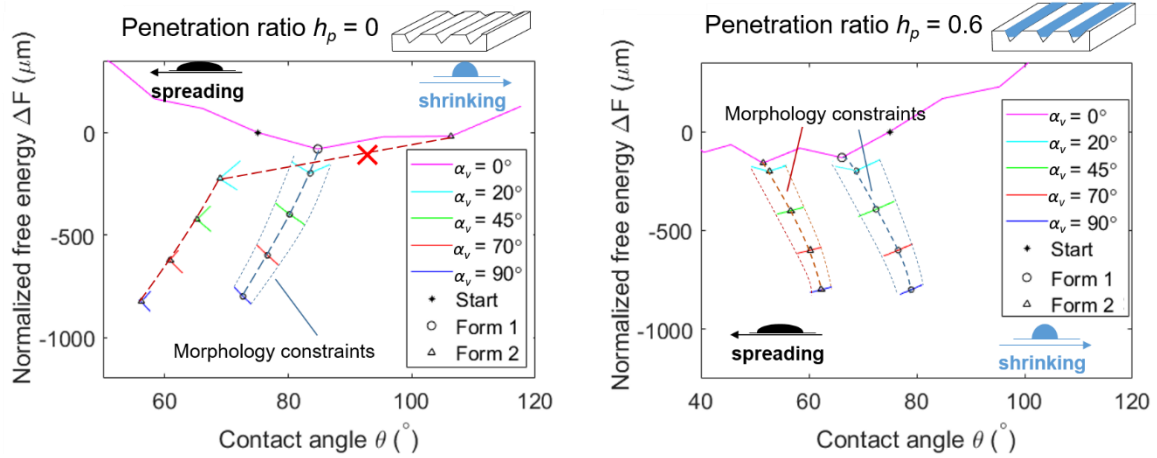


Figure 151. Free energy analysis of the water droplet on the laser-trenched surface under (a) no liquid penetration and (b) relative penetration depth of depth of 0.6

After further searching, it is found when penetration ratio is around 0.32, more viewing angles start to see meta-stability along with the main orientation (from 0 to 45°) like demonstrated in **Figure 152**.

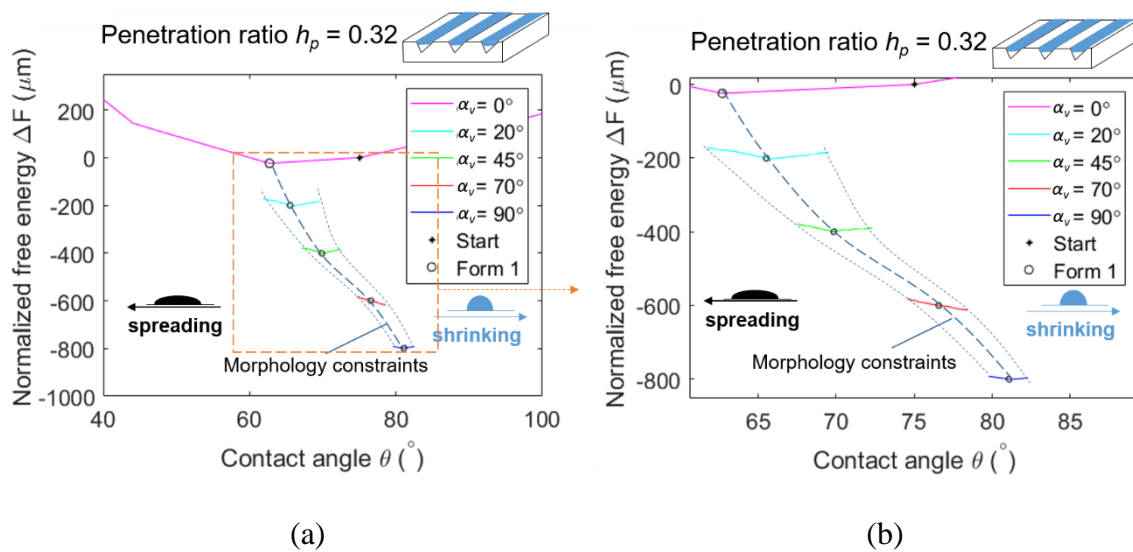
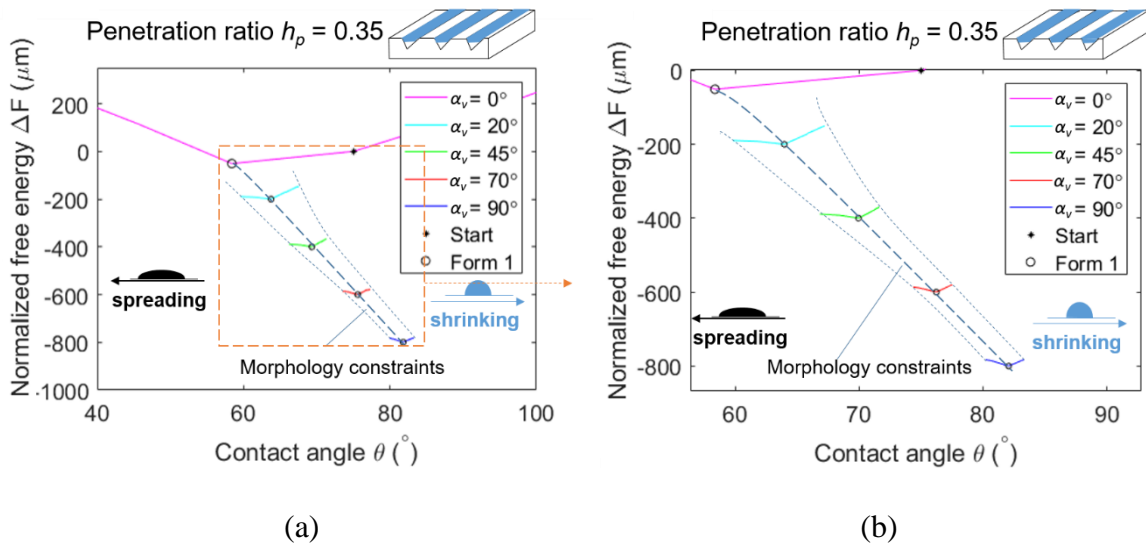


Figure 152. Free energy analysis of the water droplet on the laser-trenched surface under relative penetration depth of depth of 0.32

However, it is not until the relative penetration depth rises to around 0.35 (0.345 to 0.36 in a brief test), all viewing angles experience meta-stability, like shown in **Figure 153**. Even though only a few viewing angles are listed for demonstration, in the modelling process many more viewing angles (every 1 degree) were tested and checked in program. Under this condition, the predicted contact angles in main and subsidiary orientations (57.8° and 82.5°) are relatively

close with the measured data ( $56.12^\circ - 57.34^\circ$  and  $83.01^\circ - 84.18^\circ$ ). Meanwhile the simulated sectional shapes gave a relatively good representation of the real profiles in terms of the width, height and aspect ratio, but not perfectly matching in curvatures (probably from the assumption of a perfect ellipsoid) as shown in **Figure 154**. Therefore, it can be seen that the liquid has to penetrate into the trenches to a certain extent so that the overall equilibrium can be reached.



*Figure 153. Free energy analysis of the water droplet on the laser-trenched surface under relative penetration depth of depth of 0.35*

Overall, to explain the phenomenon observed and modelled a revisit to the free-energy formula (equation 6.10) can help. Firstly, from equation 6., an increase in solid-liquid interface can help minimizing free energy, so on surfaces with micro/nano-roughness the droplet would always tend to ‘spread’ more to get in contact with more solid surface. On the laser-turned surface studied in this thesis, if viewed from close to  $0^\circ$ , this effect would be most prominent, while viewed from parallel to the trenches ( $90^\circ$ ), it is not influenced as the ‘ripples’ are parallel to the trenches. In fact, in contrast, on the  $90^\circ$  orientation ‘shrinking’ is always favoured as analysed in **Figure 145**. This contrast in the of orthogonal directions lead to the anisotropic tendency to ‘spread’ or ‘shrink’ (i.e. wetting behaviour). Then, considering the morphological coherence and volumetric consistency, the change of the wetting behaviour from one extreme to another (in the orthogonal directions) can only be gradual and continuous for the orientations in-between, so a balancing point within ‘full-penetration’ and ‘no-penetration’ is needed to keep all orientations in meta-stable positions.

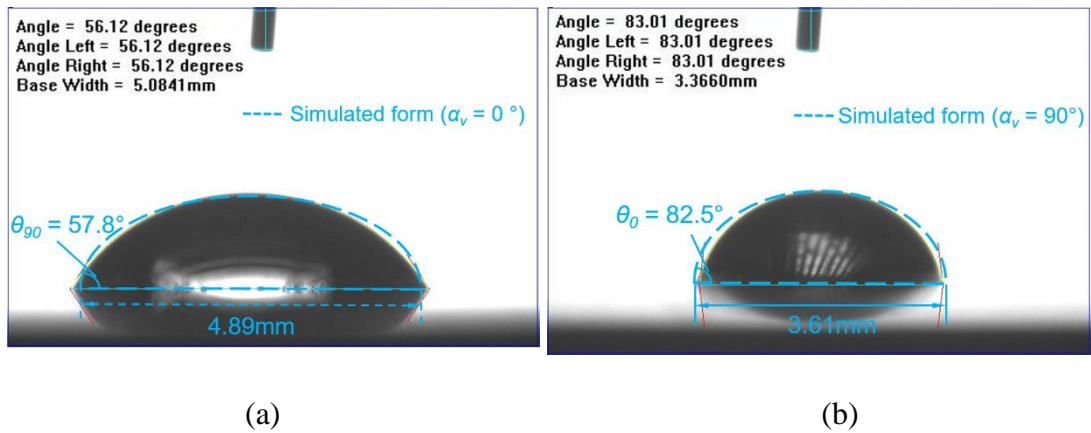


Figure 154. The comparison of the modelled droplet section morphology in viewing angle of (a)  $0^\circ$  and (b)  $90^\circ$

### - Further evaluation on the improved model

Finally, to further evaluate the model, the model was tested against the measured contact angles on three more laser-turned surfaces. These surfaces have the same parameters with the previous laser-turned surface, except for that the trench depth was made around  $10\ \mu\text{m}$ ,  $5\ \mu\text{m}$  and merely  $1\ \mu\text{m}$  by adjusting the moving speed of the laser, as demonstrated in Figure 157.

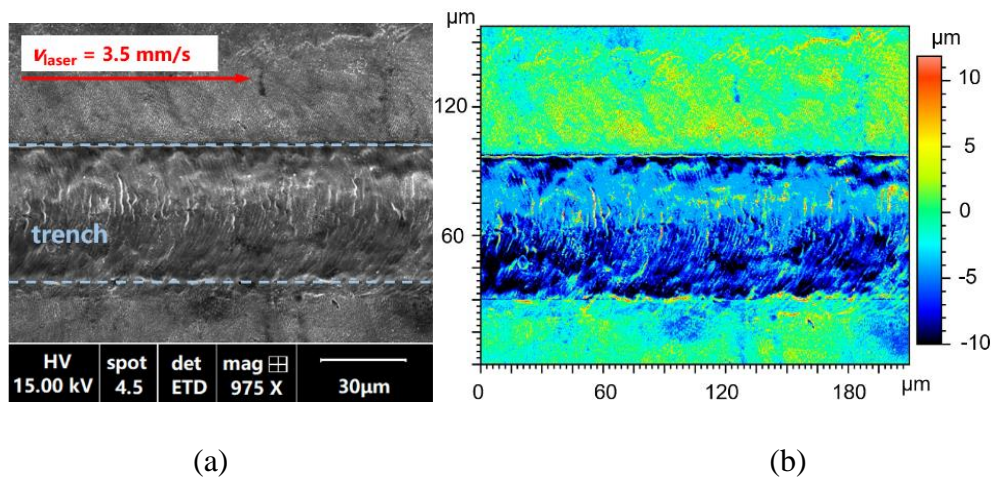


Figure 155. The (a) SEM (SE mode) image and (b) surface interferometry image of a laser-turned surface with trench depth of around  $10\ \mu\text{m}$

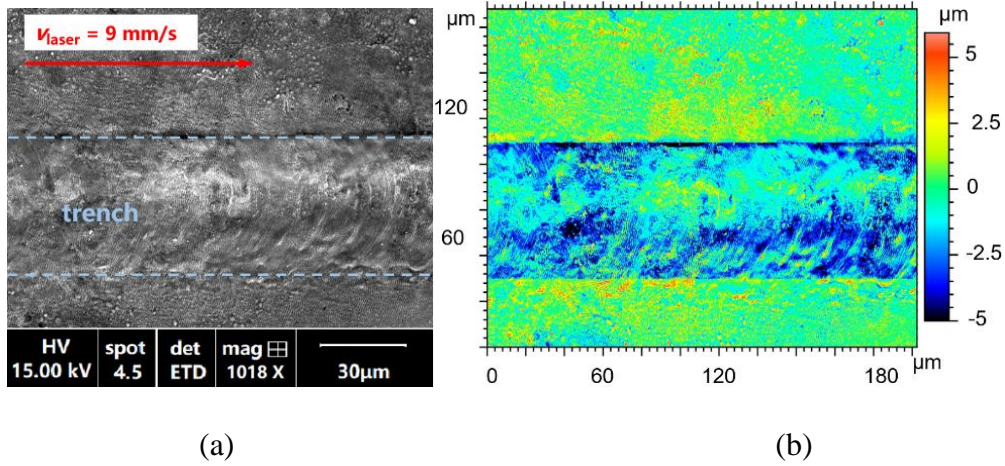


Figure 156. The (a) SEM (SE mode) image and (b) surface interferometry image of a laser-turned surface with trench depth of around 5  $\mu\text{m}$

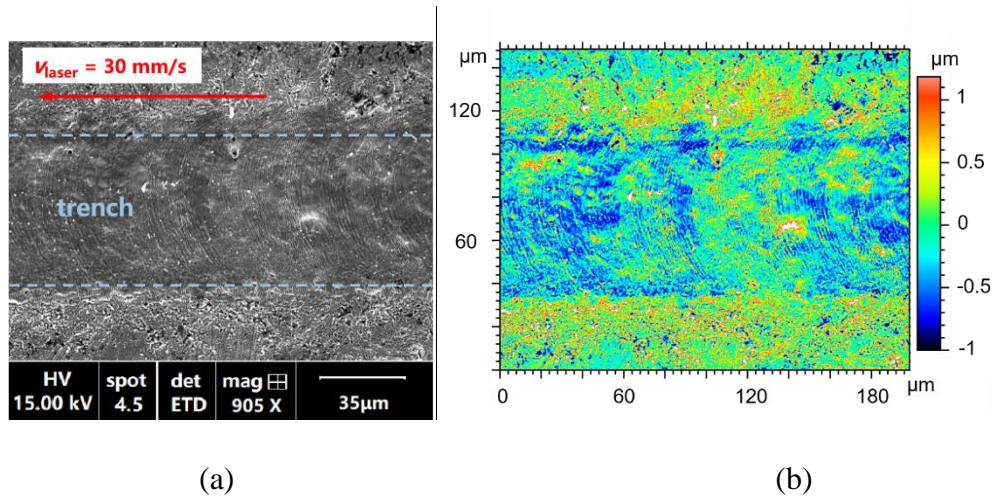
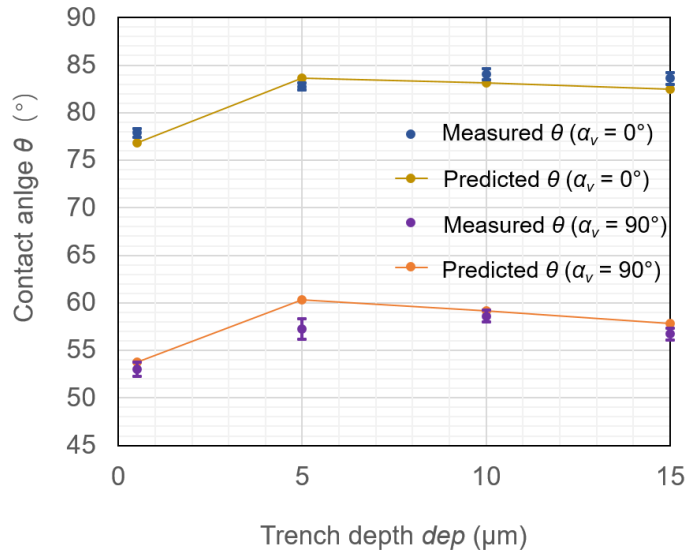


Figure 157. The (a) SEM (SE mode) image and (b) surface interferometry image of a laser-turned surface with trench depth of around 0.5  $\mu\text{m}$

Through the comparison, as shown in **Figure 158**, it can be seen that the predicted contact angles in both directions (parallel and vertical to the trenches) match well with the measured data, indicating a good applicability of the model in predicting the anisotropy. The biggest discrepancy, however, occurs at when the trench depth is around 5  $\mu\text{m}$  – the real contact angle measured vertically to the trenches is around 3 to 4 degrees smaller than the predicted value (60.28°). This kind of issue with low-depth grooves was also observed with previous studies based on free energy analysis [229], in which an explanation given was that the capillary effect, (which boosts further wetting) becomes unneglectable when the concavity is shallow. Considering that the penetration depth (4.38-4.55  $\mu\text{m}$ ) in this case does get close to the depth of the trench (5) as predicted in **Figure 159**, this postulation is reasonable.



*Figure 158. Comparison between the contact angles in orthogonal directions ( $0^\circ$  and  $90^\circ$ ) measured and predicted by the free-energy analysis model with volumetric morphology constraints*

What is more, **Figure 159** also indicates that instead of a fixed penetration ratio, there exists an almost constant value for the absolute penetration depth (as predicted by the model) when the trench is sufficiently deep ( $dep > 5\mu\text{m}$ ). As for when the trench depth is below this threshold depth value, it seems that almost the whole trench will be immersed.

Even though this model has not been adopted on other laser-textured surfaces due to geometry discrepancy, it is reasonable to postulate that these surfaces with similar dual-tier microstructures should also experience a certain degree of liquid penetration within the textured concavities, thus leading to the deviation of prediction using conventional wettability models.

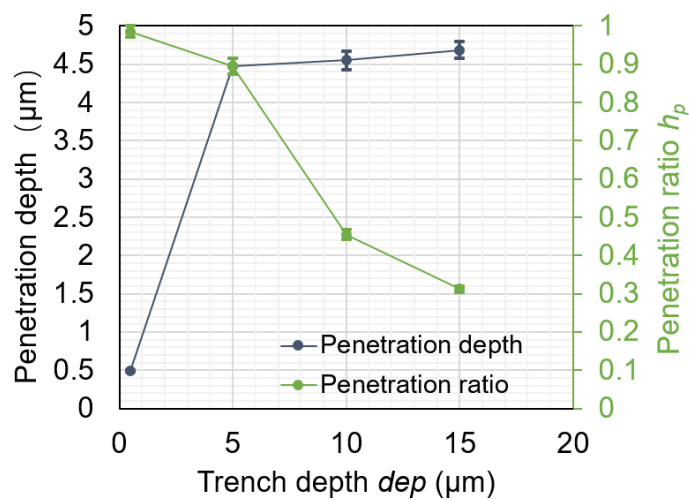


*Figure 159. Evolution of the penetration depth and penetration ratio predicted by the free-energy analysis model with volumetric morphology constraints*

## 6.6 Conclusions

In this chapter, both quantification and qualification tests were performed to evaluate the capability of some conventional texturing techniques and novel surface roughening methods in improving bonding strength. Through the tests, the processes inducing significant benefits were found – laser roughening. Common properties of the benefiting surfaces were identified, and the functioning mechanism were investigated through assisting analysis methods (SEM analysis and wettability measurement). Considering the correlation found between the bonding strength and the wettability, a contact angle model with novel approach on wetting behaviour with textured surfaces was developed, aiming at providing theoretical support for future texture design.

The contributions and findings achieved in this chapter are:

*The potential was explored on conventional surface texturing techniques and two novel methods developed for surface roughening, targeting at bonding strength improvement. The two novel surface roughening process were established as effective methods for bonding strength improvements. With the assistance of the analysis conducted (surface analysis and wettability measurement), the following findings were established:*

- The production of micro/nano irregularities is the key for significant bonding strength improvement. Apart from that this feature can naturally enhance the adhesive-surface contact area, it was also found that mechanical-interlocking (only observed with laser-roughening) and higher resistance to adhesive failure can be generated.
- The bonding strength of the surface was found strongly linked with the wettability of the surface. The surfaces with significantly improved bonding strength, i.e. those with micro/nano roughness also possess super-hydrophilicity.

*To relate the influence on wettability with the pattern of roughness/textures created, a modified model of contact angles based on free energy analysis and the assumption of penetration-depth was developed. Benefiting from a volumetric-morphology constraint model, this model is capable of simulate the anisotropic wetting performance of surfaces with directional textures (e.g. grooves). Through the analysis, the following findings were established:*

- A theoretical explanation for the super-hydrophilicity of surfaces with well spread micro/nano roughness was established. If within unit ‘spreading’ length, the liquid-solid interfacial area is sufficiently high- as with micro/nano roughness, the energy reduction effect from liquid-solid contact would always prevail the energy increase effect occurring simultaneously with larger liquid-gas contact area, so the liquid would always tend to ‘spread’ to reach a lower free energy state.
- The cause of the anisotropic wettability of the surfaces with directional textures (e.g. grooves) can also be explained by the free-energy theory: the free-energy paths in varied viewing angles are different, so to achieve an overall equilibrium state, the contact angles on different directions need to vary for individual meta-stable states.
- Partial penetration was found to be a more accurate reflection of the wetting behaviour on textured surfaces produced with short-pulse lasers (i.e. with LIPSS inside concavities). This is a combined result of the two basic phenomenon stated above: from certain viewing angles (perpendicular to the LIPSS ripples), the effect of micro/nano roughness is most prominent, while in other directions (parallel with the LIPSS ripples) the micro/nano roughness would be viewed as vanished. As a result, the overall condition can be treated as a mid-way between the two extremes- complete wetting of the micro/nano roughness, and no wetting (all gas pockets) of the larger scale concavities as indicated by CB’s model.

Overall, this chapter reports on the understanding of the effects of surface topographic features (textures and roughness) on the bonding strength of the surface. The developed novel surface roughening methods are promising in become industrialised process for bonding strength improvement. Moreover, because the developed contact angle model provide more accurate and more realistic prediction of the wetting behaviour with textured surfaces, and strong link was found between the wettability and bonding strength of the surface, the study on the wettability provided possibility to predict the influence of surface texturing on bonding strength. It should be noted that limitations still exist in the studies. For example, approximation was used for texture geometry as well droplet morphology in the wettability model, and the model may not be extended to explain transformation between hydrophilicity and hydrophobicity. However, the methodologies developed and the basic physical phenomenon revealed in this study can still contribute to advancement in both the industrial application and knowledge in this field.

## 7 Conclusions, discussions and future work

The research conducted in this thesis focus on the effects of surface texturing in dry-lubricated bearings concerning both the tribological and bonding performance aspects.

For the study on the tribological effects of surface texturing, a systematic tribological test series was conducted to simulate a typical dry-lubricated condition- PTFE/glass fibre composite liner sliding against steel counterface in helicopter spherical plain bearings. With the test series, optimal surface texture parameters were found.

To analyse the tribological performance and the associated phenomenon in this special contact condition, a novel characterising method for the dry-lubricating transfer-film was developed. This new technique solved the issues and difficulties under this real engineering contact condition, and provided film thickness information- valuable to the film reservation effect.

To understand the basic contact mechanics condition, a Finite element (FE) model was developed to analyse the contact pressure and stress condition under dry-lubricated contact. With the help of the model, the improved approach in employing the Limiting-Pressure-Velocity (*LPV*) criterion was formed for instructing parametric design of counterface textures. Consideration of the pressure elevation and stress concentration due to hard fibres and texture edges was found to be key to compute the ‘real *PV*’ for the polymer composite.

With the development of a kinematic model for the helicopter main rotor, the significance of sliding motions in dry-lubricated contact with composite bearing liner was addressed. Guided by the model, the anisotropic tribological performance of the pitch-control-bearings were studied by the wear tests. The origin of the anisotropy and the influencing factor, including the addition of counterface textures were investigated.

Finally, to improve the bonding strength of the sleeve surface, novel sleeve surface texturing/roughening methods were developed. Using surface analysis and wettability tests, the principle for sleeve surface texturing was established, and the correlation with wettability was found. With the help of the improved wettability model based on surface free energy analysis and proposed new assumptions, theory behind the effects of surface texture on wettability was formulated.

In the research work, the completed aims and objectives, achieved contributions in the application and progress in knowledge, as well as the proposed future work are presented in this chapter.

## 7.1 Aims and objectives met

Through the experimental and modelling work conducted in this thesis, the aims and objectives set initially for the project have been fulfilled:

- ❑ The key analysis method – transfer film characterisation technique has been developed, with identified issues and difficulties solved. Through a thorough literature review (section 2.1.2.3), and a comprehensive comparison between different characterising techniques (section 4.4.1), issues existing in the previous methods of film characterisation, and the difficulty in realistic contact condition of self-lubricating bearings have been identified. Through analysing the transfer film by layers with SEM in different accelerating voltages (with Tof-SIMS as an assisting calibration technique), the addressed issues were solved, and a reliably characterising method was built (section 4.4.1). With the new method, progress has been made on understanding the transfer film's formation in realistic contact condition of self-lubricating bearings.
- ❑ The main effects of counterface texturing in self-lubricating sliding contact were identified (transfer film reservation, pressure and stress concentration) with a systematic tribological test series, and related with the texturing parameters (diameter, depth and coverage) using a comprehensive surface analysis and the contact mechanics analysis session (chapter 4).
- ❑ A new kinematic model for the spherical plain bearings used in helicopter main rotor was developed, based on the output-oriented principle proposed (chapter 5). Guided by the model, the wear tests reveal the anisotropy in the tribological performance of the dry-lubricated bearing, and the influence of counterface textures. The theory behind the influence of the counterface textures was formulated through surface analysis and the contact mechanics analysis (section 5.3.2 and 5.3.3).
- ❑ Different surface texturing/roughening methods have been developed for bonding strength improvement (chapter 6). Among them, the novel surface roughening process laser roughening stand out as effective method inducing significant performance improvement. Through assisting analysis (surface analysis and wettability measurement), the main physical phenomena related with superior bonding strength were identified, including the micro/nano roughness and super-hydrophilicity. Meanwhile, theoretical support and designing principle were established through the new wettability model developed (section 6.5).

## 7.2 Contributions and conclusions obtained

### *Counterface texturing in dry-lubricated bearings*

Contributions for the application: An optimized range of the dimple parameters were produced for benefiting the frictional and wear performance of the dry-lubricated contact. The dimple depth (*dep*) should be around 2 $\mu$ m to benefit transfer film formation, and the diameters and densities need to be in a narrow range ( $d \leq 20 \mu\text{m}$ ,  $p_c \leq 1.6\%$  for the tested condition) to avoid significant micro-abrasion.

Concluded knowledge and principles: The key in benefiting transfer film formation is to the consistency between the dimple depth and the film thickness (thicker form, 2~3  $\mu\text{m}$ ). As for the micro-abrasion, the smaller and fewer the textures are, the milder the effect will be. However, too few dimples would lead to little change in performance. To find the balance and determine the feasible range, the *PV* factor and stress can serve as useful index, while consideration needs to be given to the difference of real contact pressure/stress on the polymer part induced by the hard filler/fibres and the stress concentration near the dimple edges.

### *Transfer film characterisation*

Contributions for the application: The developed surface analysis method based on multi-voltage SEM analysis, and assisted with Monte-Carlo simulation and SIMS analysis, can identify the PTFE transfer film in varied thickness formed on the steel counterface sliding against the PTFE/ glass fibre composite. This method can overcome the difficulty induced by counterface wear tracks in the dry-lubricated contact.

Concluded knowledge and principles: The transfer film can exist in two forms on the counterface: nano-meter degree ultra-thin film, and thick film in a few micrometre thick. Only with a surface analysis method that can minimize the influence from counterface topography, and identify the composition on the surface by different information depths, can this information of transfer film be obtained.

### ***Kinematics of dry-lubricated bearings***

Contributions for the application: A novel kinematic model based on the output-oriented principle was developed for the pitch-control-bearings in helicopter main rotor. A more realistic reflection of the sliding in this typical dry-lubricated contact was achieved.

Concluded knowledge and principles: The real sliding path of the pitch-control-bearings is a transcendental spherical curve, depending on the pitch angle of the helicopter main rotor. The distribution of sliding directions is not symmetrical about  $90^\circ$  like in the conventional empirical model, and may have a prominent peak deviated from  $90^\circ$  instead of a considerably uniform distribution. The real kinematics can only be obtained considering both the mechanism and the output motion of the system.

### ***Anisotropic tribological performance of dry-lubricated bearings***

Contributions for the application: A guidance for aligning the composite liner has been achieved- aligning the shortest side perpendicular to the sliding direction can lead to optimal tribological performance by minimizing the counterface abrasion.

Concluded knowledge and principles: The anisotropic tribological performance of the dry-lubricated contact derives from the mutual interaction between the contact pair. The hard fibres would cause counterface wear tracks, and the wear tracks would in turn lead to higher wear rate on the composite liner. In this process, the width of the wear track depends on the projected length or the glass fibres perpendicular to the sliding direction. This anisotropy can be reduced by the counterface textures, as the textures can lead to local stress concentration, relieve the stress in hard fibre areas.

### ***Sleeve texturing in dry-lubricated bearings***

Contributions for the application: Process developed to create well-spread micro/nano roughness (laser roughening) has been proven effective to improve bonding strength for sleeve surfaces. The developed contact angle model based on surface free energy analysis, partial penetration assumption and volumetric consistency can reliably predict wettability of texture surfaces and assist texture design for bonding strength improvement.

Concluded knowledge and principles: Micro/nano irregularity is the key for significant bonding strength improvement. Apart from increase on adhesive-surface contact area, improvement on wettability was another main functioning mechanism by this feature. With the improved surface free energy analysis, it can be explained that the super-hydrophilicity of surfaces with derives from high liquid-solid interfacial area that would attract further wetting to minimize surface free energy. Moreover, the anisotropic wettability of the surfaces with directional textures (e.g. grooves) can also be explained by the difference in free energy paths in varied viewing angles.

### **7.3 Discussion based on the findings**

For advancement on the understanding of the surface texturing in dry-lubricated contact and bonding process, with the findings obtained in different chapters integrated, the generated points concerning the overall picture of the studied issues are discussed in this section.

#### ***A comprehensive view of the tribological behaviour of dry-lubricated bearings***

- In the dry-lubricated bearings, the hard fibres in the composite liner enhance the load-carrying-capacity by taking more pressure under normal load, relieving the pressure/stress on the self-lubricating polymer part. This has been explicitly revealed through the FE analysis with different components modelled (section 4.5.1). However, the addition of hard fibres is not always beneficial- it may incur counterface abrasive tracks, which would in turn cause higher wear rate on the composite liner (section 5.3.2). Therefore, one point for the composite development (although may be out of the scope of this study) is strengthened explicitly: the balance between the reinforcing effect and the abrasion effect of the hard fibres/fillers is critical.
- Considering the abrasion effect from hard fibres, for a certain pattern of the composite liner, the orientation can be optimized – aligning the shortest side of the hard fibres perpendicular to the sliding direction should lead to the optimal wear performance, since the abrasive wear can be reduced the most (section 5.3). This strategy should be integrated with a realistic kinematic model of the application though, as the sliding direction would vary according to the system kinematics. Considering this, without clear understanding of the kinematics, the bearing manufacturer’s approach of always aligning the liner at 45° may be conservative, but is also a relatively safe and a cost-saving way.

- Due to the pressure relieving effect, the real pressure imposed on the polymer parts of the composite would vary from the nominal one. Therefore, when applying the  $PV$  factor to evaluate the performance of the tribological performance, it is essential to obtain the 'real  $PV$ ' on the polymer parts under real contact pressure, since the  $PV$  factor reflects the thermal input- an important influencer to the polymer properties.

### *An improved view of the tribological effects of counterface textures*

- The main effects of the counterface textures can be categorised in two: the transfer film reservation and the contact pressure/stress elevation. The key in transfer film reservation is the consistency between the texture depth and transfer film thickness, so the difficulty lies on the identification of the film thickness. Meanwhile, the influence in contact pressure/stress elevation can be perceived in two aspects: the lead to micro-abrasion neighbouring the texture edges, and the switch of peak pressure/stress zone from the glass fibre areas.

- For the polymer parts, the micro-abrasion neighbouring the texture edges should be the combined result of the thermal effect and stress concentration, given that the local  $PV$  factor gave a more accurate prediction of the occurrence than simply the local stress (section 4.5.2). Moreover, even though it seems that the stress concentration is only detrimental, it may also create benefit: by taking more pressure/stress near the dimple edges, the pressure/stress level on the glass fibre areas and the resultant abrasion on the counterface can possibly be relieved.

- The extent of the influence from counterface textures is dependent on the dimple dimensions, coverages as well as the original state of each effect. For example, in the studied contact condition, the range of dimple diameter and coverage has to be confined within a very small range to avoid significant micro-abrasion because the original local pressure (and  $PV$ , stress) can be easily lifted to the threshold value as the gap between them is not significant. However, if the textures were applied in a much lower load, or the  $LPV$  of the material was high, there should be a larger feasible region for the texture dimensions, and the incurred overall effect may also be magnified. Moreover, the relieving effect on the counterface abrasion has also been found dependant on the original abrasion track (influenced by composite orientation).

Overall, as stated above, friction and wear are complex conceptions, and many influencing factors and relevant physical phenomenon have to be considered when analysing them. To reflect the relationships, Figure 160 demonstrates the influences from different aspects, serving

as a guidance for the texture design in the self-lubricating bearings. As can be seen, the texture parameters have to be considered together with the composite properties and operation parameters (load and sliding speed also need to be included for benchmarking) because the tribological performance is a reflection of the whole system, and therefore could not be evaluated without any aspect.

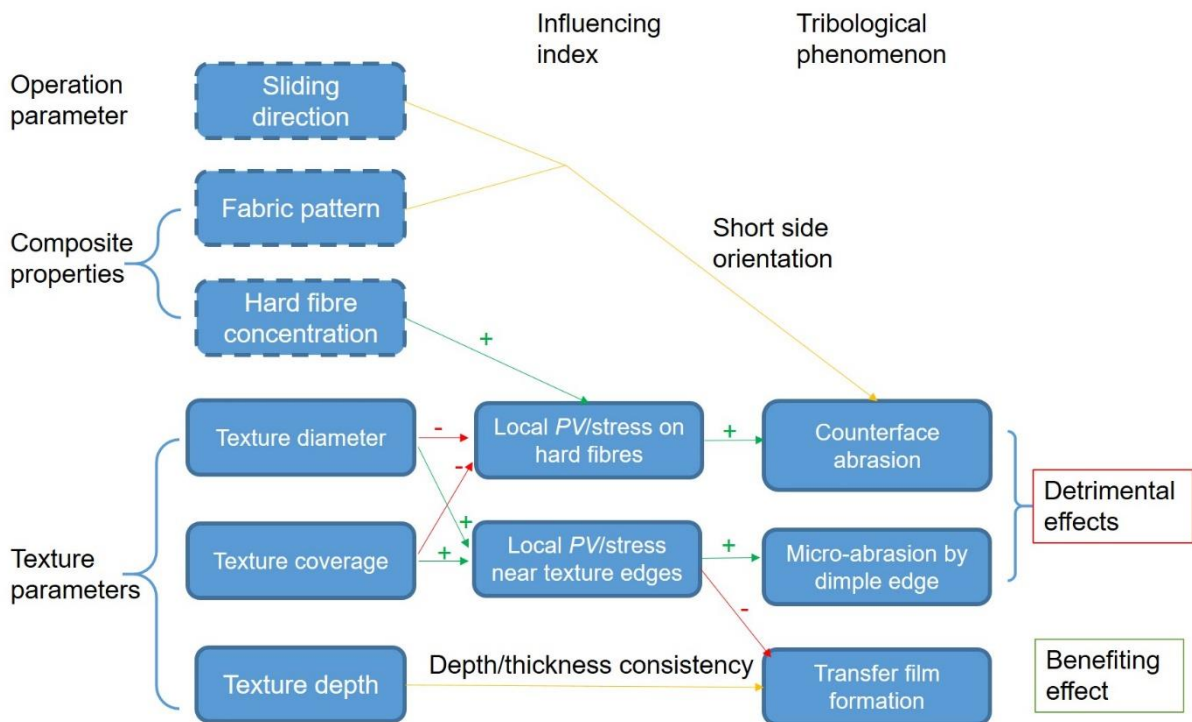


Figure 160. Overall graph of the impact of different variables on the tribological phenomenon, where '+' means positively influencing and '-' means reversely influencing

### ***On the effects of sleeve surface texturing on bonding strength***

- For bonding strength improvement, the key was the production of micro/nano roughness, which is believed to work by increasing the real surface area and mechanical interlocking. With the wettability analysis, it was also found that the micro/nano roughness also has the capability of promoting super-hydrophilicity, which is found correlated with adhesive strength (section 6.3.2). The theory behind the super-hydrophilicity was found through the surface free energy analysis: wetting is always favoured on surfaces with micro/nano roughness as it is towards the direction of equilibrium energy state (minimized surface free energy).

What was interesting was that for all the surfaces that achieved significant increasing in bonding strength (grit-blasted and laser roughened), they also simultaneously have the

dramatically improved wettability (super-hydrophilicity). For this link, the enhancement in surface areas should be the connecting point. According to the theoretical expression (equation 2.3 in section 2.2.3), the bonding strength or ‘practical adhesion’ is composed of two terms: the ‘fundamental adhesion’ (related with wettability) and the extra term created by the mechanical interactions. In the process of pursuing the increase in one or the other, the enhancement of contact areas can contribute to both. Therefore, the impression that surfaces of higher wettability also has better bonding performance was often formed. However, whether the increase in wettability directly leads to the significance in bonding strength, i.e. whether the extent of variation in bonding strength is always ‘proportional’ to the improvement of wettability would need more discussion, as the weighting factor of ‘fundamental adhesion’ in ‘practical adhesion’ may not be as great as the mechanical term, as some claimed [161].

With all these studies done, it can be seen how versatile surface topographic features can be by changing the form: in one form, it can reduce the friction of a sliding contact (observed in section 4.3), while in another, it can dramatically increase the interfacial shear resistance (observed in section 6.3).

## **7.4 Future work**

The aims and objectives generated for this project by the partnership between the University of Nottingham and SKF Ltd have been well completed, with relevant advancement in both understanding and applications being achieved. However, this thesis has also raised some questions which can be further explored, as stated in the following:

### ***Experimental work***

- Effective as the pin-on-plate test scheme is in revealing the contact condition in real bearings. There might still be some points lost in transformation, incurred by the discrepancy in geometry and dimensions. For example, on real bearings, particularly spherical bearings, there might still be a small degree of non-conformity between the contact surfaces, leading to a certain extent of pressure variation. Small as the extent may be, real scale test on bearings would always be valuable for identifying possible differences. Overall, it can be useful to conduct real scale bearing tests prior to applying the optimized textures on real production. Actually, this is the next-step under plan by SKF Ltd.
- As the conducted test series have revealed the tribological effects of counterface textures, and formed principles to consider the effects of basic operating conditions like load and speed, it

can be useful to test how textures can make a difference for environmental influencers like humidity and contamination. For example, for many aircrafts working in humid environments (coastal), water contamination is an issue. In the short run, it may benefit frictional performance, but in the long run corrosion may be incurred, how textures can influence this, and how different textures can make varied impact are worth investigation.

- After the basic physical phenomena have been identified with the simple texture pattern employed (uniform circular concavities), the study on the effect of counterface textures can be expanded to more complex texture pattern, investigating the influence of other geometric features. For example, how the orientation of a trench (parallel or perpendicular to the sliding direction) would influence the abrasion of glass-fibre particles, and whether a very narrow elliptical hole may further minimize the stress concentration effect are both aspects worth investigation.

- Experimentally, more investigation can be done on the thermal-effect-related physical phenomenon, given that a more sophisticated contact temperature measurement system can be built. For example, since it has been deduced that the micro-abrasion may not only derive from stress concentration neighbouring the texture edges, but may also be affected by the local thermal effect considering high 'local PV', whether local temperature rise occur in this regions would assist assessing this point. The difficulties here are the measurement of a closed contact (thermal camera may therefore not be feasible), and the sliding contact should be kept uninfluenced by the measuring (thermal couples may therefore not be feasible). Moreover, since the 'local PV' refers to a really small region (micron level), spatial resolution of micro-meter level is required. Therefore, the establishment of a more sophisticated temperature measurement system would be the starting point.

- The employment of the pin-on-plate test scheme to study the anisotropic tribological performance of the self-lubricating bearing may be exclusive to the studied case. In other scenario (another fashion of flight, or simply with another helicopter), the real distribution of sliding direction is not so concentrated within a small range. Therefore, it is worth developing a universal method to simulate the real kinematics of the spherical plain bearings in main rotors. A good starting point may be modification on the pin-on-disc test set-up (single-axis rotation), to simulate the transcendental spherical curves, and another straightforward approach is to directly develop a bearing test rig that can simulate any multi-axis rotations.

### ***Modelling work***

- For the FE model of the contact mechanics, consideration had to be given to the computation efficiency, so approximation and simplification were adopted (section 4.5.1). However, real scale model always give the most accurate reflection of the real condition. If real scale models or at least the unit fabric model including the glass fibres can be implemented, some other physical phenomenon occurring during the sliding contact with textured counterface may be revealed. For example, how the condition may differ when a glass fibre slides through a concavity compared with the case with the polymer part. This simulation may give an estimation of the stress condition on the glass fibres, and indicate how the surface textures may affect the occurrence of abrasive particles and consequent wear tracks. To achieve this, the complexity of modelling this interaction and the requirement of computation force (meshing strategy may need to be improved) are the main issues.

- Another point that can be done to improve the FE model is the inclusion of explicit thermal analysis. As has pointed out the thermal effect is crucial for the polymer tribology. In the current model, the consideration was given by keeping the consistency in temperature for the calibration of the material property (section **Error! Reference source not found.**), and using PV factor as an index for the thermal effect. However, integration of an explicit thermal analysis would give direct description for the temperature field, and even evolution of the temperature during sliding. A promising aspect of this is to detect the occurrence thermal stress and rise of local temperature near the texture edges due to higher contact pressure (high local *PV*), assisting explaining this detrimental side of the counterface textures. Naturally, the thermal analysis would add another instruction for the texture design. However, apart from the demand in computation force or reduction of computation cost, an accurate modelling of the thermal properties of the materials would be another issue to be solved.

- For the wettability model, the current surface free energy analysis is integrated with the droplet penetration assumption and morphology analysis of the liquid droplet. However, in both aspects there have been more sophisticated models. For example, [230] reported different penetration ratios on different the texture locations within the droplet, and droplet shapes other than a perfect elliptical cap was observed [178]. Therefore, it is worth investigation whether adopting this model would give an even more accurate prediction of the contact angle, while consideration needs to give to the more complex iterations and higher computation force requirement.

### *Towards industrial application of the outcome*

- Firstly, as has been pointed out, prior to employing the optimal texturing pattern to bearing production, tests on real scale bearing would be essential to check possible discrepancies posed by the differences in geometry and dimensions.
- Besides, how the developed processes can be adopted to real manufacturing process need to be determined. Apart from the performance, the cost and time-efficiency of the processes are also important factors to be considered. For instance, due to its long processing time, laser may not be the best option for producing counterface dimples. Meanwhile, the modified hard-turning process (with oscillating tool) may have higher potential in this application as the conventional hard- turning is sometime already a part of the common manufacturing procedures.
- Detailed evaluation of the ‘side-effects’ of the texturing process, such as impact on surface integrity of the surface texturing process is needed. Correspondingly, necessary improvement of the process should be investigated. In the current development of the processes, for example, to minimize the ‘side-effects’, special attention was given to the selection in process (employing ‘cold laser’ for counterface texturing to minimize HAZ). However, whether the resultant surfaces can meet industrial standard and application requirement, and whether further improvement on the processes is demanded need to be investigated.

## Reference

- [1] European Environment Agency, European Aviation Environmental Report 2019, 2019. <https://doi.org/10.2822/309946>.
- [2] Council of the European Union, Council Decision (EU) 2020/954, 2020. <https://eur-lex.europa.eu/eli/dec/2020/954/oj>.
- [3] J.K. Lancaster, Accelerated wear testing as an aid to failure diagnosis and materials selection, *Tribology International*. 15 (1982) 323–329. [https://doi.org/10.1016/0301-679X\(82\)90141-4](https://doi.org/10.1016/0301-679X(82)90141-4).
- [4] G. Russell, Friction and wear behaviour of self lubricating bearing liners (PhD Dissertation), Institute of Theoretical, Applied and Computational Mechanics, Cardiff University, 2013. <http://orca.cf.ac.uk/51031/>.
- [5] J. Li, Y. Ran, Evaluation of the friction and wear properties of PTFE composites filled with glass and carbon fiber, *Materialwissenschaft Und Werkstofftechnik*. 41 (2010) 115–118. <https://doi.org/10.1002/mawe.200900545>.
- [6] J.K. Lancaster, R.W. Bramham, D. Play, R. Waghorne, Effects of Amplitude of Oscillation on the Wear of Dry Bearings Containing PTFE, *Journal of Lubrication Technology*. 104 (1982) 559–567. <https://doi.org/10.1115/1.3253288>.
- [7] F.E. Kennedy, S.C. Cullen, J.M. Leroy, Contact temperature and its effects in an oscillatory sliding contact, *Journal of Tribology*. 111 (1988) 63–69. <https://doi.org/10.1115/1.3261880>.
- [8] M.B. Harrison, Self Lubricating Bearings, US patent 4666318, 1987.
- [9] Minebea Co. Ltd., Sliding bearing having self-lubricating liner, US patent 9080605B2, 2015.
- [10] P. Smith, Bearing with a self- lubricating liner of one bearing element in sliding contact with a nitride hardened counterface of a titanium bearing element, European Patent 1666628A2, 2007.
- [11] Glyco-Metall-Werke Glyco B.V., Self-lubricating bearing material and friction bearing made of such a material, World Intellectual Property Organization Patent 1996026975, 1996.

- [12] D. Dowson, J.H. Bernard, NASA Technical Memorandum 81689: History of ball bearings, Cleveland, Ohio, 1981.
- [13] J. Needham, L. Wang, Physics and Physical Technology: Mechanical Engineering, in: Science and Civilisation in China, Cambridge University Press, Cambridge, 1965.
- [14] C. Rossi, F. Russo, F. Russo, Lift and Transports, in: Ancient Engineers& Inventions. History of Mechanism and Machine Science, Vol 8, Springer Netherlands, Dordrecht, 2009. [https://doi.org/10.1007/978-90-481-2253-0\\_10](https://doi.org/10.1007/978-90-481-2253-0_10).
- [15] F. Friedrich, Kugelfräsmaschine - Ball milling machine, German patent 55783, 1890.
- [16] S.G.Wingqvist, Anordning vid kullager - Ball bearing device, Swedish patent No.25406, 1907.
- [17] SKF Group, Thrust ball bearings, (2020). [www.skf.com/group/products/rolling-bearings/ball-bearings/thrust-ball-bearings](http://www.skf.com/group/products/rolling-bearings/ball-bearings/thrust-ball-bearings) (accessed August 16, 2020).
- [18] I.M. Hutchings, Leonardo da Vinci's studies of friction, *Wear*. 360–361 (2016) 51–66. <https://doi.org/10.1016/j.wear.2016.04.019>.
- [19] A. Guillaume, Moyen de substituer Commodement L'Action du Feu, a la Force des Hommes et des Chevaux pour mouvoir les Machines, *Mémoires de l'Academie Royale Des Sciences*. 4 (1699) 112–116.
- [20] A. Guillaume, Remarques et Éxpériences Physiques sur la Construction d'Une Nouvelle Clepsydre, Charles-Antoine Jombert Publisher, Paris, 1695.
- [21] F.P. Bowden, D. Tabor, The Friction and Lubrication of Solids, *American Journal of Physics*. 19 (1951) 428. <https://doi.org/10.1119/1.1933017>.
- [22] R. Stribeck, Die wesentlichen eigenshaften der gleitund rollenlager - The key qualities of sliding and roller bearings, *Zeitschrift Des Vereines Deutscher Ingenieure*. 46 (1902) 1342–1348.
- [23] H. Hertz, On the contact of elastic solids, *Journal Für Die Reine Und Angewandte Mathematik*. 92 (1881) 156–171. <https://ci.nii.ac.jp/naid/10015562849/en/>.
- [24] D. Dowson, G.R. Higginson, A. V. Whitaker, Elasto-Hydrodynamic Lubrication: A Survey of Isothermal Solutions, *Journal of Mechanical Engineering Science*. 4 (1962) 121–126. [https://doi.org/10.1243/jmes\\_jour\\_1962\\_004\\_018\\_02](https://doi.org/10.1243/jmes_jour_1962_004_018_02).

- [25] D. Dowson, G.R. Higginson, The Effect of Material Properties on the Lubrication of Elastic Rollers, *Journal of Mechanical Engineering Science*. 2 (1960) 188–194. [https://doi.org/10.1243/jmes\\_jour\\_1960\\_002\\_028\\_02](https://doi.org/10.1243/jmes_jour_1960_002_028_02).
- [26] Great Britain Department of Education and Science, Lubrication (tribology), education and research; a report on the present position and industry's needs, H.M. Stationery Office, London, 1966.
- [27] D.M.J.S. Bowman, J.K. Balch, P. Artaxo, W.J. Bond, J.M. Carlson, M.A. Cochrane, C.M. D'Antonio, R.S. DeFries, J.C. Doyle, S.P. Harrison, F.H. Johnston, J.E. Keeley, M.A. Krawchuk, C.A. Kull, J.B. Marston, M.A. Moritz, I.C. Prentice, C.I. Roos, A.C. Scott, T.W. Swetnam, G.R. Van Der Werf, S.J. Pyne, Fire in the earth system, *Science*. 324 (2009) 481–484. <https://doi.org/10.1126/science.1163886>.
- [28] Koyo Bearing (JTEKT corporation), Bearing Trivia: Leonardo da Vinci Was the Father of the Bearing!?! The amazing history of bearings, (2019). <https://koyo.jtekt.co.jp/en/2019/07/column01-02.html> (accessed April 23, 2020).
- [29] K. Knobling, First Helicopters and Rotor Systems, in: E.H. Hirschel, H. Prem, G. Madelung (Eds.), *Aeronautical Research in Germany: From Lilienthal until Today*, Springer Berlin Heidelberg, Berlin, Heidelberg, 2004: pp. 293–309. [https://doi.org/10.1007/978-3-642-18484-0\\_12](https://doi.org/10.1007/978-3-642-18484-0_12).
- [30] J.N. Daniel, Introduction, in: *Papers Presented At the Elastomeric Bearing*, US Army Aviation Materiel Laboratories, Fort Eustis, Virginia, 1969: pp. 1–13.
- [31] J.K. Lancaster, The effect of carbon fibre reinforcement on the friction and wear of polymers, *Journal of Physics D: Applied Physics*. 1 (1968) 549–559. <https://doi.org/10.1088/0022-3727/1/5/303>.
- [32] S. Ricklin, Review of design parameters for filled PTFE bearing materials, *Lubrication Engineering*. 33 (1977) 487–490.
- [33] T.A. Blanchet, F.E. Kennedy, Sliding wear mechanism of polytetrafluoroethylene (PTFE) and PTFE composites, *Wear*. 153 (1992) 229–243. [https://doi.org/10.1016/0043-1648\(92\)90271-9](https://doi.org/10.1016/0043-1648(92)90271-9).
- [34] B.J. Briscoe, M.D. Steward, A.J. Groszek, The effect of carbon aspect ratio on the friction and wear of PTFE, *Wear*. 42 (1977) 99–107. <https://doi.org/10.1016/0043->

- 1648(77)90171-5.
- [35] D.R. Wheelie, The transfer of polytetrafluoroethylene studied by x-ray photoelectron spectroscopy, *Wear*. 66 (1981) 355–365. [https://doi.org/10.1016/0043-1648\(81\)90128-9](https://doi.org/10.1016/0043-1648(81)90128-9).
- [36] B. Arkles, J. Theberge, M. Schireson, Wear Behavior of Thermoplastic Polymer- Filled PTFE composites, *Lubrication Engineering*. 33 (1977) 33–38.
- [37] H. Moon-Hee, P. Su-II, Effect of fluorinated ethylene propylene copolymer on the wear behaviour of polytetrafluoroethylene, *Wear*. 143 (1991) 87–97. [https://doi.org/10.1016/0043-1648\(91\)90087-B](https://doi.org/10.1016/0043-1648(91)90087-B).
- [38] D.L. Burris, Effects of nanoparticles on the wear resistance of polytetrafluoroethylene (PhD Dissertation), University of Florida, 2007.
- [39] D.C. Evans, G.S. Senior, Self-lubricating materials for plain bearings, *Tribology International*. 15 (1982) 243–248. [https://doi.org/10.1016/0301-679X\(82\)90077-9](https://doi.org/10.1016/0301-679X(82)90077-9).
- [40] GGB Bearing Technology, GGB DU and DX Metal-Polymer Self-lubricating Bearing Solutions, (2016). <https://www.ggbearings.com/sites/default/files/2020-03/GGB-DU-and-DU-B-Metal-Polymer-Self-Lubricating-Bearings-Brochure-English.pdf> (accessed September 16, 2020).
- [41] GGB Bearing Technology, DP4, DP10 and DP11 Metal-Polymer Self-Lubricating Lead Free Bearing Solutions, (2015). <https://www.ggbearings.com/sites/default/files/2020-03/ggb-dp4-dp10-dp11-metal-polymer-self-lubricating-lead-free-bearings-brochure.pdf> (accessed September 1, 2020).
- [42] D.C. Evans, G.S. Senior, Self-lubricating materials for plain bearings, *Tribology International*. 15 (1982) 243–248. [https://doi.org/10.1016/0301-679X\(82\)90077-9](https://doi.org/10.1016/0301-679X(82)90077-9).
- [43] M. Qiu, Y. Miao, Y. Li, J. Lu, Film-forming mechanisms for self-lubricating radial spherical plain bearings with hybrid PTFE / aramid fabric liners modified by ultrasonic, *Tribology International*. 87 (2015) 132–138. <https://doi.org/10.1016/j.triboint.2015.02.025>.
- [44] D. Gu, C. Duan, B. Fan, S. Chen, Y. Yang, Tribological properties of hybrid PTFE/Kevlar fabric composite in vacuum, *Tribology International*. 103 (2016) 423–431. <https://doi.org/10.1016/j.triboint.2016.08.004>.

- [45] H.A. Aisyah, M.T. Paridah, A. Khalina, S.M. Sapuan, M.S. Wahab, O.B. Berkalp, C.H. Lee, S.H. Lee, Effects of fabric counts and weave designs on the properties of Laminated Woven Kenaf/Carbon fibre reinforced epoxy hybrid composites, *Polymers*. 10 (2018) 1–19. <https://doi.org/10.3390/polym10121320>.
- [46] D. Gu, Y. Yang, X. Qi, W. Deng, L. Shi, Influence of weave structures on the tribological properties of hybrid Kevlar/PTFE fabric composites, *Chinese Journal of Mechanical Engineering (English Edition)*. 25 (2012) 1044–1051. <https://doi.org/10.3901/CJME.2012.05.1044>.
- [47] SKF Group, AMPEP High performance plain bearings, (2012). [https://www.skf.com/binaries/pub12/Images/0901d1968020a6fc-13089EN-\\_tcm\\_12-99107.pdf#cid-99107](https://www.skf.com/binaries/pub12/Images/0901d1968020a6fc-13089EN-_tcm_12-99107.pdf#cid-99107) (accessed November 10, 2019).
- [48] S.K. Biswas, K. Vijayan, Friction and wear of PTFE, *Wear*. 158 (1992) 193–211. [https://doi.org/10.1016/0043-1648\(92\)90039-B](https://doi.org/10.1016/0043-1648(92)90039-B).
- [49] D.L. Burris, P.L. Dickrell, P.R. Barry, C. Santos, S.S. Perry, S.R. Phillpot, S.B. Sinnott, Sliding orientation effects on the tribological properties of polytetrafluoroethylene, *Journal of Applied Physics*. 102 (2007) 1–7. <https://doi.org/10.1063/1.2821743>.
- [50] B.J. Briscoe, P.D. Evans, J.K. Lancaster, The influence of debris inclusion on abrasive wear relationships of PTFE, *Wear*. 124 (1988) 177–194. [https://doi.org/10.1016/0043-1648\(88\)90243-8](https://doi.org/10.1016/0043-1648(88)90243-8).
- [51] J.K. Lancaster, On the initial stages of wear of dry-bearing composites, in: 8th Leeds–Lyon Symposium on Tribology, Lyon, 1981: pp. 33–43.
- [52] J.K. Lancaster, Estimation of the limiting PV relationships for thermoplastic bearing materials, *Tribology*. 4 (1971) 82–86. [https://doi.org/10.1016/0041-2678\(71\)90136-9](https://doi.org/10.1016/0041-2678(71)90136-9).
- [53] J.K. Lancaster, Accelerated wear testing of PTFE composite bearing materials, *Tribology International*. 12 (1979) 65–75. [https://doi.org/10.1016/0301-679X\(79\)90004-5](https://doi.org/10.1016/0301-679X(79)90004-5).
- [54] AS81820, General Specification For Low Speed Oscillation Self-Lubricating Self-Aligning Plain Bearings, SAE International, Warrendale, PA, 1998. <https://doi.org/10.4271/AS81820>.
- [55] Y. Yang, D. Zu, R. Zhang, X. QI, Effects of Friction Heat on the Tribological Properties

- of the Woven Self-lubricating Liner, *Chinese Journal of Mechanical Engineering*. 22 (2009) 918–927. <https://doi.org/CNKI:SUN:YJXB.0.2009-06-018>.
- [56] Y. Yang, C. Ma, S. Huang, L. Jing, H. Pang, Effects of mechanical properties of Kevlar/PTFE fabric-reinforced self-lubricating liners on performance of self-lubricating spherical plain bearings, *Applied Mechanics and Materials*. 29–32 (2010) 197–202. <https://doi.org/10.4028/www.scientific.net/AMM.29-32.197>.
- [57] F. hua Su, Z. zhu Zhang, W. min Liu, Friction and wear behavior of hybrid glass/PTFE fabric composite reinforced with surface modified nanometer ZnO, *Wear*. 265 (2008) 311–318. <https://doi.org/10.1016/j.wear.2007.10.013>.
- [58] K. Tanaka, Y. Uchiyama, S. Toyooka, The mechanism of wear of polytetrafluoroethylene, *Wear*. 23 (1973) 153–172. [https://doi.org/10.1016/0043-1648\(73\)90081-1](https://doi.org/10.1016/0043-1648(73)90081-1).
- [59] D. Play, B. Pruvost, Comparative dry wear of PTFE liner bearing in cylindrical and spherical geometry, *Journal of Tribology*. 106 (1984) 185–191.
- [60] G. Zhao, C. Wu, L. Zhang, J. Song, Q. Ding, Friction and wear behavior of PI and PTFE composites for ultrasonic motors, *Polymers for Advanced Technologies*. 29 (2018) 1487–1496. <https://doi.org/10.1002/pat.4260>.
- [61] E. Omrani, P.K. Rohatgi, P.L. Menezes, Self-Lubricating Polymer Matrix Composites, in: *Tribology and Applications of Self-Lubricating Materials*, CRC Press, 2017: pp. 69–120.
- [62] K. Tanaka, Effects of Various Fillers on the Friction and Wear of PTFE-Based Composites, *Composite Materials Series*. 1 (1986) 137–174. <https://doi.org/10.1016/B978-0-444-42524-9.50009-0>.
- [63] H. Pihtili, N. Tosun, Effect of load and speed on the wear behaviour of woven glass fabrics and aramid fibre-reinforced composites, *Wear*. 252 (2002) 979–984. [https://doi.org/10.1016/S0043-1648\(02\)00062-5](https://doi.org/10.1016/S0043-1648(02)00062-5).
- [64] C. Ettles, Polymer and elastomer friction in the thermal control regime, *ASLE Transactions*. 30 (1987) 149–159. <https://doi.org/10.1080/05698198708981743>.
- [65] C. Ettles, The thermal control of friction at high sliding speeds, *Journal of Tribology*. 108 (1986) 98–104. <https://doi.org/10.1115/1.3261151>.

- [66] X. Tian, F.E. Kennedy, Maximum and average flash temperatures in sliding contacts, *Journal of Tribology*. 116 (1994) 167–174. <https://doi.org/10.1115/1.2927035>.
- [67] F.E. Kennedy, X. Tian, The Effect of Interfacial Temperature on Friction and Wear of Thermoplastics in the Thermal Control Regime, *Tribology Series*. 27 (1994) 235–244. [https://doi.org/10.1016/S0167-8922\(08\)70312-2](https://doi.org/10.1016/S0167-8922(08)70312-2).
- [68] K. Friedrich, Advanced Industrial and Engineering Polymer Research Polymer composites for tribological applications, *Advanced Industrial and Engineering Polymer Research*. 1 (2018) 3–39. <https://doi.org/10.1016/j.aiepr.2018.05.001>.
- [69] F. Song, Q. Wang, T. Wang, Tribology International Effects of glass fiber and molybdenum disulfide on tribological behaviors and PV limit of chopped carbon fiber reinforced polytetra fluoroethylene composites, 104 (2016) 392–401. <https://doi.org/10.1016/j.triboint.2016.01.015>.
- [70] F. Song, Q. Wang, T. Wang, The effects of crystallinity on the mechanical properties and the limiting PV ( pressure × velocity ) value of PTFE, *Tribology International*. 93 (2016) 1–10. <https://doi.org/10.1016/j.triboint.2015.09.017>.
- [71] J.E. Morgan, W.J. Plumbridge, The effect of humidity on dry bearing torque, *Wear*. 119 (1987) 215–223. [https://doi.org/https://doi.org/10.1016/0043-1648\(87\)90111-6](https://doi.org/https://doi.org/10.1016/0043-1648(87)90111-6).
- [72] R.W. Bramham, K.B. King, J.K. Lancaster, The Wear of PTFE-Containing Dry Bearing Liners Contaminated by Fluids, *Tribology Transactions*. 24 (1981) 479–489. <https://doi.org/10.1080/05698198108983046>.
- [73] A. Zmitrowicz, Models of kinematics dependent anisotropic and heterogeneous friction, *International Journal of Solids and Structures*. 43 (2006) 4407–4451. <https://doi.org/10.1016/j.ijsolstr.2005.07.001>.
- [74] D. Tabor, D.E.W. Williams, The effect of orientation on the friction of polytetrafluoroethylene, *Wear*. 4 (1961) 391–400. [https://doi.org/10.1016/0043-1648\(61\)90007-2](https://doi.org/10.1016/0043-1648(61)90007-2).
- [75] F. Zhang, K. Liu, Y. Wan, L. Jin, B. Gu, B. Sun, Experimental and numerical analyses of the mechanical behaviors of three-dimensional orthogonal woven composites under compressive loadings with different strain rates, *International Journal of Damage Mechanics*. 23 (2014) 636–660. <https://doi.org/10.1177/1056789513505301>.

- [76] X. Ning, M.R. Lovell, C. Morrow, Anisotropic strength approach for wear analysis of unidirectional continuous FRP composites, *Journal of Tribology*. 126 (2004) 65–70. <https://doi.org/10.1115/1.1631008>.
- [77] D. Godet, M., Play, Third-body formation and elimination on carbon-fibre/epoxy composite, in: *Space Tribology Proceedings of the First European Space Tribology*, Fracasti, Italy, 1975: pp. 165–173.
- [78] Z. Rasheva, G. Zhang, T. Burkhart, A correlation between the tribological and mechanical properties of short carbon fibers reinforced PEEK materials with different fiber orientations, *Tribology International*. 43 (2010) 1430–1437. <https://doi.org/10.1016/j.triboint.2010.01.020>.
- [79] B.J. Briscoe, T.A. Stolarski, Transfer wear of polymers during combined linear motion and load axis spin, *Wear*. 104 (1985) 121–137. [https://doi.org/10.1016/0043-1648\(85\)90057-2](https://doi.org/10.1016/0043-1648(85)90057-2).
- [80] B.J. Briscoe, T.A. Stolarski, Combined rotating and linear motion effects on the wear of polymers [5], *Nature*. 281 (1979) 206–208. <https://doi.org/10.1038/281206a0>.
- [81] B.J. Briscoe, T.A. Stolarski, The influence of contact zone kinematics on wear process of polymers, *Wear*. 149 (1991) 233–240. [https://doi.org/10.1016/0043-1648\(91\)90376-6](https://doi.org/10.1016/0043-1648(91)90376-6).
- [82] F. Ning, H. Wang, Y. Hu, W. Cong, M. Zhang, Y. Li, Rotary Ultrasonic Surface Machining of CFRP Composites: A Comparison with Conventional Surface Grinding, *Procedia Manufacturing*. 10 (2017) 557–567. <https://doi.org/10.1016/j.promfg.2017.07.049>.
- [83] T.J. Joyce, C. Vandelli, T. Cartwright, A. Unsworth, A comparison of the wear of cross-linked polyethylene against itself under reciprocating and multi-directional motion with different lubricants, *Wear*. 250 (2001) 206–211. [https://doi.org/10.1016/S0043-1648\(01\)00660-3](https://doi.org/10.1016/S0043-1648(01)00660-3).
- [84] V. Saikko, T. Ahlroos, Wear simulation of UHMWPE for total hip replacement with a multidirectional motion pin-on-disk device: Effects of counterface material, contact area, and lubricant, *Journal of Biomedical Materials Research*. 49 (2000) 147–154. [https://doi.org/10.1002/\(SICI\)1097-4636\(200002\)49:2<147::AID-JBM1>3.0.CO;2-H](https://doi.org/10.1002/(SICI)1097-4636(200002)49:2<147::AID-JBM1>3.0.CO;2-H).

- [85] T.J. Joyce, D. Monk, S.C. Scholes, A. Unsworth, A multi-directional wear screening device and preliminary results of UHMWPE articulating against stainless steel, *Bio-Medical Materials and Engineering*. 10 (2000) 241–249.
- [86] M. Qiu, Z.L. Gao, G.F. Wang, L. Chen, Tribological Properties of Spherical Plain Bearings with Self-Lubricating PTFE Woven Liners, *Advanced Materials Research*. 338 (2011) 607–610. <https://doi.org/10.4028/www.scientific.net/AMR.338.607>.
- [87] W. Wieleba, The statistical correlation of the coefficient of friction and wear rate of PTFE composites with steel counterface roughness and hardness, *Wear*. 252 (2002) 719–729. [https://doi.org/10.1016/S0043-1648\(02\)00029-7](https://doi.org/10.1016/S0043-1648(02)00029-7).
- [88] P.L. Menezes, S.V. Kailas, Role of surface texture and roughness parameters on friction and transfer film formation when UHMWPE sliding against steel, *Biosurface and Biotribology*. 2 (2016) 1–10. <https://doi.org/10.1016/j.bsbt.2016.02.001>.
- [89] K.R. Makinson, D. Tabor, The friction and transfer of polytetrafluoroethylene, *Royal Society*. 281 (1964) 49–61. <https://doi.org/10.1038/2011172c0>.
- [90] C.W. Bunn, A.J. Cobbold, R.P. Palmer, The fine structure of polytetrafluoroethylene, *Journal of Polymer Science*. 28 (1958) 365–376. <https://doi.org/10.1002/pol.1958.1202811712>.
- [91] C.W. Bunn, E.R. Howells, Structures of molecules and crystals of fluoro-carbons, *Nature*. 174 (1954) 549–551. <https://doi.org/10.1038/174549a0>.
- [92] C.M. Pooley, D. Tabor, Friction and Molecular Structure: The Behaviour of Some Thermoplastics, *Proceedings of the Royal Society A: Mathematical, Physical and Engineering Sciences*. 329 (1972) 251–274. <https://doi.org/10.1098/rspa.1972.0112>.
- [93] W.A. Brainurd, D.H. Bivckley, NASA Technical Note D-6524: Adhesion of polymers to tungsten as studied by field ion microscopy, Cleveland, Ohio, 1971.
- [94] S. V Pepper, D.H. Buckley, NASA Technical Note D-6983: Adhesion and transfer of polytetrafluoroethylene to metals studied by auger emission spectroscopy, Cleveland, Ohio, 1972.
- [95] J.L. Lauer, B.G. Bunting, W.R. Jones Jr, NASA Technical Memorandum 89844: Investigation of PTFE transfer films by infrared emission spectroscopy and phase-locked ellipsometry, Cleveland, Ohio, 1987.

- [96] K.I. Alam, A. Dorazio, Polymers Tribology Exposed : Eliminating Transfer Film Effects to Clarify Ultralow Wear of PTFE, *Tribology Letters*. 68 (2020) 1–13. <https://doi.org/10.1007/s11249-020-01306-9>.
- [97] J. Ye, H.S. Khare, D.L. Burris, Quantitative characterization of solid lubricant transfer film quality, *Wear*. 316 (2014) 133–143. <https://doi.org/10.1016/j.wear.2014.04.017>.
- [98] J. Ye, W. Sun, Y. Zhang, X. Liu, K. Liu, Measuring Evolution of Transfer Film–Substrate Interface Using Low Wear Alumina PTFE, *Tribology Letters*. 66 (2018) 1–14. <https://doi.org/10.1007/s11249-018-1054-6>.
- [99] J. Ye, D. Burris, T. Xie, A Review of Transfer Films and Their Role in Ultra-Low-Wear Sliding of Polymers, *Lubricants*. 4 (2016) 1–15. <https://doi.org/10.3390/lubricants4010004>.
- [100] G. Beamson, D.T. Clark, D.E. Deegan, N.W. Hayes, D.S.L. Law, J.R. Rasmusson, W.R. Salaneck, Characterization of PTFE on silicon wafer tribological transfer films by XPS, imaging XPS and AFM, *Surface and Interface Analysis*. 24 (1996) 204–210. [https://doi.org/10.1002/\(SICI\)1096-9918\(199603\)24:3<204::AID-SIA90>3.0.CO;2-C](https://doi.org/10.1002/(SICI)1096-9918(199603)24:3<204::AID-SIA90>3.0.CO;2-C).
- [101] M.H. Cho, The role of transfer film and back transfer behavior on the tribological performance of polyoxymethylene in sliding †, *Journal of Mechanical Science and Technology*. 23 (2009) 2291–2298. <https://doi.org/10.1007/s12206-009-0354-z>.
- [102] Z. Zuo, Y. Yang, X. Qi, W. Su, X. Yang, Analysis of the chemical composition of the PTFE transfer film produced by sliding against Q235 carbon steel, *Wear*. 320 (2014) 87–93. <https://doi.org/10.1016/j.wear.2014.08.019>.
- [103] G. Jintang, Tribochemical effects in formation of polymer transfer film, *Wear*. 245 (2000) 100–106. [https://doi.org/10.1016/S0043-1648\(00\)00470-1](https://doi.org/10.1016/S0043-1648(00)00470-1).
- [104] S. Bahadur, The development of transfer layers and their role in polymer tribology, *Wear*. 245 (2000) 92–99. [https://doi.org/10.1016/S0043-1648\(00\)00469-5](https://doi.org/10.1016/S0043-1648(00)00469-5).
- [105] E.E. Nunez, S.M. Yeo, K. Polychronopoulou, A.A. Polycarpou, Tribological study of high bearing blended polymer-based coatings for air-conditioning and refrigeration compressors, *Surface and Coatings Technology*. 205 (2011) 2994–3005. <https://doi.org/10.1016/j.surfcoat.2010.11.008>.
- [106] I. Minami, T. Kubo, H. Nanao, S. Mori, H. Iwata, M. Fujita, *Surface Chemistry for*

- Improvement in Load-Carrying Capacity of Poly (Ether-Ether-Ketone)-Based Materials by Poly (Tetrafluoroethylene ), Japanese Society of Tribologists. 3 (2008) 190–194. <https://doi.org/10.2474/trol3.190>.
- [107] J. Tuominen, H. Pajukoski, P. Vuoristo, S. Thieme, S. Nowotny, J. Näkki, Sliding wear performance of metallic laser coatings against composite PTFE seals, *Materialwissenschaft Und Werkstofftechnik*. 49 (2018) 1263–1277. <https://doi.org/10.1002/mawe.201800013>.
- [108] D.C.J. J.I. Goldstein, D.E. Newbury, J.R. Michael, N.W.M. Ritchie, J.H.J. Scott, Electron-Specimen Interactions, in: *Scanning Electron Microscopy and X-Ray Microanalysis*, Springer, New York, 1992: pp. 69–147. [https://doi.org/10.1007/978-1-4613-0491-3\\_3](https://doi.org/10.1007/978-1-4613-0491-3_3).
- [109] F. Kennedy, L. Smidhammar, D. Play, Wear of polyethylene in small-amplitude oscillatory motion, in: *Proceedings of Eurotrib 85: 4th European Tribology Congress*, Ecully, France, 1975: pp. 1–9.
- [110] D.F. Play, Counterface Roughness Effect on the Dry Steady State Wear of Self-Lubricating Polyimide Composites, *Journal of Tribology*. 106 (1984) 177–184. <https://doi.org/10.1115/1.3260874>.
- [111] C. Lopes, R. Tschopp, Titanium spherical plain bearing with liner and treated surface, US patent 2007/0223850A1, 2007.
- [112] P. Beausoleil, R.A. Arnold, A. Tyler, C. Whelen, Tungsten carbide enhanced bearing, US patent 7828482B2, 2010.
- [113] B.C. Kim, D.C. Park, H.S. Kim, D.G. Lee, Development of composite spherical bearing, *Composite Structures*. 75 (2006) 231–240. <https://doi.org/10.1016/j.compstruct.2006.04.027>.
- [114] R.A. Pethrick, Composite to metal bonding in aerospace and other applications, in: M.C. Chaturvedi (Ed.), *Welding and Joining of Aerospace Materials*, Woodhead Publishing Limited, 2012: pp. 288–319. <https://doi.org/10.1533/9780857095169.2.288>.
- [115] A.J. Kinloch, The science of adhesion, *Journal of Materials Science*. 15 (1980) 2141–2166. <https://doi.org/10.1007/bf00552302>.
- [116] P.J. Pearce, D.R. Arnott, A. Camilleri, M.R. Kindermann, G.I. Mathys, A.R. Wilson,

- Cause and effect of void formation during vacuum bag curing of epoxy film adhesives, *Journal of Adhesion Science and Technology*. 12 (1998) 567–584. <https://doi.org/10.1163/156856198X00795>.
- [117] K. TOSHA, J. LU, Effect of shot peening and grit blasting on surface integrity: Influence on residual stresses, *Transactions of Nonferrous Metals Society of China (English Edition)*. 16 (2006) 230–235.
- [118] K. Poorna Chander, M. Vashista, K. Sabiruddin, S. Paul, P.P. Bandyopadhyay, Effects of grit blasting on surface properties of steel substrates, *Materials and Design*. 30 (2009) 2895–2902. <https://doi.org/10.1016/j.matdes.2009.01.014>.
- [119] L.R. Millman, J.W. Giancaspro, Environmental Evaluation of Abrasive Blasting with Sand, Water, and Dry Ice, *International Journal of Architecture, Engineering and Construction*. 1 (2012) 174–182. <https://doi.org/10.7492/ijaec.2012.019>.
- [120] G.W. Critchlow, D.M. Brewis, Influence of surface macroroughness on the durability of epoxide-aluminium joints, *International Journal of Adhesion and Adhesives*. 15 (1995) 173–176. [https://doi.org/10.1016/0143-7496\(95\)91628-J](https://doi.org/10.1016/0143-7496(95)91628-J).
- [121] B.L.S. Martz, Preliminary Report of Developments in Interrupted Surface Finishes, *Journal of the American Society for Naval Engineers*. 62 (1950) 487–504. <https://doi.org/10.1111/j.1559-3584.1950.tb02844.x>.
- [122] W.J.A. Hamilton D. B., C.M. Allen, A Theory of Lubrication by Micro-irregularities, *ASME Journal of Basic Engineering*. 88 (1966) 177–185. <https://doi.org/10.1115/1.3645799>.
- [123] E. Teng, N. Ballard, Anisotropy induced signal waveform modulation of DC magnetron sputtered thin film disks, *IEEE Transactions on Magnetics*. 22 (1986) 579–581. <https://doi.org/10.1109/TMAG.1986.1064570>.
- [124] S. Uchinami, F. Beppu, S. Ito, N. Tokubuchi, K. Noda, Y. Notohara, K. Kanai, Magnetic anisotropies in sputtered thin film disks, *IEEE Transactions on Magnetics*. 23 (1987) 3408–3410. <https://doi.org/10.1109/TMAG.1987.1065487>.
- [125] K. Tonder, H. Christensen, Waviness and Roughness in Hydrodynamic Lubrication, *Proceedings of the Institution of Mechanical Engineers*. 186 (1972) 807–812. [https://doi.org/10.1243/pime\\_proc\\_1972\\_186\\_096\\_02](https://doi.org/10.1243/pime_proc_1972_186_096_02).

- [126] R. Ranjan, D.N. Lambeth, M. Tromel, P. Goglia, Y. Li, Laser texturing for low-flying-height media, *Journal of Applied Physics*. 69 (1991) 5745–5747. <https://doi.org/10.1063/1.347908>.
- [127] K.Y. Etsion I., G. Halperin, Analytical and Experimental Investigation of Laser-Textured Mechanical Seal Faces, *Tribology Transactions*. 42 (1999) 511–516. <https://doi.org/10.1080/10402009908982248>.
- [128] A.D. McNickle, I. Etsion, Near-Contact Laser Surface Textured Dry Gas Seals, *Journal of Tribology*. 126 (2004) 788. <https://doi.org/10.1115/1.1792695>.
- [129] I. Etsion, State of the Art in Laser Surface Texturing, *Journal of Tribology*. 127 (2005) 248–253. <https://doi.org/10.1115/1.1828070>.
- [130] Y. Kligerman, I. Etsion, A. Shinkarenko, Improving Tribological Performance of Piston Rings by Partial Surface Texturing, *Journal of Tribology*. 127 (2005) 632–638. <https://doi.org/10.1115/1.1866171>.
- [131] M. Varenberg, G. Halperin, I. Etsion, Different aspects of the role of wear debris in fretting wear, *Wear*. 252 (2002) 902–910. [https://doi.org/10.1016/S0043-1648\(02\)00044-3](https://doi.org/10.1016/S0043-1648(02)00044-3).
- [132] A. Volchok, G. Halperin, I. Etsion, The effect of surface regular microtopography on fretting fatigue life, *Wear*. 253 (2002) 509–515. [https://doi.org/10.1016/S0043-1648\(02\)00148-5](https://doi.org/10.1016/S0043-1648(02)00148-5).
- [133] D. Xing, J. Zhang, X. Shen, Y. Zhao, T. Wang, Tribological properties of ultrasonic vibration assisted milling aluminium alloy surfaces, *Procedia CIRP*. 6 (2013) 539–544. <https://doi.org/10.1016/j.procir.2013.03.008>.
- [134] Y. Hong, P. Zhang, K.-H. Lee, C.-H. Lee, Friction and wear of textured surfaces produced by 3D printing, *Science China Technological Sciences*. 60 (2017) 1–7. <https://doi.org/10.1007/s11431-016-9066-0>.
- [135] R. Kovacevic, Surface texture in abrasive waterjet cutting, *Journal of Manufacturing Systems*. 10 (1991) 32–40. [https://doi.org/10.1016/0278-6125\(91\)90045-4](https://doi.org/10.1016/0278-6125(91)90045-4).
- [136] J.C. Campbell, Cylinder Bore Surface Roughness in Internal Combustion Engines : Its Appreciation and Control, *Wear*. 19 (1972) 163–168. [https://doi.org/10.1016/0043-1648\(72\)90302-X](https://doi.org/10.1016/0043-1648(72)90302-X).

- [137] L. Li, D.M. Chai, The Research and Application of Honing Technology, *Key Engineering Materials*. 202–203 (2001) 385–388. <https://doi.org/10.4028/www.scientific.net/KEM.202-203.385>.
- [138] T. Korpela, M. Suvanto, T.T. Pakkanen, Wear and friction behavior of polyacetal surfaces with micro-structure controlled surface pressure, *Wear*. 328–329 (2015) 262–269. <https://doi.org/10.1016/j.wear.2015.02.017>.
- [139] Q.J. Wang, A. Greco, K. Ehmann, Surface Texturing by Vibro Machining, in: Q.J. Wang, Y.-W. Chung (Eds.), *Encyclopedia of Tribology*, Springer US, Boston, MA, 2013: pp. 3505–3509. [https://doi.org/10.1007/978-0-387-92897-5\\_11](https://doi.org/10.1007/978-0-387-92897-5_11).
- [140] Wang X., K. Kato, Improving The Anti-Seizure Ability of SiC Seal in Water with RIE Texturing, *Tribology Letter*. 14(4) (2003) 275–280.
- [141] U. Pettersson, S. Jacobson, Influence of surface texture on boundary lubricated sliding contacts, *Tribology International*. 36 (2003) 857–864. [https://doi.org/10.1016/S0301-679X\(03\)00104-X](https://doi.org/10.1016/S0301-679X(03)00104-X).
- [142] A. V Gorbunov, V.K. Belov, D.O. Begletsov, Texturing of rollers for the production of auto-industry sheet, *Steel in Translation*. 39 (2009) 696–699. <https://doi.org/10.3103/S0967091209080178>.
- [143] L. Zhou, K. Kato, N. Umehara, Y. Miyake, Nanometre scale island-type texture with controllable height and area ratio formed by ion-beam etching on hard-disk head sliders, *Nanotechnology*. 10 (1999) 363–372. <https://doi.org/10.1088/0957-4484/10/4/301>.
- [144] W. Tang, Y. Zhou, H. Zhu, H. Yang, The effect of surface texturing on reducing the friction and wear of steel under lubricated sliding contact, *Applied Surface Science*. 273 (2013) 199–204. <https://doi.org/10.1016/j.apsusc.2013.02.013>.
- [145] N. Zaafarani, D. Raabe, R.N. Singh, F. Roters, S. Zaefferer, Three-dimensional investigation of the texture and microstructure below a nanoindent in a Cu single crystal using 3D EBSD and crystal plasticity finite element simulations, *Acta Materialia*. 54 (2006) 1863–1876. <https://doi.org/10.1016/j.actamat.2005.12.014>.
- [146] U. Pettersson, S. Jacobson, Friction and wear properties of micro textured DLC coated surfaces in boundary lubricated sliding, *Tribology Letters*. 17 (2004) 553–559. <https://doi.org/10.1023/B:TRIL.0000044504.76164.4e>.

- [147] S. Cupillard, S. Glavatskih, M.J. Cervantes, Computational fluid dynamics analysis of a journal bearing with surface texturing, *Proceedings of the Institution of Mechanical Engineers, Part J: Journal of Engineering Tribology*. 222 (2008) 97–107. <https://doi.org/10.1243/13506501JET319>.
- [148] S. Cupillard, M.J. Cervantes, S. Glavatskih, A CFD study of a finite textured journal bearing, in: *IAHR 24th Symposium on Hydraulic Machinery and Systems*, Foz Do Iguassu, Brazil, 2008.
- [149] R. Ranjan, D.N. Lambeth, M. Tromel, P. Goglia, Y. Li, Laser texturing for low-flying-height media, *Journal of Applied Physics*. 69 (1991) 5745–5747. <https://doi.org/10.1063/1.347908>.
- [150] Y. Xing, J. Deng, X. Wang, K. Ehmann, J. Cao, Experimental Assessment of Laser Textured Cutting Tools in Dry Cutting of Aluminum Alloys, *Journal of Manufacturing Science and Engineering*. 138 (2016) 071006. <https://doi.org/10.1115/1.4032263>.
- [151] D. Jianxin, W. Ze, L. Yunsong, Q. Ting, C. Jie, Performance of carbide tools with textured rake-face filled with solid lubricants in dry cutting processes, *International Journal of Refractory Metals and Hard Materials*. 30 (2012) 164–172. <https://doi.org/10.1016/j.ijrmhm.2011.08.002>.
- [152] S. Amini, H.N. Hosseinabadi, S.A. Sajjady, Experimental study on effect of micro textured surfaces generated by ultrasonic vibration assisted face turning on friction and wear performance, *Applied Surface Science*. 390 (2016) 633–648. <https://doi.org/10.1016/j.apsusc.2016.07.064>.
- [153] T. Korpela, M. Suvanto, T.T. Pakkanen, Friction and wear of periodically micro-patterned polypropylene in dry sliding, *Wear*. 289 (2012) 1–8. <https://doi.org/10.1016/j.wear.2012.04.023>.
- [154] Y. Xing, J. Deng, Z. Wu, F. Wu, High friction and low wear properties of laser-textured ceramic surface under dry friction, *Optics & Laser Technology*. 93 (2017) 24–32. <https://doi.org/10.1016/j.optlastec.2017.01.032>.
- [155] Q. Sun, T. Hu, H. Fan, Y. Zhang, L. Hu, Dry sliding wear behavior of TC11 alloy at 500°C: Influence of laser surface texturing, *Tribology International*. 92 (2015) 136–145. <https://doi.org/10.1016/j.triboint.2015.06.003>.

- [156] S.K. Mishra, S. Ghosh, S. Aravindan, 3D finite element investigations on textured tools with different geometrical shapes for dry machining of titanium alloys, *International Journal of Mechanical Sciences*. 141 (2018) 424–449. <https://doi.org/10.1016/j.ijmecsci.2018.04.011>.
- [157] Z. Wu, H. Bao, L. Liu, Y. Xing, P. Huang, G. Zhao, Numerical investigation of the performance of micro-textured cutting tools in cutting of Ti-6Al-4V alloys, *International Journal of Advanced Manufacturing Technology*. 108 (2020) 463–474. <https://doi.org/10.1007/s00170-020-05428-1>.
- [158] A. Olleak, T. Özel, 3D Finite Element Modeling Based Investigations of Micro-textured Tool Designs in Machining Titanium Alloy Ti-6Al-4V, *Procedia Manufacturing*. 10 (2017) 536–545. <https://doi.org/10.1016/j.promfg.2017.07.042>.
- [159] S. Hoshino, C. Tadokoro, S. Sasaki, Effect of Surface Texturing on Friction Transition of C/C Composite Material, *Tribology Online*. 11 (2016) 426–431. <https://doi.org/10.2474/trol.11.426>.
- [160] M. Wang, C. Zhang, X. Wang, The wear behavior of textured steel sliding against polymers, *Materials*. 10 (2017) 1–14. <https://doi.org/10.3390/ma10040330>.
- [161] D.E. Packham, Theories of Fundamental Adhesion, in: R.D. Adams (Ed.), *Handbook of Adhesion Technology*, Springer International Publishing, Cham, 2017: pp. 1–31. [https://doi.org/10.1007/978-3-319-42087-5\\_2-2](https://doi.org/10.1007/978-3-319-42087-5_2-2).
- [162] C.W. Jennings, Surface Roughness and Bond Strength of Adhesives, *The Journal of Adhesion*. 4 (1972) 25–38. <https://doi.org/10.1080/00218467208072208>.
- [163] K. Uehara, M. Sakurai, Bonding strength of adhesives and surface roughness of joined parts, *Journal of Materials Processing Technology*. 127 (2002) 178–181. [https://doi.org/10.1016/S0924-0136\(02\)00122-X](https://doi.org/10.1016/S0924-0136(02)00122-X).
- [164] J.W. McBain, D.G. Hopkins, On Adhesives and Adhesive Action, *The Journal of Physical Chemistry*. 29 (1925) 188–204. <https://doi.org/10.1021/j150248a008>.
- [165] W. V. Chang, J.S. Wang, Enhancement of Adhesive Joint Strength By Surface Texturing, *Journal of Applied Polymer Science*. 26 (1981) 1759–1776. <https://doi.org/10.1002/app.1981.070260602>.
- [166] H.R. Jahani, B. Moffat, R.E. Mueller, D. Fumo, W. Duley, T. North, B. Gu, Excimer

- laser surface modification of coated steel for enhancement of adhesive bonding, *Applied Surface Science*. 127–129 (1998) 767–772. [https://doi.org/10.1016/S0169-4332\(97\)00738-1](https://doi.org/10.1016/S0169-4332(97)00738-1).
- [167] X.M. Zhang, T.M. Yue, H.C. Man, Enhancement of ceramic-to-metal adhesive bonding by excimer laser surface treatment, *Materials Letters*. 30 (1997) 327–332. [https://doi.org/10.1016/S0167-577X\(96\)00229-7](https://doi.org/10.1016/S0167-577X(96)00229-7).
- [168] F. Henari, W. Blau, Excimer-laser surface treatment of metals for improved adhesion, *Applied Optics*. 34 (1995) 581–584. <https://doi.org/10.1364/ao.34.000581>.
- [169] P. Maressa, L. Anodio, A. Bernasconi, A.G. Demir, B. Previtali, Effect of surface texture on the adhesion performance of laser treated Ti6Al4V alloy, *Journal of Adhesion*. 91 (2014) 518–537. <https://doi.org/10.1080/00218464.2014.933809>.
- [170] D. Xu, M.K. Ng, R. Fan, R. Zhou, H.P. Wang, J. Chen, J. Cao, Enhancement of adhesion strength by micro-rolling-based surface texturing, *International Journal of Advanced Manufacturing Technology*. 78 (2015) 1427–1435. <https://doi.org/10.1007/s00170-014-6736-0>.
- [171] T. Young, An essay on the cohesion of fluids, *Philosophical Transactions of the Royal Society of London*. 95 (1804) 65–87. <https://doi.org/10.1098/rstl.1805.0005>.
- [172] R.N. Wenzel, Surface Roughness and Contact Angle, *The Journal of Physical and Colloid Chemistry*. 53 (1949) 1466–1467. <https://doi.org/10.1021/j150474a015>.
- [173] D.I. Yu, S.W. Doh, H.J. Kwak, H.C. Kang, H.S. Ahn, H.S. Park, M. Kiyofumi, M.H. Kim, Wetting state on hydrophilic and hydrophobic micro-textured surfaces: Thermodynamic analysis and X-ray visualization, *Applied Physics Letters*. 106 (2015) 1–6. <https://doi.org/10.1063/1.4919136>.
- [174] S.Y. Misyura, G. V. Kuznetsov, D. V. Feoktistov, R.S. Volkov, V.S. Morozov, E.G. Orlova, The influence of the surface microtexture on wettability properties and drop evaporation, *Surface and Coatings Technology*. 375 (2019) 458–467. <https://doi.org/10.1016/j.surfcoat.2019.07.058>.
- [175] G. V. Kuznetsov, D. V. Feoktistov, E.G. Orlova, I.Y. Zykov, A.G. Islamova, Droplet state and mechanism of contact line movement on laser-textured aluminum alloy surfaces, *Journal of Colloid and Interface Science*. 553 (2019) 557–566.

<https://doi.org/10.1016/j.jcis.2019.06.059>.

- [176] K.J. Kubiak, M.C.T. Wilson, T.G. Mathia, P. Carval, Wettability versus roughness of engineering surfaces, *Wear.* 271 (2011) 523–528. <https://doi.org/10.1016/j.wear.2010.03.029>.
- [177] W. Li, A. Amirfazli, A thermodynamic approach for determining the contact angle hysteresis for superhydrophobic surfaces, *Journal of Colloid and Interface Science.* 292 (2005) 195–201. <https://doi.org/10.1016/j.jcis.2005.05.062>.
- [178] Y. Liang, L. Shu, W. Natsu, F. He, Anisotropic wetting characteristics versus roughness on machined surfaces of hydrophilic and hydrophobic materials, *Applied Surface Science.* 331 (2015) 41–49. <https://doi.org/10.1016/j.apsusc.2014.12.071>.
- [179] P.C. J. Long, M.N. Hyder, R.Y.M. Huang, Thermodynamic modeling of contact angles on rough, heterogeneous surfaces, *Environmental Monitoring and Assessment.* 111 (2005) 173–222. <https://doi.org/10.1016/j.cis.2005.07.004>.
- [180] Z.L. Wang, E.H. Chen, Y.P. Zhao, The effect of surface anisotropy on contact angles and the characterization of elliptical cap droplets, *Science China Technological Sciences.* 61 (2018) 309–316. <https://doi.org/10.1007/s11431-017-9149-1>.
- [181] V.A. Lubarda, K.A. Talke, Analysis of the equilibrium droplet shape based on an ellipsoidal droplet model, *Langmuir.* 27 (2011) 10705–10713. <https://doi.org/10.1021/la202077w>.
- [182] D. Baptista, L. Muszyński, D.J. Gardner, E. Atzema, An experimental method for three-dimensional dynamic contact angle analysis, *Journal of Adhesion Science and Technology.* 26 (2012) 2199–2215. <https://doi.org/10.1163/156856111X610135>.
- [183] K. Li, X. Shen, Y. Chen, R. Li, Numerical Analysis of Woven Fabric Composites Lubricated Spherical Plain Bearings, in: *Proceedings of the 11th International Congress and Exposition on Experimental and Applied Mechanics, Orlando, Florida, 2008*: pp. 1392–1399. <http://toc.proceedings.com/03294webtoc.pdf>.
- [184] A.H. Hamad, Effects of Different Laser Pulse Regimes (Nanosecond, Picosecond and Femtosecond) on the Ablation of Materials for Production of Nanoparticles in Liquid Solution, in: R. Viskup (Ed.), *High Energy and Short Pulse Lasers (EBook)*, IntechOpen, 2016: pp. 305–325. <https://doi.org/10.5772/63892>.

- [185] R. Agrawal, C. Wang, Laser Beam Machining, in: B. Bhushan (Ed.), Encyclopedia of Nanotechnology, Springer, Dordrecht, 2016: pp. 1739–1753. [https://doi.org/10.1007/978-94-017-9780-1\\_101020](https://doi.org/10.1007/978-94-017-9780-1_101020).
- [186] A.I. Aguilar-Morales, S. Alamri, A.F. Lasagni, Micro-fabrication of high aspect ratio periodic structures on stainless steel by picosecond direct laser interference patterning, Journal of Materials Processing Technology. 252 (2018) 313–321. <https://doi.org/10.1016/j.jmatprotec.2017.09.039>.
- [187] A. Ancona, S. Döring, C. Jauregui, F. Röser, J. Limpert, S. Nolte, A. Tünnermann, Femtosecond and picosecond laser drilling of metals at high repetition rates and average powers, Optics Letters. 34 (2009) 3304–3306. <https://doi.org/10.1364/ol.34.003304>.
- [188] National Instruments, Measuring Strain with Strain Gages, (2016). <http://www.ni.com/white-paper/3642/en> (accessed January 15, 2019).
- [189] J. Jeswiet, M. Arentoft, P. Henningsen, Methods and devices used to measure friction in rolling, Proceedings of the Institution of Mechanical Engineers, Part B: Journal of Engineering Manufacture. 220 (2006) 49–57. <https://doi.org/10.1243/095440506X77580>.
- [190] National Instruments, User Manual SCXI-1520, (2009). <https://www.ni.com/pdf/manuals/372583e.pdf> (accessed December 21, 2019).
- [191] Pico Technology, User Manual USB TC-08: 8-channel thermocouple data logger, (2009). <https://www.picotech.com/download/datasheets/usb-tc-08-thermocouple-data-logger-data-sheet.pdf> (accessed May 22, 2020).
- [192] J.C. Vickerman, SIMS, Time-of-flight, and Surface Analysis, in: K.H.J. Buschow (Ed.), Encyclopedia of Materials: Science and Technology, Elsevier, 2001: pp. 8624–8628. <https://doi.org/10.1016/B0-08-043152-6/01538-2>.
- [193] ION-TOF GmbH, Brochure for ION-TOF ToF-Sims 5 : Superior Performance for all SIMS Applications, (2016). [https://www.iontof.com/download/IONTOF\\_TOF-SIMS\\_5\\_Brochure.pdf](https://www.iontof.com/download/IONTOF_TOF-SIMS_5_Brochure.pdf) (accessed July 7, 2019).
- [194] Dassault Systèmes, Abaqus 6.11 Theory Manual, 2011. [http://130.149.89.49:2080/v6.11/pdf\\_books/THEORY.pdf](http://130.149.89.49:2080/v6.11/pdf_books/THEORY.pdf).
- [195] ASTM D4541-09, Standard Test Method for Pull-Off Strength of Coatings Using

- Portable Adhesion Testers, West Conshohocken, PA, 2009. <https://doi.org/10.1520/D4541-09E01>.
- [196] ASTM D3164-03, Standard Test Method for Strength Properties of Adhesively Bonded Plastic Lap-Shear Sandwich Joints in Shear by Tension Loading, West Conshohocken, PA, 2017. <https://doi.org/10.1520/D3164-03R17>.
- [197] ASTM D3528-96, Standard Test Method for Strength Properties of Double Lap Shear Adhesive Joints by Tension Loading, West Conshohocken, PA, 2016. <https://doi.org/10.1520/D3528-96R16>.
- [198] ASTM D903-98, Standard Test Method for Peel or Stripping Strength of Adhesive Bonds, West Conshohocken, PA, 2017. <https://doi.org/10.1520/D0903-98R17>.
- [199] ASTM D1876-08, Standard test method for peel resistance of adhesives (T-Peel test), West Conshohocken, PA, 2015. <https://doi.org/10.1520/D1876-08R15E01>.
- [200] J. Comyn, Contact angles and adhesive bonding, *International Journal of Adhesion and Adhesives*. 12 (1992) 145–149. [https://doi.org/10.1016/0143-7496\(92\)90045-W](https://doi.org/10.1016/0143-7496(92)90045-W).
- [201] A. Rudawska, Assessment of surface preparation for the bonding/adhesive technology, in: A. Rudawska (Ed.), *Surface Treatment in Bonding Technology*, Academic Press, 2019: pp. 227–275. <https://doi.org/10.1016/b978-0-12-817010-6.00009-6>.
- [202] R.P. Woodward, FTÅ200 Measurement Capabilities, First Ten Ångstroms Technical Paper. (2003). <https://www.jascoinc.co.jp/products/contact-angle/pdf/04.pdf> (accessed August 26, 2020).
- [203] J. Ye, D.L. Burris, T. Xie, A Review of Transfer Films and Their Role in Ultra-Low-Wear Sliding of Polymers, *Lubricants*. 4 (2016) 1–15. <https://doi.org/10.3390/lubricants4010004>.
- [204] C. Gachot, A. Rosenkranz, L. Reinert, E. Ramos-Moore, N. Souza, M.H. Müser, F. Mücklich, Dry friction between laser-patterned surfaces: Role of alignment, structural wavelength and surface chemistry, *Tribology Letters*. 49 (2013) 193–202. <https://doi.org/10.1007/s11249-012-0057-y>.
- [205] C. Gachot, A. Rosenkranz, S.M. Hsu, H.L. Costa, A critical assessment of surface texturing for friction and wear improvement, *Wear*. 372–373 (2017) 21–41. <https://doi.org/10.1016/j.wear.2016.11.020>.

- [206] B. Zhang, W. Huang, J. Wang, X. Wang, Comparison of the effects of surface texture on the surfaces of steel and UHMWPE, *Tribology International*. 65 (2013) 138–145. <https://doi.org/10.1016/j.triboint.2013.01.004>.
- [207] D. He, S. Zheng, J. Pu, G. Zhang, L. Hu, Improving tribological properties of titanium alloys by combining laser surface texturing and diamond-like carbon film, *Tribology International*. (2015) 20–27. <https://doi.org/10.1016/j.triboint.2014.09.017>.
- [208] R.A.J. Van Ostayen, A. Van Beek, Thermal analysis of an LPV test-rig, *Tribology International*. 32 (1999) 33–38. [https://doi.org/10.1016/S0301-679X\(99\)00006-7](https://doi.org/10.1016/S0301-679X(99)00006-7).
- [209] J. Piňos, MikmekovÁ, L. Frank, About the information depth of backscattered electron imaging, *Journal of Microscopy*. 266 (2017) 335–342. <https://doi.org/10.1111/jmi.12542>.
- [210] L.F. Richardson, P. Trans, R.S. Lond, The approximate arithmetical solution by finite differences of physical problems involving differential equations, with an application to the stresses in a masonry dam, *Philosophical Transactions of the Royal Society of London. Series A, Containing Papers of a Mathematical or Physical Character*. 210 (1911) 307–357. <https://doi.org/10.1098/rsta.1911.0009>.
- [211] M. Sherburn, *Geometric and Mechanical Modelling of Textiles (PhD Dissertation)*, University of Nottingham, 2007. <http://eprints.nottingham.ac.uk/10303/1/thesis-final.pdf>.
- [212] D.G. Flom, R. Komanduri, Some indentation and sliding experiments on single crystal and polycrystalline materials, *Wear*. 252 (2002) 401–429. [https://doi.org/10.1016/S0043-1648\(01\)00879-1](https://doi.org/10.1016/S0043-1648(01)00879-1).
- [213] S.E. Kadijk, A.B. Van Groenou, Wear anisotropy of MnZn ferrite part I: Recorder and sphere-on-tape experiments, *Wear*. 139 (1990) 93–113. [https://doi.org/10.1016/0043-1648\(90\)90211-R](https://doi.org/10.1016/0043-1648(90)90211-R).
- [214] T.J. Joyce, P. Thompson, A. Unsworth, The wear of PTFE against stainless steel in a multi-directional pin-on-plate wear device, *Wear*. 255 (2003) 1030–1033. [https://doi.org/10.1016/S0043-1648\(03\)00084-X](https://doi.org/10.1016/S0043-1648(03)00084-X).
- [215] D. Nečas, M. Vrbka, I. Křupka, M. Hartl, The effect of kinematic conditions and synovial fluid composition on the frictional behaviour of materials for artificial joints,

- Materials. 11 (2018) 1–12. <https://doi.org/10.3390/ma11050767>.
- [216] B.B. Seedhom, D. Dowson, V. Wright, E.B. Longton, A technique for the study of geometry and contact in normal and artificial knee joints, *Wear*. 20 (1972) 189–199. [https://doi.org/10.1016/0043-1648\(72\)90381-X](https://doi.org/10.1016/0043-1648(72)90381-X).
- [217] H. Endoh, B.B. Seedhom, T. Takeda, Mobility, Stability and Stress in Artificial Knees, *Engineering in Medicine*. 7 (1978) 93–100. [https://doi.org/10.1243/emed\\_jour\\_1978\\_007\\_024\\_02](https://doi.org/10.1243/emed_jour_1978_007_024_02).
- [218] X.H. Wang, H. Li, X. Dong, F. Zhao, C.K. Cheng, Comparison of ISO 14243-1 to ASTM F3141 in terms of wearing of knee prostheses, *Clinical Biomechanics*. 63 (2019) 34–40. <https://doi.org/10.1016/j.clinbiomech.2019.02.008>.
- [219] S.M. Yeo, A.A. Polycarpou, Fretting experiments of advanced polymeric coatings and the effect of transfer films on their tribological behavior, *Tribology International*. 79 (2014) 16–25. <https://doi.org/10.1016/j.triboint.2014.05.012>.
- [220] M. Qiu, Y. Miao, Y. Li, L. Chen, R. Hu, J. Lu, Effects of woven liners treated by LaCl<sub>3</sub> or CeO<sub>2</sub> solution on film formation mechanisms of self-lubricating radial spherical plain bearings, *Industrial Lubrication and Tribology*. 68 (2016) 308–314. <https://doi.org/10.1108/ILT-04-2015-0048>.
- [221] J. Lu, M. Qiu, Y. Li, Numerical analysis of self-lubricating radial spherical plain bearings and investigations on fatigue damage mechanisms of the liner, *Tribology International*. 96 (2016) 97–108. <https://doi.org/10.1016/j.triboint.2015.12.025>.
- [222] M. Pierce, *Geometry, Plane, Solid and Spherical*, in *Six Books*, Baldwin and Cradock Publisher, London, 1830.
- [223] J. Bonse, S. Hohm, S. V. Kirner, A. Rosenfeld, J. Kruger, Laser-Induced Periodic Surface Structures-A Scientific Evergreen, *IEEE Journal on Selected Topics in Quantum Electronics*. 23 (2017) 1–17. <https://doi.org/10.1109/JSTQE.2016.2614183>.
- [224] S. Banerjee, Simple derivation of Young, Wenzel and Cassie-Baxter equations and its interpretations, *ArXiv Open-Access Archive (Condensed Matter:Materials Science)*. 1 (2008) 1–10. <http://arxiv.org/abs/0808.1460>.
- [225] E. Bormashenko, Why does the Cassie-Baxter equation apply?, *Colloids and Surfaces A: Physicochemical and Engineering Aspects*. 324 (2008) 47–50.

<https://doi.org/10.1016/j.colsurfa.2008.03.025>.

- [226] W. Li, G. Fang, Y. Li, G. Qiao, Anisotropic wetting behavior arising from superhydrophobic surfaces: Parallel grooved structure, *Journal of Physical Chemistry B*. 112 (2008) 7234–7243. <https://doi.org/10.1021/jp712019y>.
- [227] J.P. Youngblood, T.J. McCarthy, Ultrahydrophobic polymer surfaces prepared by simultaneous ablation of polypropylene and sputtering of poly(tetrafluoroethylene) using radio frequency plasma, *Macromolecules*. 32 (1999) 6800–6806. <https://doi.org/10.1021/ma9903456>.
- [228] Y. Chen, B. He, J. Lee, N.A. Patankar, Anisotropy in the wetting of rough surfaces, *Journal of Colloid and Interface Science*. 281 (2005) 458–464. <https://doi.org/10.1016/j.jcis.2004.07.038>.
- [229] K.J. Kubiak, T.G. Mathia, Anisotropic wetting of hydrophobic and hydrophilic surfaces - Modelling by Lattice Boltzmann Method, *Procedia Engineering*. 79 (2014) 45–48. <https://doi.org/10.1016/j.proeng.2014.06.307>.
- [230] W. Choi, A. Tuteja, J.M. Mabry, R.E. Cohen, G.H. McKinley, A modified Cassie-Baxter relationship to explain contact angle hysteresis and anisotropy on non-wetting textured surfaces, *Journal of Colloid and Interface Science*. 339 (2009) 208–216. <https://doi.org/10.1016/j.jcis.2009.07.027>.